UNIVERSIDADE BEIRA INTERIOR

Numerical Modelling of Complex Flows With Sprays Including Electrostatic Effects

Mohammad-Reza Pendar

Thesis submitted for the degree of Doctor of Philosophy in
Mechanical Engineering
(3rd Cycle of Studies)

Supervisor: Prof. Dr. José Carlos Páscoa Marques

Covilhã, October of 2021

Numerical Modelling of Complex Flows With Sprays Including Electrostatic Effects

Jury of the Doctoral Exam

The doctoral exam took place on October 6, 2021, at 14:30, with a jury consisting of the following members:

Doctor Paulo Jorge dos Santos Pimentel de Oliveira, Full Professor at University of Beira Interior;

Doctor João Manuel Melo de Sousa, Associate Professor at Instituto Superior Técnico University of Lisbon;

Doctor José Carlos Páscoa Marques, Associate Professor at University of Beira Interior;

Doctor Miguel Rosa Oliveira Panão, Assistant Professor at faculty of Science and Technology of University of Coimbra;

Doctor André Resende Rodrigues da Silva, Assistant Professor at University of Beira Interior;

Doctor Ana Sofia Oliveira Henriques Moita, Assistant Professor at Military Academy of Lisbon.

Dedication

This thesis work is dedicated to my wife, Sahar, who has been a constant source of support and encouragement during the challenges of graduate school and life. I am truly thankful for having you in my life.

Acknowledgment

First of all I would like to express my sincere thanks to my advisor, Prof Jose Páscoa for believing in me and for his invaluable guidance and support during my graduate studies. Thank you Prof Páscoa, as much for the entire thing that you have provided for me to work. I really enjoyed the moments that we had conversations about work and future and everything, specially the moments that you put me back in the correct way of thinking. It was a great pleasure and honor to have your support. It will be a pleasure for me to have opportunities to do research under your supervision.

I want to thank all my colleges in the ClusterDEM lab that made me happy and made the working condition full of energy and happiness. Indeed, besides being colleagues you were my truly friends that helped me to adapt myself to the new life in Covilhã.

Thank you All

Resumo

Durante as últimas duas décadas os pulverizadores electroestáticos de bocal rotativo (ERBSs) atraíram a atenção de diversos investigadores da indústria de revestimentos devido possuírem uma eficiência de transferência (TE) e desempenho de revestimento elevados, possuem ainda efeitos ambientais mais reduzidos e contribuem para a diminuição de custos. Nesta tese foi desenvolvido um algoritmo 3D integrado Euleriano-Lagrangiano de modo a investigar os comportamentos fundamentais do escoamento num pulverizador electroestático de bocal rotativo (ERBS), em particular durante a formação das gotículas e respetiva deposição no alvo. Este algoritmo, que mostrou ser eficiente, contêm um modelo para o campo de escoamento de ar, inclui a dinâmica da pulverização, o campo elétrico, a carga nas gotículas, e ainda a monitorização da trajetória das gotículas e a dinâmica da película de parede. A dinâmica de fluidos é simulada pela resolução das equações de *Navier-Stokes* para escoamento compressível 3D. O escoamento é do tipo não-estacionário e a turbulência é modelada usando uma abordagem *"Large eddy Simulation"* (LES), enquanto o movimento das partículas é simulado por uma metodologia de seguimento que considera a distribuição e tamanho das gotículas. O algoritmo de cálculo é implementado na estrutura do pacote OpenFOAM.

É proposta uma condição inicial para a distribuição das partículas no ERBS a qual corresponde às condições experimentais em aplicações práticas. O presente trabalho contém uma análise sistemática do comprimento da zona de recirculação, do vórtice toroidal, do fenómeno de pulverização excessiva e das características do campo de escoamento tais como: velocidade média, pressão, energia cinética turbulenta e flutuações de velocidade. Além disso, os resultados apresentados descrevem valores exatos de tamanho, distribuição, velocidade e trajetória das partículas no ERBS. Estes resultados são importantes para a indústria de revestimentos, em particular para otimizar as suas condições de funcionamento. O efeito dos parâmetros de funcionamento, tais como: velocidade de rotação do bocal, ar de conformação, caudal de tinta, valores de carga elétrica e distribuições de tamanho das gotículas são considerados com precisão. Os resultados indicam que o caudal de escoamento de ar-tinta e a tensão aplicada como parâmetros principais de funcionamento, os quais afetam

profundamente a forma da pulverização. O efeito da velocidade de rotação do bocal, em comparação com outros parâmetros, é dominante. A distribuição de tinta pulverizada obtida no presente trabalho foi validada em comparação com resultados experimentais de revestimento, tendo mostrado uma precisão adequada.

A investigação dos diversos modelos de separação, primários e secundários, é um dos principais objetivos deste trabalho, em particular de modo a prever o tamanho das gotículas com precisão. Os modelos de Reitz-KHRT, Reitz-Diwakar, Pilch-Erdman e um novo modelo TAB modificado são examinados com cuidado de modo a prever o processo de separação secundária no ERBS. A função de cálculo da pelicula na parede, que também foi implementada, é capaz de prever o transporte na camada limite sobre o alvo. Este estudo também apresenta uma avaliação de desempenho do ERBS com foco particular na carga das gotículas, no campo elétrico, nas condições ambientes, nomeadamente através da proposta e implementação de um anel de efeito sobre o campo elétrico que, por sua vez, influencia o escoamento de ar turbulento e ainda a fase discreta das gotículas atomizadas. Os resultados indicam que o funcionamento do anel de controlo melhora o desempenho e a eficiência de transferência (TE) do ERBS e, para além disso, ajuda a harmonizar a direção das gotículas de tinta carregadas. Também, um novo sistema de pulverização eletrostática usando lâminas retráteis de alta tensão ou anel de controle ajustável de alta tensão é apresentado no estudo atual como uma patente recente.

Além disso, são ainda apresentadas outras aplicações para o código implementado, as quais mostram a sua utilidade e versatilidade. Primeiramente, o modelo mais sofisticado da pulverização é usada para obter um conhecimento mais aprofundado sobre os mecanismos de transmissão de doenças transportadas por gotículas de saliva, como sejam gotículas atomizadas pelo espirro, tosse ou respiração. Numa outra aplicação, foi usado o modelo do campo elétrico implementado, sem injeção de gotículas, de modo a simular de forma precisa o escoamento do plasma, provocado pela diferença de potencial, em múltiplos atuadores a plasma de barreira dielétrica de descarga (DBDPA), neste caso sobre um perfil alar 3D.

Palavras-Chave

Pulverizador electroestático de bocal rotativo (ERBS); Modelo numérico de revestimento por pulverização; OpenFOAM; Bicos de injeção de ar de conformação; “Large eddy simulation” (LES); Separação de gotículas; Espessura da pelicula de revestimento; Diâmetro médio de Sauter (SMD); Escoamento de ar de conformação; Partículas carregadas; Simulação de pintura electroestática; Bocal rotativo de alta velocidade; Distribuição de tamanho de gotículas; Rácio carga-massa; Trajetória de partículas; Anel de controlo de alta tensão; Gotículas de saliva transportadoras de doença; Atuadores a plasma; Controlo ativo de escoamento.

Abstract

During the past two decades, the Electrostatic Rotary Bell Sprayers (ERBSs), because of their superior transfer efficiency (TE) and coating performance, lower environmental destructive effects and cost decrement, attract the attention of many researchers in the coating industry. In this thesis, we developed a 3D comprehensive Eulerian-Lagrangian algorithm in order to investigate the fundamental behaviors of the flow in an electrostatic rotary bell sprayer (ERBS) during the formation of the droplets and depositing on a target. This efficient extended algorithm contains a model for airflow field, spray dynamics, electric field, droplet charge, droplet trajectory tracking and wall film dynamics. The fluid-dynamics is simulated by solving the unsteady 3D compressible Navier-Stokes equations. Unsteady flow is computed by using a Large eddy simulation (LES) turbulence approach, while the motion of the particles is simulated by tracking the droplet size distribution approach. The algorithm is implemented under the framework of the OpenFOAM package.

Creating an initial condition of the particle approach has been proposed that is matched with practical applications. The present work contains a systematic analysis of the recirculation zone length, the toroidal vortex, the overspray phenomena and the flowfield characteristics like mean velocity, pressure, turbulent kinetic energy and velocity fluctuation. Also, the presented results describe exact values for the size, distribution, velocity, and trajectory of the particles in the ERBS. These results are important for coating industries to optimize their working conditions. The effect of operational parameters like bell rotational speed, shaping air and paint flow rate, electrical charge values and droplet size distributions are considered precisely. The results indicate as a main operating parameter the air-paint flow rate with voltage level deeply affecting the spray shape. The effect of the bell rotational speed in comparison with other parameters is dominant. The paint spray distribution obtained in the present work is validated against coating experimental results with suitable accuracy.

Investigation of the various primary and secondary breakup models is one of the main goals of this work to predict the droplet size more precisely. The Reitz-KHRT, Reitz-Diwakar, Pilch-Erdman and the newly modified TAB model are examined in order to predict the secondary breakup process in the ERBS. Here, the implemented wall film function is able to predict the transport in the boundary layer over the target. This study also presents a performance evaluation of the ERBS with a particular focus on droplet charge, electric field, ambient conditions with the implementation of a high-voltage control-ring field pattern effect into the fully turbulent airflow and by including the atomized droplets discrete phase. The results indicate that the new proposal of

using a control-ring operation improves the performance and transfer efficiency (TE) of the ERBS, and it also helps to harmonize the direction of the charged paint droplets.
Furthermore, a novel electrostatic spraying system by using high-voltage retractable blades or high-voltage adjustable control ring is also presented in the current study as a recent patent.
Also, some other useful applications of the implemented code are presented. First, the modified spraying part of the code is used, leading to a deeper understanding of the saliva-disease-carrier droplets transmission mechanisms as an atomized droplets during sneezing, coughing, or even exhaling. This is particularly important to ensure safety conditions in the work environment. Second, the implemend electrical field that was added to the code is considered without injecting droplets to accurately simulate the plasma flow by using a multi dielectric-barrier-discharge (DBD) plasma actuator over a 3D-airfoil difference. This shows the versatility of the developed model.

Keywords

Electrostatic rotary bell sprayer (ERBS); Numerical spray coating; OpenFOAM; Shaping air nozzles; Large eddy simulation (LES); Droplet breakup; Coating film thickness; Sauter mean diameter (SMD); Shaping airflow; Charged particles; Electrostatic painting simulation; High-speed rotary bell; Droplet size distribution; Charge-to-mass ratio; Particle trajectories; High-voltage control ring; Saliva-disease-carrier droplets; Plasma actuators; Active flow control.

Contents

1 Introduction and Objectives 1

1.1. Introduction 1

1.2 Literature Survey 4

1.2.1. Atomization and formation of droplet 7

1.2.2. Droplets charging mechanisms 8

1.2.2.1. Corona charging 9

1.2.2.2. Triboelectric charging 10

1.2.2.3. Induction and conduction charging 10

1.3 Objectives of current research 11

1.3.1 Numerical simulation of electrostatic coating process 11

1.4 Thesis organization 12

2 Implementation of numerical electrostatic spray painting transfer processes modelling in rotary bell cup for automotive painting 15

Abstract 15

2.1 Introduction 16

2.2. Governing Equations for ERBS Flow 19

2.2.1 Continuous phase: Large Eddy Simulation (LES) turbulence model 20

2.2.2 Electric Field 20

2.2.3 Discrete phase 21

2.3. Numerical setup 23

2.3.1 The Rotating Bell Cup Problem 23

2.3.2 Boundary Conditions 26

2.3.3 Discretization Schemes 29

2.3.4. Pressure-Velocity Coupling 30

2.3.5 Solution convergence and procedure 31

2.3.6 Grid Sensitivity Analysis 32

2.4. Results and Discussion 33

2.4.1 The Solver Validation: Comparison with the experimental and numerical data 33

2.4.2 Analysis of ERBS flows 36

2.4.2.1 Electrical analysis of the particle injected from single spray inlets 36

2.4.2.2 Representation of the discrete Phase 37
2.4.2.3 Features of the unsteady continuous phase 44
2.4.2.4 Boundary-Layer investigation close to the Bell Cup 51
2.5. Conclusions 54
3 Atomization and spray characteristics around an ERBS using various operational models and conditions 55
Abstract 55
3.1. Introduction 56
3.2. Governing Equations: Breakup Models 58
3.2.1. Modified TAB Breakup Model 58
3.2.2 Pilch-Erdman Breakup Model 59
3.2.3 Reitz-Diwakar Breakup model 60
3.2.4 Reitz-KHRT Hybrid Breakup Model 61
3.3. Numerical Procedure 62
3.4. Results and discussion 67
3.4.1 Code Validation 67
3.4.2 Spray Characteristics 70
3.5. Conclusions 85
4 Analysis of droplets charge and size distribution in the electrostatic coating process 87
Abstract 87
4.1. Introduction 87
4.2. Governing equations: Paint film formula 90
4.2.1. Discrete paint droplets phase: two-way coupling 90
4.2.1.1 Evolution of mass 90
4.2.1.2 Evolution of momentum 91
4.2.1.3 Evolution of energy 91
4.2.1.4 Evolution of breakup process 91
4.2.2. Liquid paint film equations 92
4.2.2.1. Mass conservation equation of film 92
4.2.2.2. Momentum conservation equation of film 92
4.2.2.3. Energy conservation equation of film 92
4.2.3. Film thickness equation 93
4.3. Simulation setup 93
4.4. Results and Discussion 102
4.5. Conclusion 120

5 Other useful applications of the implemented code: (I) Investigation of aerosol dispersion in the indoor work environment and (II) Numerical Investigation of Plasma Actuator Effects on Flow Control over a Three-dimensional Airfoil with a Sinusoidal Leading Edge 121

Abstract 121

5.1. Introduction 122

5.1.1. Aerosol dispersion investigation 122

5.1.2. Flow control with DBD plasma actuators 124

5.2. Governing Equations 127

5.2.1. Governing Equations for aerosol dispersion investigation 127

5.2.1.1. Continuous phase 127

5.2.1.2 Discrete Phase 128

5.2.2. Governing Equations for flow control with DBD plasma actuators 130

5.3. Numerical setup 132

5.3.1. Numerical simulation methodology for aerosol dispersion investigation 132

5.3.2. Numerical procedure for flow control with DBD plasma actuators 136

5.4. Results and discussion 141

5.4.1. Results of aerosol dispersion 141

5.4.2. Results of flow control with DBDPA 156

5.5. Conclusion 174

6 Electrostatic Sprayer Based on High-voltage Retractable Blades or High-voltage Adjustable Control Ring 177

6.1. Electrostatic Sprayer Based on Retractable Blades or Adjustable Control Ring System Definition 177

6.2. Description 178

6.2.1 Technical Domain 178

6.2.2 Summary 178

6.2.3 Prior Art 178

6.3. General description 180

6.4. Description of the Drawings 182

6.5. Matching numbers 188

6.6. Detailed Description 189

6.7. Application Examples 192

6.8. Claims 192

7 Final remarks, conclusions and future work 194
7.1 Final Remarks and Conclusions 194
7.2 Recommendations for future work 197
Bibliography 199
Appendix A 215
Publications and Achievements During Current Project 215
A.1 Articles in international journals 215
A.2 Articles in international conferences 215
A.3 Patent 216

List of Figures

1.1 The photograph of the PPH 308 high-speed electrostatic rotary bell sprayer (ERBS). Image gently provided by SAMES-KREMLIN (Stevenin et al, 2015; SAMES Technology, 2019)..... 1
1.2 Schematic representation of a standard automotive spray booth (SAMES Technology, 2019)..... 2
1.3 Fundamental problems in automotive painting systems..... 3
1.4 Fundamental problems in automotive conventional coating systems..... 3
2.1 Paint particles electrical charging procedure for electrostatic spray painting process in the ERBS, acted forces on the charged particle..... 19
2.2 The computational domain with all the applied dimensions which non-dimensions by the diameter of the bel cup..... 24
2.3 Schematic representation of a standard automotive spray booth..... 25
2.4 A description for the electrostatic spray coating procedure in the ERBS..... 25
2.5 Electrostatic field and flow field boundary conditions in the overall computational domain..... 26
2.6 Details of the implemented boundary condition in the area close to the bell cup of the ERBS..... 27
2.7 The photograph of the PPH 308 high-speed electrostatic rotary bell sprayer (ERBS). Image gently provided by SAMES-KREMLIN (Stevenin et al, 2015; SAMES Technology, 2019)..... 27
2.8 Flowchart of the iterative procedure in the electrostatic spray coating process in the current numerical study..... 29
2.9 The turbulence statistics: The Power spectrum density (PSD) for the turbulent kinetic energy..... 30
2.10 PIMPLE solution flowchart procedure used in OpenFOAM..... 31
2.11 Convergence of residuals for a typical spraying simulation $\omega_{bell} = 30K\,rpm$, $VOLT_{cup} = -90\,kV$: (a) entire run time (b) first time steps (c) last time steps..... 32
2.12 Mesh distribution around the electrostatic rotary bell sprayers (ERBS) which is used in the current simulation..... 33
2.13 (a) Evolution the recirculation region length with the blockage ratio DR2. (b) Comparisons of dimensionless values of computed velocity with the experimental data. (Martinez, 2013) (c) Comparison of the potential field and (d) the electrostatic field distribution between the cup and the target along the gun centerline with the numerical results (Viti et al., 2008)..... 34
2.14 Spray paint particle distribution over the ERBS in various operational condition: experimental results were taken by the low-speed photographer (Martinez, 2013) (right column) Numerical results of code implemented in the current study (left column) (Reference conditions: $\dot{m}_{air} = 350\,norm.l/\min$, $\dot{m}_{paint} = 350\,ml/\min$, $\omega_{bell} = 30K\,rpm$, $VOLT_{cup} = -60\,kV$)..... 35
2.15 The Computational domain and mesh of a cube with a spray inlet..... 36
2.16 The cut plane through the 3D domain shows the electrostatic fields. Screen capture of the color scale of the droplets is according to their velocity..... 37

2.17 Contours of the potential field and particle color is according to their diameter..... 37
2.18 Particle trajectories colored by their velocity magnitude, and the direction of the arrows representing their velocity vectors: Comparisons for various electrostatic voltages and rotational speeds captured during one complete spraying cycle (T)..... 39
2.19 The formation of the paint particles at the initial time near the bell cup extracted from numerical data..... 40
2.20 The qualitative comparison of transfer efficiency (TE) for the injected particles..... 41
2.21 Paths of the paint particles in the high-speed rotary bell sprayer..... 42
2.22 The two rows correspond, respectively, to (a) mass and (b) diameter of the particle. Applicator condition parameter: $\omega_{bell}=30\,krpm$, $VOLT_{cup}=-90\,kV$, $\dot{m}_{air}=150\,norm.l/\min$, $\dot{m}_{paint}=150\,l/\min$, $N=175000$..... 43
2.23 The three columns correspond to 3D views of particles trajectory with their velocity magnitude ($N=175000$)..... 44
2.24 Time evolution of film thickness on the target surface, LES, $VOLT_{cup}=-90\,kV$, $\omega_{bell}=30\,krpm$..... 44
2.25 Temporal growth of the paint film thickness..... 45
2.26 Visualizing of five consecutive temporal frames of velocity with the shaping airflow obtained during a complete cycle (T) ($\omega_{bell}=30\,krpm$, $D=0.25\,m$, $VOLT_{cup}=-90\,kV$, $\dot{m}_{air}=150\,norm.l/\min$, $\dot{m}_{paint}=150\,l/\min$)..... 46
2.27 Visualization of the potential field as 3D iso-surface among the ERBS and target..... 46
2.28 Contours of the x-velocity (m/s) component along the vertical plane of symmetry..... 47
2.29 Detailed 3D views of the toroid shape inside the ERBS and created vortex shedding from the toroid-shaped vortex tube: Time evolution during one spraying cycle (T) ($\omega_{bell}=30K\,rpm$, $VOLT_{cup}=-90\,kV$, $\dot{m}_{air}=150\,norm.l/\min$, $\dot{m}_{paint}=150\,l/\min$)..... 48
2.30 Dynamic pressure contours at three different distances X, ($\omega_{bell}=30\,krpm$, $VOLT_{cup}=-90\,kV$, $\dot{m}_{air}=150\,norm.l/\min$, $\dot{m}_{paint}=150\,l/\min$)..... 49
2.31 Instantaneous (right frames) and mean (left frames) velocity contours at ($\omega_{bell}=30\,krpm$, $VOLT_{cup}=-90\,kV$, $t=35$ (ms))..... 49
2.32 Comparison of different turbulence models (LES/ k-ω SST) at the same time and boundary condition..... 50
2.33 Contour of velocity (m/s) with visualization of streamline via LIC (Line Integral Convolution) approach along 2D plane..... 50
2.34 Turbulent stress distribution ($<u'u'>,<u'v'>,<u'w'>,<v'v'>,<v'w'>,<w'w'>$) are plotted in the radial direction exactly close to the rim that normalized by the initial air velocity of the nozzle (U_N), LES and k-ω SST approaches, various bell rotational speed *N*= 20, 30, 40 krpm..... 52
2.35 Turbulence kinetic energy (TKE) distribution at the same operational condition of Fig. 2.29..... 53
2.36 Comparison of mean velocity at the same operation condition and position of Fig. 2.29..... 53
2.37 Radial profiles of longitudinal velocity, comparison between experimental results (Martinez, 2013) and numerical results of the code implemented in the current study..... 54
2.38 Comparisons of pressure distribution in the same location of Fig. 2.29 54

which normalized by atmospheric air pressure..... 62
3.1 A schematic diagram of the electrostatic spray deposition process and mechanism of the coating..... 63
3.2 (a) A schematic visualization of the droplet trajectories and the shaping airflow dynamics around the ERBS (b) The effect of the rotational speed increase on the shaping airflow (c) Two various bell cup head with a diameter of 50 mm and 65 mm..... 64
3.3 The distribution of the structures meshes around the ERBS that is implemented in the current study..... 65
3.4 Iterative solution and progressive steps for the electrostatic spraying analysis in the current work..... 66
3.5 The computational domain dimensions and computing boundary condition (airflow field and electrostatic field)..... 67
3.6 Propagation of the paint film on the rotating bell cup surface: experimental snapshots (Shen et al., 2019) (a-c) and current numerical results (d-f) ($\omega_{bell} = 30kRPM$, $\dot{m}_{paint} = 400ml/\min$)..... 68
3.7 Comparison of the droplet distribution: Infrared images of experimental data (Temperature contour) (Darwish Ahmad et al. 2018) (right frames), Current numerical results (Velocity magnitude value) (left frames) ($\dot{m}_{air} = 150LPM$, $\dot{m}_{paint} = 0.1LPM$, $Modified\,TAB$)..... 69
3.8 3D views of the airflow outward the ERBS; various rotational speeds of the bell cup at a fixed $\dot{m}_{air} = 150LPM$ and $Reynolds = 5.1\times10^3$: (a) Schlieren images of the experimental result (Darwish Ahmad et al., 2018) and (b) Contour of the velocity and air density obtained from the numerical results..... 70
3.9 Longitudinal velocity distribution comparison of the current work with the experimental result of Stevenin et al. (2015)..... 71
3.10 Spray shapes for various breakup models at $t = 42\,ms$ ($\omega_{bell} = 25kRPM$, $SF_{Droplet} = 100$)..... 72
3.11 Time evolution of the spray patterns for the modified TAB breakup model ($\omega_{Bell} = 25kRPM$, $SF_{Droplet} = 40$)..... 73
3.12 3D views of the spray pattern for two different ω_{Bell}. Inset frames illustrate magnified views of (a) mechanism of instabilities (b) Overspray flow (c-d) rebounded torus-shaped droplet..... 74
3.13 Visualization of 3D paint film wetted area on the target surface for different ω_{Bell} 74
3.14 3D paint film displaying on the workpiece surface for $d_{cup} = 65mm$ ($\omega_{Bell} = 40kRPM$)..... 75
3.15 Paint film thickness distribution for different breakup model and ω_{Bell} 75
3.16 Thickness deposition of the paint droplets along the target surface for various d_{cup} 75
3.17 Changing of the shaping airflow rate at fixed bell cup rotational speed ($\omega_{Bell} = 10kRPM$, $t = 20ms$, $SF_{Droplet} = 20$)..... 77
3.18 Velocity magnitude contour (m/s) with the streamline pattern, which is visualized by the LIC (Line Integral Convolution) method in different ω_{Bell} and d_{cup} 77
3.19 Shows the developed velocity contour with streamline in the ERBS with $d_{cup} = 65mm$, $modified\,TAB$, (a) $\omega_{Bell} = 20kRPM$ (b) $\omega_{Bell} = 50kRPM$ .....

3.20 Periodical time evolution of the electrostatic spraying pattern ($d_{cup} = 50mm$, $modified\,TAB$, $\omega_{Bell} = 25kRPM$)..... 78
3.21 Radial mean velocity profiles for various breakup models and ω_{Bell} in the turbulent boundary layer close to the cup rim..... 78
3.22 3D visualization of the droplet trajectory, exactly over the bell cup surface that is valued by their velocity magnitude ($SF_{Droplet} = 40$, $t = 3ms$)..... 80
3.23 (a) The size distribution of the particle at different rotational speeds (b) ($Modified\,TAB$, $SF_{Droplet} = 40$, $t = 40ms$)..... 80
3.24 Sprayed droplet size distribution in the computational domain..... 82
3.25 Sprayed droplet size distribution in the computational domain for the various bell cup diameter: (a) $d_{cup} = 50mm$ (b) $d_{cup} = 65mm$ 82
3.26 The x-axis in the plots indicates the droplet velocity magnitude and the y-axis shows the number of the droplet, which is located in the computational domain..... 82
3.27 Sprayed droplet velocity magnitude distribution on the computational domain for the various bell cup diameters: (a) $d_{cup} = 50mm$ (b) $d_{cup} = 65mm$ 83
3.28 Compared mean velocity near the bell cup rim (a) various airflow rates. (b) different breakup model..... 83
3.29 Q-criterion visualization of the vortical structures (by using mean velocity)($t = 42ms$): effect of rotational speed (b, c, d) and bell diameter (a,b)..... 84
4.1 (a) Schematic representation of the electrostatic spray deposition process; (b) Schematic view of the automotive spray coating process, droplet atomization, induction and corona charging procedure..... 95
4.2 The PPH 308 high-speed ERBS photograph that was provided by SAMES-KREMLIN (Stevenin et al., 2015; SAMES Technology 2019)..... 96
4.3 Detailed visualization of the computational domain dimension and the flow field boundary conditions: (a) overall computational domain; (b) close to the bell cup surface of the ERBS..... 97
4.4 Visual representation of the electrostatic equipotential lines distribution around ERBS (a) with a surround control ring field pattern (b) without a spray control-ring..... 98
4.5 Illustration of grid distribution around the sprayer with and without the high voltage control-ring (a-e)..... 100
4.6 Comparison of the airflow: (a) angle (Darwish Ahmad et al. 2018) (b) longitudinal velocity (Stevenin et al., 2015)..... 101
4.7 Comparison of the current numerical results with experimental data: (a) atomized droplet distribution (Darwish Ahmad et al. 2018) (b) paint film propagation (Shen et al., 2019)..... 102
4.8 Comparison of the paint spray plume field (a) with and (b) without the presence of a control-ring field pattern ($V_{cup} = -40kV$, $V_{Ring} = -40kV$, $\rho_m^q = -0.5mC/kg$, $\omega_{Bell} = 30kRPM$, $SF_{Droplet} = 200$, $t = 70ms$)..... 103
4.9 3D views of the paint spray field pattern for different voltages in the case in which the control-ring is present (a-e) ($\rho_m^q = -0.5mC/kg$, $\omega_{Bell} = 30kRPM$, $SF_{Droplet} = 200$, $t = 70ms$)..... 105
4.10 Comparison of different charge to mass ratio (ρ_m^q) for the atomized droplet (a, b) ($V_{Ring} = -40kV$, $V_{cup} = -40kV$, $t = 70ms$, $\omega_{Bell} = 30kRPM$, $SF_{Droplet} = 200$)..... 106
4.11 (a) Flow velocity magnitude contour with streamline over the distance between the ERBS an target. (b) close-up vie near the rotary bell cup and control-ring surface ($\rho_m^q = 0.5mC/kg$, $V_{Ring} = -40kV$, $V_{cup} = -40kV$, $\omega_{Bell} = 30kRPM$, $SF_{Droplet} = 200$)..... 108

4.12 Bell-cup and control-ring voltage effect on the coating deposition pattern (a-c). Droplet charge values effect on the paint deposition distribution (d)..... 110
4.13 Droplet size distribution: (a) striking on the workpiece (b) missing the goal surface (c) initial size. (e) Position of these droplet over the domain..... 111
4.14 Distributions of the (a) vorticity magnitude, (b) vortex dilatation term, (c) vortex stretching term. ERBS with control-ring (left frames) and without control-ring (right frames) ($\rho_m^q = -0.5 mC/kg$, $V_{Ring} = -40 kV$, $V_{cup} = -40 kV$, $\omega_{Bell} = 30 kRPM$)..... 112
4.15 Deposited droplets pattern illustration on the target under different operating voltages and droplet charge ($\omega_{Bell} = 30 kRPM$, $SF_{Droplet} = 200$)..... 113
4.16 Droplet surface temperature (a) active droplets as a spray plum, (b) deposited droplets on the target surface, (c) inside the rotary bell cup..... 114
4.17 Airflow temperature visualization on the vertical cross-section of the domain during the coating process..... 114
4.18 Densities of the atomized droplets during the coating: (a) spray-plume; (b) deposited droplet..... 115
4.19 3D paint film pattern visualization on the target, produced by the ERBS, with the control-ring field pattern for various: (a) droplet charges and (b) operating voltages..... 116
4.20 3D deposition of the coating film produced by the conventional ERBS for different: (a) operating voltages; (b) initial droplet sizes..... 117
4.21 Paint droplet size distribution under various voltages (a, b) and charge values (c)..... 118
4.22 Sauter Mean Diameter (SMD_{32}) values at different: (a) bell-cup voltage; (b) control ring voltages and; (c) droplet charge values..... 119
4.23 Particle trajectories colored by their size at different voltage and charges..... 119
5.1 The computational domain dimensions and boundary conditions. Case (a) subject facing a table at 0.75 m distance. Case (b) face to face position at 2 m distance. Case (c) meeting position at 1.5 m distance. Case (d) subject facing a table while wearing a face mask. Case (e) subject standing close to the side wall..... 131
5.2 Computational grid with specific refinement near the mouth. The total cell count is about 5.1×10^6 cells..... 132
5.3 Velocity magnitude compared between coarse, medium, and fine grid near the mouth (at a distance of 0.03 m near the mouth)..... 132
5.4 Comparison between the cross-section of humpback whale pectoral flipper and NACA 63_4-021 profile: (a) Flippers on a humpback whale, Photo by Sho Hatakeyama (Hrynuk and Bohl, 2020), (b) Scalloped pattern of tubercles, (c) cross-section of the flipper, (d) NACA 634-021 profile..... 136
5.5 Three dimensional views of the overall computational domain with dimensions and boundary conditions..... 137
5.6 Three-dimensional computational grid created around the NACA 634-021 airfoil. The colored area indicates the fine resolution zone with the presence of the DBD plasma actuators..... 139
5.7 (a) Schematic configuration of two DBD plasma actuators over WLE airfoil ($h_{LE}/c_{ref} = 0.05$, $\lambda_{LE}/c_{ref} = 0.25$, $\alpha = 18^\circ$), and (b) the corresponding boundary conditions. Comparison of the (c) lift coefficient, and (d) drag coefficient with the experimental data of Johari et al. (2007)..... 140
5.8 The distribution of the normalized (a) body force, and (b) electric potential produced by the DBD plasma actuators ($V_{\max} = 16 kV$, $f = 20 kHz$). 141
5.9 A human sneeze: Kinematic visualization of the expelled saliva disease-carrier droplets for cases: (I) Face-to-Face (II) Meeting standing (III) Near the 144

table; (a) t=0.06s, (b) t=0.16s, (c) t=0.3s, (d) t=1 s. (The initial velocity, the total mass, diameter, scale factor and the number of the saliva are $V_{Initial}=14.3ms^{-1}$, $m_{Saliva}=15mg$, $D_{average}=360\mu m$, $D_{\min}=10\mu m$, $D_{\max}=980\mu m$, $SF_{Droplet}=15$ and $N_{Saliva}=95000$, respectively).....

5.10 A human sneeze: Saliva disease-carrier droplets diameter distribution for diverse cases: (I) Face-to-Face (II) Meeting standing (III) Near the table; (a) t=0.06s, (b) t=0.16s, (c) t=0.3s, (d) t=1 s. (Same operational conditions as Fig. 5.4)..... 146

5.11 Comparison of the velocity distribution of saliva droplets for two different sneezes: normal ($V_{Initial}=6.5ms^{-1}$) (blue droplets) and hard ($V_{Initial}=14.3ms^{-1}$) (red droplets); (a) face-to-face position. (b) meeting standing position. (c) near the table position..... 147

5.12 The deposition pattern of micro-droplets of saliva under various operating conditions: (a) $D_{Average}=540\ (\mu\mathrm{m})$ (b) $D_{Average}=390\ (\mu\mathrm{m})$ (c) $D_{Average}=190\ (\mu\mathrm{m})$ (d) $D_{Average}=90\ (\mu\mathrm{m})$..... 149

5.13 Time evolution of the transport processes of saliva droplets as a function of their diameter during a human sneeze ($D_{Average}=90\mu\mathrm{m}$): (a) $V_{Initial}=14.3\ \mathrm{ms}^{-1}$, (b) $V_{Initial}=6.3\ \mathrm{ms}^{-1}$..... 150

5.14 Different modes of interaction between the mask and droplets..... 151

5.15 Sneeze over one cycle with mask: (I) Saliva droplet velocity (II) diameter ($D_{average}=360\mu m$, $V_{Initial}=14.3\ \mathrm{ms}^{-1}$)..... 152

5.16 The interaction between the two phases of gas (air) and fluid (saliva). The arrows illustrate the apparent circulation within the cloud..... 153

5.17 The maximum fall out distance, contamination risk distances, for a broad range of droplet size and velocity ($D_{mean}=90-540\mu m$, $V_{Initial}=6.3-14.3\ ms^{-1}$): maximum (a) length (b) width ($\theta_{inj}=33^{\circ}$, $Mouth\,area=314mm^2$)..... 153

5.18 The velocity of the sprayed cloud during a sneeze as compared with various diameters, for a different time, from expelling to fall out ($V_{Initial}=11.3\ ms^{-1}$)..... 155

5.19 Comparison of various injection angles for a specific sneeze ($V_{Initial}=14.3\ ms^{-1}$, $D_{mean}=90\mu m$)..... 155

5.20 Comparison of various mouth area for a specific sneeze ($V_{Initial}=8.3\ ms^{-1}$, $D_{mean}=290\mu m$)..... 156

5.21 Mean pressure coefficient distribution along the surface of the airfoil with and without the presence of DBD plasma actuators, cases with WLE: (a) α=12°, (b) α=18°..... 157

5.22 Mean pressure coefficient distributions along the surface of the airfoil, comparison between the WLE (at peak) and SLE cases: (a) α=12°, (b) α=18°..... 158

5.23 Comparison of mean pressure coefficients along the airfoil surface at the peak and trough of the WLE case, with and without presence of the DBDs: (a) α = 12°, (b) α = 18°..... 159

5.24 Time development of lift and drag coefficients at $\mathrm{Re}=0.5\times10^5$ and $\alpha=12^{\circ}$ for various cases. Solid black and red lines indicate lift and drag coefficients, respectively..... 160

5.25 Power spectral density (PSD) analysis of the measured aerodynamic forces at $\mathrm{Re}=0.5\times10^5$. Solid red and black lines indicate $\alpha=12^{\circ}$ and $\alpha=18^{\circ}$, respectively.... 162

5.26 (a) Wavelet transform analysis of plasma flow passing over the studied WLE and SLE airfoil at $\mathrm{Re}=0.5\times10^5$, AOA=18°..... 164

5.27 Wavelet transform contour of turbulence flow passing over the modified airfoil at $\mathrm{Re}=0.5\times10^5$, AOA=12°..... 164

5.28 The isosurface of zero streamwise velocity, showing flow separation, for the baseline and tubercled airfoil at AOA=18° and $\mathrm{Re} = 0.5\times10^5$, with and without plasma flow control..... 166
5.29 The contour of the normalized velocity magnitude with the presence of streamline pattern (visualized by the Line Integral Convolution (LIC) method) at AOA=18°, for the WLE (Peak) cases with plasma on (a) 2DBD (b) 1DBD and (c) plasma off. Each set of images shows 0.25T, 0.5T, 0.75T, and T in one typical cycle..... 168
5.30 The visualization of the vortex structures with the LIC method on the contour of the velocity magnitude at AOA=12°, for the same operational condition of Fig. 5.28..... 169
5.31 The contour of normalized velocity magnitude with visualization of streamline via LIC approach along 2D plane for the SLE cases (a) Plasma on (2DBD) AOA=12° (b) Plasma on (2DBD), AOA=18° (c) Plasma off, AOA=18°..... 170
5.32 The contour of velocity magnitude contour with the streamline patterns at trough in the fully developed time of the flow, for the same operational condition of Fig. 5.28 and 5.29..... 171
5.33 The 3D iso-surfaces of second invariant of the velocity gradient tensor (Q) at $\mathrm{Re} = 0.5\times10^5$, AOA=18°, for the WLE cases with plasma on (a) 2DBD, (b) 1DBD, (c) plasma off and the SLE with plasma on (d) 2DBD (left frames). Besides, the planes at trough and peak are visualized (right frames)..... 173
5.34 The 3D iso-surfaces of second invariant of the velocity gradient tensor (Q) at $\mathrm{Re} = 0.5\times10^5$, AOA=18°, for the same operational condition of Fig. 5.31..... 174
6.1 Schematic representation of the electrostatic rotary atomizer, in combination with (a) the high-voltage retractable blades, and (b) high-voltage adjustable control-ring..... 183
6.2 Close-up view of the sprayer apparatus' head..... 183
6.3 Perspective view of the electrostatic rotary atomizer with the high-voltage retractable blades in (a) semi-closed, (b) fully-closed, modes..... 184
6.4 Representation of the electrostatic equipotential lines distribution around sprayer with (a) high-voltage retractable blades, (b) high-voltage adjustable control-ring, and (c) typical ones..... 185
6.5 Schematic representation of the new electrostatic sprayer in a standard automotive spray booth..... 186
6.6 Schematic pattern of the paint droplet trajectory around sprayer with high-voltage adjustable control-ring..... 187
6.7 Complicated airflow pattern (visualized with the Line Integral Convolution (LIC) method) around sprayer with high-voltage adjustable control-ring..... 187

List of Tables

2.1 Map of spray painting variables 28

2.2 Discretization Summary of the schemes employed in the current study..... 30

2.3 Details of different grid sizes..... 33

2.4 Boundary conditions and test data for the current numerical simulation..... 38

2.4 Overall numerical transfer efficiency results for the three cases..... 45

3.1 Electrostatic spraying modeling baseline specifications..... 66

4.1 Variable parameters in Electrostatic spraying simulation..... 99

4.2 Overall values of the Transfer efficiency (TE) for different cases..... 107

5.1 Element description of the coarse, medium, and fine grid for the "face to face" case..... 134

5.2 The various situations considered: (a) Data for the distribution of micro-droplet diameters and sneezing initial velocity comparisons ($\theta_{inj} = 33^{\circ}$, $Mouth\,area = 314\,mm^2$)..... 135

5.3 Considering the effect of four different grid resolutions used for a grid dependence test based on the WLE case on the average lift and drag coefficients. The list shows the number of grid cells used in the streamwise (n_ξ), vertical (n_η), and spanwise (n_ς) directions..... 138

5.4 Coefficients of polynomial equation for the deposited saliva droplet area for maximum length and width..... 154

5.5 Averaged lift and drag coefficients comparison for cases in Fig.5.24..... 161

Nomenclatures

AoA	Angles of attack
CFD	Computational fluid dynamic
CO	Courant number
DBDPA	Dielectric barrier discharge plasma actuator
DR	Diameter ratio
ERBS	Electrostatic rotary bell sprayer
GS	Grid-scale
LES	Large eddy simulation
LIC	Line integral convolution
OEEVM	One equation eddy-viscosity model
PIV	Particle Image Velocimetry
Re	Reynolds number
SGS	Subgrid-scale
STK	Stokes number
TE	Transfer efficiency
TI	Turbulence intensity
TKE	Turbulent kinetic energy
Δ	Filter width
δ	Film thickness
ε	Emissivity
ε_o	Electrical permittivity
$\chi_\circ$	Free space relative permittivity
ε_r	Medium space relative permittivity
Λ_{RT}	Droplet wavelength
ζ_M	Potential function driving the evaporation
λ_d	Debye length
λ_{LE}	Wavelength
η	Location parameter
μ	Dynamic viscosity
μ_f	Dynamic viscosity of the fluid
μ_k	Viscosity of the vortex
ρ	Density

ρ_C	Charge density
ρ_f	Fluid density
ρ_p	Paint particle density
ς	Boltzmann constant
σ	Charge density
τ_{ij}	Sub-grid scale stress tensor
τ_p	Particle relaxation time
ϕ	External electric field
φ	Potential
$\overline{\varphi}$	Net charge density
ω_{bell}	Bell rotational speed
Ω_{RT}	Fastest-growing frequency
A_{LE}	Amplitude
A_p	Droplet surface
B	Empirical constant of Pilch and Erdman model
C_ε	LES empirical constant coefficients
C_k	LES empirical constant coefficients
C_D	Drag coefficient
C_{eq}	Equivalent capacitance
c_p	Droplet specific heat capacity
d	Diameter of injected particle
$\vec{E}$	Electric field vector
e	Flow thickness over the bell-cup surface
F_D	Stokes drag force
F_E	Electric force
F_{es}	Electric stress
F_g	Buoyancy force
F_m	Added mass force
F_{st}	Surface tension

f	AC voltage frequency
G	Filter function
I	Radiation intensity
$H[\mathrm{U}]$	Contributions of viscous shear
H_p	Particle enthalpy
h	Heat transfer coefficient
$K_1 \approx K_2$	Constant (0.2)
k_{br}	TAB proportional constant
K_{RT}	Wavenumber
k	Kinetic energy
L_{rz}	Length of the recirculation area
l_0	Obstacle characteristic dimension
l_p	Plasma region' length
m_p	Mass of paint particle
ms	millisecond
$m_{pa\,\mathrm{int}}^{\cdot}$	Paint mass flow rate
$m_{air}^{\cdot}$	Shaping air mass flow rate
Nu	Nusselt number
n	Exponential factor of injected particle (2.65)
P	Pressure
p_P	Hydrostatic contribution
p_g	Surrounding gas influence
q_p	Droplet charge
q_{abs}	Radiation heat transfer
$q_{con\upsilon}$	Convection heat transfer
q_{em}	Emitted radiation heat
$\mathrm{R_P}$	Radius of the particle
$r_{product}$	Radius of the product droplets
r_{parent}	Radius of the parent droplets
r_{st}	New stable radius of Reitz-Diwakar model

r	Droplet radius
S_{ij}	Rate-of-strain tensor
S	Forces like gravity
Sh	Sherwood number
Sc	Schmidt number
$S_{\delta,imp}$	Source term of impingement of droplets
$S_{\delta,eva}$	Source term of evaporation of the film
T	Complete spraying cycle period
t_0	Particle relaxation time
t_{br}	Characteristic breakup time
T_f	Temperature of the fluid
T_p	Temperature of the particle
U	Velocity
$\vec{u}_f$	Fluid velocity vector
$\vec{u}_p$	Particle velocity vector
U_N	Initial air velocity on the surface of the nozzle
U_{rel}	Relative velocity
V_{bd}	Critical breakdown voltage
V_{pp}	Peak to peak voltage
V_{pa}	Voltage peak amplitude
V_p	Volume of the particles
We	Weber number
We_{crit}	Supercritical Weber number
y^+	non-dimensional wall distance

Chapter 1

Introduction and Objectives

1.1. Introduction

There is often a requirement to coat the surface of objects for specific purposes. For instance, metals are coated to protect them from rust, and crops are sprayed to protect them from pests and diseases. The transfer efficiency of paint and finish quality of the target are the ultimate goals in all industrial applications. During the past two decades the electrostatic rotary bell sprayer (ERBS) attracts the attention of many researchers in the coating industry because of its higher transfer efficiency (TE). Moreover, nowadays it provides a higher quality of the paint film in comparison with the pneumatic sprayer. This process has been used extensively in industrial applications, such as food spraying, automobile manufacturing, printing, medicine and pharmaceutical sciences. Figure 1.1 illustrates the actual 3D close-up view of a conventional high-speed electrostatic rotary bell sprayer (ERBS) with all components, which is commercialized via SAMES Technologies, as this was used in the current study (Stevenin et al., 2015; SAMES Technology 2019). Frame (b) of this figure shows the operational condition of the PPH 308 high-speed electrostatic rotary bell sprayer (ERBS).

The fundamental principle of electrostatic spray painting is to deposit charged liquid droplets onto a specified grounded workpiece. The evolution history of the electrostatic coating process is fascinating, and its brief review was made by Castle (2011). The electrostatic spray painting procedure is divided into three main stages: 1) atomization and charging, 2) transportation and 3) deposition (as shown in Fig. 1.1 (b)).

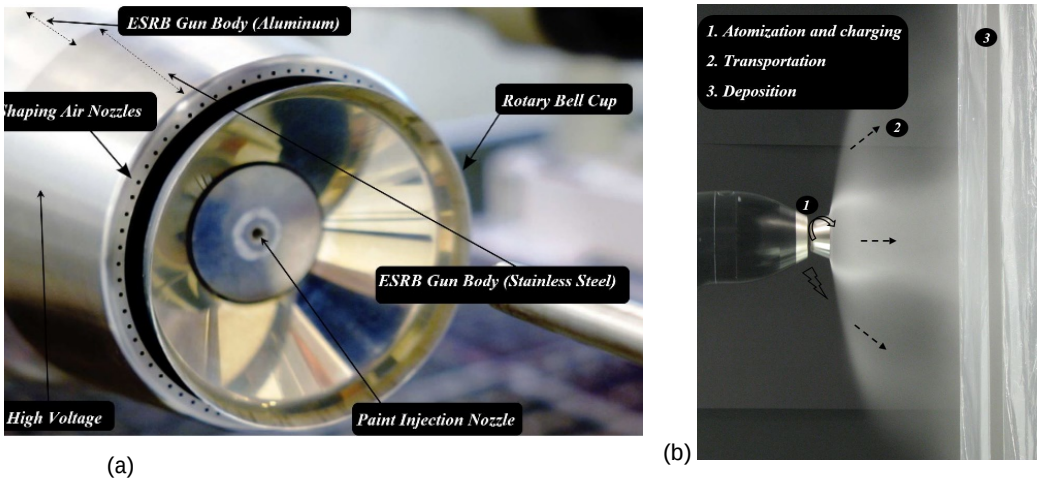

Figure 1.1: The photograph of the PPH 308 high-speed electrostatic rotary bell sprayer (ERBS). Image gently provided by SAMES-KREMLIN (Stevenin et al, 2015; SAMES Technology, 2019).

The atomization is a procedure of liquid paint disintegrating into a very fine spray of droplets by a combination of mechanical and electrical means. There are different kinds of atomizers used in practical applications, such as pressure, rotary, air-blast, air-assisted, electrostatic and ultrasonic. A very extensive discussion about this topic was presented by Lefebvre (1989), Michelson (1990) and Bailey (1988). The recent evolution of high-speed rotary bell sprayer has received growing industrial attention among other atomizers. They use mechanical techniques to atomize the liquid into droplets and the electrostatic methods to charge the droplets. The motion of the particles between the atomizer and the target is generally governed by both electrical and mechanical forces. In the charging stage, the particles are charged by being exposed to a strong electrical field. By using the conducting fluid with the presence of an electric field during the atomization, the droplets can become electrically charged and can have different charge distributions. The obtained electrostatic forces can affect the charged droplets trajectories, so that the thickness and pattern of the deposition onto a grounded target can be controlled. For accurate electrostatic coating process prediction, understanding of the charging mechanism is required. Cross (1987) discussed about four electrostatic charging mechanisms, known as corona, induction, conduction and tribo-charging, used in many industrial applications.

In the region between the atomizer and the target transport of charged droplets occurs. The transport procedure is very complicated because the charged droplets experience simultaneous action of several forces like aerodynamic, electrostatic, gravitational, and inertial forces. The accumulation of these forces determines the charged droplets' trajectories. The gravitational force is negligible and the aerodynamic and electric forces are dominant when the droplets are very small.

Figure 1.2 represents a view of an automotive spray booth (SAMES Technology, 2019) that contains main parts of: ERBSs, robot arms, inlet air supplier and sliding rails—the portion above the floor grating, and air exhauster, water pond, scrubber tube and return sluice —the portion below the floor grating.

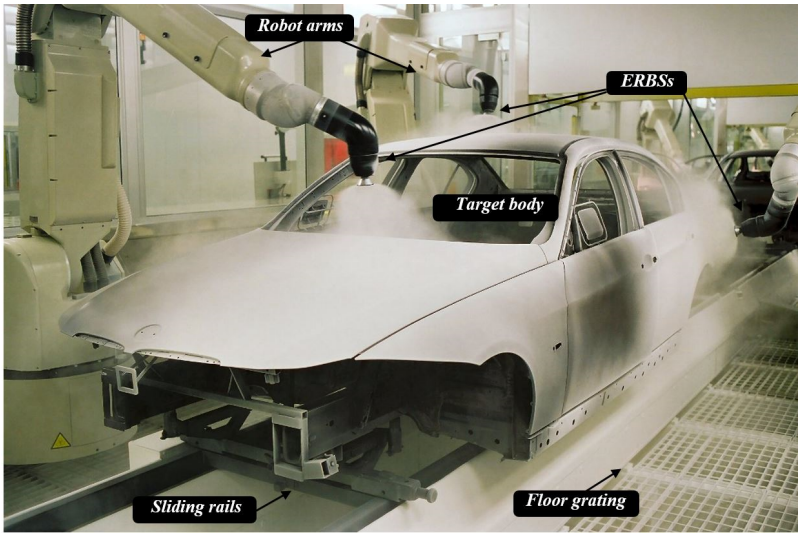

Figure 1.2: Schematic representation of a standard automotive spray booth (SAMES Technology, 2019).

Figure 1.3 shows the interactions between the three main components of the transport field. The dynamics of the spray coupled with the electric field and high Reynolds swirling turbulent flow that is produced by the rotation of the ERBS is a very complicated phenomenon. The charged paint droplets interact with the electrical field and then the shaping airflow is affected by the momentum, mass and energy of them. The paint particles' motion is influenced by the airflow drag force, the electrical force and the charged particles' repulsive forces.

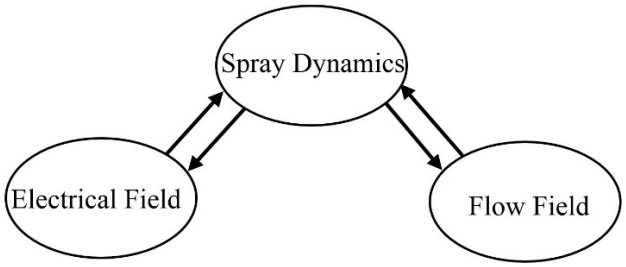

Figure 1.3: Fundamental problems in automotive painting systems.

Figure 1.4 conveys the fundamental problems during the automotive coating, which are related to (a) environmental implications and (b) the quality of finish implications. By implementing the electrostatic coating, the paint spraying transfer efficiency (TE), paint layer thickness that directly impacts the film quality will be increased. The low transfer efficiency is a fundamental problem and is either the source or aggravates of the remaining five issues. Solving the problem of low TE, increasing around 25 % and reaching almost 80 % by using an ERBS with high-voltage control ring field pattern, as will be investigated in this work, the other five problems will be diminished. Capturing more overspray with less energy expenditure is a fundamental concern that affects both the environment and the operational cost of the plant. Minimizing and controlling the greenhouse gas generation as well as efficiently oxidizing any remaining VOCs constitutes another fundamental point that we have called the VOCs and greenhouse gas emission problem. To ensure that the product—the painted auto—meets or surpasses manufacturer specifications and satisfies the expectations of the customer, its quality of finish needs to be controlled constantly.

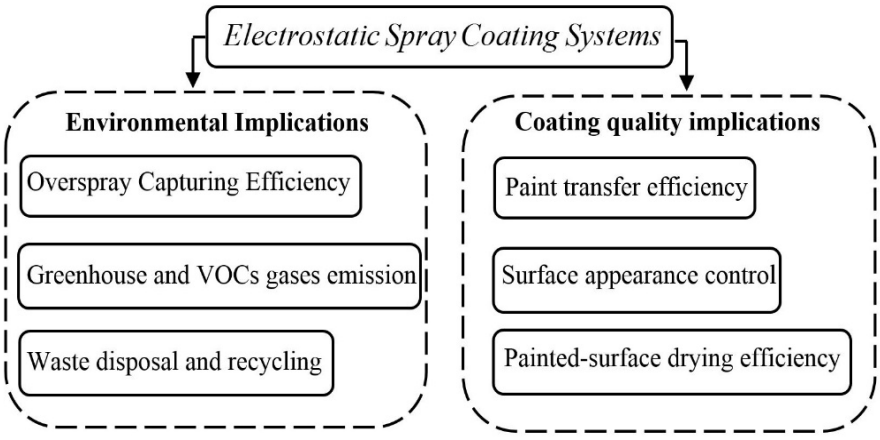

Figure 1.4: Fundamental problems in automotive conventional coating systems.

1.2 Literature Survey

In the first three paragraphs, the formation of the electrostatic spray concept, other applications in addition to the industrial coating, and the start of modern electrostatic sprayer design will be presented, respectively.

Electrostatic phenomena involving liquids were studied as early as 1745 when Bose first noticed that an atomized spray would be ejected from a capillary when a high potential was applied to it (Bailey, 1974). Bailey's review was quite extensive – covering the aspects of the energy balances, charge balances, and mass balances; and how these three all relate to the formation of droplets. In 1867, Lord Kelvin developed an electrostatic generator that ran on water using induction to charge the spray. Because of the increased field at the nozzle of the generator, the flow rate of the liquid was increased; therefore, this generator was one of the very first electrostatic sprayers (Bailey, 1988). These principles were not put into industrial practice until World War II, when electrostatic spray was used to paint Navy ships. In one of its earliest industrial uses, electrostatic spraying was used to apply paint to metal parts in the automotive industry, where it is still widely used today (Meesters et al., et al., 1990).

Because of efficiency of material usage, and completeness of coverage, the electrostatic spraying technique has been applied to many other areas. One such area is in agriculture for crop dusting. The ability of charged droplets to turn a corner and coat the underside of leaves makes electrostatic application of pesticides highly effective (Bologa and Makalsky, 1989). Another innovation in the use of electrostatic spraying is in the pharmaceutical industry with charged inhalers (Bailey, 1998). Also, the ability of electrostatic atomization to produce uniform droplet sizes is exploited in the production of thin-film ceramics (Balachandran et al., 2001). However, the bulk of the electrostatic spray industry is still the application of coatings. A wide variety of methods have been implemented to calculate this electrostatic field surrounding charged objects such as finite difference, finite element, boundary element, boundary integration, and charge simulation (Rarraud, 2001).

Although modeling of electrostatic fields has been an area of scientific curiosity for nearly two centuries. Elmoursi (1989; 1992) developed modeling techniques for electrical characterization of complex bell-cup geometries, the results of which were used in the design of modern bell-cups such as the ones used in this research. While there is a scarcity of authors publishing on rotary bell-cup atomization, there is some who have focused on one or two aspects of it.

In the following, studies that were examined various effective parameters on the spray are presented briefly. Bailey et al. (1983) explore the nature of the droplet size distribution of sprayed liquids and define the limits in which a Rosin-Rammler distribution, a volume-based size distribution, and he proposed the use of a log-normal distribution to describe particle or droplet sizes. Davies and Cheah (1984) investigate the mechanisms of atomization and outline the different modes of atomization for a spinning, non-charged disc. They link the mode of atomization to non-dimensional parameters. Kazama (2003) performed a study of how the flow rate of liquid paint over the internal structure of various bell-cup designs affects atomization. Bell and Hochberg (1981) measured how different spray parameter sets affect the mean droplet

size of paints in an electrostatic rotary atomizer. Their findings were illustrated that the mechanical shear is deemed the dominant contributor to atomization in electrostatic rotary atomizers. Frazer et al. (1963) studied the effects of air impingement on a liquid sheet formed by a rotating bell-cup. Extending the theory of Rayleigh (1882), a theory relating the stability of a liquid droplet to the balance of forces between the electrostatic repulsion on the surface to the surface tension, Zeleny in 1917 measured a relationship between the meniscus at a charged capillary tip and the current received at a grounded electrode (Zeleny, 1917). Shkadov and Shutov (2001) focused their investigation on non-linear, non-axisymmetric perturbations in the spray stream. Atten and Oliveri (1992) studied the kinetics of charge migration during the breakup of a circular jet. Their analysis produced a model for the electrostatic potential build-up on a droplet versus time for various shapes of jet. Also their study provides a closer look at the dynamics of droplet charging during electrostatic atomization. Tanasescu et al. (1989) modeled an electrostatic sprayer using an irrotational flow model. In 1968, Marshall collaborated with Dickinson to elaborate further on the phenomena involved in droplet evaporation (Dickinson and Marshall, 1968). They determined that the rate at which a droplet evaporates when at a high velocity is less than that of a stationary droplet of the same size. Doyle et al. (1964) investigated the evaporation of electrostatically charged droplets with the size in the range of 60-200 μm in diameter while they were suspended between two charged plates. Abbas and Latham (1967) find that droplets over one millimeter in diameter do not succumb to disruption as a means of stabilizing the electrostatic surface pressure present during the evaporation of charged droplets. The deposition of droplets, like its counterpart, atomization, is a very complicated phenomenon to model. Some researchers like Perel et al. (1981) have developed empirical models based on physical measurements and built an electrostatic atomization unit for the production of metal powders where they characterized the behavior of these molten metal droplets. Inkpen (1986), in his thesis, examined how an electrostatic field local to a deposited coating altered the appearance of metallic paints. In 2002, Hurevich et al. (2002) developed a simulation of a plasma spray. By using distributions in droplet size and initial velocity, they were able to construct a stochastic model determining the coating profile produced at various operating conditions. Ivosevic et al. (2006) also developed a droplet deposition simulation, the focus of which was on individual droplet impacts based on the first principles. However, because both groups were dealing with either plasma or thermal sprays, electromotive effects were not relevant and therefore not taken into account.

After a few years some researchers start working in this field with deeper focus. Ye et al. published in 2002 a series of papers on electrostatic spraying. While most of these papers dealt with corona-charged powder spray systems, the computer simulation written was able to be modified to accommodate various spray application techniques from a pneumatic atomizer to a rotary bell electrostatic spray gun (Ye et al., 2002; 2003; Ye and Domnick, 2003). Ye et al. (2002) analyzed a complex spray gun using a corona charging mechanism to predict the deposition thickness on a stationary target plate. The particle size and charge distributions in their study were based on actual measurements. Adamiak (1997, 2001) performed a 2D simulation of tribo-charged powder particle trajectories. He assumed a cylindrical tribo gun at

some distance from a vertical infinite ground plane. He assumed mono- and poly-dispersed powder particles for injection and found that modeling a triboelectric system is much more difficult than a corona system because in the corona system the space charge field is dominant by ions and the field due to the charged particles can be ignored, but in the triboelectric system space charge density depends only on particles.

Böttner et al. (2002) performed CFD numerical simulations of a 2D axisymmetric stationary spray gun. Their simulations included the coupling of the flow field with the electrostatic field, and the effect of the paint particles on the continuous phase assuming a laminar model. They showed that the space charge has a great impact on the particle trajectories and, therefore, it highly influences the results. Also, they found that the coupling of the particles with the continuous phase is very important only in the region near the injection locations, where the particle concentration is high. The calculated results were compared with the experimental ones and a significant effect of the space charge on the particle deposition pattern was found. Another perspective was shown by Colbert et al. (2005), where they presented parametric studies of the effect of the individual variables involved in the electrostatic spray system on the overall spray pattern and transfer efficiency. Their results showed a ring pattern with no deposition at the center of a flat target and increased accumulation on the edge. Im et al. (2004) performed a numerical simulation of the spray transfer process in an electrostatic rotary bell applicator using CFD method. They found that the spray shape is very sensitive to changing the charge-to-mass ratio and electric force, which strongly affects the numerical transfer efficiency. Also, they found that although the transfer efficiency is decreased with increasing the shaping airflow rate, the spray pattern is more uniform on the target surface. A comparison between the experimental and numerical results of the deposition thickness produced by high speed rotary bell atomizer has been attempted by Domnick et al. (2005) for simple target geometry. They considered a direct charging mechanism, where high voltage was applied directly to the rotating bell and the effect of the corona was neglected. They also used a rotary bell atomizer with six external corona needles which were arranged symmetrically around the atomizer body to predict the deposition thickness and transfer efficiency on a curved object. They choose the target geometry as a rear part of a car body. When they compared their numerical results of the deposition pattern with the experimental ones, they found a good agreement, but the simulated coating thickness at the positions very close to the edges was overestimated due to the edge effect (Domnick et al., 2006). Reznik et al. (2004) discussed numerical and experimental results for the droplet evolution and jet formation in a strong electric field. They distinguished between three different jetting characteristics: subcritical electric field, supercritical electric field with contact angle less than 0.8π and greater than 0.8π in electrospinning of nanofibers.

During the last decade, the following investigation focuses on the electrostatic coating precisely. Toljic et al. (2012, 2013) described a full 3D numerical model using FLUENT to predict the coating thickness for a moving target surface. They assumed a conduction charging in their model and the target took the shape of a car door. Their results showed some improvements in the deposition uniformity compare with the case of a stationary target. The transfer efficiency was also higher for the cases of charged particles as compared with the case of neutral particles.

They also examined the effect of different model parameters on the deposition pattern, such as the shaping air mass flow rate, the applied voltage, the particle mass flow rate and the charge-to-mass ratio. Their results revealed that the deposition profile is strongly affected by the shaping air mass flow rate. In most parts of their previous studies (Toljic et al. 2012), considerable work has been carried out to clarify the importance of the injection parameters (i.e. number of injection points, total number of super-particles, etc.), but there was a problem with having insufficient coverage at the central part inside the cone of the spray pattern. Their results of injecting polydiseprsed particles showed that the deposition thickness is a "ring-shaped" pattern, where the thickness decreases gradually from the ring to the edge of the target and also decreases sharply from the ring to the center of the target, and therefore, there was no deposition at the central part of the target surface.

Osman et al. (2015a) assumed different injection angles along three virtual rings that were assumed to form a shower injection pattern. Some parameters, such as the total number of injection points, the radii of the rings and the fractional mass flow rate in each injection ring, which affect the numerical results of the deposition thickness was investigated. Toljic et al. (2010) investigated the charge to radius dependency for conductive particles atomized in an electric field between planar electrodes. The results showed that the ligament length has a strong effect on the particle charge to radius dependency. They found that the radius exponent is equal to two when the particle is in direct contact with a planar electrode, and decreases rapidly as the ligament length increases approaching a limit of 1.1. Osman et al. (2015b) studied numerically the effect of the presence of previously formed droplets, the presence of adjacent ligaments as well as the ligament radius and length on the predicted droplet charging levels for ligaments formed from a planar high voltage electrode. The effect of the ligament radius on the charging level was found to be significant with larger charge resulting when the ligament radius is smaller than the droplet radius. This is important because in practice a narrow necking normally occurs prior to the droplet ejection. They also investigated the dynamic modeling of droplet formation at different inlet velocities. The results showed that the droplet shape prior to detachment is actually a prolate ellipsoid and that the spherical model underestimates the actual charge. The complex theoretical and practical problems with the electrospray modeling are discussed on this topic by Agostinho et al. (2018), Gañan-Calvo et al. (2018) and Rosell-Llompart et al. (2018).

An overview of the scientific literature that deals with two specific issues of atomization and the particles charging, which will be analyzed deeply in the current thesis, is presented in the following.

1.2.1. Atomization and formation of droplet

Lefebvre (1989) discussed about various techniques of liquid sheet atomization into a spray. The development of the liquid sheet leads to disintegration into ligaments and then further surface disturbances produce droplets. In order to explain the relationship between different model parameters, many empirical equations have been derived due to the complexity of the

electrostatic spraying process. For the first time, the liquid jet disintegration phenomenon was investigated theoretically by Rayleigh (1878), who studied the instability of a non-viscous liquid jet at low velocity and little perturbations. He observed that when the disturbance wavelength is greater than the jet circumference droplets can be produced by the breakup phenomenon.

Weber (1931) extended Rayleigh's analysis by including viscous liquids. He found that if the disturbance wavelength is lower than a certain value, the tension of the surface leads to damping out the disturbance; otherwise, it causes fast jet disintegration. His theoretical achievements did not match well with experimental data, as Sterling and Sleicher (1975) pointed out, who developed Weber's theory with a partial success. Schneider et al. (1967) extended and generalized Rayleigh's work by adding the electric charge effect on the jet to the Rayleigh analysis. Hines (1966) analyzed theoretically and experimentally the charging and atomization of an individual fluid jet in an electrostatic field. He found a good agreement between the theoretical and experimental values of the droplet size as a function of charge-to-mass ratio and surface tension. In his work, both theoretical and experimental results showed that by increasing the electric field at the atomizing surface, the atomization rate increases. He also provided estimated formulas for different quantities, such as the droplet size, charge-to-mass ratio and the electric field intensity.

The breakup of a liquid sheet into ligaments and further disintegration into droplets are governed by two groups of forces: bulk forces (e.g. gravitational force, electric force, drag force and inertial force) and normal and tangential stresses at the liquid surface (e.g. electric stress due to the surface charge density and the local electric field stress due to dynamic viscosity of fluid, and stress due to pressure difference on both sides of the liquid surface). The liquid's physical characteristics determine the properties of the droplets, but the most important factor responsible for the liquid droplets' shape is surface tension. The liquid surface properties or the interface between liquid and air are usually related to the surface density of energy. The attraction force between the liquid's molecules is greater than the one between molecules in the air. Because of that, the liquid has higher surface tension. The surface tension has a major impact on the atomization procedure. Tolman (1949) illustrated that the surface tension depends on the droplet radius. The effect of other factors on the surface tension, such as active agents and ionic salts has been studied in (Davies and Rideal, 1961; Davies and Makepeace, 1978; Van den Bogaert and Joos, 1979). Adamiak et al. (2011) investigated the dynamic modeling of droplet formation at different inlet velocities. The results showed that the droplet shape prior to detachment is actually a prolate ellipsoid and that the spherical model underestimates the actual charge. Distortion of the droplet shape agrees with previous studies of droplet deformation in an external electric field.

1.2.2. Droplets charging mechanisms

At first, an overview of the scientific literature dealing with the charging process is presented in the following, and then the particle charging mechanisms will be considered. Anestos et al. (1977) measured the charge-to-mass distribution of electrostatic sprays. Their work was done on

non-rotating, electrostatically-charged, air-assisted nozzles. Artana et al. (1993) derives models for the charge-to-mass ratio of inductively charged sprays originating from a capillary nozzle. Higashiyama et al. (1999) made comparative measurements of droplet diameter and specific charge in charged and non-charged water sprays. Hartman et al. (1999) identify a relationship between the size and charge of a droplet for a capillary electrostatic sprayer operating in cone-jet mode noting that size segregation occurs as the result of changes in inertia and electrostatic interaction. Filippov (1991) developed models of electrostatically charged droplets in flight through a quiescent domain (i.e. no focusing air involved).

Osman et al. (2015c) have estimation of droplet charge forming out of an electrified ligament in the presence of a uniform electric field. A 2D axisymmetric model is presented which can be used to predict the electric charge on a conductive spherical droplet ejected from a single ligament directly supplied with high voltage. The effect on droplet charge and its radius was estimated for several cases of different boundary conditions. Toljic et al. (2010) investigated the charge to radius dependency for conductive particles atomized in an electric field between planar electrodes. The results showed that the ligament length has a strong effect on the particle charge to radius dependency. They found that the radius exponent is equal to two when the particle is in direct contact with a planar electrode, and decreases rapidly as the ligament length increases approaching a limit of 1.1.

There are four basic particle charging mechanisms used in industrial electrostatic applications: corona, triboelectric, conduction and induction charging. Each charging mechanism has its advantages and disadvantages, and field of usage. A brief overview of each mechanism is presented in the following:

1.2.2.1. Corona charging

Corona charging is a widespread mechanism efficient for charging liquid droplets (Bailey, 1988) or powder particles (Hughes, 1984) in various applications. It includes applying a high potential to a very sharp needle, adequate to produce continuous gas discharge in the air. An electrode with negative potential attracts positive ions and also repels electrons away by the high electric field. These electrons will be accelerated, causing additional collisions, which produce an avalanche of electrons and positive ions. This process continues until the new electrons are formed far enough away, such that they are unable to gain sufficient energy to ionize more neutral molecules.

The corona discharge area can be subdivided into two regions: the ionizing region that contains the charge carriers of both polarities and the drift region characterized by the presence of only one polarity charge carrier. The great advantage of corona charging guns is that they offer dependable ions and a strong electrostatic field source, resulting in efficient charging and higher deposition. A comprehensive literature review about the basic physical processes in corona discharge was presented in (Loeb, 1956).

1.2.2.2. Triboelectric charging

Triboelectric charging is another mechanism that is used for particle charging, mainly for powders. It is based on the particles rubbing with the spray gun's material for sufficient time, without using a high voltage source. The material with a higher work function gains electrons and charges negatively, while the material with a lower work function loses electrons and charges positively. The charge flow ends when the work functions of both materials are equalized.

Mazumder et al. (1994) measured the electric charge values for different powder particle sizes that were triboelectrically charged. Their experimental data illustrated that the charge magnitude increases linearly with the particle's surface area and they also noticed that 20%-60% of the droplets were charged with opposite polarity. Thomas et al. (2008) developed a device allowing the measurement of tribo-charging powder particles during the conveying through a metallic pipe. The electric field in tribo-charging system is produced only by the space charge of the tribo-charged particles. Thus, the electric field is weaker and insufficient for transporting the droplets toward the grounded target. Because of the electric field reduction, the edge effect, Faraday cage effect and back ionization become less important. Moyle and Hughes (1985) performed a comparison among the triboelectric and the corona charging system in coating.

1.2.2.3. Induction and conduction charging

Induction charging refers to a method where an electrode that is placed near a grounded atomized liquid is supplied with a voltage. Because of the induced electrical field, the electrical charge flows from the ground to the surface of the liquid material and resides on the surface after droplet separation. But the conduction charging needs a direct connection between the applied voltage and the atomized liquid. The charge on the droplets is trapped when the liquid is dispersed into droplets. Generally, induction and conduction charging mechanisms are widely used in various liquid spraying processes for conductive liquid material, such as food spraying and industrial painting. In an ideal two-electrode induction and conduction charging arrangements, the nozzle serves as one electrode and the target as the other ones, but they are isolated from adjacent virtual grounds.

Zhao et al. (2005) presented a very good comparison between the conduction and induction charging mechanisms. They reported that the conduction charging produces a larger target current, smaller electrode current and larger drift current. On the other hands, in the induction charging the target current depends only on the space charge field that causes larger electrode current and surface discharge at lower voltage. A limitation of induction and conduction charging is that they cannot be used to charge insulating materials and are limited to relatively well-conducting coatings.

1.3 Objectives of current research

The objectives of this research that will focus on the numerical modeling are:

(a) Implementation of a 3D comprehensive Eulerian-Lagrangian algorithm under the framework of the OpenFOAM package, which contains spray dynamics, airflow, paint droplets tracking and an electrostatic effect, in order to investigate the electrostatic spray transfer processes in the high-speed rotary bell sprayer.
(b) A systematic analysis of unsteady, complex dynamic and three-dimensional behavior of flow behind the ERBS, like the recirculation zone length, the toroidal vortex, the overspray phenomena and the flowfield characteristics like mean velocity, pressure, turbulent kinetic energy and velocity fluctuation.
(c) Investigation of the dominant operational parameters effect like bell rotational speed, shaping air and paint flow rate, electrical charge values and droplet distributions
(d) Adding wall film function to the presented code to predict the transport in the boundary layer and capture the paint film distribution over the target.
(e) Investigation and modification of the various breakup models in order to predict the breakup process and droplet size in the ERBS more precisely.
(f) Examination of the droplet charging inclusion and electric field coupling, with different parametric values, and their impacts on the atomized droplet distribution over the spray plume and the deposition rate.
(g) Design a new version of ERBS by adding a high-voltage control ring and changing the cup's dimensions and curvature to increase the performance and transfer efficiency (TE) of the ERBS and harmonize the direction of the charged paint droplets.
(h) Developing the available code for simulating the plasma flow that is created due to potential difference, and also predicting the trajectory of the saliva droplets as an atomized droplets during sneezing, coughing, or even exhaling. By these, we illustrate the versatility of the developed model.
(i) During a detailed analysis of the transport characteristics due to sneeze these topics were discussed: (I) Identifying the micro-droplet transmission mechanisms, (II) Characterization of the expelled micro-droplet, including size distribution and velocity, in order to mimic the experimental conditions, (III) Compare the effect of the different size-range of micro-droplets, and its influence on the transmission routes and deposition pattern (IV) Determine a safe settling area based on information from a hundred cases with various initial velocities, micro-droplet size distribution, injection angle, and mouth opening area. (V) Considering various social distancing positions: face-to-face, meeting standing, and near an equipment.

1.3.1 Numerical simulation of electrostatic coating process

In this research, the electrostatic coating process has been analyzed numerically with the aid of Computational Fluid Dynamics (CFD) under the framework of the OpenFOAM package. This numerical tool proves its capability to solve the dynamic motion of the droplets under the

influence of different kinds of forces, including the electrical and mechanical forces. Due to the complexities in this process, it is essential to keep the computation time within an acceptable level but preserving sufficient accuracy when a large number of model parameters need to be analyzed for optimization.
The numerical modeling of the spraying procedure includes the liquid in the form of droplets as the discrete phase and the compressed air as the continuous phase. In order to create a charging electrode, the surface of the atomizer is connected to a high voltage while the surface of the target is grounded. Evaporation, breakup, collisions and coalescence of particles were considered. The injection pattern was proposed to achieve a good agreement with experimental data. A comparison between the numerical and experimental results was also made for cases of a stationary target.

1.4 Thesis organization

This thesis is organized in the following Chapters:

Chapter 1: Introduction; this is the introductory chapter, which includes the motivation for writing this thesis and covers a thorough review of the scientific literature dealing with the atomization process, breakup procedure and the most important mechanisms of charging the particles, as it is considered to be the first stage of the electrostatic coating process. There is also a summary of previously published work that is related to the investigation of the electrostatic painting of simple as well as complicated surfaces using different numerical and experimental techniques, which were exploited for the purpose of this research.

Chapter 2: Implementation of numerical electrostatic spray painting transfer processes modelling in rotary bell cup for automotive painting; In this chapter, an implementation of a 3D comprehensive Eulerian-Lagrangian algorithm under the framework of the OpenFOAM package, which is contains spray dynamics, airflow, paint droplets tracking and an electrostatic effect, is described in order to investigate the electrostatic spray transfer processes in the high-speed rotary bell sprayer. A systematic analysis of the fundamental behaviors of flow behind the ERBS like the recirculation zone length, the toroidal vortex, the overspray phenomena and the flowfield characteristics like mean velocity, pressure, turbulent kinetic energy and velocity fluctuation, have been implemented. Also, unsteady, complex dynamic and three-dimensional behaviors of flow behind the ERBS that was solved by the LES turbulence approach are compared with the $k\omega$-SST turbulence model.

Chapter 3: Atomization and spray characteristics around an ERBS using various operational models and conditions; In this chapter, Investigation and modification of the various breakup models in order to predict the breakup process and droplet size in the ERBS is implemented. The wall film function is added to the presented code to predict the transport in the boundary layer and capture the paint film distribution over the target. The effect of dominant operational parameters like bell rotational speed, shaping air and paint flow rate, electrical charge values

and droplet distributions are considered precisely. Also, for validation purposes, a comparison between our numerical and several experimental results were presented.

Chapter 4: Analysis of droplets charge and size distribution in the electrostatic coating process; Examination of the droplet charging inclusion and electric field coupling, with different parametric values, and their impacts on the atomized droplet distribution over the spray plume and the deposition rate is presented in this chapter. Also, a new version of ERBS by adding a high-voltage control ring and changing the cup's dimensions and curvature is designed to increase the performance and transfer efficiency (TE) of the ERBS and harmonize the direction of the charged paint droplets.

Chapter 5: Other useful application of the presented code: (I) Investigation of aerosol dispersion in the indoor work environment and (II) Study of the DBD plasma actuators effect on the flow characteristic; in this chapter, the available developed code is examined for simulating the plasma flow that is created due to potential difference and also predicting the trajectory of the saliva droplets as an atomized droplets during sneezing, coughing, or even exhaling.

Chapter 6: This chapter is based on our patent which is presenting a novel electrostatic spraying mechanism for industrial coating with high rotary bell sprayer based on high-voltage retractable blades or high-voltage adjustable control ring.

Chapter 7: Final remarks, conclusions and future work; the conclusions and summary of this thesis is presented. Also, this chapter contains recommendations for future work.

Chapter 2

Implementation of numerical electrostatic spray painting transfer processes modelling in rotary bell cup for automotive painting[1]

Abstract

Here we implemented a 3D comprehensive Eulerian-Lagrangian model in order to investigate the electrostatic spray transfer processes in the high-speed rotary bell sprayer. This efficient algorithm contains spray dynamics, airflow, paint droplets tracking and an electrostatic effect to simulate atomization. The algorithm is implemented using the OpenFOAM package. A solver for the particle trajectory was used to illustrate the process of spray transport and also the interaction of the airflow and the particle that is solved by momentum coupling. Creating an initial condition of the particle approach has been proposed that is matched with practical applications. The fluid-dynamics is simulated by solving the unsteady 3D compressible Navier-Stokes equations. Unsteady flow is computed by using a Large eddy simulation (LES) turbulence approach, while the motion of the particles is simulated by tracking the droplet size distribution approach. The model correctly predicts that the bell cup spin forces the paint particles to fall off from the bell surface towards the high-velocity airflow. The present work illustrates a tentative benchmark and contains a systematic analysis of the recirculation zone length, the toroidal vortex, the overspray phenomena and the flowfield characteristics like mean velocity, pressure, turbulent kinetic energy and velocity fluctuation. The results indicate as dominant operating parameter the air-paint flow rate with voltage level deeply affecting the spray shape. A more uniform distribution of the coating is obtained by growing this high-velocity shaping airflow, although the values of the transfer efficiency (TE) are reduced. The distribution of the particle size is very sensitive to changes in the rotational speed. Experimental results obtained in this study put forward a clear link between the shaping air flow rate and the rotation frequency on the aerodynamics and also provide valuable insights to design modern ERBS. The paint spray distribution obtained in the present work is validated against coating experimental results with suitable accuracy.

[1] Based on the work published in the International Journal of Heat and Fluid Flow, https://doi.org/10.1016/j.ijheatfluidflow.2019.108499, and, SAE International Journal of Advances and Current Practices in Mobility, https://doi.org/10.4271/2019-01-1856.

2.1 Introduction

During the past two decades the electrostatic rotary bell sprayer (ERBS) attracts the attention of many researchers in the coating industry because of its higher transfer efficiency (TE), up to 90% in an ideal conditions. Moreover, nowadays it provides a higher quality of the paint film in comparison with the pneumatic sprayer. The electrostatic spray painting process has been used extensively in the painting industry. Therefore, numerical simulating of this procedure can introduce a deeper understanding and this knowledge can highly improve the coating technology. The definition of the transfer efficiency (TE) can be expressed as a ratio of the total droplet mass deposited on the workpiece to that injected from the applicator. One of the main components of the costs of automotive production is related to painting processes, about 10 % of the cost of producing a car, and also including 50 % consumption of energy (Clément et al., 1963). The painting process, in comparison with other manufacturing procedures, needs more attention due to the lack of accurate practical investigation and detailed and well-validated numerical simulation, especially for the paint thickness. The operational condition of the ERBS is so advance and complex that includes millions of injected paint droplets, an electric field and turbulent airflow.

The traveling procedure of droplets from the atomizer to reach the target can be divided into near-bell, transport distance, and goal body regions. At first, near the ERBS three main phenomena occur: atomization, ionization and electrical charge of the liquid paint particles. Secondly, the transport field includes capturing the turbulent flow of the shaping-air and swirling rotary bell and also the electrostatic field. The swirling turbulent flow in the ERBS is an unsteady, three-dimensional and complex flow (Im et al., 2001; Liu et al., 2003). Finally, the characteristics of the paint film, downdraft flows that affect the position of the droplets, and transfer efficiency (TE) and also considered in the body regions. The electrical distribution and the force that created by it play a vital role in the trajectory of the sprayed particle, more important than the aerodynamic force. Interaction between the airflow and the particles accrues by momentum, mass, and energy interchange. In the flow field, the drag force of the shaping airflow affected the paint particle movement in association with the electric field and other particle's repulsive actions. Some challenging procedures, such as selection of a suitable turbulence approach, a technique for tracking the particle trajectory and the injection model for paint particles, all these need to be considered in the electrostatic spray painting numerical simulation. Precise simulation of the operational conditions of an ERBS requires the use of an accurate numerical model for capturing the sharp interface between the paint particle and shaping airflow, as well as a real situation.

In the following, we consider some studies about the trajectory of the paint particle by applying a discrete flow model in order to measure and evaluate the quality of the coating. In the automotive painting industry the gun sprayer is moved via a robotic manipulator, based on a predicted trajectory plan. Moving spray guns can be simulated in two different ways by CFD, by using a dynamic mesh approach (Toljic et al., 2012; Toljic et al., 2013) or a static integration thickness (Domnick et al., 2005; Dominick and Thieme, 2006; Toljic et al., 2005). Toljic et al.

(2012; 2013) considered the electrostatic painting procedure numerically to investigate the paint thickness for a moving body as a target by employing a commercial CFD program. Their results in a vehicle indicate that some progress is achieved on the deposition uniformity, compared with the case which the goal body is stationary. Moreover, they have realized dramatic increase in a transfer efficiency (TE) for the charged particle in comparison with the neutral ones. The effects of applied voltage, shaping air mass flow rate, paint mass flow rate and the charge-to-mass ratio was considered in their study. As a result of this study, they concluded that the profile of the deposition is strongly modified by changing the shaping air mass flow rate. Domnick et al. (2005) used a high-speed rotary bell atomizer to numerically simulate the deposition thickness and compare it with the experimental results for a simple target geometry and neglected the corona effect. In the next step, they (Domnick et al., 2006) add some external corona needles with symmetric arrangement all around their previous atomizer's body for creating electrostatic field. They investigated the thickness affecting the deposition and other important factors of transfer efficiency on a curved object. They choose the rear part of a car body as a target geometry. They have found a very good agreement between their numerical simulation results and the experiments, especially in the deposition pattern and even if due to the edge effect some overestimated was observed. Colbert and Caircross (2005) presented parametric studies related to the electrostatic sprayer and analyzed how each individual variable affect the transfer efficiency and the spray pattern. They found out that accumulation increased on the edge when a ring model and a deposition at the flat target center was used.

Im et al. (2004) have also performed a numerical analysis the mechanism of the electrostatic rotary bell sprayer and their transfer process. They calculated that the shape and formation of the spray are so sensitive to the electric force, the charge-to-mass ratio and the transfer efficiency. Also, they concluded that by increasing the amount of shaping airflow, the transfer efficiency will be decreased. These simulation results indicate that under zero, -80 KV and -90 KV voltage conditions the TE reaches about 44%, 90% and 94%, respectively. These results also show that by increasing the shaping airflow rate to double, to reach 300 l/min, or increasing the rotational speed from 25k to 50K rpm leads to a TE decrease. Ye et al. (2002) simulated the spraying mechanism by using a commercial CFD software. They imposed a corona charge procedure and then analyzed the deposition quality and thickness on a goal plate. They applied an actual particle size and charge amount, and then compare their obtained results with the experimental data in the same operational condition, significant dependence on the space charge was identified. Viti et al. (2008) simulated the electrostatic spray coating process in a rotary bell cup by applying the realizable k-ε turbulence model for computing the airflow, a Lagrangian method for tracking the particle trajectory and a random-walk model for turbulent dispersion of each particle.

Böttner et al. (2002) simulated a station 2D symmetric sprayer via coupling the electrostatic field by the computational flow-field. These authors investigated the interaction of the injected particles with the continuous airflow, especially in the area near to the injection nozzle. Also, they have realized that the electrical space charge has a significant impact on the particle trajectory. Yasumura et al. (2011a) performed a CFD simulation in the rotary bell sprayer and

realized that the electrical voltage has more impressive effects on the medium size of the droplet (10–40 μm) and also the shaping air has changed the pattern of the large (<40 μm) or small (<10 μm) size of the paint particle. Kazama (2003), Panneton (2002), Tanasawa et al. (1978) and Dominick et al. (2006) studied experimentally the spray painting process and investigated the different effective parameter on the paint film quality in various types of the atomizers. They described the distribution of the paint particles and behavior of them by changing the rotating body structure. Toljic et al. (2010) simulated the electrical field among planar electrodes to investigate the dependency of the atomized particles radius to their charge. They found that the length of the ligament has a high effect on the charge of the particle to its radius. Also, their results showed that the exponent of the radius in the direct contact with the planar electrode is equal to two, and reduce dramatically when the length of the ligament growth approaching a limit of 1.1.

Yasumura et al. (2011b) simulated the spray flow around a high-speed rotary bell to find a solution to decrease the transfer efficiency. The influence of the inner re-circulating flow was investigated numerically by adhering and non-adhering droplets. They found that the flow of inner re-circulation draws smaller droplets and these droplets placed on the inner side of the radial direction and don't adhere to the surface of the target. Also, the ghost and the inner re-circulation have a huge effect on the large and small droplets, respectively. Zuzio et al. (2017) developed an Eulerian-Lagrangian coupling to consider the accuracy of transition among these two models. They validated the atomization process on a planar sheet of liquid. Yu et al. (2017) applied Eulerian-Lagrangian coupling procedure in parallel simulating of the complex dynamics of a diesel spray. They demonstrated small and separated scale of liquid with a Lagrangian Parcel Tracking method. Kim et al. (2010) investigated the air-assisted-droplet behavior in diesel atomization from the aspect of droplet size, break up, trajectory and deformation ratio. Stefanitsis et al. (2019) modified the break-up solution in diesel spraying applications. Dastourani et al. (2018) improved a mathematical approach of the electrospray process in the cone-jet that contain the surrounding air by using OpenFOAM software. Tsang et al. (2014) investigated the accuracy of the large eddy simulation turbulence approach for implementing a test on a high-speed liquid spray in an internal engine for combustion. Selection of a suitable turbulence approach is a determinant issue to provide accurate and precise results in a simulation. LES approach is more appropriate to capture the details of the computed flow and demonstrate the principle of the internal flow (Pendar and Roohi, 2015; 2016; 2018; Roohi et al., 2016; Kolahan et al., 2019). The implementation of the electric field is an important issue for have an accurate simulation and capture the details of the flow precisely which performed on the other similar studies (Mushyam et al., 2019).

In the present study, we describe an implementation within OpenFOAM to analyze the electrostatic spray transfer process flow around the ERBS. A finite-volume approach along with the LES turbulence model was used for solving the electrostatic and airflow field, and also Lagrangian approach was implemented for computing the discrete particle field. This work provides details of the velocity field and vortex flow structure and also the trajectory of the particles around the ERBS. The particle distribution characteristics grasp in detail and are

compared with the available experimental results at the same conditions with accurate. As an overview, section 2.2 presented the governing equations of this work after an introduction to the electrostatic spray painting technology that in section 2.1 of the current work. Section 2.3 introduces the 3D numerical simulation method. To validate the numerical approach a comparison among this work and other experimental and numerical data is presented in section 2.4.1. Particles dynamic characteristics (section 2.4.2.1), features of the airflow (section 2.4.2.2) and electrical analysis (section 2.4.2.3), are reported comprehensively. Fig. 2.1 describes the physical properties of the paint droplets electrical charging procedure of electrostatic spray painting in an ERBS. During this process, the air around the ERBS ionized via a high voltage electrostatic field that can reach around -90 KV with small values of current and then affect the sprayed paint droplets. The target surface attracts the paint droplets which charged with a high negative voltage. The generated electrostatic force affects the paint particles proportional to charge value. The amount of this force relies on the particle's physical location and own charge. The high values of voltage harmonized the uniformity and reduced the size of the paint particles. In the water-based paints due to conductivity and as a result of the voltage leakage problems it is better to use an external or indirect charging method that we used in this numerical study.

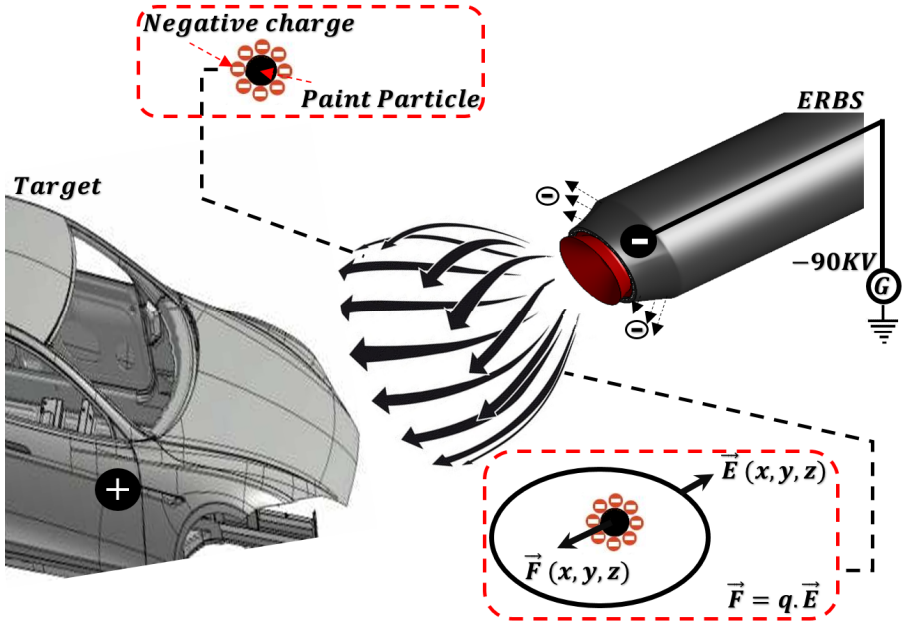

Figure 2.1: Paint particles electrical charging procedure for electrostatic spray painting process in the ERBS, acted forces on the charged particle.

2.2. Governing Equations for ERBS Flow

The numerical algorithm and mathematical formula of the three various phases that were considered in the results obtained with this numerical research are: continuous phase (airflow) (2.2.1), Electric flow field (2.2.2), and Discrete phase paint particles (2.2.3), and they will be explained precisely in the following parts.

2.2.1 Continuous phase: Large Eddy Simulation (LES) turbulence model

The LES turbulence model is structured based on modeling the smaller sub-grid eddies, while the large scale structures are computed on the overall computational domain. Any variable, i.e., *f*, is separated into grid scale (GS) and subgrid scale (SGS) components, i.e., where $\overline{f} = G * f$ is the GS component, $G = G(x, \Delta)$ is the filter function, and also $\Delta=\Delta(x)$ is the filter width (Ghosal, 1996). The Favre-filtered compressible Navier-Stokes (NS) equations, and the equation of state, in their non-dimensional form are given as:

$$\frac{\partial \overline{\rho}}{\partial t} + \frac{\partial(\overline{\rho u_j})}{\partial x_j} = 0, \tag{2.1}$$

$$\frac{\partial(\bar{\rho}\,\bar{u}_j)}{\partial t} + \frac{\partial(\bar{\rho}\,\bar{u}_i\bar{u}_j)}{\partial x_j} = -\frac{\partial \bar{p}}{\partial x_i} + \frac{\partial \bar{\sigma}_{ij}}{\partial x_j} - \frac{\partial \tau_{ij}}{\partial x_j} + F_{st} + F_{es} + S. \tag{2.2}$$

Here, all of the variations with an overbar explain filtered parameters. The additional body forces are included into the Navier-Stokes equations for considering the surface tension (F_{st}) and electric stress (F_{es}) and S denoting other forces that are acting on the fluid such as the gravity. In our case, S also refers to the created droplet source term that affects the airflow due to the motion and electric charge. The most important aspect of the above-mentioned equations is term of $\partial\tau_{ij}/\partial x_j$, that is unknown a priori. It is feasible to express τ_{ij} as:

$$\tau_{ij} \approx \rho(\overline{u_i u_j} - \overline{u_i}\,\overline{u_j}) \tag{2.3}$$

,Where S_{ij} is the rate-of-strain tensor for the resolved scale and the subgrid scale turbulent viscosity, μ_k, is closed by a "Local Eddy-Viscosity" model. Here, the "*one equation eddy viscosity model*" (OEEVM) subgrid scale is used. To obtain turbulence kinetic energy *k,* OEEVM solves the following equation:

$$\partial\left(\bar{\rho}k\right) + \nabla.\left(\bar{\rho}k\tilde{u}\right) = -\tau_{ij}.\overline{S_{ij}} + \nabla.(\mu_k \nabla k) + \bar{\rho}\varepsilon\ , \tag{2.4}$$

$$\varepsilon = c_\varepsilon k^{3/2} / \Delta\ . \tag{2.5}$$

Subgrid-scale turbulent viscosity, μ_k is then calculated by:

$$\mu_k = c_k \bar{\rho}\Delta\sqrt{k}, \tag{2.6}$$

, while C_k and C_ε are set as 0.094 and 1.048 in the present code.

2.2.2 Electric Field

In this simulation, the electric field is generated by the potential difference among the ERBS applicator, high negatively charged, and the earthed workpiece. This electric field can be

modeled by a Poisson's equation, which supplies a relation between the space charge density (ρ^q), due to the ions, and the potential (ϕ):

$$\nabla^2\phi = -\frac{\rho^q}{\varepsilon'}. \tag{2.7}$$

Where ε' is the electrical permittivity of the air. Then, the electric field intensity (E) is given by taking the gradient of the potential field:

$$\vec{E} = -\nabla\phi, \quad \varepsilon' \nabla . E = \rho^q . \tag{2.8}$$

The charge on each individual particles is

$$Q_i = m_{P_i}\ \rho^{\mathrm{q}}_{\mathrm{m_i}} = (\rho_P V_{P_i})\rho^{\mathrm{q}}_{\mathrm{m_i}}, \tag{2.9}$$

Where ρ_P, V_{P_i} and $\rho^{\mathrm{q}}_{\mathrm{m_i}}$ are density, volume and charge-to-mass ratio of an individual particle, respectively. It must be mentioned that Q_i has units of charge, while ρ^q has the units of charge per unit volume. The electric force per unit mass, F_E, is defined as the influence of the electric field on the air flow field, i.e., the so-called ion wind can be simulated straightforward on the droplet:

$$F_E = q_{P_i}\ E = m_{P_i}\ \rho^{\mathrm{q}}_{\mathrm{m_i}} E, \quad E.\nabla\rho^q = -\frac{\rho^{q^2}}{\varepsilon'}. \tag{2.10}$$

Where q_{P_i} and m_{P_i} are the charge and the mass of an individual droplet, respectively.

2.2.3 Discrete phase

The discrete phase focused on the movement of charged paint particles with the identical polarity of those that movement is described by solving a series of differential equations and computing the velocity and position of droplets at each time. Our presented code computes and predict the trajectory of the particles of the discrete phase via integrating the balance of the forces that is relying on the Newton's law, which is defined in a Lagrangian reference area. The equation that using for paint droplet must be includes different forces, like the fluid force created by the viscous stress and pressure gradient, the force of the Stokes drag, added-mass force, electrostatic force, gravity and buoyancy forces. In the current study, a powerful shaping airflow also helps particles to transfer to the direction of the body surface. Also, the top boundary is specified using a mass flow inlet boundary condition which corresponds to a downdraft of 0.1 m/s, representative of a typical booth airflow effects on particles. It contains the interaction of the mentioned forces determined on the path of the particles and their final destination. We used some simplifying assumptions and ignore to consider some of the mentioned forces. With considering the mentioned simplifications, the droplet movement equation is formulated as below:

$$m_p \frac{\partial^2 \vec{x}}{\partial t^2} = m_p \frac{\partial \vec{u}_p}{\partial t} = \vec{F}_D + \vec{F}_g + \vec{F}_E + \vec{F}_m. \tag{2.11}$$

Here $m_p = \rho_p V_p$ is the droplet mass that is a function of its density and volume, $\vec{x}$ is the particle's position vector, equal to the product of its density and volume, $\vec{u}_p$ and $\vec{u}_f$ are the particle and fluid velocity vector, respectively. The effective force on the each separated particle, $\vec{F}_P$, is the sum of the following forces:

$$F_D = Stokes\ drag = \frac{3}{4} C_d \frac{\rho_f}{\rho_p} \frac{m_p}{2\mathrm{R_p}} \left|(\vec{u}_f - \vec{u}_p)\right| (\vec{u}_f - \vec{u}_p), \tag{2.12}$$

$$F_g = Buoyancy = (\rho_p - \rho_f) V_p \vec{g}, \tag{2.13}$$

$$\vec{F}_E = Electric\ force = \vec{E} q_p, \tag{2.14}$$

$$F_m = Added\ mass = \frac{\rho_f V_p}{2} \frac{\partial(\vec{u}_f - \vec{u}_p)}{\partial t}. \tag{2.15}$$

where ρ_p and ρ_f are the particle (paint) and fluid (air) density, r , V_p , m_p and q_p are the radius, the volume, the mass and the charge of the particles, respectively. $\vec{E}$ is the electric field and C_D is the drag coefficient, which depends on the particle's Reynolds number defined as follow (Schiller and Neumann, 1933; Clift et al, 1978; Laín and Grillo, 2007):

$$C_D = \begin{cases} \dfrac{24}{\mathrm{Re}_P}, & if\ \mathrm{Re}_P < 1 \\ \dfrac{24}{\mathrm{Re}_P}(1 + 0.5\,\mathrm{Re}_P^{0.687}), & if\ 1 \le \mathrm{Re}_P \le 1000 \\ 0.44, & if\ \mathrm{Re}_P > 1000 \end{cases} \tag{2.16}$$

$$\text{Where} \quad \mathrm{Re_p} = \frac{2\mathrm{R_p}\left|\vec{\mathrm{u}}_\mathrm{f} - \vec{\mathrm{u}}_\mathrm{p}\right| \rho_f}{\mu_f}, \tag{2.17}$$

Here μ_f is the dynamic viscosity of the fluid (air). The mentioned drag coefficient formula is roughly near the measured empirical values except for higher values of Reynolds number. As it can be realized, a constant value of 0.44 is set for Reynolds numbers above 1000.

$$\frac{\partial \vec{\mathrm{u}}_\mathrm{p}}{\partial \mathrm{t}} = \frac{3}{4} \frac{C_d}{2\mathrm{R_p}} \frac{\rho_f}{\rho_p} \left|\vec{u}_f - \vec{u}_p\right| (\vec{u}_f - \vec{u}_p) + \frac{(\rho_p - \rho_f)}{\rho_p} \vec{g} + \frac{\rho_f}{2\rho_p} \frac{\partial(\vec{u}_f - \vec{u}_p)}{\partial t} + \frac{\vec{E} q_p}{m_p}. \tag{2.18}$$

The above differential equation (Eq. (2.18)) for the motion and the velocity of the particle is isolated as the final following expression that implemented:

$$\frac{\partial \vec{\mathrm{u}}_{\mathrm{p}}}{\partial \mathrm{t}}(1+\frac{\rho_f}{2\rho_p}) = \frac{3}{4}\frac{C_d}{2\mathrm{R}_{\mathrm{p}}}\frac{\rho_f}{\rho_p}\left|\vec{u}_f - \vec{u}_p\right|(\vec{u}_f - \vec{u}_p) + (1-\frac{\rho_f}{\rho_p})\vec{g} + \frac{\rho_f}{2\rho_p}\frac{\partial \vec{u}_f}{\partial t} + \frac{\vec{E}q_p}{m_p}. \quad (2.19)$$

The left side of the above equation indicates the acceleration of the particle as if it had an added mass of half of the fluid it displaces. Also, the right hand of the additional force contributed due to the acceleration of the fluid. For solving Eq. (2.18) the interpolated values of the electric and the fluid velocity field are calculated at the exact position of the grid points.

2.3. Numerical setup

2.3.1 The Rotating Bell Cup Problem

Fig. 2.2 indicates a schematic view of the computed full 3D computational domain of ERBS which consists of all the relevant electrical mechanical phenomena. As represented in this figure, the computational region includes a rectangular box of 1.2 m× 2.5 m× 2.5 m in width, height and length, respectively. The surface of the target is represented by a circle with a diameter of 0.9 m. Its distance from the bell of ERBS is intended 0.25 m. The mean high pressure airflow is injected from the outlet of ninety injection nozzles, 0.5mm in diameter with the annular pattern slot cut flush to the gun spatially uniform along the x-axis, and also the paint particles sprayed from the nozzle that is located at the center of the using ERBS, which has 2.5 mm in diameter. A constant values of downdraft velocity U_∞= 0.1 m/s is set at the top face inflow boundary condition. The value of the shaping airflow is 150 (norm. l/min = 2.044×10^{-5} kg/s) with the air initial velocity speed of 15.0 m/s. The rotary bell cup of the ERBS rotates clockwise along the x-axis at a very high speed with no-slip boundary condition. The bell rotational speed determined the droplet tangential velocity, at 25K rpm and 50K rpm rotational speed of the bell tangential velocity is equal to 70 m/sec and 140 m/sec, respectively. The maximum number of the paint injected particles is around 200,000. The liquid droplet size was set up to 50 microns, injected at the bell tangential speed.

Figure 2.3 represents a schematic view of an automotive spray booth that contains: main parts of ERBSs, robot arms, inlet air supplier and sliding rails—the portion above the floor grating, and air exhauster, water pond, scrubber tube and return sluice —the portion below the floor grating. After cleaning by the insect and dust filters, the supply plenum is blown the air to the upper section air supplier. The paint droplets of overspray are removed and drawn out through the outlet return sluice.

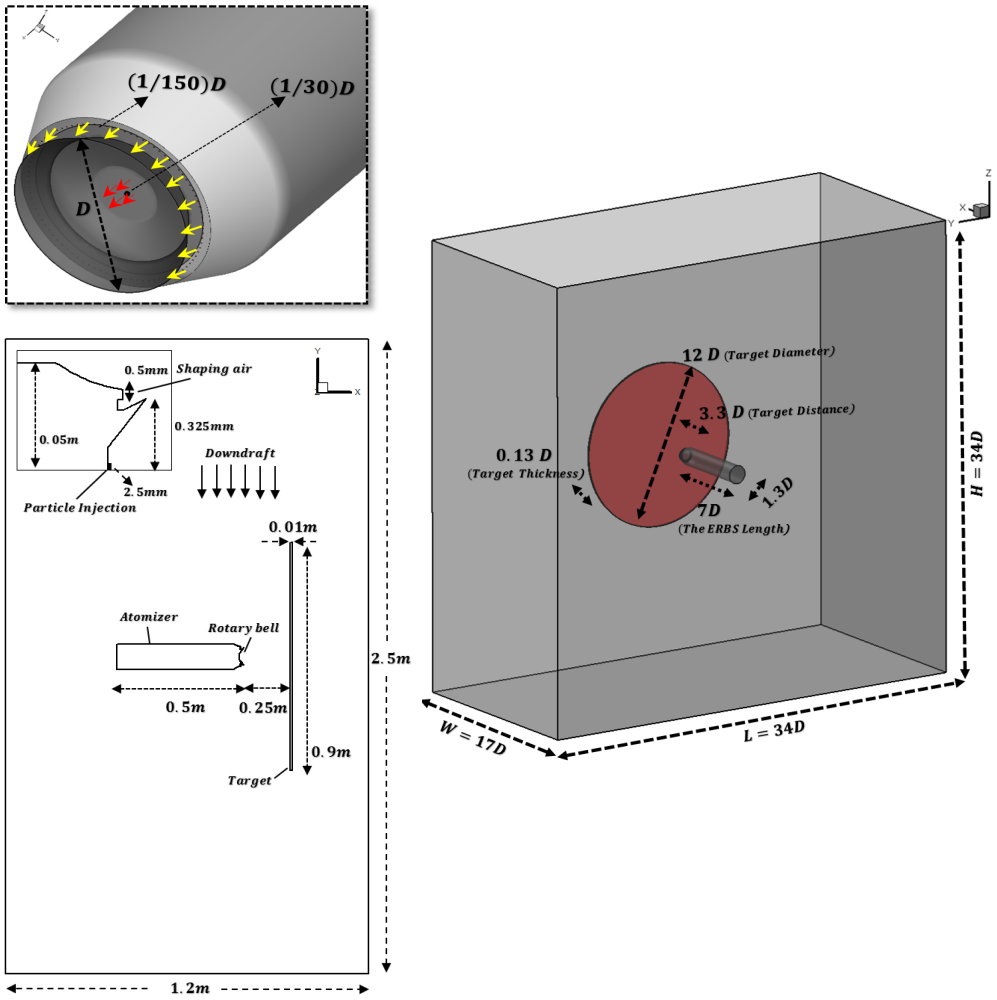

Figure 2.2: The computational domain with all the applied dimensions which non-dimensions by the diameter of the bel cup.

Figure 2.4 schematically explains the procedure of the atomization and electrostatic spray painting process in the ERBS. In this process the paint droplet that distributed with high-velocity from the edge of the bell cup affected by the ionized airflow and shaping airflow which is injected from the nozzles and then impinging to the target surface.

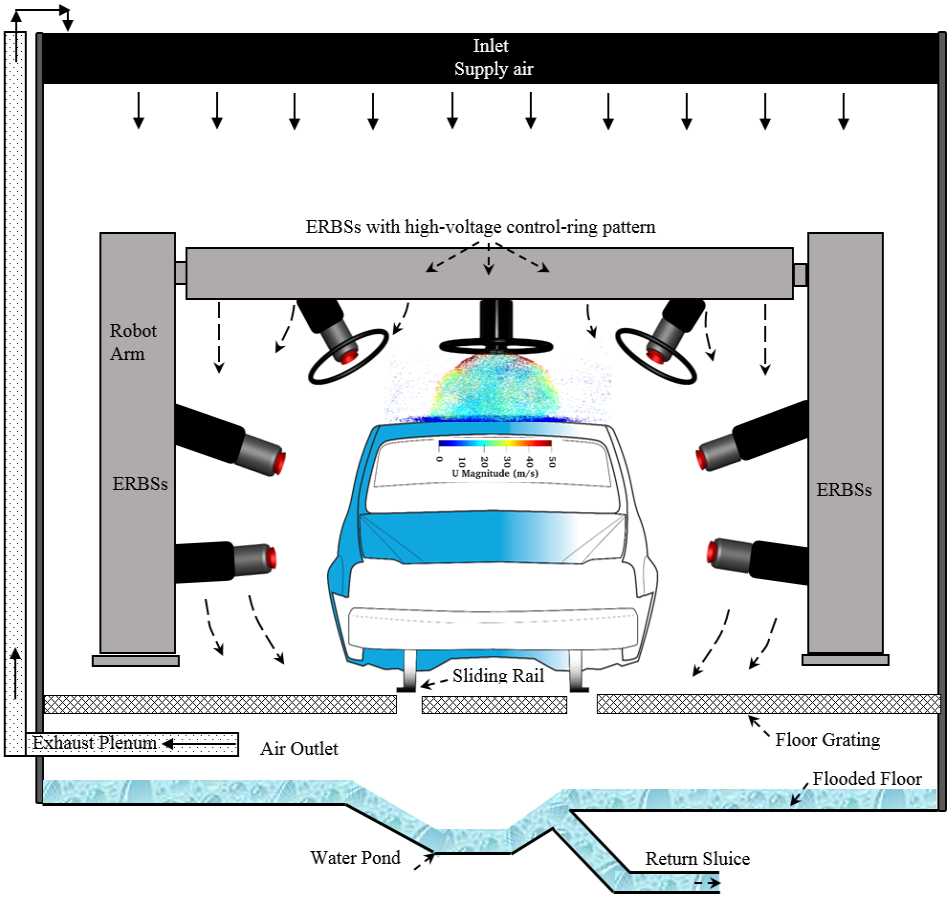

Figure 2.3: Schematic representation of a standard automotive spray booth.

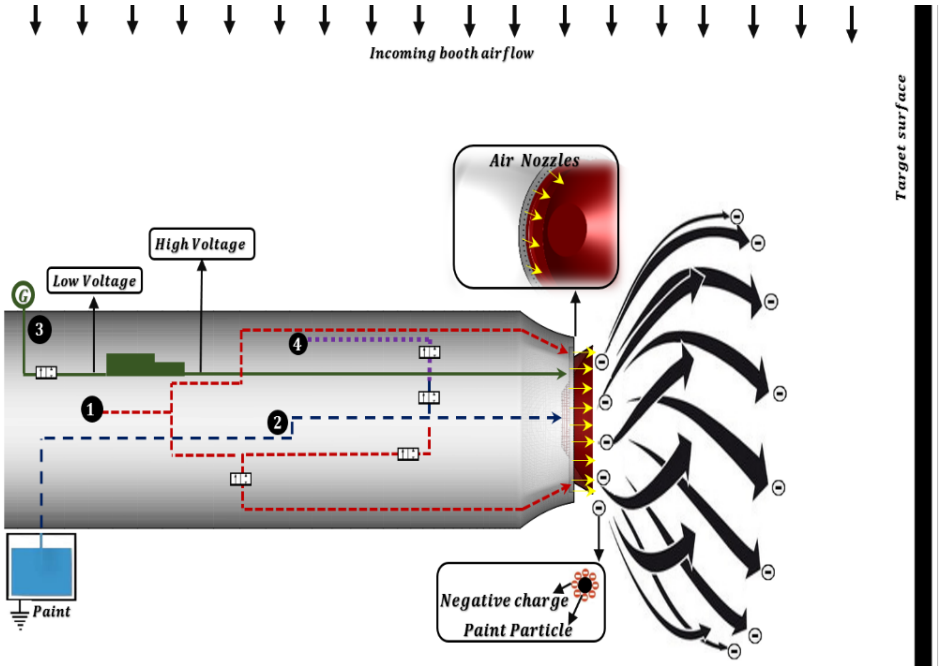

Figure 2.4: A description for the electrostatic spray coating procedure in the ERBS.

2.3.2 Boundary Conditions

In this part the boundary conditions of the continuous phase, comprising the electrical field and the airflow, together with the paint droplet will be discussed. At first, we considered the continuous phase boundary conditions. Figs. 2.5 and 2.6 indicate the boundary conditions applied for the ERBS computational domain. All sides of the domain, except the top boundary, are set at a constant atmospheric air temperature (293 K) and pressure (101.325 kPa). A downdraft airflow inlet with a specified velocity of 0.1 m/s is considered for the upside border of the computational domain. The turbulence intensity (TI) is kept at 2% for inlet flow from the upside and also injected airflow of the nozzles. Air is determined as an ideal-gas with the buoyancy forces created via the gravity in the negative z-axis. The fixed potential values for instance -90 kV are set on the cup and the gun of the ERBS and the grounded (0 V) values is determined for the body surface as a target. All other solid surfaces are considered insulated with 0 V/m specification normal gradient. All other surfaces are considered insulated with specified normal gradient of 0 V/m. In the following, we will investigate the boundary conditions for the discrete phase. The initial size and distribution of particles are set to be nearly linked with experimental conditions. In the present study, a Rosin-Rammler distribution is used that closely matched with the experimental distribution, $Y_d = \exp(-d/\overline{d})^n$. An exponential factor and the average diameter of injected particle are set as n= 2.6 and d= 75 μm, respectively. Determination of the accurate specific charge boundary conditions is a critical issue that must be considered. The material of the injected paint particles is considered as water at a standard condition and these particles charged by means of a negative voltage of the ERBS rotary cup through conduction.

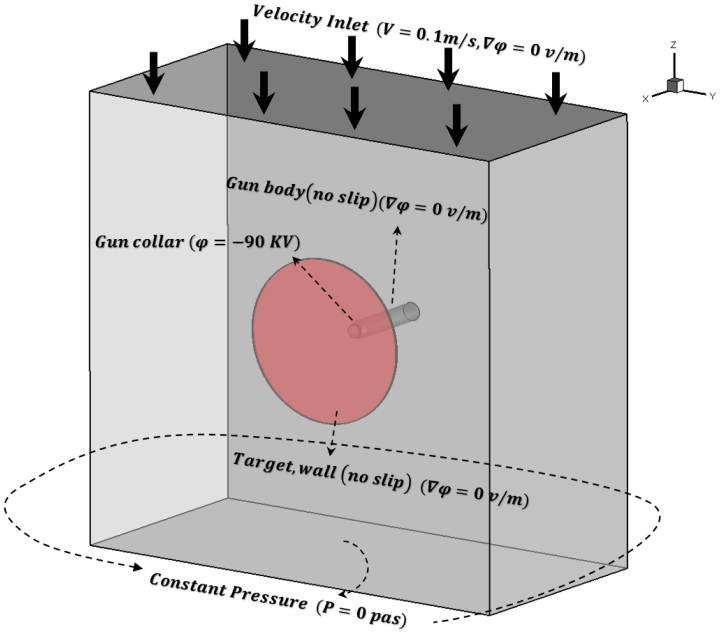

Figure 2.5: Electrostatic field and flow field boundary conditions in the overall computational domain.

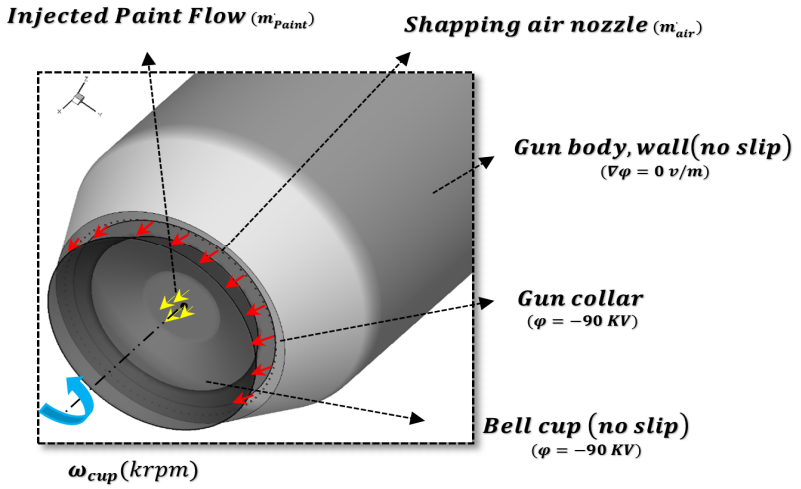

Figure 2.6: Details of the implemented boundary condition in the area close to the bell cup of the ERBS.

Fig. 2.7 illustrates the actual 3D close-up view of a conventional high-speed electrostatic rotary bell sprayer (ERBS) with all components which is commercialized via SAMES Technologies, as this was used in the current study (Stevenin et al, 2015; SAMES Technology, 2019). Frame (b) of this figure shows the operational condition of the PPH 308 high-speed electrostatic rotary bell sprayer (ERBS).

(a) (b)

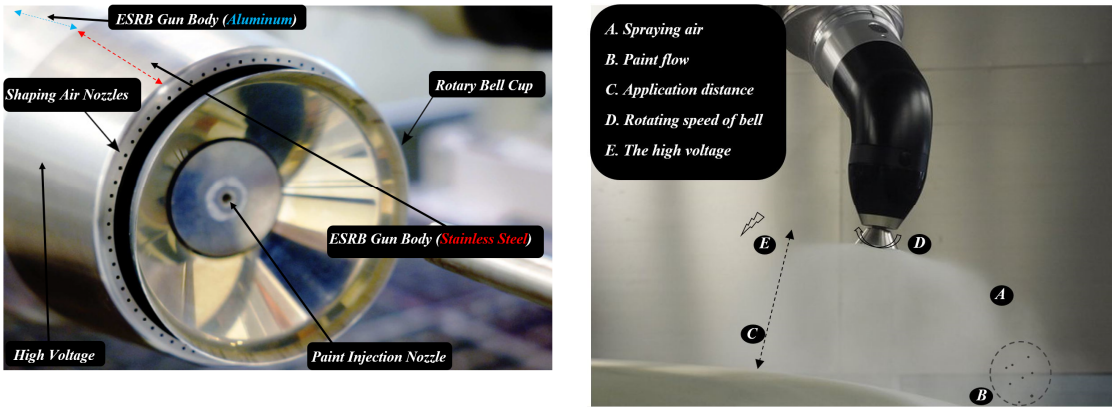

Figure 2.7: The photograph of the PPH 308 high-speed electrostatic rotary bell sprayer (ERBS). Image gently provided by SAMES-KREMLIN (Stevenin et al, 2015; SAMES Technology, 2019).

Tab. 2.1 shows the map of the overall effective sub-area input factors on the paint deposition rate in the ERBS that is considered in the present study. The group is focused on studies that include the set up for the geometry, the paint droplet and the shaping airflow pattern.

Table 2.1: Map of spray painting variables.

<table>
<tr><td></td><td>1-Atomizer geometry</td><td rowspan="2">a. Shaping Air Flow Patern</td><td rowspan="4">Spray/Particle Properties</td><td rowspan="6">Deposition Rate</td></tr>
<tr><td>1- Shaping Air Velocity
2- Shaping Air Pressure</td><td>2-Shaping Air Flow Rate</td></tr>
<tr><td></td><td>1-Pipe geometry</td><td rowspan="2">b. Paint Flow Patern</td></tr>
<tr><td>1- Paint viscosity
2- Injection System Pressure
3-Injection System Velocity
4- Paint Surface Tension</td><td>2-Paint Flow Rate</td></tr>
<tr><td colspan="2">1-Particle Size
2- Particle density
3- Particle injected initial velocity
4- Specific droplet charge
5- Injection models</td><td>c. Injection Pattern</td></tr>
<tr><td colspan="2">1- Distance From Surface
2-Paint nozzle diameter
3-Surface Geometry
4-Number of Shaping Air Nozzle
5-Spray Cone Angle
6-Air Nozzle Diameter
7-Number Of Shaping Air Nozzle Rows</td><td>a. Physically</td><td rowspan="2">physical /operational conditions</td></tr>
<tr><td colspan="2">1-Target Voltage
2-Potential Value
3-Cup Rotational Speed
4-Domain Air Flow
5-Downdraft Velocity
6-Number Of Particle Per Second</td><td>b. Initial values</td></tr>
</table>

Fig. 2.8 shows the flow diagram of an iterative process for the computation of the electric field, charging and the flow field. The specific amount of the paint particles injected with special size and their trajectory are computed based on the airflow and the electrical fields. The Poisson equation will be solved due to the initial space charge that is added to the Laplace equation until the convergence. This procedure is repeated until reaching the overall convergence.

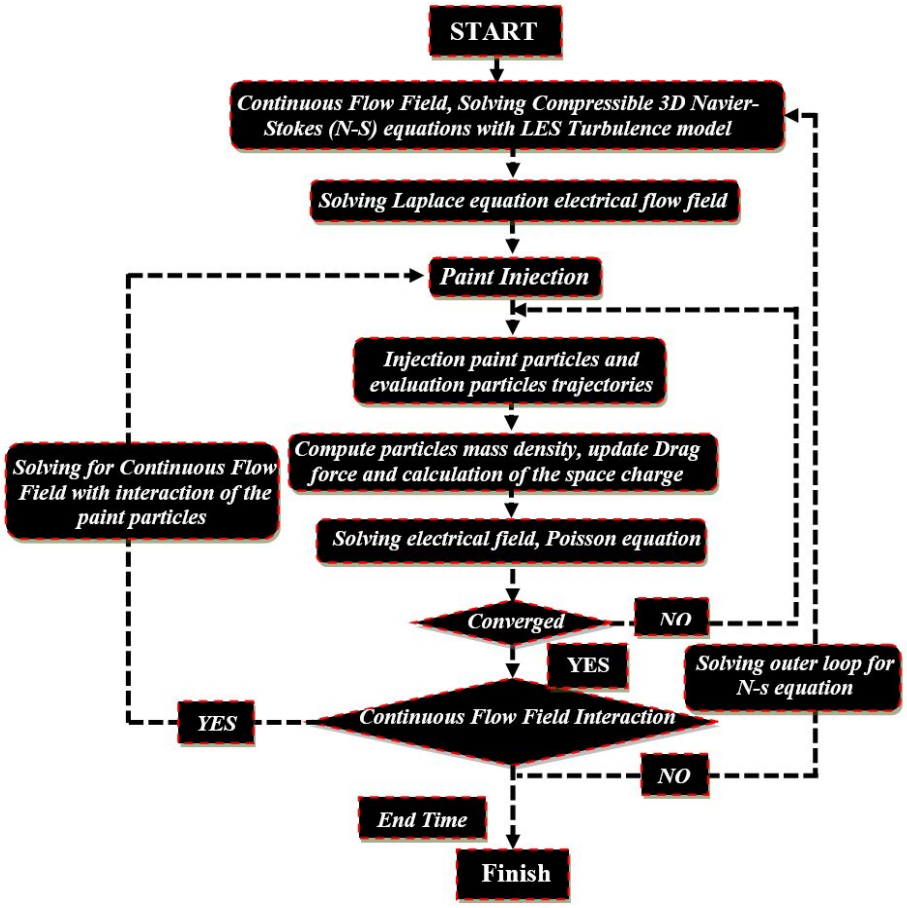

Figure 2.8: Flowchart of the iterative procedure in the electrostatic spray coating process in the current numerical study.

2.3.3 Discretization Schemes

Tab. 2.2 explains the detail of the used discretization scheme in gaining the results that we reported in the current work. Second order accuracy is employed for all terms discretized in the momentum and continuity equations.

Fig. 2.9 shows the turbulent kinetic energy (TKE) power spectrum density (PSD) at a position close to the rim of the ERBS. The presence of the Kolmogorov power law-decay ($f^{-5/3}$) indicates the statistical scaling accuracy to evaluate the flow field inertial scales.

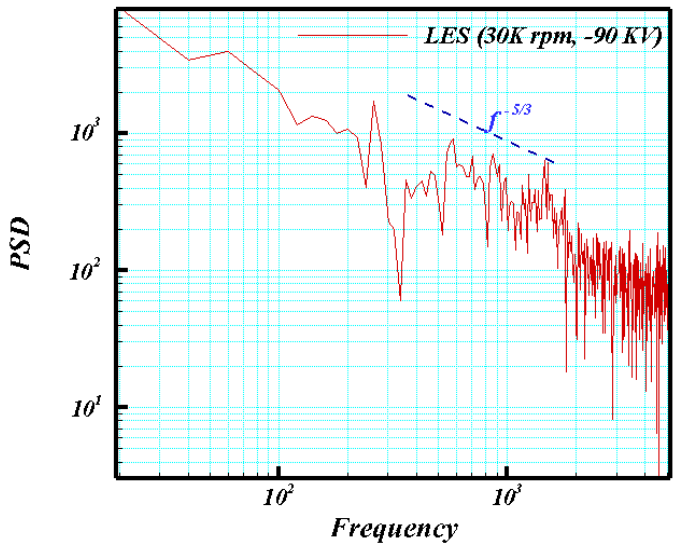

Figure 2.9: The turbulence statistics: The Power spectrum density (PSD) for the turbulent kinetic energy.

Table 2.2: Discretization Summary of the schemes employed in the current study.

Discretization		Schemes	Description
Time schemes		Backward difference	Second order, implicit
Spatial discretization	Gradient	Gauss linear	Second order (Gaussian integration), Linear interpolation (central differencing)
	Divergence	Gauss upwind	Second order unbounded (Gaussian integration), Upwind differencing
	Laplacian surface normal gradient	Gauss linear corrected	Unbounded, Second order, Conservative
Wall functions	*K*	kqRWallFunction	Acts as a zero-gradient condition for modeled k
	νt	nutkWallFunction	Generates near-wall profile of νt based on modeled k
Pressure–velocity coupling		PIMPLE	Merged PISO-SIMPLE algorithm

2.3.4. Pressure-Velocity Coupling

The pressure- velocity coupling is implemented by using the algorithm of PIMPLE that is a hybrid of SIMPLE (Patankar and Spalding, 1983) and PISO (Issa, 1986) algorithm, as shown in Fig. 2.10. This algorithm proposed a stronger pressure–velocity coupling by using a PISO inner-corrector loop with a SIMPLE outer-corrector loop. The pimple algorithm indicates a better

stability in numerical solution for the larger values of time-steps or higher Courant number in comparison with the PISO.

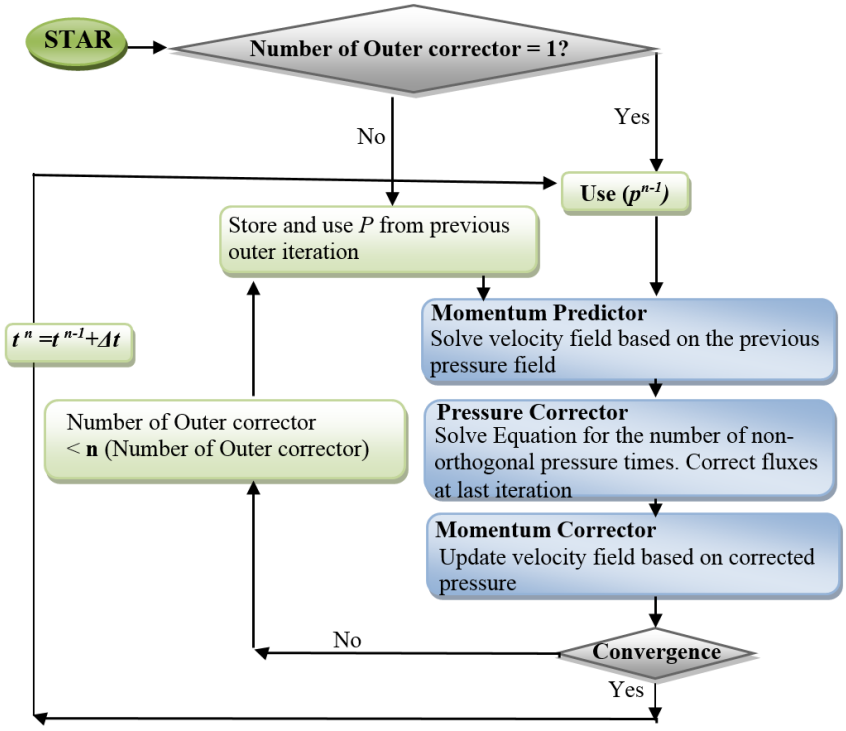

Figure 2.10: PIMPLE solution flowchart procedure used in OpenFOAM.

2.3.5 Solution convergence and procedure

Fig. 2.11 (a) shows the residuals convergence history of the velocity, pressure and turbulence kinetic energy for the entire run time for a typical test case ($\omega_{bell} = 30K\,rpm$, $VOLT_{cup} = -90kV$). Residual of each parameter is defined as the normalized difference between the current and previous value of that parameter. Fig. 2.11 (b)-(c) show residual variations at the beginning and end of the simulations, respectively. Residuals increase at the beginning of each time step and then drop by two to three orders of magnitude.

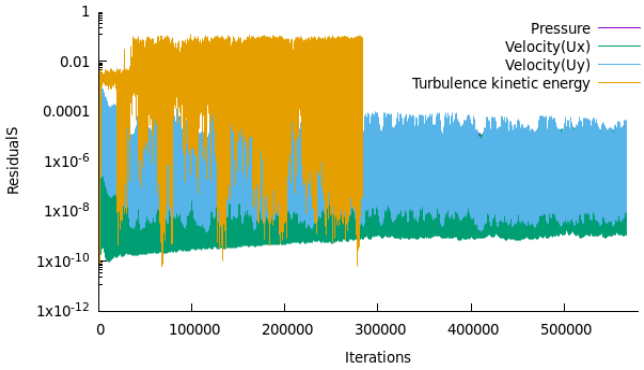

(a)

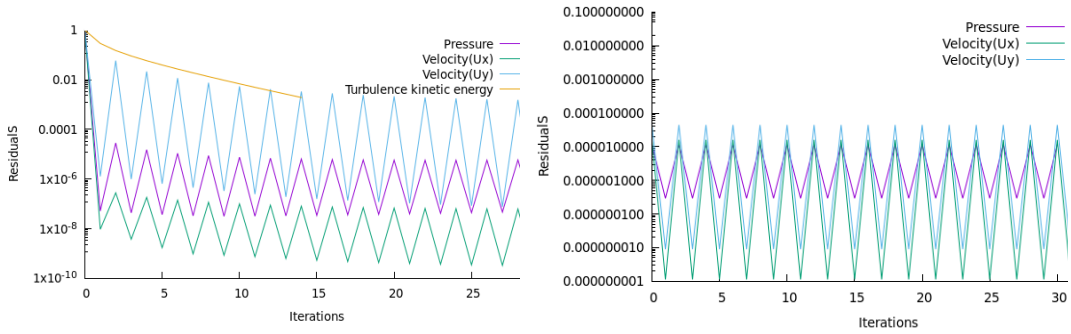

(b) (c)

Figure 2.11: Convergence of residuals for a typical spraying simulation, $\omega_{bell} = 30K\ rpm$, $VOLT_{cup} = -90kV$: (a) entire run time (b) first time steps (c) last time steps.

2.3.6 Grid Sensitivity Analysis

Fig. 2.12 illustrates the structured quadrilateral mesh applied in nearly all parts of the computational domain, and also an unstructured hexahedral mesh is utilized for a very small region just close to the nozzles of shaping airflow. We decompose the computational domain into the smaller linked volume in order to control more efficiently the grid density. Accessing the accurate results is strongly dependent on the size of the used mesh, especially the region around the cup of the sprayer and areas close to the target, in which there are stronger flow gradients and the interaction among the airflow and paint particle are crucial and therefore the mesh must be very well refined. Fig. 2.12 (c) shows that there is a dense mesh near the two above mentioned areas and an increase is progressively in the other regions, that gradient of the flow variables is small.

We evaluate the accuracy of the obtained simulation results by examination of the different grid sizes and eventually we performed our numerical simulations using about 8.5 M cell, the minimum values of mesh length is 2×10^{-4}, near the ninety airflow nozzles, as depicted in Fig. 2.12. Details of the grid sizes are reported in Tab. 2.3. The average cell size around the paint particle injector is near 1.5×10^{-4} and the minimum and the mean values of y^+ were 0.35 and 5.1 in the ERBS. For $30 < y^+ < 300$ at most positions, i.e., near to the body area, the implemented solver applies wall functions. At the beginning of the simulation the size of the time step was calculated automatically according to the specified Courant number with values of 0.5 that resulted in an average time step of around 10^{-8} s, this is a sufficiently small period to capture the details of the initial phenomenon that happens in the ERBS working procedure. Then, the modeling continued with a constant time step value of 10^{-7} s. We realize that the lower values of the Courant number do not change the simulation results. The total computational expense for the simulation time of the LES and k-ω SST turbulence models, for the case with the condition of $\omega_{bell} = 30K\ rpm$ and voltage of $VOLT_{cup} = -90kV$ are 660 and 490 hours, respectively, using 60 processor cores.

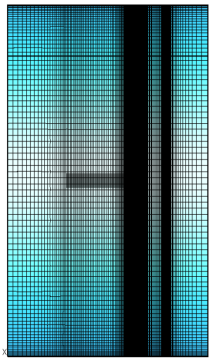

(a) Z-axis

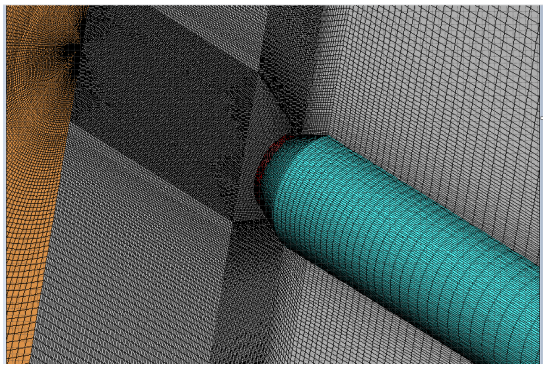

(b) Computational grid

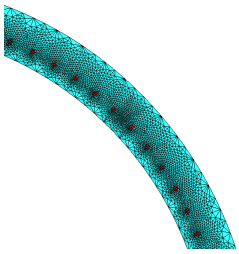

(c) Shaping air nozzle

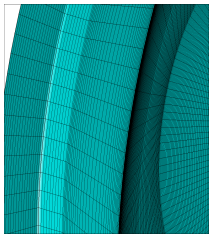

(d) Edge of the bell cub

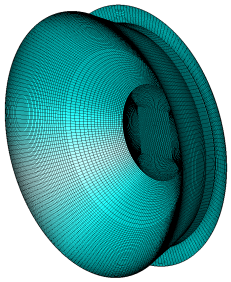

(e) The bell cub

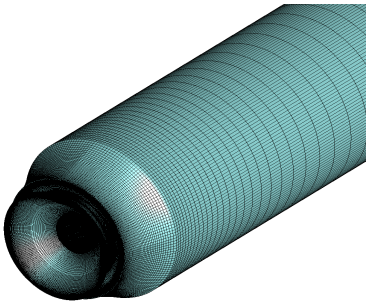

(g) ERBS

Figure 2.12: Mesh distribution around the electrostatic rotary bell sprayers (ERBS) which is used in the current simulation.

Table 2.3: Details of different grid sizes.

Mesh for	Number of cells ($\times 10^6$)	Region				
		Front surface (from the center of the Cup)	Upper surface (from the center of the Cup)	Behind Surface (from the center of the Cup)	On the Cup along the radius	Thickness of the Target
Grid1	4.5	150	135	100	100	7
Grid2	8.5	160	190	120	180	10
Grid3	13.5	195	225	120	272	12

2.4. Results and Discussion

2.4.1 The Solver Validation: Comparison with the experimental and numerical data

Before presenting the results of the electrostatic spray painting (ESP) process over the ERBS, the accuracy of the applied numerical code is evaluated by comparing with the available numerical result and experimental data. Fig. 2.13 (a) illustrates the length of the recirculation

area (L_{rz}) that is measured from the bell-cup rim to the position where the longitudinal velocity on the axis reaches its maximum value. The diameter ratio defined as $DR = d_{cup}/(d_{cup}+2e)$ is 0.97 where e is the flow thickness over the bell-cup surface that is assumed at approximately 1 mm. A value of $L_{rz} = 0.72\ d_{cup}$ is found in the current study is coherent with the values of $L_{rz} = 0.7\ d_{cup}$ reported by Stevenin et al. (2015) (just around 2 mm) and also there is a good agreement with the correlation proposed by Taglia (2003). Also, we compare our measured values for L_{rz} with other references with different blockage ratios (DR^2) (Ko and Chan, 1978; Chigier and Beer, 1964; Durao and Whitelaw, 1978). In frame (b) of this figure the dimensionless values of computed velocity in our study compared with those obtained from experimental data (Martinez, 2013) and the accuracy of the implement code can be clearly observed. Additionally, for validation purposes, we compare our results, potential and electrostatic fields, with the Viti et al. (2008) work in the same simulation condition and a suitable agreement with their results is observed (frame b and c).

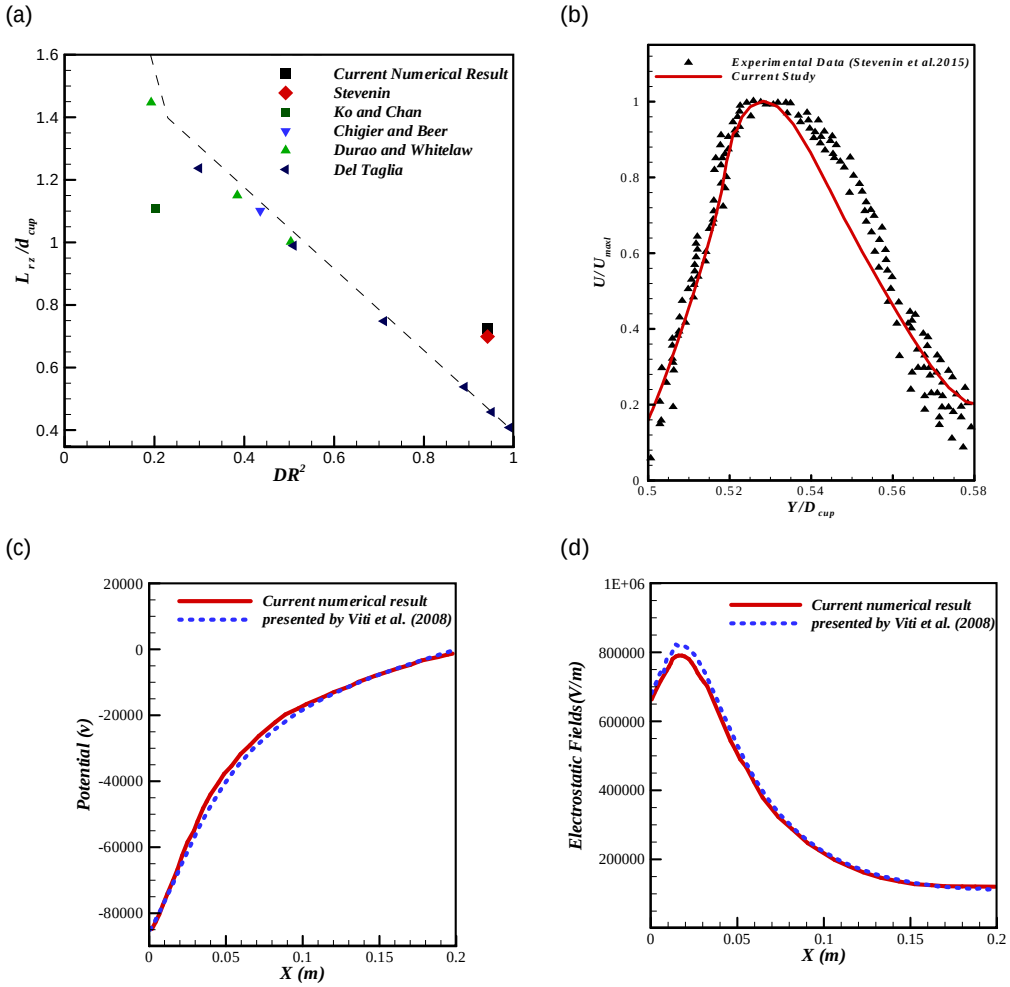

Figure 2.13: (a) Evolution the recirculation region length with the blockage ratio DR2. (b) Comparisons of dimensionless values of computed velocity with the experimental data. (Martinez, 2013) (c) Comparison of the potential field and (d) the electrostatic field distribution between the cup and the target along the gun centerline with the numerical results (Viti et al., 2008).

Fig. 2.14 shows close-up views of the injected paint and shaping airflow behavior just near the bell of the ERBS. Our numerical computed spray flow compared with a series of low-speed photographic images which are gained from experimental results (Martinez, 2013). As Fig. 2.14 illustrates, there are appropriate qualitative agreements among the current numerical solutions with those of the experiments, indicating that the numerical method can handle spray flows on ERBS appropriately. As it is obvious, especially in the frame (a), the re-circulated flow, which is created between the ERBS and the surface of a target because of the shaping airflow and high-speed rotational speed of the bell ensures the suitable overall agreement in comparison with the experimental results. In addition, a higher amount of the paint droplets stayed on the outside of the bell cup rim in comparison to the re-circulating zone. The Sauter mean radius of the injected particle of the numerical computing was set at the values of 75 μm. It must be mentioned that the experimental research in the ERBS supplied reliable and valuable insights on the spray transfer processes, but the control and set of the flow with precision are difficult and costly. On the contrary, the numerical investigations have some advantages such as lower cost, full detailed information, parameter control and higher efficiency.

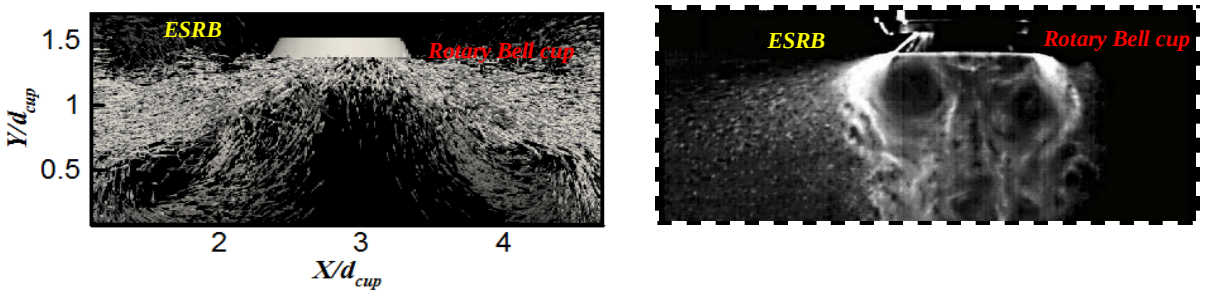

(a) $\omega_{bell} = 40K\ rpm$

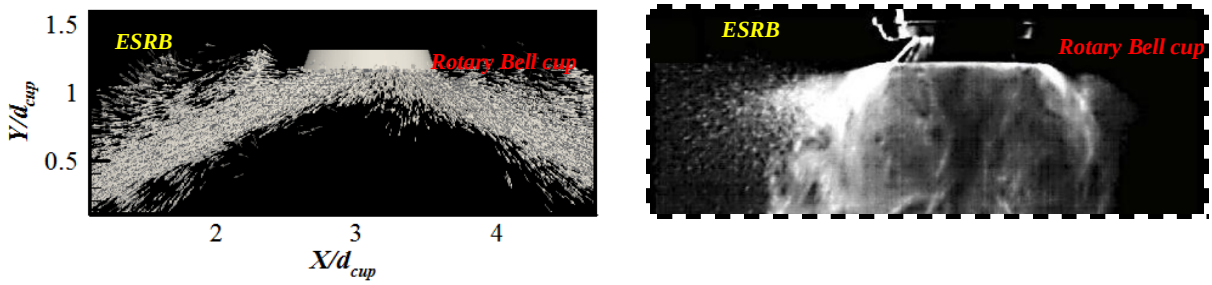

(b) $VOLT_{cup} = -90\,kV$

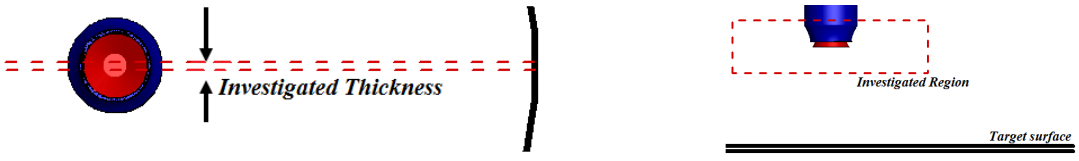

(c) Determination of shown zoomed area in the domain

Figure 2.14: Spray paint particle distribution over the ERBS in various operational condition: experimental results were taken by the low-speed photographer (Martinez, 2013) (right column) Numerical results of code implemented in the current study (left column) (Reference conditions: $\dot{m}_{air} = 350\,norm.l/\min$, $\dot{m}_{paint} = 350\,ml/\min$, $\omega_{bell} = 30K\ rpm$, $VOLT_{cup} = -60\,kV$)

2.4.2 Analysis of ERBS flows

2.4.2.1 Electrical analysis of the particle injected from single spray inlets

At first, the effect of the electric voltage was considered in the case of a cube with a spray inlet for injection of the particle in its upper surface in a various range of it. The computational domain and utilized mesh for this case are shown in Fig. 2.15. Fig. 2.16 illustrates the cut plane of the electrostatic field contour and the velocity magnitude values for the particles over a broad range of voltage charge from 0 to 100kv volts. For the smaller values of voltage, no change occurs in the distribution of the sprayed particle. The effect of the electrostatic field first starts at the voltage of around 20kV and appears near the injection area. By increasing the voltage values of electrical force affect more on the injected particles. This procedure confirms that the implemented models and the numerical procedures used for the electrostatic field in this study can accurately capture the spray mechanism. Also, the frames in Fig. 2.17 show the contour of the potential values and particles with their diameter values at the same working conditions of Fig. 2.16.

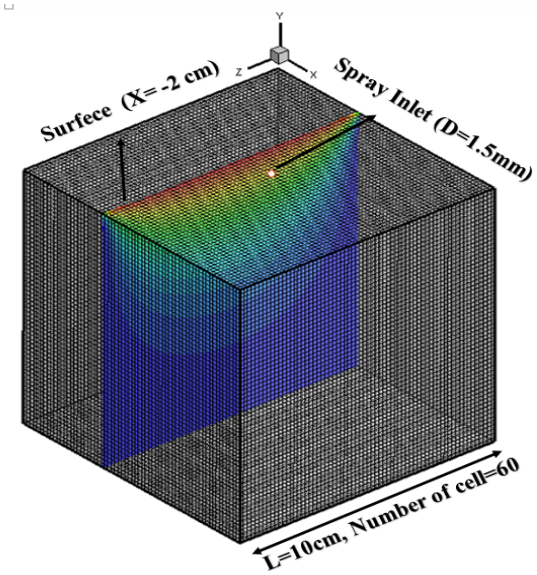

Figure 2.15: The Computational domain and mesh of a cube with a spray inlet.

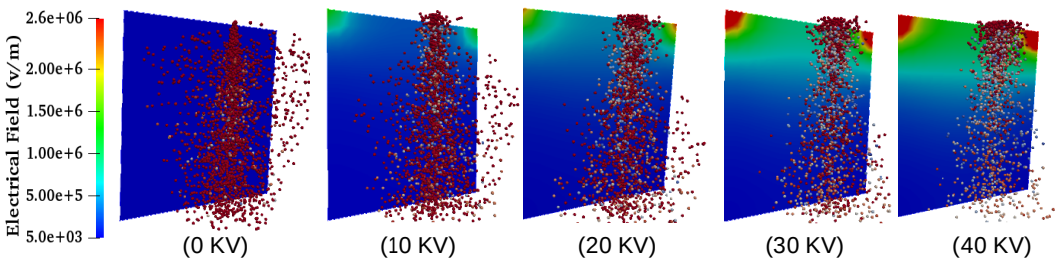

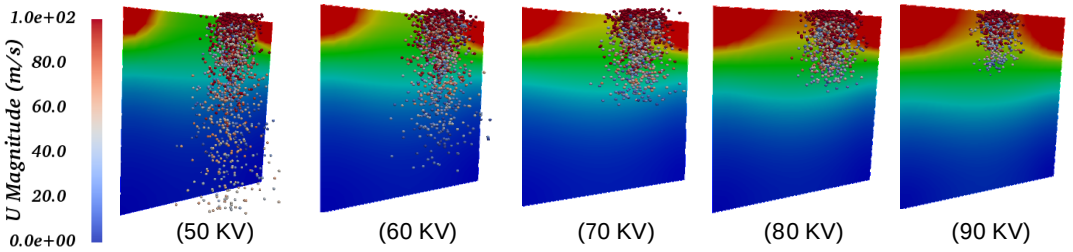

Figure 2.16:The cut plane through the 3D domain shows the electrostatic fields. Screen capture of the color scale of the droplets is according to their velocity.

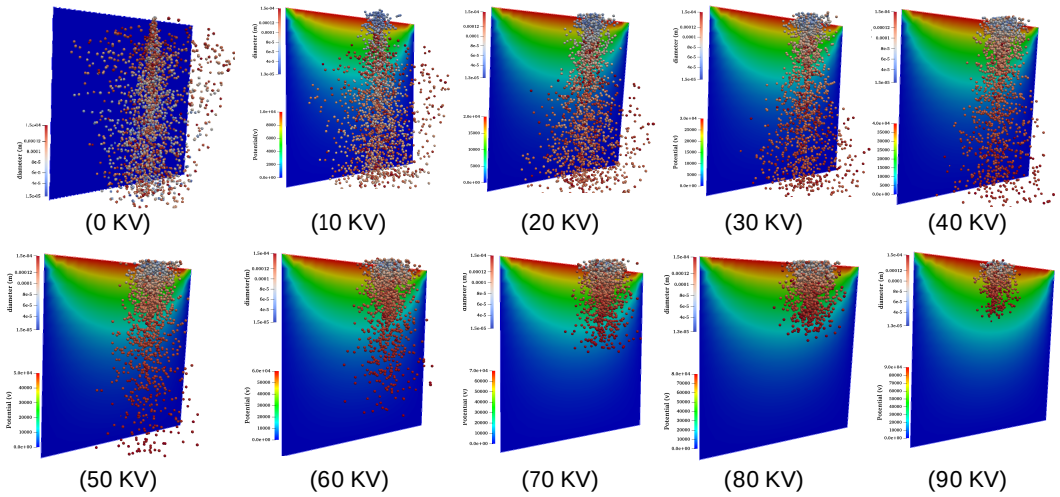

Figure 2.17: Contours of the potential field and particle color is according to their diameter.

2.4.2.2 Representation of the discrete Phase

The spraying process in the ERBS is a three-dimensional complex turbulent flow of tremendously unsteady swirling nature. In the first part of this section, we consider the behavior of the discrete phase. These injected spray droplets surrounded with the high velocity shaping airflow. The data of the implemented tests and also the properties of used material are presented in Tab. 2.4. The electrostatic field and the rotational speed of the electrostatic rotary bell sprayer are compared in Fig. 2.18 (a-c) for different temporal sequences. Also, this figure contains a perpendicular view as small images in each frame. The higher amount of the voltage drive away from the paint particle to the target surface is faster with size reduction of the paint particle cone (Fig. 2.18 (b)). Also, it can be understood from these figures, the shaping airflow supports the transport of the paint particles and stabilizes particles primary movement path. This flow pattern limits the particles cone dimension. The radial size traveled by the particle decrease dramatically with a decrease in the rotational speed of the bell cup, from 20K rpm to 40K rpm (Fig. 2.18 (a, c)).

Table 2.4: Boundary conditions and test data for the current numerical simulation.

Cup rotational speed (K rpm)	20, 30, 40K rpm
Shaping air mass flow rate (norm. l/min)	150 norm. l/min
Paint flow rate (ml/min)	150, 200 ml/min
Paint density (kg/m^3)	998 kg/m^3
Air density (kg/m^3)	1.225 kg/m^3
Cup voltage (KV)	-20, -90 KV
Target voltage (KV)	0 KV
Air viscosity (Pa.s)	Ideal gas law (R=287J/Kg/K) Pa.s
Paint resistivity (MOhm)	200, 250 MOhm
Target distance (mm)	250 mm
Charge-mass ratio (C)	-6e-10 C
Downdraft air flow rate (m/s)	0.1 m/s

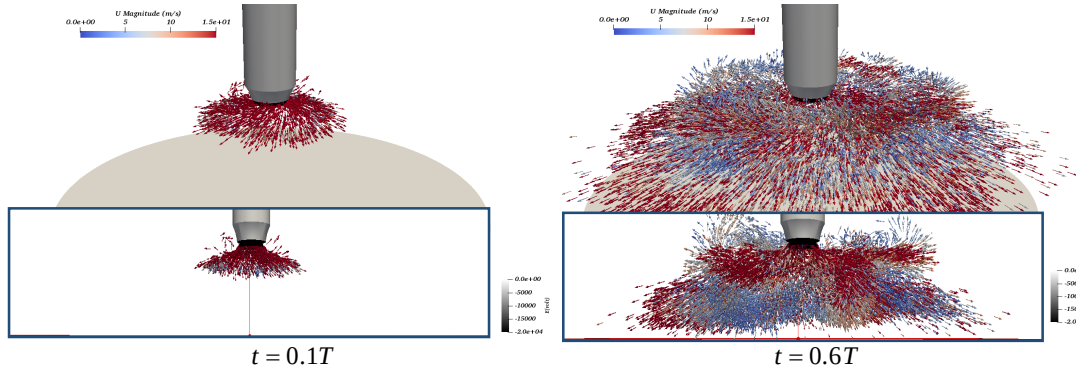

$t = 0.1T$ $t = 0.6T$

$t = 0.8T$ $t = T$

(a) $\omega_{bell} = 40K\,rpm$, $VOLT_{cup} = -20\,kV$

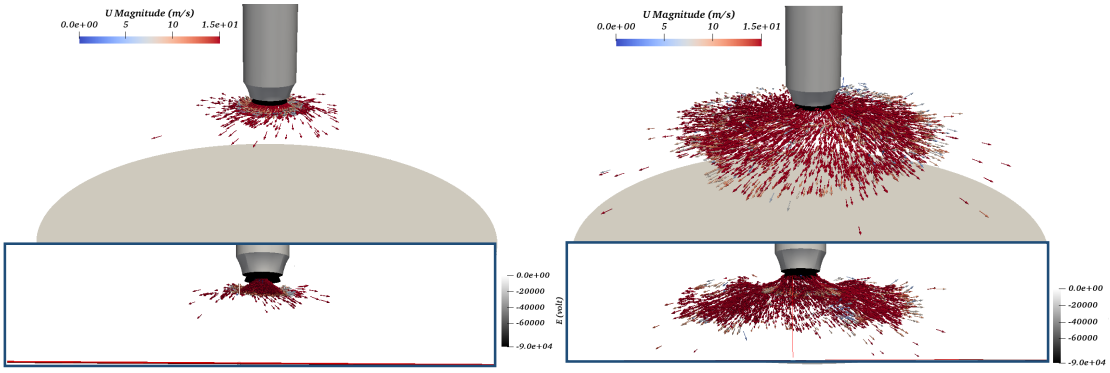

$t = 0.1T$ $t = 0.6T$

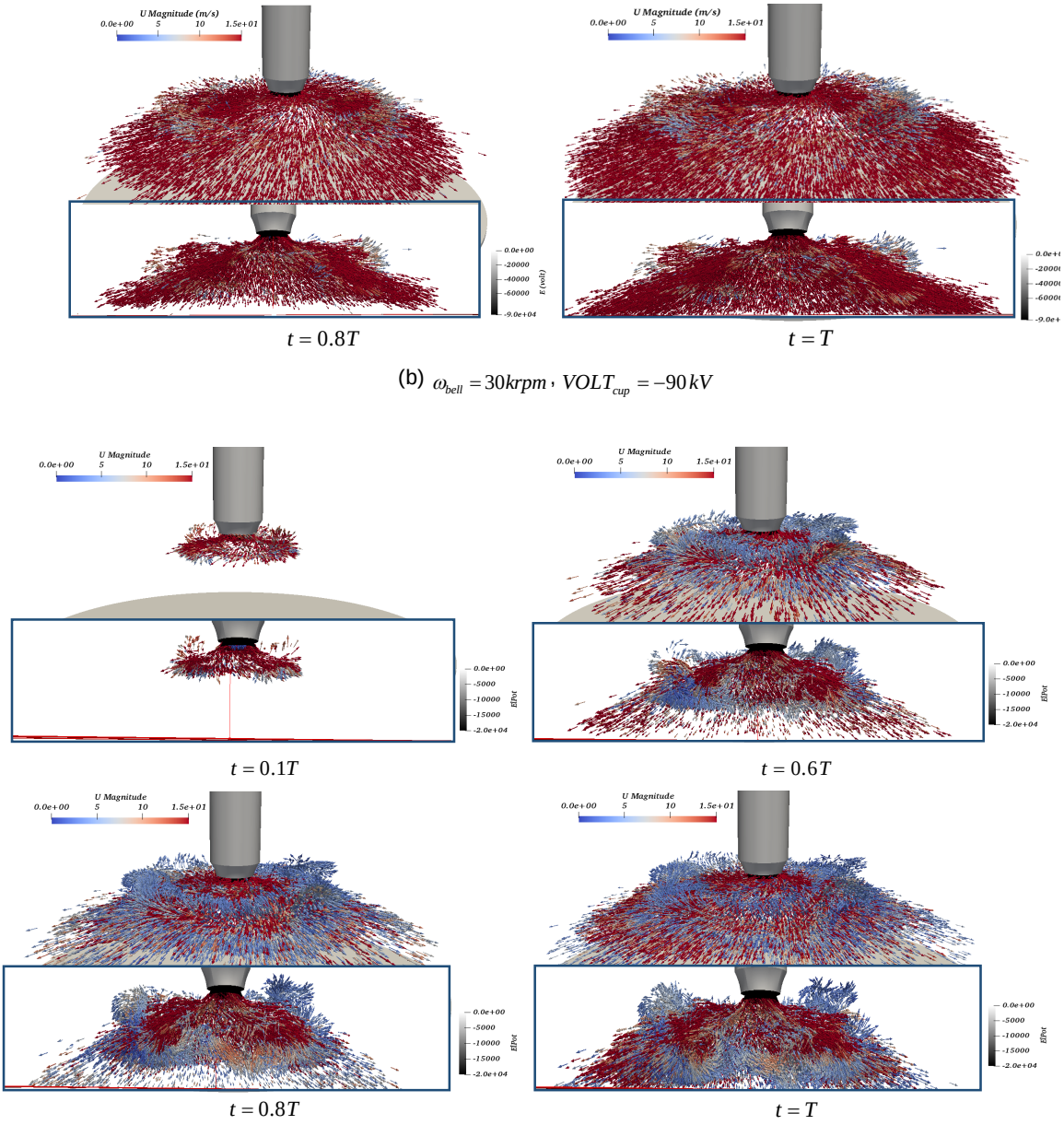

Figure 2.18: Particle trajectories colored by their velocity magnitude, and the direction of the arrows representing their velocity vectors: Comparisons for various electrostatic voltages and rotational speeds captured during one complete spraying cycle (T).

Fig. 2.19 graphically shows the initial positions of the injected paint particles corresponding to the various speed of the rotary bell cup and different rate of the shaping air at the similar time of the spraying procedure. The uniformity and accumulation of the paint particles in higher potential values (-90 kV) due to the effect of the electrical force are higher than lower ones (-20 kV). Also, the size distribution of the paint particles in the lower values of electrical potential is more non-uniform. Overspray generally happen by the smaller size of the droplets due to their lower momentum and this phenomenon decrease their power of penetration. But, the larger size of the paint particles due to their higher momenta are more effective in increasing the values of the transfer efficiency (TE). The formulation of the transfer efficiency (TE) is expressed as

$\mathrm{TE} = (m_f - m_i) \times 100 / \mathrm{m}_{out})$, where m_i is the sample initial mass, m_f is the sample mass after drying and painting and m_{out} is the paint mass that exists the nozzle in the spraying process. It can be clearly identified that the backward flow runs towards the rear part of the ERBS, and it decreases with an increase in potential, or with a decrease in rotational speed. We thus observe a lower amount of erratic turbulent atomization.

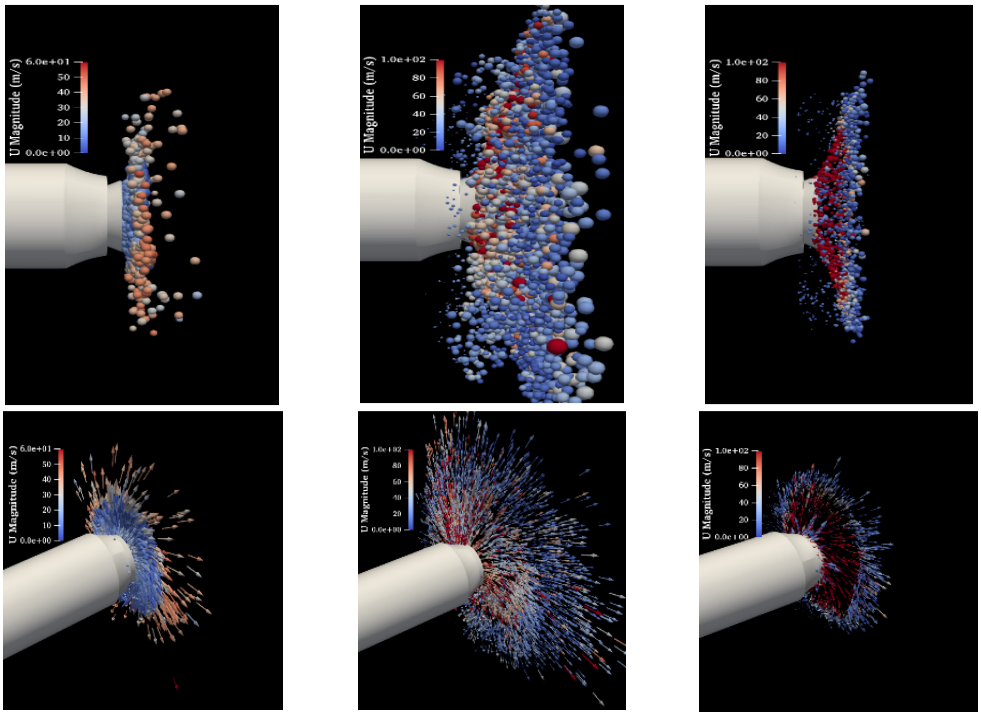

$\omega_{bell} = 20\,krpm$, $VOLT_{cup} = -20\,kV$ | $\omega_{bell} = 40\,krpm$, $VOLT_{cup} = -20\,kV$ | $\omega_{bell} = 30\,krpm$, $VOLT_{cup} = -90\,kV$

Figure 2.19: The formation of the paint particles at the initial time near the bell cup extracted from numerical data.

The parameters affecting the TE can be divided into two classes, the physical parameters (paint density, viscosity, surface tension and percent solids) and the operational conditions (gun pressure, angle of spray cone and spray relative to target, the distance between the gun and the surface, size and shape of the target, skill level of operator, mass flow rate of paint). Fig. 2.20 illustrates the behavior of the particle qualitatively in two various simulation conditions. Fig. 2.20 (a) indicates that a growth in the rotational speed produces the same behavior in air flow. But, the advantage of increasing the electrical potential values produced a more uniform mass distribution of the paint and a lower amount of turbulent atomization. As Fig. 2.20 shows, decreasing the gun-to-target distance, or increasing the size of the workpiece, tends to increase the TEs. In the higher values of the rotational speed, the coating particle leaves the gun of ERBS rapidly, as a result, the pattern of spray may experience overshoot and overspray. This figure also shows that an increase in the rotational speed of the bell cup produces a decrease in the size of the paint particles and, as a result, the effect of the shaping airflow is curtailed.

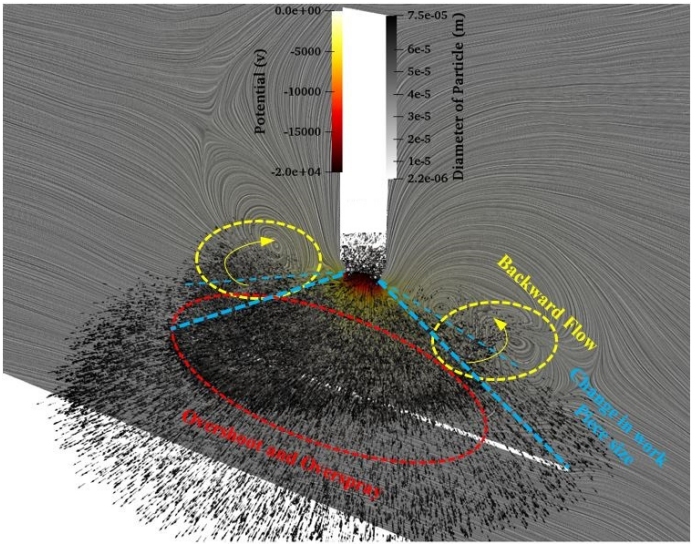

(a) $VOLT_{cup} = -20\,kV$, $\omega_{bell} = 40\,krpm$

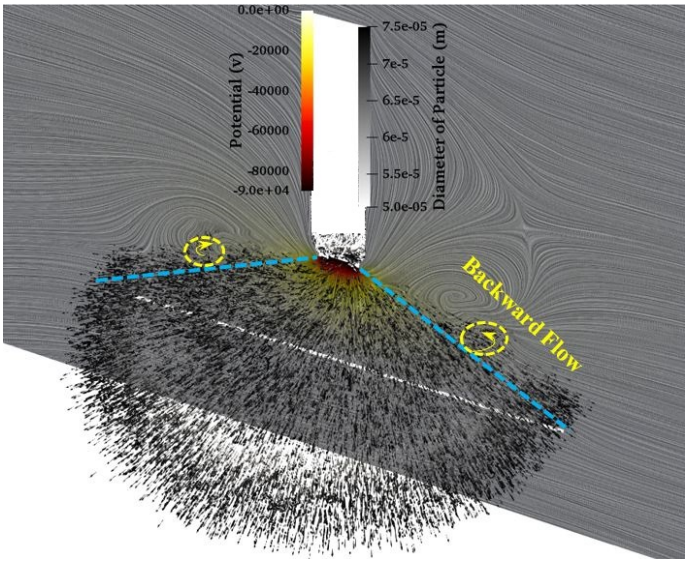

(b) $VOLT_{cup} = -90\,kV$, $\omega_{bell} = 30\,krpm$

Figure 2.20:The qualitative comparison of transfer efficiency (TE) for the injected particles.

One important non-dimensional number to be considered is the Stokes number ($Stk = t_0 u_0 / l_0$), that determines the behavior of suspended particles in fluid flow. It is defined on the characteristic response time of the particle divided by the characteristic response time of the flow. Here is the fluid velocity well away from the obstacle u_0, relaxation time particle is the t_0 and actor in is the obstacle characteristic dimension. The Stokes number is a determinative f l_0 the particle behavior, especially close to the stagnation area, the streamline curvature of the continuous flow as shown in Fig. 2.21. As it is clear from Fig 2.21, particles usually follow one of these three paths after impressed by the shaping air: i) Particles with high Stoke's number move towards the workpiece. By the sharp turning of the flow, it is crashed with the solid target droplets having lower values of the Stokes number who pursue the curve. ii) Either they trapped

in a very powerful recirculation flow and tend to move radially outward and lost in the booth air and do not reach to the target. iii) Or they convected radially inward of the jet.

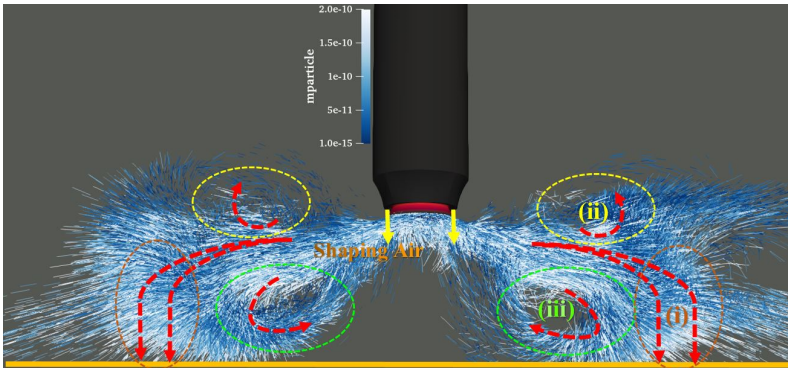

(a) $VOLT_{cup} = -20\,kV$, $\omega_{bell} = 40\,krpm$

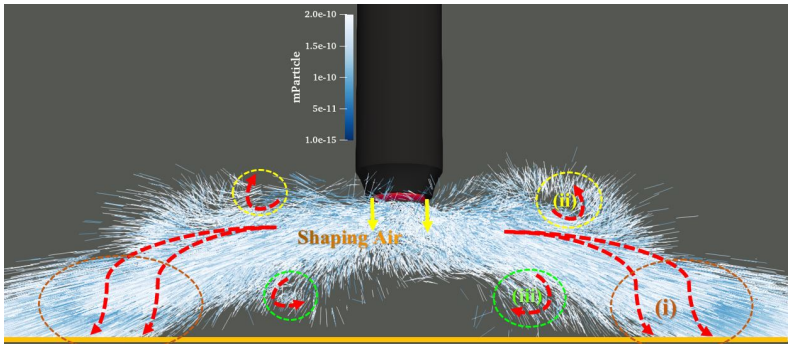

(b) $VOLT_{cup} = -90\,kV$, $\omega_{bell} = 30krpm$

Figure 2.21: Paths of the paint particles in the high-speed rotary bell sprayer.

Fig. 2.22 shows the instantaneous distribution of the paint particles that are colored by (a) the mass and (b) the diameter of the particle in the condition of $\omega_{bell} = 30\,krpm$, $VOLT_{cup} = -90\,kV$, $\dot{m}_{air} = 150\,norm\,.l/\min$, $\dot{m}_{paint} = 150\,l/\min$. This figure shows that the particle's weight is very low near the cup of the ERBS in comparison with farther areas. As is seen in the second row of this figure indicates, the diameter of the particles have also a direct relation with their mass. The smaller particle size is simply moved via a downward flow that is strengthened by the shaping air system and, generally, they are placed at the center of the cone. This row also illustrates that the bigger particles cross the strong downward flow being unaffected by it. They move forward in the radial direction until they lose all their velocities.

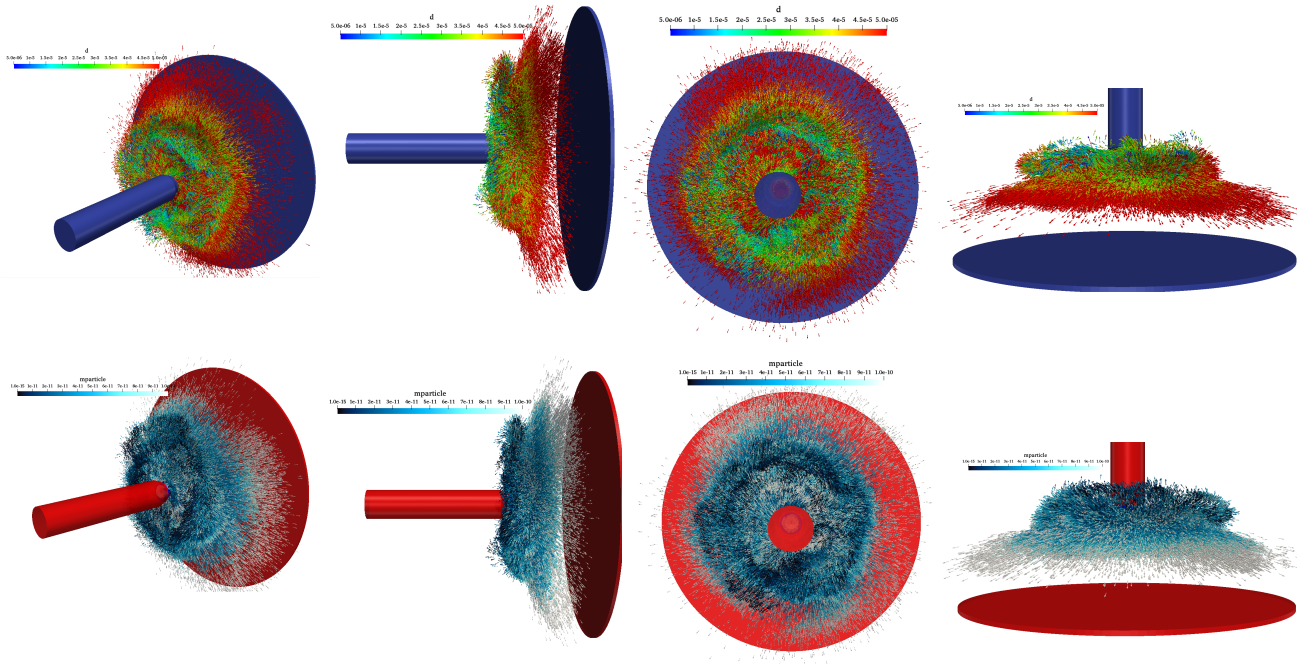

Figure 2.22: The two rows correspond, respectively, to (a) mass and (b) diameter of the particle. Applicator condition parameter: $\omega_{bell} = 30\,krpm$, $VOLT_{cup} = -90\,kV$, $m_{air}^{\cdot} = 150\,norm\ .l/\min$, $m_{paint}^{\cdot} = 150\,l/\min$, $N = 175000$ particles.

Fig. 2.23 (a-c) allows us to visualize a dense pattern of paint particle trajectory created when the droplets are charged. This framework tracked the paint particles over different three dimensional space in three types of perspective views for the mentioned operational conditions. The particles in this figure are colored by the velocity magnitude of the particles. The particles spread with a circular pattern and the electric force pulled them toward the surface of the target. In the case (b) the operational condition exerts a more powerful force on the droplets and they tend to be collected on the surface of the target in a very compact style. Also, from this figure it can be observed how the velocities of the paint particles presented higher speed near the surface of the bell and lose their velocity rapidly in the further distance. We qualitatively conclude that by increasing the rotational speed the TE decreases. Also, our simulation results indicate that for -90 kV, in comparison with the -20 kV voltage condition, the TE increase quite significantly.

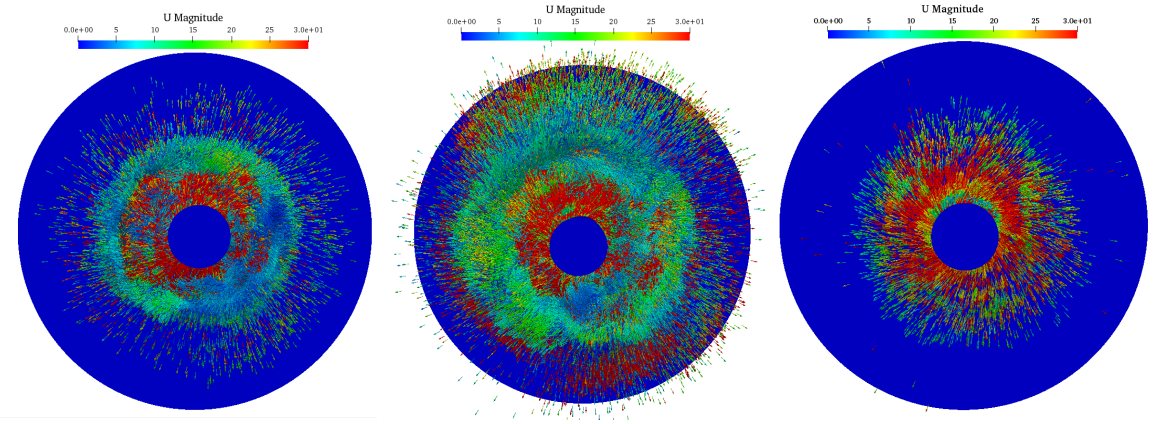

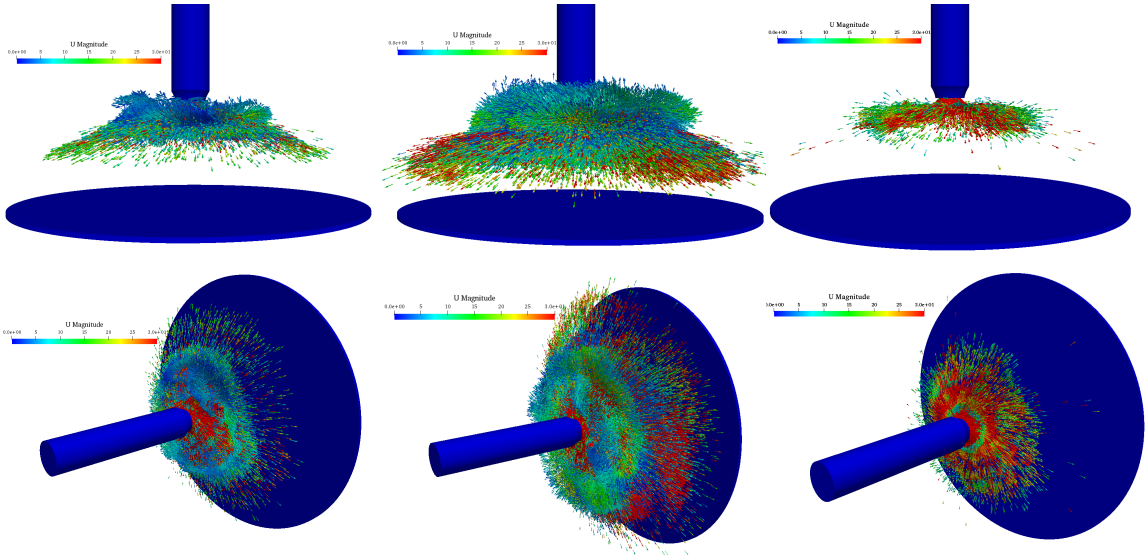

(a) $\omega_{bell} = 20\,krpm$, $VOLT_{cup} = -20\,kV$ (b) $\omega_{bell} = 30\,krpm$, $VOLT_{cup} = -20\,kV$ (c) $\omega_{bell} = 40\,krpm$, $VOLT_{cup} = -90\,kV$

Figure 2.23: The three columns correspond to 3D views of particles trajectory with their velocity magnitude ($N = 175000$ particles).

The deposition growth patterns obtained from the case with the operational condition of $\omega_{bell} = 30\,krpm$, $VOLT_{cup} = -90\,kV$ are presented in five consecutive frames in Fig. 2.24. A circular pattern of the paint film is formed with very low values of thickness in the center and also far away from the center. Also, Fig. 2.25 illustrates the temporal variation of the simulated film thickness profiles for the process parameters mentioned in Fig. 2.24.

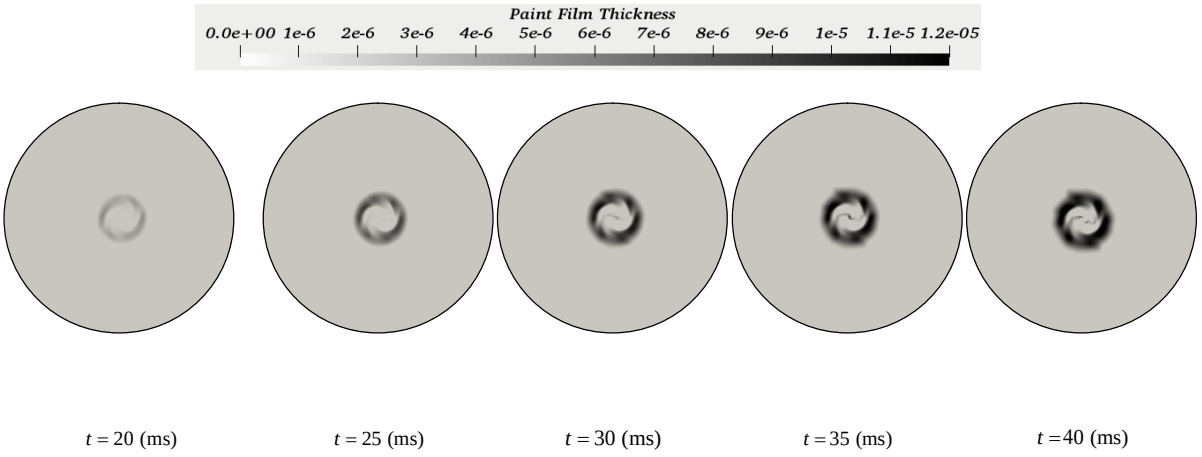

$t = 20$ (ms) $t = 25$ (ms) $t = 30$ (ms) $t = 35$ (ms) $t = 40$ (ms)

Figure 2.24: Time evolution of film thickness on the target surface, LES, $VOLT_{cup} = -90\,kV$, $\omega_{bell} = 30\,krpm$.

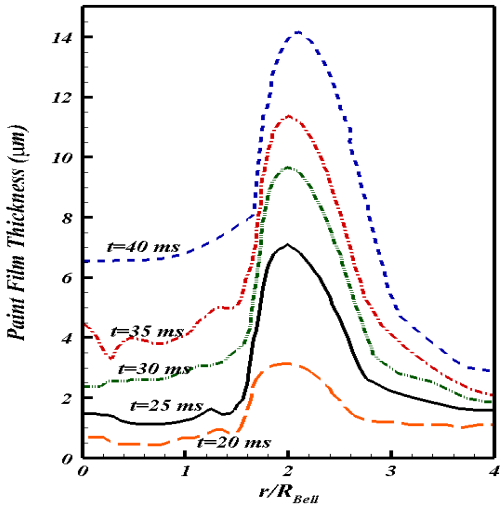

Figure 2.25: Temporal growth of the paint film thickness.

The calculation of the TE highlights the advantage of the CFD simulation for the investigation and troubleshooting of the spraying complex flow. The effects of operating conditions on the values of TE are shown in Tab. 2.5. The deposited particles were considered when the flow condition was fully developed for $t = 40\ (\mathrm{ms})$ after initial injection for the case with rotational speed of $40\ krpm$. In a $-20kV$ voltage condition and the rotational speed of $20krpm$ and $40\ krpm$, with a $q/m = 1.0\mu C$ of the charge to mass ratio, the numerical TE are 76% and 69%, respectively. The TE increases up to 91% when the electrical force is grown up to $-90kV$, at the same charge to mass ratio, at the medium rotational speed of $30krpm$. These results illustrates that the electrostatic force must consider as a critical issue effect on the TE. The TE values experience a huge increase by increasing the negative values of voltage. In addition, by increasing the rotational speed (from $20krpm$ to $40krpm$) and the swirl momentum of the droplets, the spray particles are dispersed to the outside more easily.

Table 2.5: Overall numerical transfer efficiency results for the three cases.

Simulation condition	$\omega_{bell} = 20krpm,\ -20kV$	$\omega_{bell} = 30krpm,\ -90kV$	$\omega_{bell} = 40krpm,\ -20kV$
Transfer efficiency (TE)	76%	91%	69%

2.4.2.3 Features of the unsteady continuous phase

In the second part of this section, a novel visualization of continuous phase without revealing of the paint particles was investigated quantitatively to delineate the behavior of the air flow and its interaction with the paint droplets. Fig. 2.26 indicates 2D views of the velocity contour of flow at x-y plane around our considered electrostatic rotary bell sprayer during one complete cycle corresponding to the condition of $\omega_{bell} = 30krpm$. It shows the air velocity contour, in which the maximum velocity along the x-axis reaches around 150 m/s. The value of the velocity is

higher than 15 m/s are blind out because the higher values just can be observed around the rim of the cup very close to the sprayer.

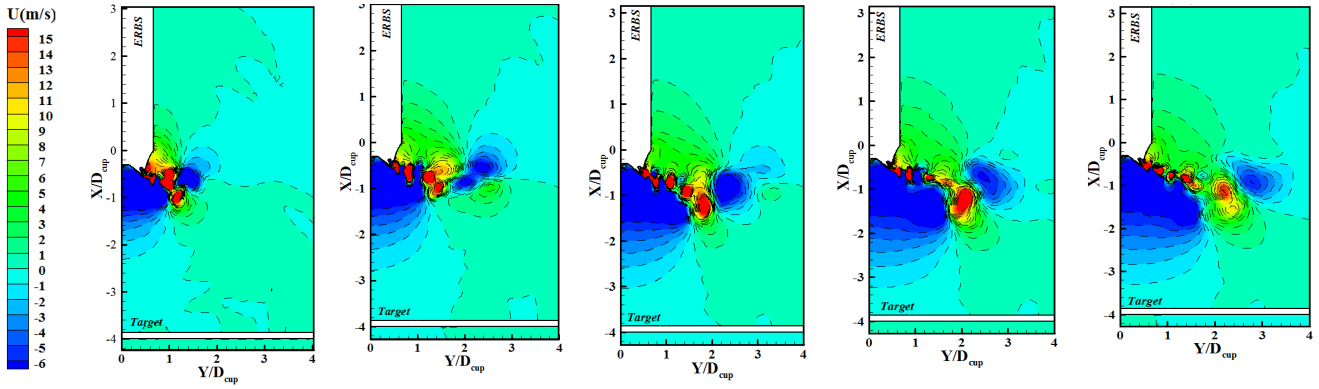

Figure 2.26: Visualizing of five consecutive temporal frames of velocity with the shaping airflow obtained during a complete cycle (T) ($\omega_{bell} = 30krpm$, $D = 0.25\ m$, $VOLT_{cup} = -90kV$, $\dot{m}_{air} = 150 norm.l/\min$, $\dot{m}_{paint} = 150\ l/\min$).

Fig. 2.27 illustrates the contour of potential fields on the center plane of the computational domain (frame (a, b)) and also its distribution on the surface of the ERBS (frame (c)). Also, this figure indicates the iso-lines around the geometry of the ERBS, near the air nozzles and cup (frame (b)) and far away from the surface of the gun (frame (a)), the lines change into a spherical shape. With the current space charge, the droplets leave the cup rim with higher values of speed. This electrostatic field produces a force on the particles proportional to their physical location and own charge. This figure clearly shows that a better efficiency obtained in the lower distance from the rim.

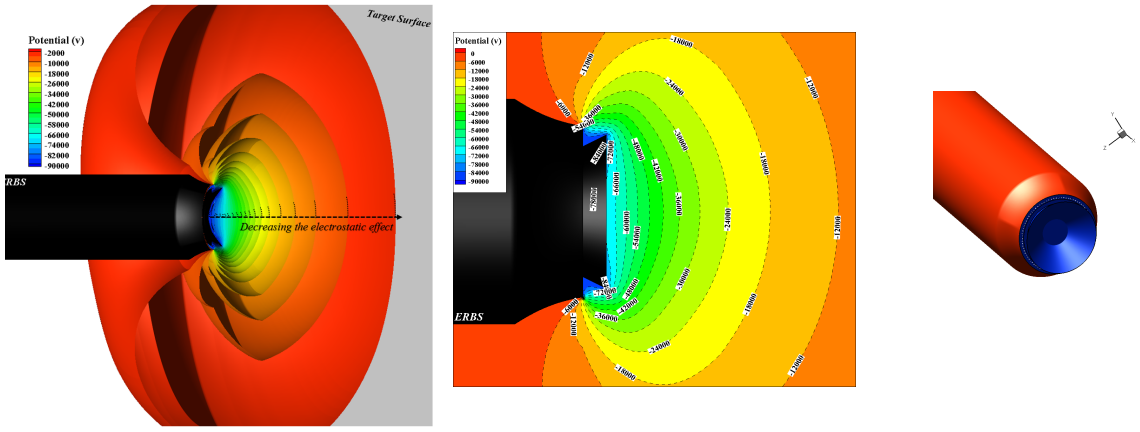

(a) Iso-potential planes on the overall domain

(b) A 2D views near the bell cup

(c) Potential values on the ERBS surface

Figure 2.27: Visualization of the potential field as 3D iso-surface among the ERBS and target.

Fig. 2.28 shows the 2D views of the velocity magnitude contour in the x-y plane past the ERBS at three different conditions. The air-paint flow of this figure illustrates that a smaller area of roughly axisymmetric high-velocity cutoff vortex tube instabilities is formed in the lower

rotational speed. The angle of high velocity vortex line enlargement by increasing the rotational speed. In the hollow conical volume of lower velocity, inside of the high-velocity vortex line, an increase in the rotational speed produces a bad effect on the wide-spreading of the particle. It has been realized from perpendicular planes to the axis of the ERBS that in the constant shaping air and at higher rotational speeds is more non-uniform especially near the shaping air inlet. The contour of the velocity is more non-uniform near the shaping air inlet. As a result of this non-uniform pattern, the particles leave the tip of the spray gun faster. Also, the airflow velocities are higher than Mach-number $Mach = 0.3$, which is why the compressibility effects of the air are considered. The rotational speed of $\omega_{bell} = 40K\ rpm$ along with the shaping air flow rate of 200 ml/min resulted in high values of velocity especially at the rim of the bell cup, with a maximum Mach number around $Mach \approx 0.45$. By the way, the velocity corresponding to the mentioned rotational speed is $\approx 155 m/s$.

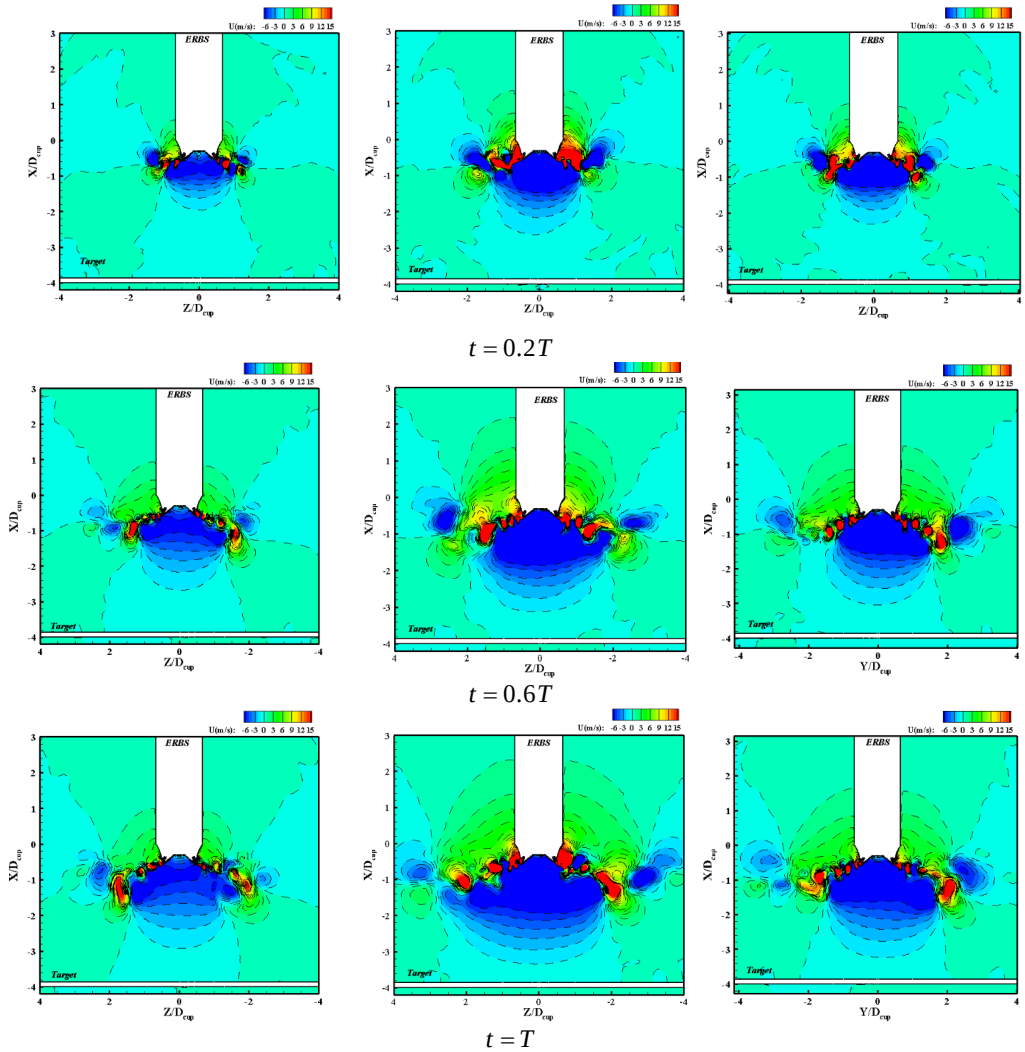

$\omega_{bell} = 20K\ rpm$, $VOLT_{cup} = -20\ KV$ | $\omega_{bell} = 40K\ rpm$, $VOLT_{cup} = -20\ KV$ | $\omega_{bell} = 30K\ rpm$, $VOLT_{cup} = -90\ KV$

$m_{air} = 150 norm.\frac{l}{\min}$, $m_{paint} = 150\frac{ml}{\min}$ | $m_{air} = 150 norm.\frac{l}{\min}$, $m_{paint} = 150\frac{ml}{\min}$ | $m_{air} = 150 norm.\frac{l}{\min}$, $m_{paint} = 200\frac{ml}{\min}$

Figure 2.28: Contours of the x-velocity (m/s) component along the vertical plane of symmetry.

Fig. 2.29 shows a novel visualization of the streamlines in the absence of the droplets for the vortex shedding and the toroid-shaped vortex ring. In the operating procedures of the ERBS, the toroid shape vortex ring is formed by impinging the two high-speed paint droplets together with the shaping airflow interactions. This figure also indicates the motion of the toroid shape vortex that produces the periodic unsteady vortex shedding happening in particular flow velocities. These vortices are then developed around the toroid vortex tube. In the last frame of this figure, the toroidal vortex is enlarging enough to reach the wall of the target. The toroid shape vortex collapses by getting away from the bell and reaching the target. The frames indicate a high swirl velocity (150 m/s), at the initial plane (x=0.0 cm), that deteriorates quickly as it comes close to the target plane.

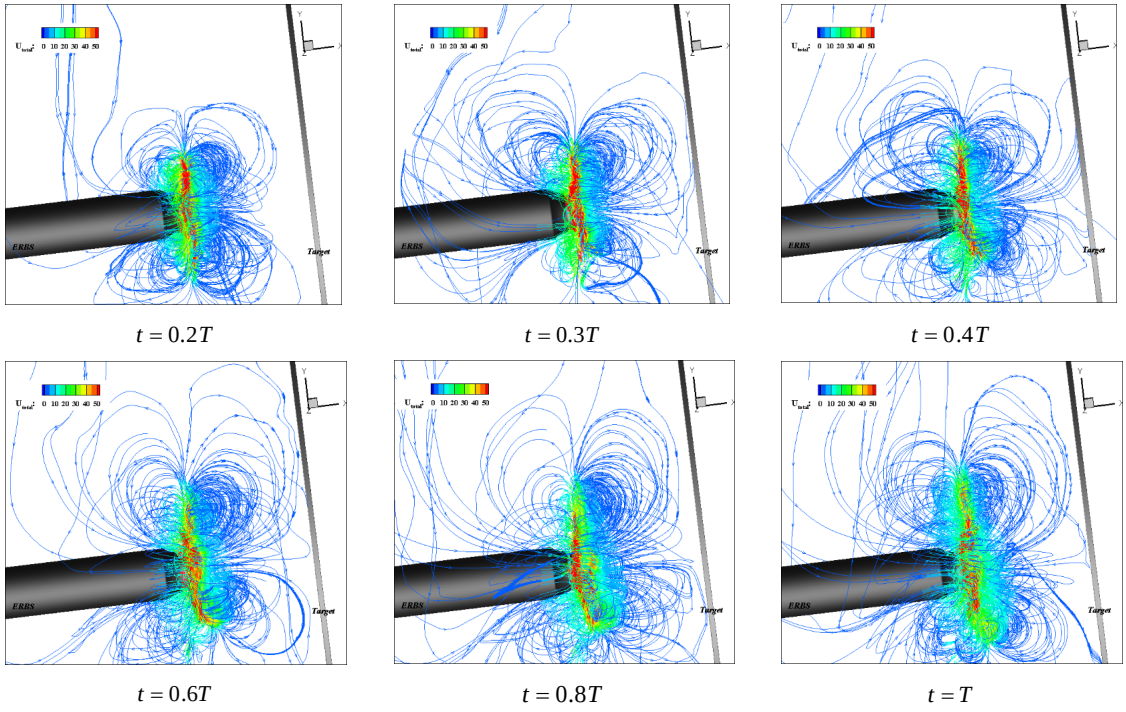

$t = 0.2T$ $t = 0.3T$ $t = 0.4T$

$t = 0.6T$ $t = 0.8T$ $t = T$

Figure 2.29: Detailed 3D views of the toroid shape inside the ERBS and created vortex shedding from the toroid-shaped vortex tube: Time evolution during one spraying cycle (T) ($\omega_{bell} = 30K\ rpm$, $VOLT_{cup} = -90\,kV$, $\dot{m}_{air} = 150 norm.l/\min$, $\dot{m}_{paint} = 150\ l/\min$).

Fig. 2.30 shows the process of formation of the dynamic pressure, the pressure that is equal to the difference between the total and the static pressure, at the sampling plane as a 2-D section at different distances of $X = 150, 175, 200\ mm$ below the rim of the cup. As shown in this figure, the strong circular movement of the flow is affected by the cup rotational speed and the downdraft velocity. The interaction between the two above mentioned events with the hollow conical shaping air jet create the turned flow towards the bottom right, that is stretched via the torsional effect of the cup. Also, it can cause to acceleration and blockage on the central and bottom parts of the picture, respectively.

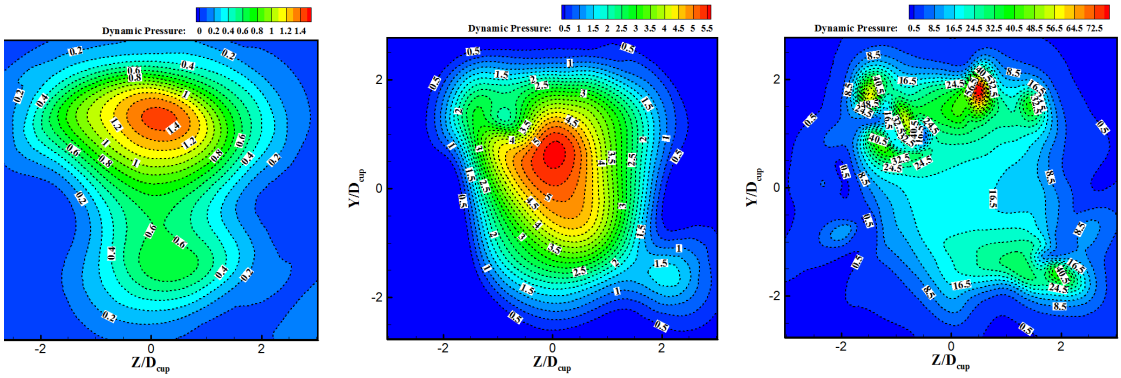

Perpendicular plane $X = 150\,mm$ Perpendicular plane $X = 175\,mm$ Perpendicular plane $X = 200\,mm$

Figure 2.30: Dynamic pressure contours at three different distances X, ($\omega_{bell} = 30\,krpm$, $VOLT_{cup} = -90\,kV$, $\dot{m}_{air} = 150\,norm.l/\min$, $\dot{m}_{paint} = 150\,l/\min$).

Fig. 2.31 shows and compare the mean and instantaneous velocity as a 2-D section in the z plane for two different turbulence models, LES and k-ω SST. In this case, with the LES model, a higher number of large velocity cutoff vortex tube instabilities is formed. By using the k-ω SST model these instabilities are smeared. In both models, the high-velocity vortex tubes are present near the bell cup, even though these vortical regions extend more behind the cup in instantaneous frames. Fig. 2.32 evaluates the LES and k-ω SST turbulence approaches at the same operating conditions. This figure demonstrates 2D contour of the velocity magnitude behind the ERBS. As it can clearly be identified from this figure, the LES solution can capture the unsteady vortex shedding in a better way near the air nozzles holes and rim of the gun. The k-ω SST is so weak to model the instabilities of the airflow.



(a) LES

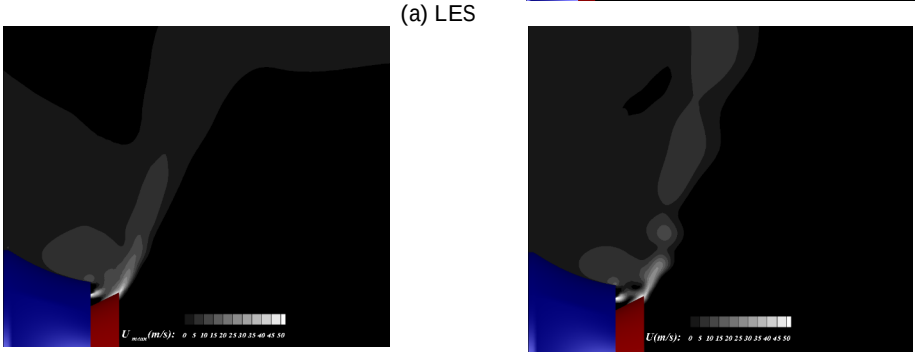

(b) k-ω SST

Figure 2.31: Instantaneous (right frames) and mean (left frames) velocity contours at ($\omega_{bell} = 30\,krpm$, $VOLT_{cup} = -90\,kV$, $t = 35$ (ms)).

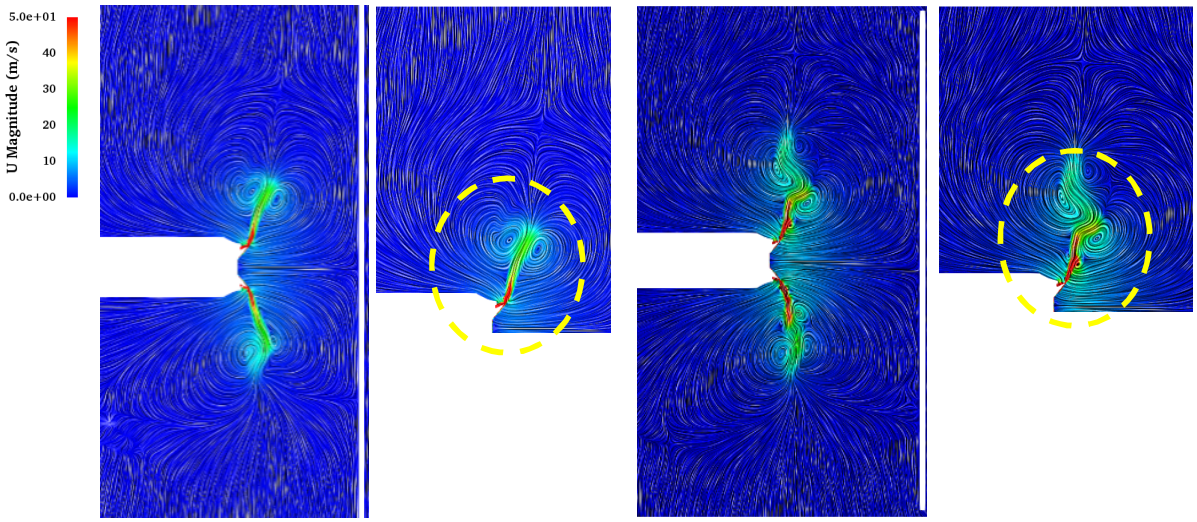

(a) K-ω SST (b) LES

Figure 2.32: Comparison of different turbulence models (LES/ k-ω SST) at the same time and boundary condition.

Fig. 3.33 shows the contour of the mean velocity with streamlines of airflow that visualized using the Line integral convolution (LIC) method (Stalling and Hege, 1997) from the LES solutions at three various operational conditions. The shaping air with high pressure exhausts axially symmetric from the ninety nozzles to the gun rim or re-directed radially toward the backside of the ERBS. This effect forms two main hollow radials high-momentum jets of air, each one impinging on the workpiece. This effect forms two main high-momentum hollow radials air jets, each one impinging on the workpiece. The generated vortical structures lead to a profound change in the front region of the ERBS as we increase the rotational speed. The figure clearly shows that the vortices are asymmetric on top and bottom with a slight difference due to a downdraft of 0.1 m/s. In addition to the mentioned two main vortex, as it is clearly obvious, lots of small-scale vortex structure can be observed around the separated layer region dividing back and front flow of the ERBS, playing a significant role in this flow.

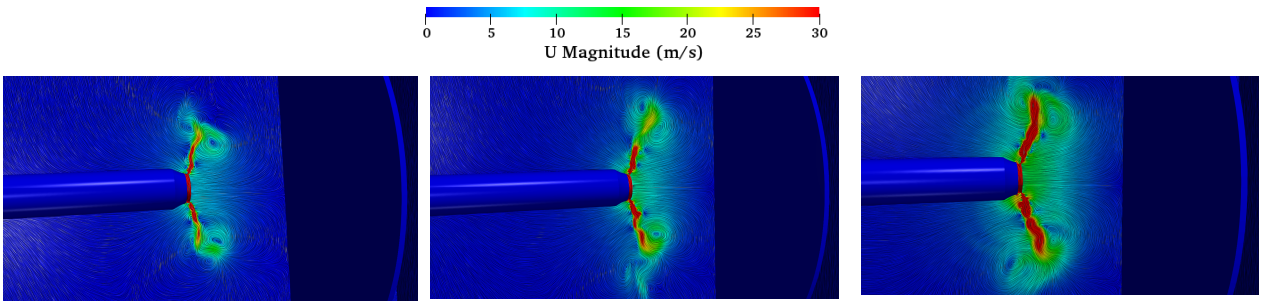

$\omega_{bell} = 20\,krpm$, $VOLT_{cup} = -20\,kV$ $\omega_{bell} = 30\ krpm$, $VOLT_{cup} = -90\,kV$ $\omega_{bell} = 40\ krpm$, $VOLT_{cup} = -20\,kV$

Figure 2.33: Contour of velocity (m/s) with visualization of streamline via LIC (Line Integral Convolution) approach along 2D plane.

2.4.2.4 Boundary-Layer investigation close to the Bell Cup

In the last part, Figs. 2.34-2.38 investigate the radial profiles of the normalized streamwise mean velocity fluctuation, mean turbulent kinetic energy (TKE), mean velocity and pressure in the region very close to the rim of the bell cup toward the outside where the turbulent layer starts to develop, for the same operational conditions of Fig. 2.28. These profiles extracted from where one of the shaping air nozzles existed. In Figs. 2.34 and 2.35 for turbulence study two various k-ω SST and LES solutions compared with each other just for one simulation condition. In these figures, the non-dimensional variables of U_N and $U_{\max}$ are the initial air velocity on the surface of the nozzle and the maximum radial velocity in the boundary layer outside the bell cup, respectively. The rotational speed of the bell of the atomizer is one of the main effective variations in the painting stability along with the airflow rate. Fig. 2.34 shows the normalized values of stress fluctuation. It is clearly obvious that the results of the LES approach are more accurate than unrealistic of k-ω SST solution (Fig. 2.37). Also, this figure also demonstrates that the values of the fluctuations significantly increase by growing of the rotational speed. Increasing of the fluctuations started exactly from the bell surface where the flow accelerates. These frames illustrate that the magnitude of these values increases at the interface of the injected airflow of the nozzle and airflow created by the rotation of the bell, especially in the higher rotational speed and confirm that the higher rotational speed accelerates the fluctuation level, even in the more distant area. However, the lines that gained from the various rotational speed of LES solution illustrates a close trend, but the location of peaks and trough are a little bit different. Fig. 2.35 presents the turbulent kinetic energy distribution in the same location reported in Fig. 2.34. The lines of various rotational speed show a close trend and also two different turbulence model shows the same results. The values of the mean velocity in the area close to the bell surface are compared in Fig. 2.36. The evaluation of the obtained results indicates that the frequency of the various rotation speed has an impressive effect on the characteristics of the airflow. By increasing the rotational speed, for instance 40K rpm, the vortex frequency also increases. The values of the turbulent energy in the lower rotational speed (20K rpm) is not strong enough to have a considerable effect on the flow. The same trend as Fig. 2.36 was observed in Fig. 2.38 for mean pressure distribution. In Fig. 2.37, comparing the velocity that obtained from the k-ω SST and LES turbulence model make clear the weakness of the k-ω SST model.

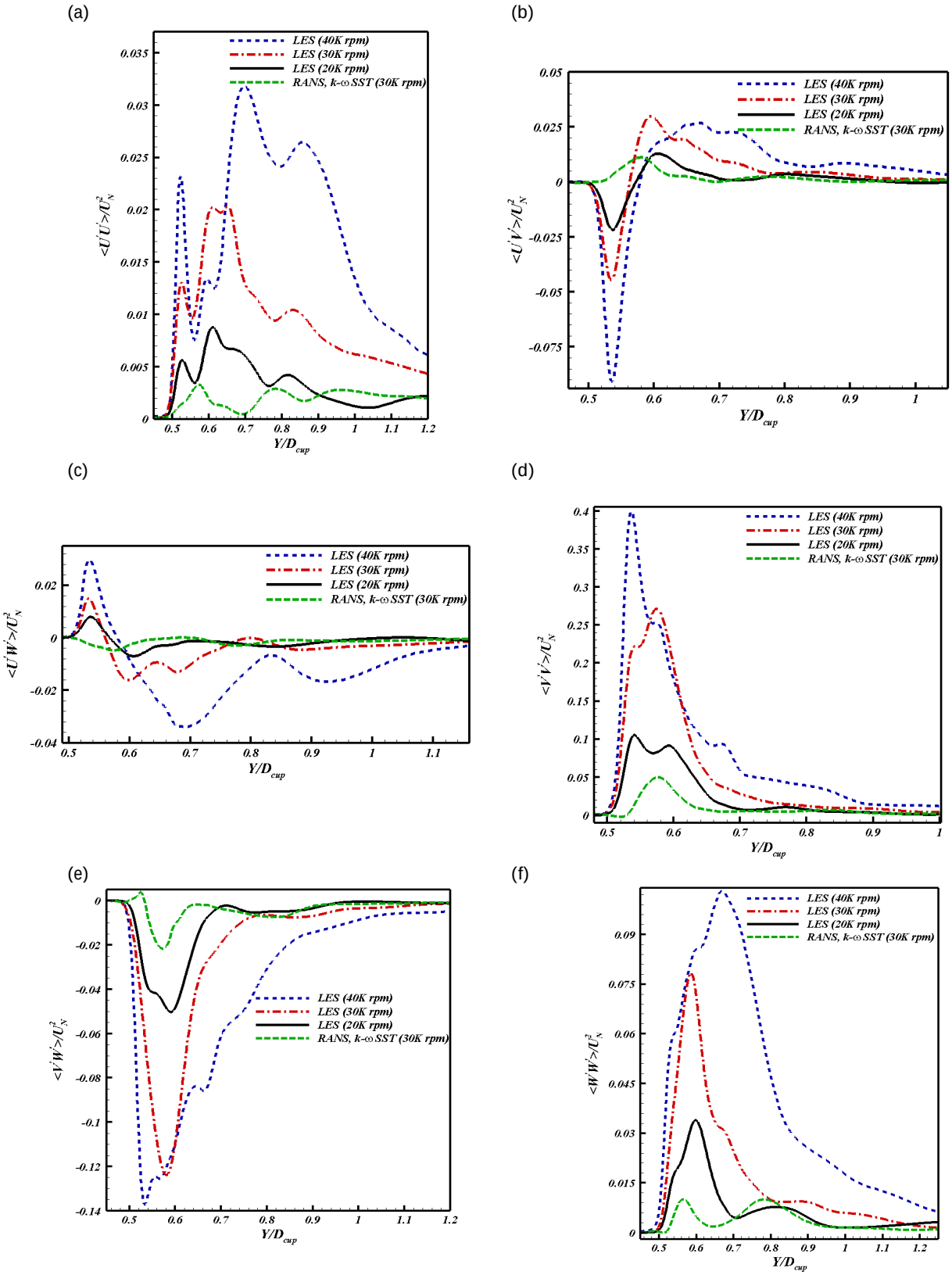

Figure 2.34: urbulent stress distribution ($<u'u'>,<u'v'>,<u'w'>,<v'v'>,<v'w'>,<w'w'>$) are plotted in the radial direction exactly close to the rim that normalized by the initial air velocity of the nozzle (U_N), LES and k-ω SST approaches, various bell rotational speed *N*= 20, 30, 40 krpm.

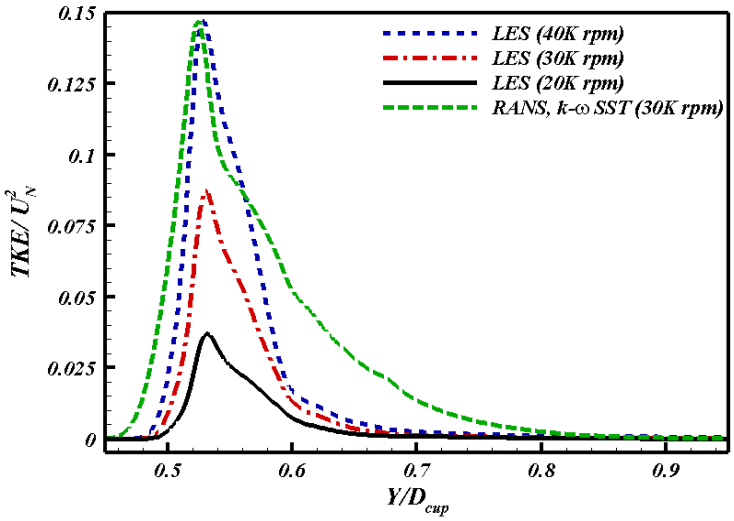

Figure 2.35: Turbulence kinetic energy (TKE) distribution at the same operational condition of Fig. 2.34.

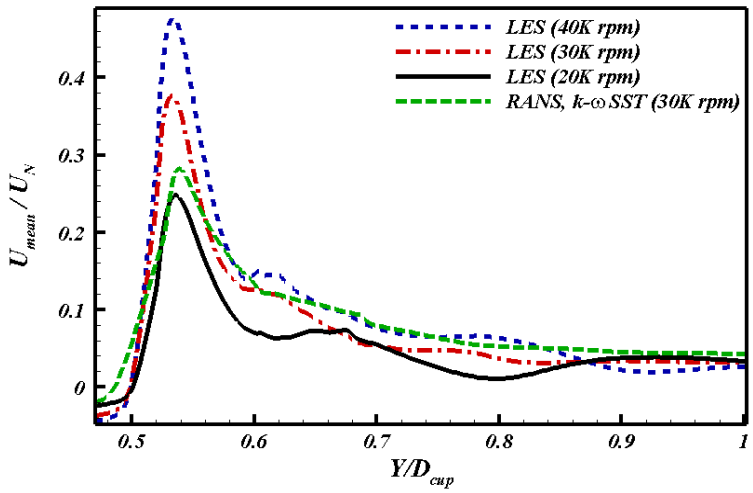

Figure 2.36: Comparison of mean velocity at the same operation condition and position of Fig. 2.34.

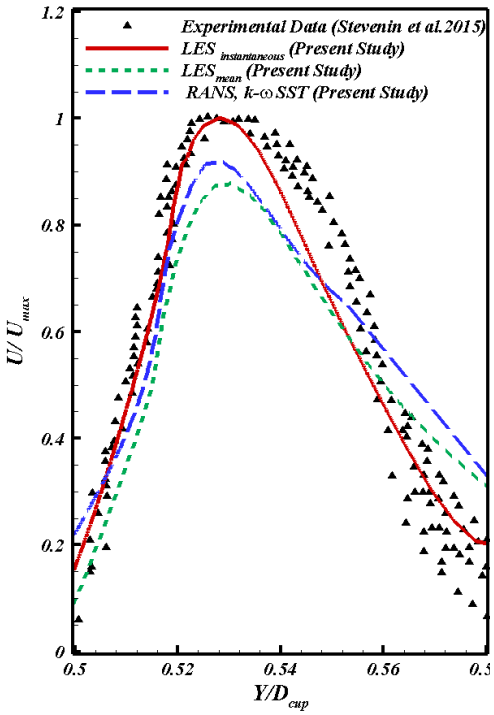

Figure 2.37: Radial profiles of longitudinal velocity, comparison between experimental results (Martinez, 2013) and numerical results of the code implemented in the current study.

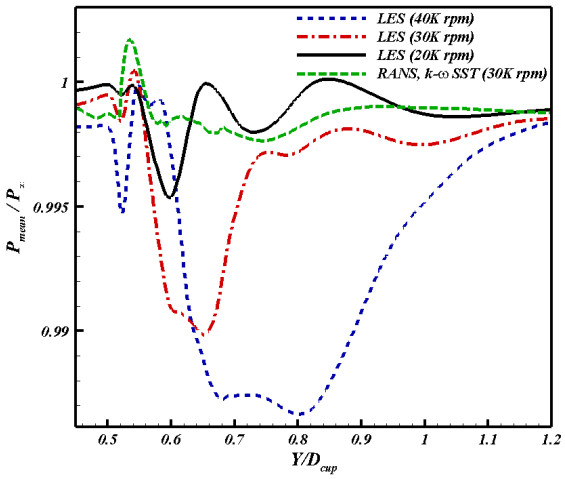

Figure 2.38: Comparisons of pressure distribution in the same location of Fig. 2.34 which normalized by atmospheric air pressure.

2.5. Conclusions

The main contribution of the current study is the implementation of a code as a strong tool to present a comprehensive investigation of the electrostatic spray transfer process in the ERBS. In addition, this work provides a thorough understanding of the complex airflows around the high-speed ERBS and the movement of the paint droplets toward the target surface for coating. The algorithm is implemented using the OpenFOAM framework. We studied the unsteady growth of the paint particles while considering the pattern of distribution. Unsteady, complex dynamic and three-dimensional behavior of flow behind the ERBS was solved by benefiting from LES turbulence approach and compared with the kω-SST turbulence model. This study reports a thorough analysis about the toroid-shaped vortex ring, air and paint particle evolution, vortex shedding, the mean velocity, electrical voltage distribution and streamwise velocity fluctuation. The wake characteristics of the spraying flows are considered in various simulated conditions. The structure of the spray is significantly sensitive to the electrostatic force and then the values of transfer efficiency (TE) depends on it. We validated our numerical results using experimental and available numerical data, which demonstrated appropriate accuracy.

Chapter 3

Atomization and spray characteristics around an ERBS using various operational models and conditions [2]

Abstract

The impetus of the current study is to conduct numerical evaluations about the fundamental behaviors of the flow in an electrostatic rotary bell sprayer (ERBS) during the formation of the droplets and depositing on a target. The effect of operational parameters like bell rotational speed, shaping air and paint flow rate, electrical charge values and droplet distributions are considered precisely. Here, an Eulerian-Lagrangian algorithm that contains a model for airflow field, spray dynamics, electric charge field, droplet trajectory tracking and wall film dynamics has been extended by using the OpenFOAM package. The fluid dynamics is computed by using a large eddy simulation (LES) turbulence model. The mechanism of atomization is facilitated by the action of the centrifugal force that conducted the disintegrated droplets to the cup edge. Following that, the high-velocity droplets affected by the shaping airflow and electric force are transported towards the workpiece. The effect of the bell rotational speed in comparison with other parameters is dominant. The measured size of the droplets is controlled by increasing the bell rotational speed or decreasing the paint flow rate, in this case, promoting a reduction in droplet size. The droplet size near the bell cup was increased noticeably, however, their radius becomes more uniform at a longer lateral distance. Investigation of the various breakup models is one of the main goals of this work to predict the droplet size more precisely. The Reitz-KHRT, Reitz-Diwakar, Pilch-Erdman and the newly modified TAB model are examined in order to predict the breakup process in the ERBS. As the paint droplets are a viscous fluid a modification of the Taylor Analogy Breakup (TAB) approach taking non-linear influences for large viscosity into account is recommended. The use of the breakup models creates a smaller droplet size and this means they are more sensitive to recirculation regions flow pattern. The implemented wall film function was able to predict the transport in the boundary layer over the target. The numerical results describe exact values for the size, distribution, velocity and trajectory of the particles in ERBS, and these results are important for coating industries, in order to optimize their working conditions.

[2] Based on the work published in the International Journal of Heat and Mass Transfer, https://doi.org/10.1016/j.ijheatmasstransfer.2020.120243, and, Proceedings of the Canadian Society for Mechanical Engineering International Congress CSME2020, doi: DOI: 10.32393/csme.2020.1132.

3.1. Introduction

Electrostatic rotary bell sprayers (ERBSs) due to their superior atomization performance have been developed rapidly during recent years. New complicated designs have been introduced and broadly used in the automotive coating industries. ERBSs produces high-quality uniform coatings with appropriate characteristics of spatial atomization and also fine size distribution of droplets. Using of the ERBS in the coating process leads to a considerable reduction of the material cost in automotive industries, improvement in performance and a decrease in the destructive impacts on the environment (Akafuah et al., 2016). High-speed rotary bell atomizers are rarely used for other different applications, e.g., spray drying or powder industry (Kuhnhenn et al., 2018), in comparison with their performance and application in automated coating processes.

ERBSs are characterized by a broad range of the bell cup diameters, varying from 20 to 70 mm, and by their extremely high rotational speed of up to 70 kRPM. Hinze and Milborn (1950) explained different rotary atomizer geometries used in industrial applications, which can be named rotary cup atomizer, spinning disk and slotted wheel.

Several numerical and experimental investigations about the electrostatic rotary bell sprayers, which were concentrated on the shaping airflow impact on the droplets atomization process and their transport (Stevenin et al., 2015; Darwish Ahmad et al., 2018), on the mapping of the droplet size distributions (Darwish Ahmad et al., 2019), on the wall film model (O'Rourke and Amsden, 2000) and in the investigation of the electrical space charge procedure (Viti et al., 2008; Ellwood and Braslaw, 1998) being performed in the most recent years. The fundamentals and mechanisms of the atomization procedure (Bailey, 1974), also the formation and behavior of the droplet in the spraying process (Frost, 1981) have been considered extensively. In addition, spraying flow properties and the effect of the operational conditions are examined broadly (Corbeels et al., 1992).

Im et al. (2001) indicated that the bell cup rotational speed dominated the atomization process, but shaping airflow and electrical charge also modify the droplet transport process remarkably. Wilson et al. (2018) and Akafuah et al. (2009) visualized the droplet formation procedure and the spray shapes, especially in the region close to the rotating bell cup surface by high-speed shadowgraph imaging and infrared thermography, respectively.

Several numerical investigations (Ye et al., 2015; Mark et al., 2013; Toljic et al., 2012) explained about the transport of the droplet and the constructed film thickness on the workpiece. Initial conditions in these studies are based on the use of empirical assumptions. This implies that the performance of the approach deeply depends on the specific sprayer and the target geometry. Even though there are some studies that are considering the shaping airflow dynamic in the ERBS (Stevenin et al., 2015), but a precise explanation about the interaction between the shaping air and sprayed droplets remains problematic.

Different breakup models had been investigated in different contexts, but their effect in ERBS' flow is still ambiguous. One of the main goals of this work is to study the ability of the available breakup models to predict the shape and size distributions of the droplets in the ERBSs.

Fujimoto et al. (2009) illustrated that the diameter of droplets, which is calculated by the breakup models, significantly affected the shape and transmittance of the spray pattern and also the droplet dispersion that is caused by the vortex structure. The effect of flow characteristics on the breakup pattern of the droplets in a rotary atomizer was studied by Ogasawara et al. (2010). Shen et al. (2019) investigated the droplet disintegration process and the behavior of a non-Newtonian fluid as an input paint in the high-speed rotary bell atomizer. Andersson et al. (2013) implemented non-linear effects on the TAB breakup model for viscous paint fluid to predict the size distribution of the droplets. They had shown that the TAB method is able to predict the breakup process in the rotary bell sprayer quantitatively. Huang et al. (2000) indicated that breakup approaches modeled a smaller size for the droplets. Peng et al. (2016) verified that increase in the flow rate caused a change in the ligament mode and led to the turbulent breakup. Considering the flowfield over high-speed rotary devices with such a high turbulent and flow gradient is an important issue (Kolahan et al., 2019; Rami and Pascoa, 2019a; 2019b). The ERBS supplies a circular pattern of paint droplets around the center of the bell rim because of the viscous advection between the surface of the cup and the particle that forces these particles to rotate approximately in the same velocity, in this case, the same as the bell cup velocity (Wilson et al., 2018). The rotation of the bell cup produces a centrifugal force that induces particles flow in a radial trajectory towards the outside of the bell cup surface. After the formation of the paint droplets, shaping air serves as a transport mechanism to conduct the droplets toward the target and helps to control the spray particle size in the secondary atomization (Fan et al., 2011). Domnick and Thieme (2006) realized that the growth of the bell cup rotational speed caused less consistency in the fragment pattern.

The numerical characteristic analysis for implementing and developing the coating process in the ERBSs is extremely useful to reach more efficient design, also for a deeper understanding and to derive the optimal operational conditions. Ahmed and Yousef (2012) correlated a relation for the Sauter mean diameter (D_{32}) with changes on the non-dimensional parameters like Reynolds number, Weber number and flow coefficient in various operational conditions. Oswald et al. (2018) showed that the disintegration process can be affected by the elongational resistance flow in the bell atomizer, but the droplet size is not influenced by the aforementioned change. Im et al. (2004) developed their code to study the shaping airflow, particle trajectory and electrostatic field in order to increase the transfer efficiency (TE). Honna and Yamasaki (1999) investigated the design of the shaping air nozzles in ERBS by changing the diameter and number of these nozzles to obtain sufficient droplet paths and velocities.

The implementation of the electric field is a crucial subject to achieve an accurate simulation and ultimately captures the flow details precisely, which was considered in the other related research (Rodrigues et al., 2019). To have an accurate simulation, selecting an appropriate turbulence model is a vital question. The LES approach is more suitable for capturing the flow features and analyzing the internal flow principle (Roohi et al., 2016; Pendar and Roohi, 2015; 2016).

The present work provides a better understanding of the influence of the cup rotational speed, the shaping air dynamic, electrical space charging, paint and airflow rate, and the droplet size on

the qualities of the coating, on the transfer efficiency and on the costs of the coating. We also introduced an appropriate initial condition for the spraying in order to prevent overspray around the bell cup of the sprayer or around the target surface. In the current study, the CFD (Computational Fluid Dynamics) code is based on the finite-volume model and implemented within the OpenFOAM package. For simulating the spraying two-phase flow, an Eulerian-Lagrangian approach was used. This work provides further data about the flow behavior in order to be able to design the next generation of the ERBS.

3.2. Governing Equations: Breakup Models

The mathematical formulation and the numerical algorithm for the three considered phases can be listed as follows: continuous phase (airflow), discrete phase (paint particles) and electric flow field. The governing equations that are used in the current study for these three fields are provided in detail in chapter 2.

Breakup model is one of the most important sub-model that must be considered in the procedure of the spraying simulation. Generally, the spraying process is divided into primary and secondary breakup. In the primary breakup, the condition of the droplets, like diameter and angle at the point, will start to determine. Moreover, the secondary breakup model explains the decomposition of the big droplets via normal stresses (instability of Rayleigh-Taylor) and also by stripping of the very small particles (instability of Kelvin-Helmholtz). In the following sections, we describe the formulation and procedure of the various breakup models.

3.2.1. Modified TAB Breakup Model

The modified TAB breakup model is a developed version of the original TAB model. In this approach, based on the regime of the breakup, there is a proportional relation between the number of droplets and their rate of production. Also, the balance of energy among the parent droplets and produced ones resulted in an expression for the velocity component of the newly produced droplet. A dimensionless weber number ($We = \rho u_{rel}^2 R_P / \sigma$) characterizes in this process. Where R_p, u_{rel}, ρ and σ are the radius of the particles, relative particle-gas velocity, air density and surface tension, respectively. In $We > We_{crit} = 6$ condition for the Weber number, the droplets can disintegrate. The droplet breakup is based on the deformation influence of the TAB model in the supercritical Weber number. When this breakup mechanism happens, $y(\mathrm{t}_{breakup}) = 1$, the product droplets are created in different sizes from the parent one. In the modified TAB approach, the parent droplets are based on the product generation rate ($dn(\mathrm{t})/\mathrm{dt}$), depends on the proportional constant (k_{br}) breaks into product droplets. It can be shown as follow:

$$dn(\mathrm{t})/dt = -3K_{br}n(\mathrm{t}). \tag{3.1}$$

The value of k_{br} is dependent on the properties of the parent droplet and on the regime of the breakup. In fact,

$$K_{br} = \begin{cases} k_1 \omega & \text{if} \quad We \le We_t \\ k_2 \omega \sqrt{We} & \text{if} \quad We > We_t \end{cases} \tag{3.2}$$

Here ω is calculated as follow (Tanner et al., 1997):

$$\omega^2 = \frac{8\sigma}{\rho_P {R_P}^3} - \frac{1}{t_d^2} \tag{3.3}$$

$$t_d = \frac{2\rho_p R_P^2}{5\mu_p} \tag{3.4}$$

, Where μ_p and ρ_p are the particle viscosity and particle density, respectively. The values of k_1 and k_2 are fully matched with the velocity and size of the droplet in the experimental data of Schneider (Eberle et al., 1996; Schneider, 1995) and are considered as $k_1 \approx k_2 = 0.2$. Also, the transient Weber number (We_t) is set as 100 for the present computation. This value is determined due to the suggestion of Liu and Reitz (1993) for a flow similar to the one of the current work with a high droplet velocity, which results on a subdivide of the bag and stripping breakup regions. The product droplet distribution in the present model has been assumed uniform as follow:

$$\frac{r_{product}}{r_{parent}} = e^{-K_{br}t} \tag{3.5}$$

, Where $r_{product}$ and r_{parent} are the radius of the product and parent droplets, respectively. Here, the initial velocity component of the product particle is perpendicular to the parent droplets path. In the modified TAB model, only 70% of the deformation velocity transfer from the parent to the product particles, in contrast to the standard TAB, where this value is considered totally at 100%.

3.2.2 Pilch-Erdman Breakup Model

Pilch and Erdman (1987) derived a breakup model for injected droplets in the flow field with high velocity. Their model is based on the three parameters: (a) breakup time, (b) critical Weber number (We_{crit}) and (c) history of the velocity. The Pilch-Erdman model presents a relationship between these three variations. In this model, total breakup times are calculated as follows:

$$t_{br}=\begin{cases}6(\mathrm{We}-12)^{-0.25}, & 12\le we\le 18,\\ 2.45(\mathrm{We}-12)^{-0.25}, & 18\le we\le 45,\\ 14.1(\mathrm{We}-12)^{-0.25}, & 45\le we\le 351,\\ 0.766(\mathrm{We}-12)^{-0.25}, & 351\le we\le 2670,\\ 5.5\ . & 2670\le we\end{cases} \tag{3.6}$$

, Which is compared with the experimental data. In the above correlations, the total breakup times are introduced for the low-viscosity particles. Pilch and Erdman (1987) recommended the following empirical modifications for the particle velocity correlation:

$$\frac{|U_P|}{|U_{rel}|}\left(\frac{\rho_P}{\rho}\right)^{0.5}=B_1\,\mathrm{t}_{br}+B_2\,\mathrm{t}_{br}^2=(3/4\,C_d)\,\mathrm{t}_{br}+(3\,\mathrm{B})\,\mathrm{t}_{br}^2 \tag{3.7}$$

Here, the drag coefficient (C_d) is set equal to what is used for a rigid constant-mass sphere, with a value of $C_d=0.5$. The empirical constant (B), which is obtained from a curve fitting of particle displacement data, here determined with $B=0.0758$ (Pilch and Erdman, 1987). Also, U_P is the velocity of the droplet cloud when all the breakup processes have been stopped. In this model, the maximum stable diameter is generated by an accounting of the droplet size reduction and relative velocity decrement:

$$d_P=We_{crit}\frac{\sigma}{\rho U_{rel}^2}\left(1-\frac{|U_P|}{|U_{rel}|}\right)^{-2}. \tag{3.8}$$

3.2.3 Reitz-Diwakar Breakup model

Reitz-Diwakar approach makes a distinction between the bag and stripping regimes of the breakup. The bag and stripping breakup regimes happen in low and high relative velocities, respectively (Reitz and Diwakar, 1986, 1987). Bag breakup happens under the following condition:

$$We>6\ . \tag{3.9}$$

Also, the stripping breakup occurs when:

$$\frac{We}{\sqrt{\mathrm{Re}_P}}>0.5\ . \tag{3.10}$$

Finally, the characteristic breakup time (t_{br}) and new stable radius (r_{st}) of the particles for the Bag (Eq. 3.11) and Stripping (Eq. 3.12) breakup regime are computed as follows:

$$t_{br}=D\left[\frac{\rho_P R_P^3}{2\sigma}\right]^{1/2},\quad r_{st}=\frac{6\sigma}{\rho\,|u_{rel}|^2}. \tag{3.11}$$

$$t_{br} = C_2 \frac{R_P}{u_{rel}} \left(\frac{\rho_P}{\rho} \right)^{1/2}, \quad r_{st} = \frac{\sigma^2}{2\rho^2 |u_{rel}|^3 \nu}. \tag{3.12}$$

Where C_2 and D are considered to be constants set to 10 and π, respectively, as mentioned in reference Reitz and Diwakar (1987).

3.2.4 Reitz-KHRT Hybrid Breakup Model

It is obvious that the paint droplets, in the electrostatic rotary bell sprayer, have high velocities near the cup, and then their velocity decelerate quickly via a drag force. The hybrid approach in the Reitz-KHRT model is based on the combination of the Rayleigh-Taylor instabilities (Taylor, 1950) and Kelvin- Helmholtz wave forces (Reitz, 1987). These forces drive through an acceleration of the shed particles, ejected from the ERBSs into the airflow, and the aerodynamic forces, respectively. Rayleigh-Taylor instabilities happen where the acceleration is perpendicular to the interface of two various fluids. In this model, by considering the effect of the surface tension and neglecting the viscosity of the liquid, two parameters of the fastest-growing frequency, Ω_{RT}, and the related wavelength, Λ_{RT}, are reported as follow (Beale and Reitz, 1999):

$$\Omega_{RT} = \sqrt{\frac{2}{3\sqrt{3\sigma}} \frac{\left[-g_t(\rho_l - \rho)\right]^{1.5}}{\rho_l + \rho}}, \tag{3.13}$$

$$\Lambda_{RT} = \frac{2\pi C_{RT}}{K_{RT}} \tag{3.14}$$

Here, g_t is the acceleration in the travel direction and is determined by $g_t = \vec{g}.\vec{j} + \vec{a}.\vec{j}$, where $\vec{a}$ is the droplet acceleration, $\vec{j}$ is the unit vector tangent to the trajectory of the droplet, K_{RT} is the wavenumber and is computed from:

$$K_{RT} = \sqrt{\frac{-g_t(\rho_P - \rho)}{3\sigma}}. \tag{3.15}$$

If the wavelength is less than the diameter of the droplet, RT waves are considered to grow on the droplet surface. Once waves started to grow on the drop surface, the time for the wave growth is tracked. Then, this time is compared to the breakup time and defined by:

$$\tau_{RT} = \frac{C_\tau}{\Omega_{RT}} \tag{3.16}$$

, Where C_τ is a constant, nominally assumed equal to one (Beale and Reitz, 1999). If the RT waves have been growing for a time greater than the breakup time, the drop is supposed to breakup. The radius of the new droplets with smaller size is computed using:

$$R_{RT} = \frac{\pi C_{RT}}{K_{RT}} \tag{3.17}$$

Here C_{RT} is set to 0.1 in the model constant, based on the reference Beale and Reitz (1999).

3.3. Numerical Procedure

Figure 3.1 describes a schematic diagram of the studied sprayer, which includes paint and purging circuit process in the ERBS based on a technology developed and commercialized by SAMES (SAMES Technology 2019). During this procedure, at first, the shaping air exhausts from ninety air nozzles. This air is supplied with an appropriate balance pressure (a). Then, through a safe distance among the workpiece and the bell cup of the ERBS, the airflow is ionized by a high-voltage with a maximum value of around -90 kV (b). The high voltage unit (c) converts the voltage and makes the connection between the low voltage from the control module (d) and the high voltage cable. The bell cup rotational speed, the implemented electrostatic force and the injected shaping airflow affect the droplet trajectory due to their location and to the charge values. The technology used in this class of sprayers makes them resilient, sturdiness and versatile painting tools for the most demanding car finishing requirements, which is created a uniform paint distribution with the highest values of transfer efficiency (TE). In this paint and purging process, the paint sucked through the rinsing product feed lines behind the manifold (e) and injected from the paint nozzle. Herein also, the dump feed line, the high-pressure air generator (g) and the robotic equipment holder base (f) are shown in Fig. 3.1.

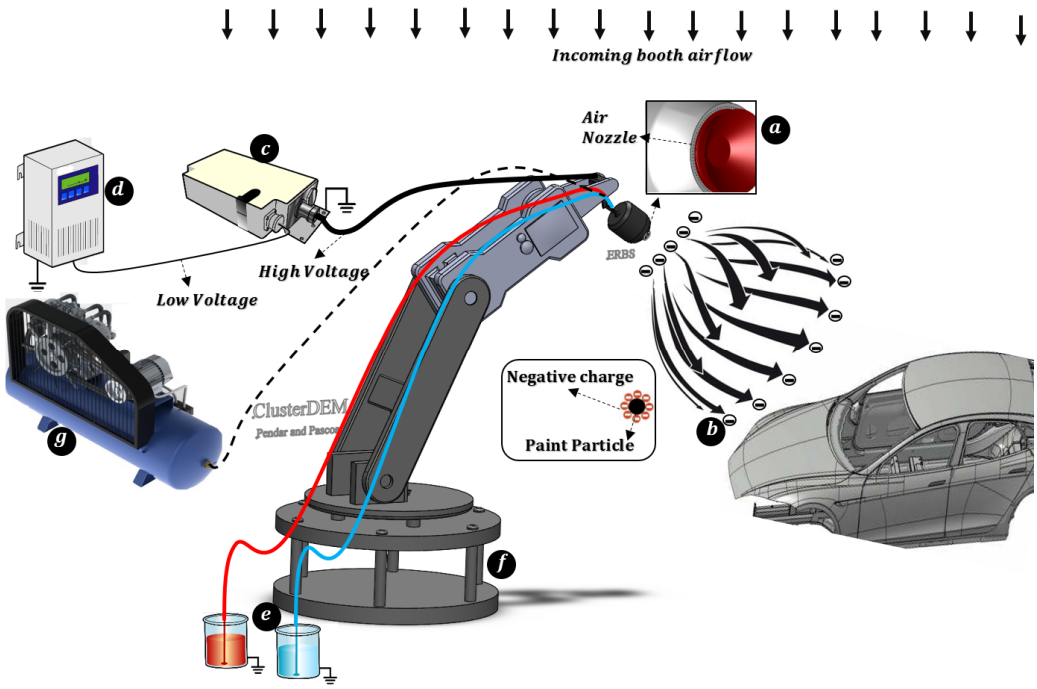

Figure 3.1: A schematic diagram of the electrostatic spray deposition process and mechanism of the coating.

Figure 3.2 (a) indicates the complicated pattern of the airflow (red line) and paint droplet trajectory (blue line) schematically that can be divided into eight various behaviors: (a) Shaping airflow stream (blown air) (b) Outside toroid–shape air vortices (c) Inside toroid–shape air vortices (d) Trapped air vortices (e) Paint droplet toroid–shape vortex (f) Large size of the paint droplet trajectory (g) Small size of the paint droplet trajectory (h) Rebounded droplet from the target with the circular pattern. All these behaviors will be discussed deeply in the result section. Shaping airflow trajectories (i) move outward by increasing the rotational speed, which is shown in Fig. 3.2 (b) schematically. The droplets leave the airflow stream through two main mechanisms, by their momentum or electric force on the charged droplet close to the grounded target. In the current study, two various bell cup geometry are considered with a diameter of 50 mm and 65 mm (Fig. 3.2 (c)). Based on the target size, shape and paint flow rate, the bell cup diameter can be altered. A diameter of 50 and 65 mm for the bell cup can provide 300 to 400 mm average diameter for the constructed spray patterns, respectively, in conjunction with shaping air assembly for each bell cup (SAMES Technology 2019).

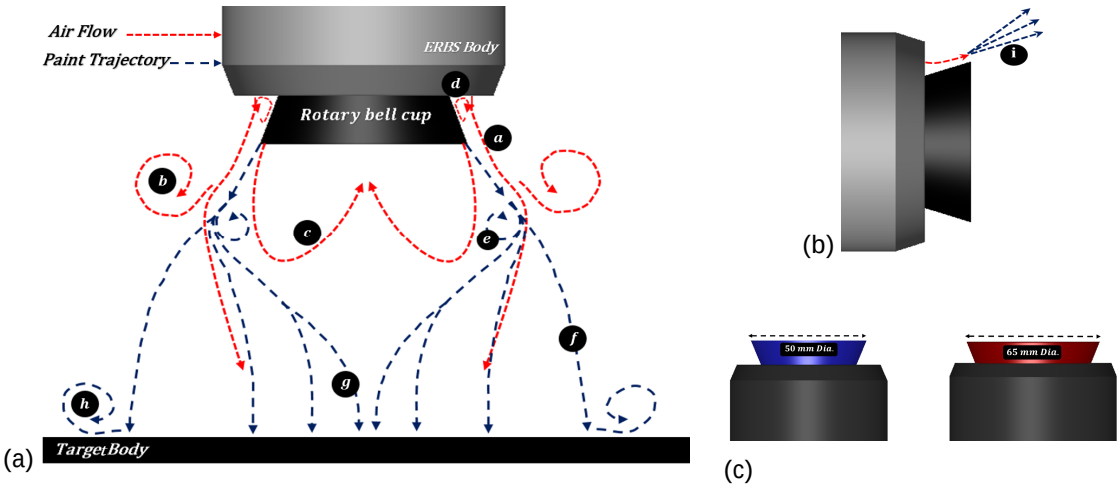

Figure 3.2: (a) A schematic visualization of the droplet trajectories and the shaping airflow dynamics around the ERBS (b) The effect of the rotational speed increase on the shaping airflow (c) Two various bell cup head with a diameter of 50 mm and 65 mm.

Figure 3.3 exhibits different views of the applied structure quadrilateral grid of the three-dimensional computational domain. The zoomed frames contain rotating bell cup and shaping air nozzles (a), target surface (b) and overall views of the sprayer and domain (c-e), which are utilized in the current study. As shown in Fig. 3.3, the computational domain is decomposed into the smaller sub-section to control the grid density properly. In the region with very high values of the flow gradient and velocity, exactly near the rotational bell surface and air nozzles, the mesh distribution must be more dense and fine. Based on the accurate evaluation of three different grid sizes (4.5, 8.5 and 13.5 million cells) in our previous study (chapter 2), here we also performed our simulation using a mesh cell with an overall account of 8.5 million. The height of the first prism layers at the ERBS surface was considered around 1.5×10^{-4}, which supports the required resolution for capturing this high turbulent flow mechanism. The

minimum value of y^+ was considered here as a 0.35. A moving wall boundary condition was used for simulating the rotary speed of the high-speed bell cup. There is a ring of the shaping air, which comprises 90 nozzles. As shown in Fig. 3.3, we used a full structured grid with a high resolution, especially close to the ERBS, which provides a suitable accuracy for comparing with the experimental results. Details of the grid sizes are reported in chapter 2. The simulation time step size was specified around 10^{-7} s to satisfy the Courant number with values of 0.5, except the beginning of the simulation that was set at 10^{-8} s.

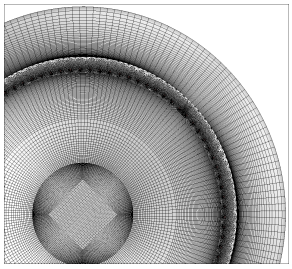

(a) Rotary bell of ERBS

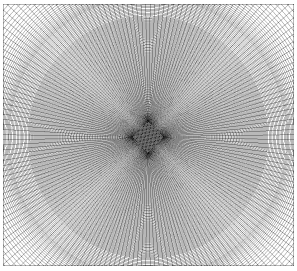

(b) Centre of the Target Surface

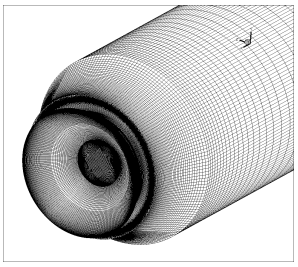

(c) ERBS

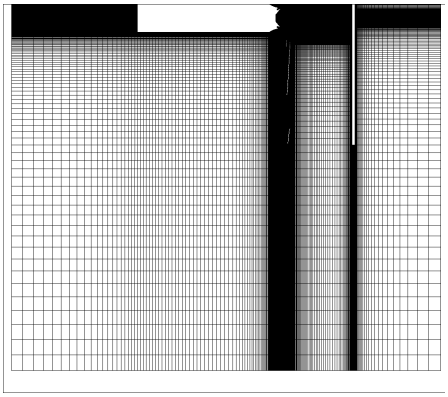

(d) 2D Views (Z-axis)

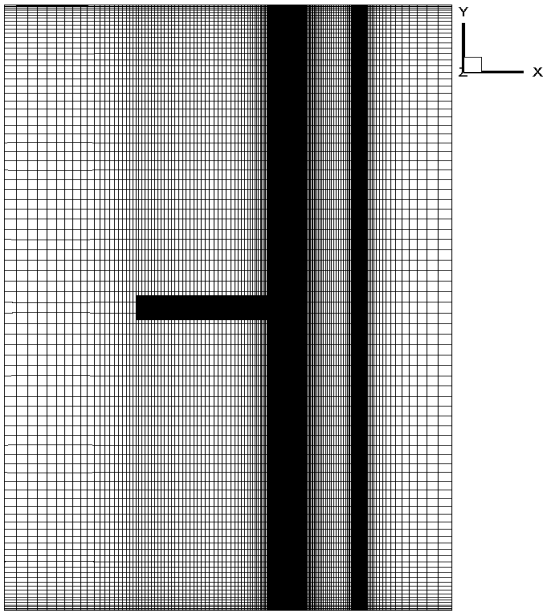

(e) Full computational

Figure 3.3: The distribution of the structures meshes around the ERBS that is implemented in the current study.

The following part explains the progressive steps of the optimization framework for the electrostatic spraying process, which is extended in the current study (see Fig. 3.4):

1) Selection of an appropriate method for the CFD simulations (Eulerian, Lagrangian and Laplacian model).
2) Developing the spraying algorithm and code by adding the wall film model, the electric field and also implementing the modified breakup model.
3) Setting an initial operating state for various computation conditions.

4) Code validation for the droplet distribution and velocity of the airflow field. Comparing the current simulation results with the available experimental data.

5) Optimization of the operational conditions for high rotational speed. Finally, the attained database helps to have a better recognize about the physics of the process.

6) CFD post-processing of the continuous phase and also of Lagrangian droplets by transforming the data into VTK.

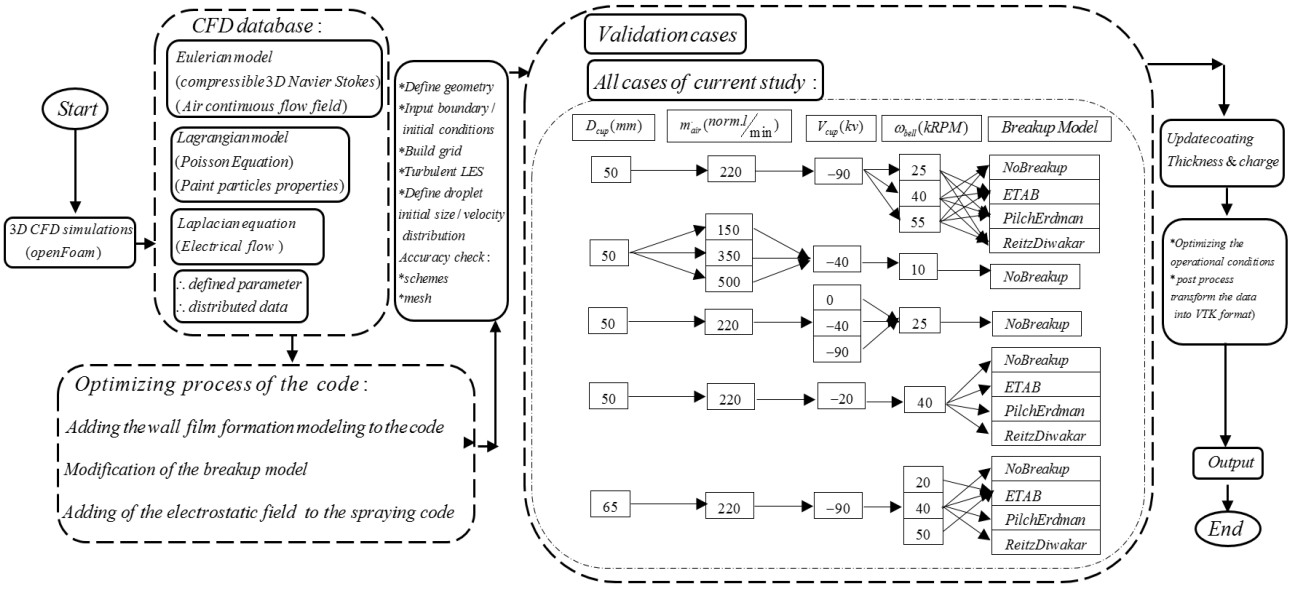

Figure 3.4: Iterative solution and progressive steps for the electrostatic spraying analysis in the current work.

Figure 3.5 shows a summary of the computational domain and the ERBS's surface dimensions and the applied boundary conditions. The material of the bell cup and retaining collar is stainless steel and aluminum that are at a specific value of potential ($\Phi = V_0$). Other parts of the sprayer's body are made by a non-conducting material (plastic), which is assumed as $(\nabla\Phi).\mathrm{n} = 0$. The potential values in all outside borders of the computational domain far from the ERBS are set $\Phi = 0$, as shown in Fig. 3.5. The effective space charge, which is produced by the sprayer surface, will be higher, especially very close to the applicator. All sides of the computational domain are considered at atmospheric air pressure and temperature. A downdraft airflow inlet with a constant velocity (0.1 m/s) is set in the upside of the ERBS.

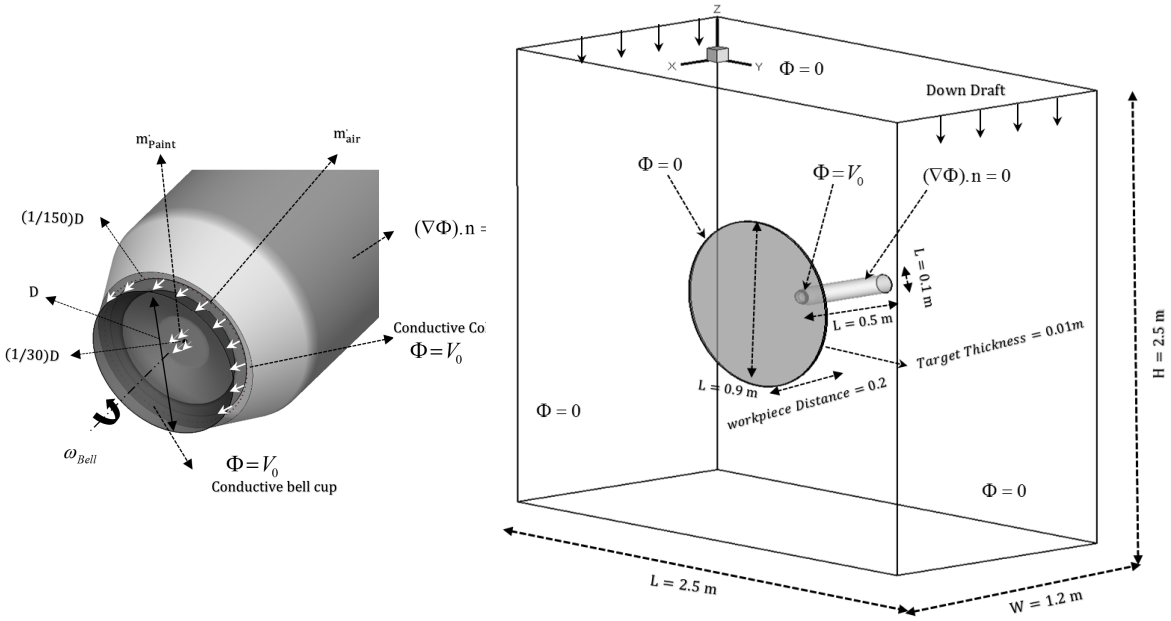

Figure 3.5: The computational domain dimensions and computing boundary condition (airflow field and electrostatic field).

The parameter values of the selected variables are shown in Tab. 3.1. Parameters for the in-hand database are the paint droplet size, flow rate, density, airflow rate, air density, cup voltage and rotational speed, including a broad range of values. After a comparison between two initial injection distribution models for the droplet size, namely the Rosin-Rammler ($Y_d = \exp(-d/\bar{d})^n$) and Chi-squared approach, the first one represents a better distribution as compared with the experimental results. The size distribution of the droplets is subdivided into a wide range, with having a diameter value between 5 to 75 µm. An exponential factor of this model is set as $n = 2.65$ in this work. All terms are discretized using second-order accuracy in the equations for continuity and momentum. The PIMPLE algorithm is implemented for the pressure-velocity coupling, such as explained in reference Pendar and Roohi (2018).

Table 3.1: Electrostatic spraying modeling baseline specifications.

Constant (Units) (Symbol)	values
Rotational speed (RPM)(ω_{bell})	$10-55$
Bell diameter (mm) (D)	$50-65$
Air viscosity(kg/m³/s) (μ)	1.8×10^{-5}
Air density(kg/m³) (ρ_{air})	1.225
Airflow rate (norm. l/min) ($\dot{m}_{air}$)	$150-500$
Paint density(kg/m³) (ρ_p)	998
Paint flow rate(ml/min)($\dot{m}_{paint}$)	$200-400$
Paint droplet size(µm)(D_p)	$5-75$
Charge-to-mass ratio(C/kg) (ρ_m^q)	1.0×10^{-6}
Cup voltage (KV) (V_0)	$0-90$
Target distance (mm) (L)	20

3.4. Results and discussion

3.4.1 Code Validation

Figure 3.6 compares the evaluation of the wall film formation on the bell cup surface between the results of the current numerical simulation and a series of experimental snapshots, which are reported by Shen et al. (2019) that is taken by a high-speed photographic camera. As this figure shows, the present numerical method can capture the temporal film distribution exactly similar to the experimental ones and a suitable qualitative agreement is clearly observed. The spiral distribution of the liquid is obviously visible at the first step of the film formation on the bell cup surface. The inner surface of the rotary bell cup becomes fully wetted after approximately 13 ms in the considered case, and shown a reasonable agreement with the experimental report.

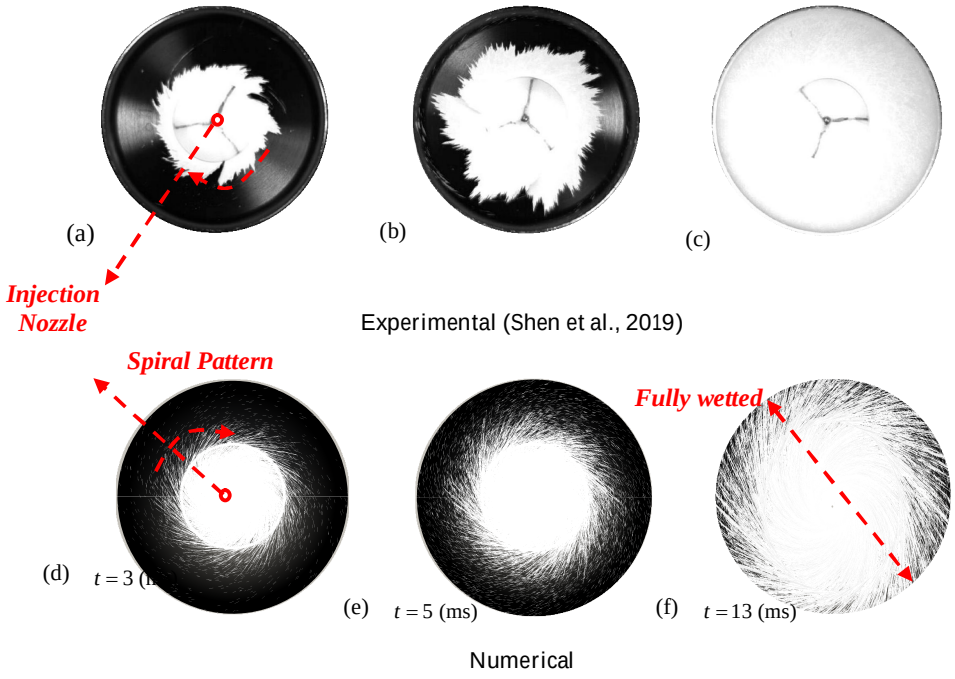

Figure 3.6: Propagation of the paint film on the rotating bell cup surface: experimental snapshots (Shen et al., 2019) (a-c) and current numerical results (d-f). ($\omega_{bell} = 30kRPM$, $\dot{m}_{paint} = 400\,ml/\min$)

Figure 3.7 compares the distribution of the sprayed paint droplets around the ERBS with our numerical results and the experimental data of Darwish Ahmad et al. (2018), at the same operational conditions. It must be mentioned that in the experimental investigations, an infrared thermographic flow visualization (IRFV) technique has been implemented to assess the spray shape qualitatively. As a short explanation, in this method the thermal waves start to attenuate after traveling through the droplets, then the transmitted waves can be captured by means of the infrared camera (Darwish Ahmad et al. 2018). As the figure exhibit lower rotational speed pronounced larger radial curvature of the spray pattern and the shaping airflow expand and redirect more in the radial. The recirculation region, which is created by air

entrainment, represents low paint concentrations in the high rotational speed and shaping airflow. As it is obviously identified in this figure, implemented numerical code by using a modified TAB breakup model can capture the mechanisms of the spray flow and instabilities of it well. The aforementioned observation is completely in agreement with the experimental reports (Darwish Ahmad et al. 2018). Figure 3.7 shows the paint droplets with scale factor ($SF_{Droplet}$) of 100, for better visualization.

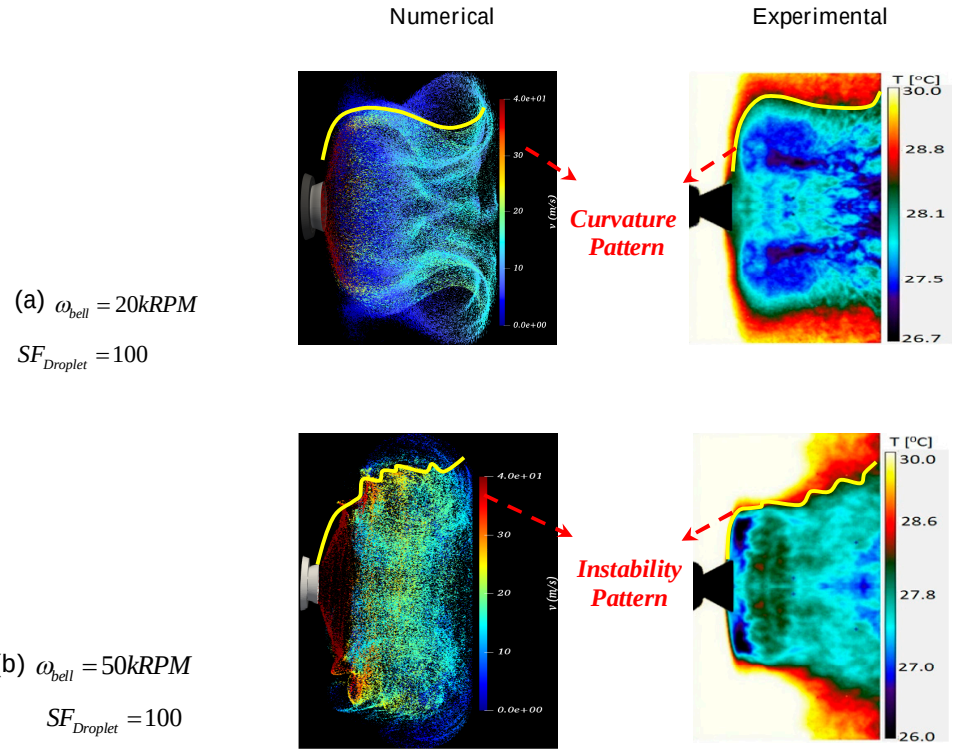

Figure 3.7: Comparison of the droplet distribution: Infrared images of experimental data (Temperature contour) (Darwish Ahmad et al. 2018) (right frames), Current numerical results (Velocity magnitude value) (left frames) ($\dot{m}_{air} = 150\,LPM$, $\dot{m}_{paint} = 0.1\,LPM$, $Modified\,TAB$).

The frames in Fig. 3.8 compare the pattern of the subtended angle of the shaping air at various rotational speeds obtained from the present numerical study and the experimental result of Darwish Ahmad et al. (2018). These frames clearly indicate that the shaping air angle increased from 73° (Exp = 78°) to 102° (Exp = 96°) and then to 134.76° (Exp=136°) at the rotational speed of zero, 20 and 50 kRPM, respectively, which is in the good agreement with the experimental data of Darwish Ahmad et al. (2018). By increasing the shaping airflow rate, the percentage of changing in the air angle experiences a reduction at different rotational speeds, but the trend stays similar in all different values. The reason for the negligible difference between the obtained values by experimental and numerical studies can be due to measurement error and numerical modeling simplifications, respectively.

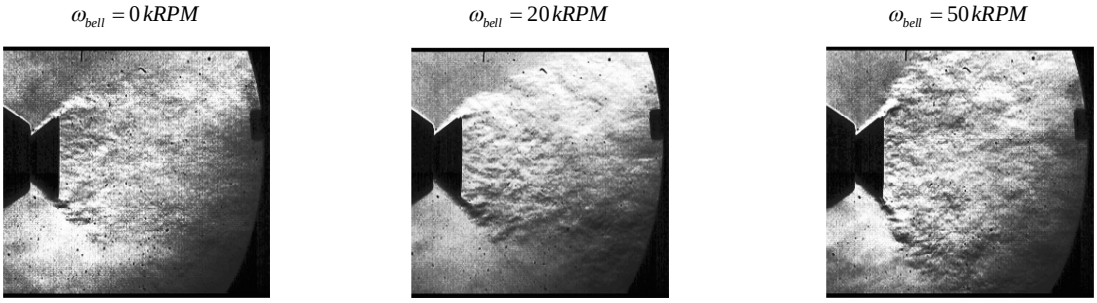

(a) Experimental (Darwish Ahmad et al., 2018)

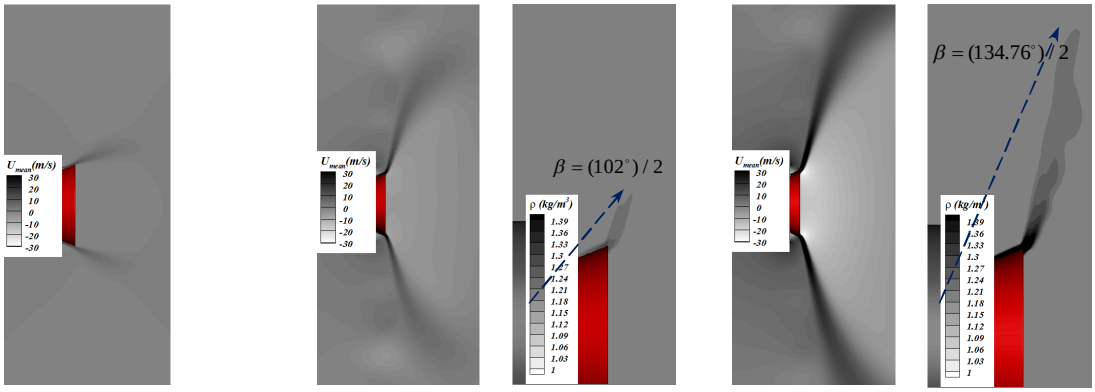

(b) Numerical

Figure 3.8: 3D views of the airflow outward the ERBS; various rotational speeds of the bell cup at a fixed $\dot{m}_{air} = 150\,LPM$ and $Reynolds = 5.1\times10^{3}$: (a) Schlieren images of the experimental result (Darwish Ahmad et al., 2018) and (b) Contour of the velocity and air density obtained from the numerical results.

Accurate results in the ERBS's system are highly dependent on the appropriate simulation of the aerodynamic flow, such as the recirculation zone. Following this goal, Fig. 3.9 compares the computed values of the velocity with the experimental result (Stevenin et al. 2015). The values of velocity are non-dimensionalized by the maximum radial velocity and extracted in the turbulent boundary layer, close to the cup surface toward the outside. An accurate prediction of the current simulation is clearly observed. The electric field was also validated in chapter 2 with numerical studies of Viti et al. (2008) in the same condition.

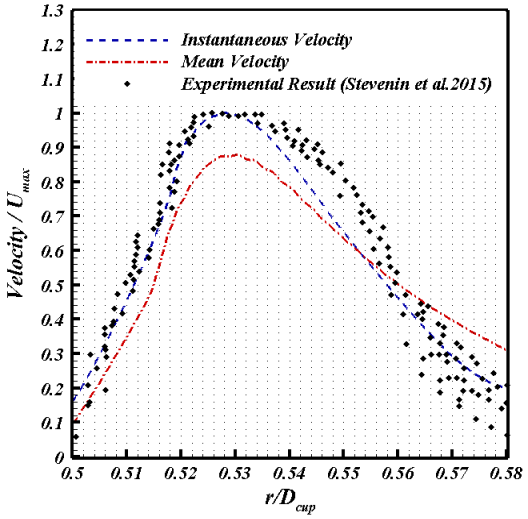

Figure 3.9: Longitudinal velocity distribution comparison of the current work with the experimental result of Stevenin et al. (2015).

3.4.2 Spray Characteristics

Choosing an appropriate breakup model is a crucial issue in the electrostatic spraying simulation because it determines the child droplet size and mass. The droplet size is a factor that has an important effect on their trajectory, overspray phenomenon and on the created film thickness on the goal body. Following that, an accurate prediction of the droplet trajectory helps to have a correct simulation. Figure 3.10 illustrates the effect of the various breakup models on the distribution of the formed spray at the time t = 42 ms. In the beginning, all breakup models predict an almost identical penetration pattern. Applying a breakup model produces a very small size of the droplets (as measured in Fig. 3.24), which are entrained into the constructed recirculation zone that is depicted in figures 3.2 and 3.18. In the prediction of the modified TAB model for droplet distribution, we may notice that it contains a broad range of particle sizes and mass, as compared to other models (as also measured in Fig. 3.24). Also, this model predicted an overspray pattern more clearly and with a higher number of droplets with a bigger diameter. Two other models, Pilch-Erdman and Reitz-Diwakar here predicted an almost uniform size distribution of droplets, in which the size values in the Reitz-Diwakar model are smaller than other ones. The droplet velocity in the modified TAB model is more non-uniform and also its value is lower than the ones of Pilch-Erdman and Reitz-Diwakar models, especially near the spray shoulder (a). After hitting the droplets on the target surface, the vortexes created by the rebound droplets are more uniform near the target surface in this modified TAB model. In the Pilch-Erdman model, because of the higher droplet velocity, the over-spraying phenomenon happens further away from the bell cup (b). The highest amount of particle velocity is predicted by the Pilch-Erdman model. Pilch-Erdman breakup model is predicted the spraying procedure acceptable, but as it was compared with the experimental distribution before the modified TAB model presents a more precise formation of the spray (Darwish Ahmad et al., 2018). Without using the breakup models (last frame in Fig. 3.10), it is not possible to capture the spraying

vortex formation procedure, which is mentioned in Fig. 3.2. As it is concluded from the validation parts, the modified TAB model can capture the spray pattern exactly like the experimental ones. It must be mentioned that comparing the computational efficiency among the different breakup models, because of the change in the child parcel number, is difficult. The various type of examined breakup models is proved to have a slight effect on the spray shape. However, its effect on the droplet diameter is more obvious.

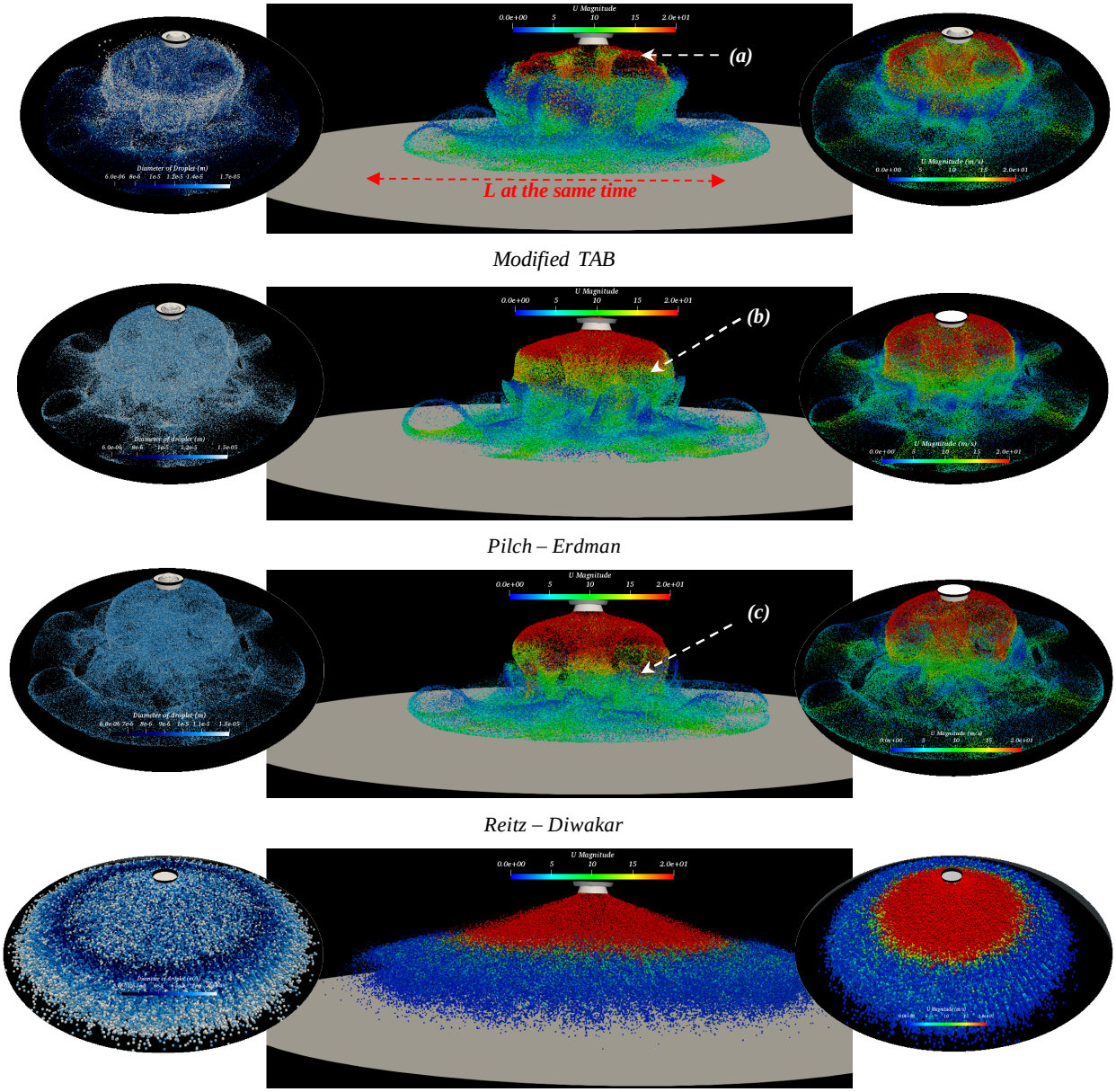

Figure 3.10: Spray shapes for various breakup models at $t = 42\,ms$. ($\omega_{bell} = 25kRPM$, $SF_{Droplet} = 100$)

Figure 3.11 indicates nine 3D frames of temporal consecutive paint distribution for a complete spraying cycle from the bell of the ERBS to the target surface at $\omega_{Bell} = 25kRPM$ by using the

modified TAB breakup model and the LES calculations. The velocity of the particles greatly depends on their positions in the computational domain. When they are near the bell surface, almost after the separation from the paint film on the bell surface, they still have dominant values of the tangential velocity greater than 150 m/s. This component of the particle velocity decreases dramatically within a growing distance because of their interaction with the airflows and the drag force. For the smaller droplet size, this deceleration will happen faster, within a short distance. The spray pattern maintains a cone shape from the very beginning to 21 ms but, after that, it is spread out by the vortex which is induced by hitting the workpiece and by the velocity difference among them (vortex $_1$). Also, the overspray pattern, which is caused by the vortex (vortex $_2$) occurs in the shoulder of the spray cone and spreads out and grow more as time goes by. This procedure is quite evident that by the time increasing, the length of the recirculation zone and the velocity of the droplet, in a reverse direction, increases especially after 33 ms.

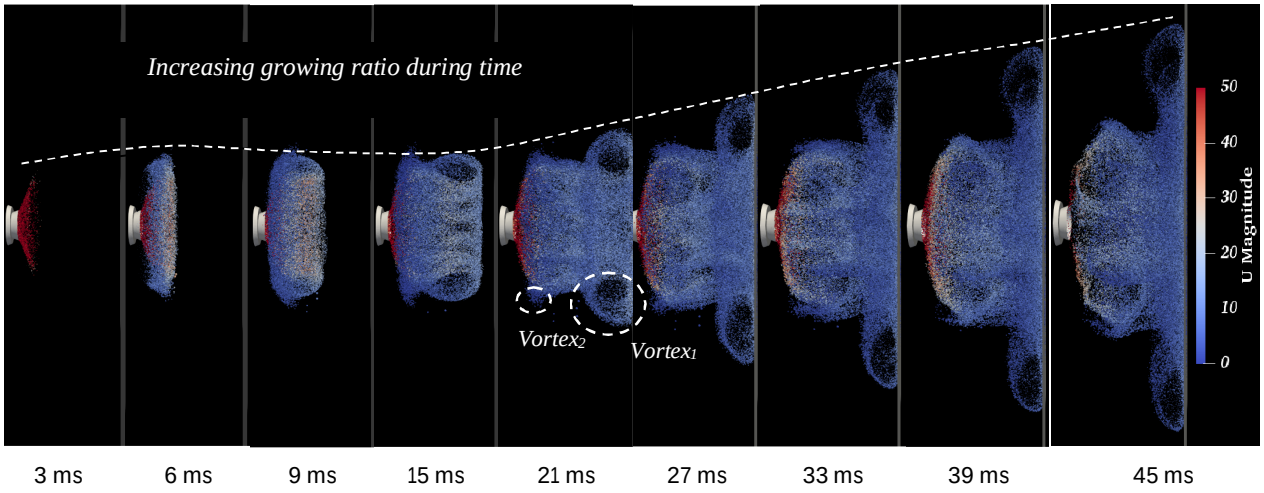

Figure 3.11: Time evolution of the spray patterns for the modified TAB breakup model ($\omega_{Bell} = 25kRPM$, $SF_{Droplet} = 40$).

Figure 3.12 shows an instantaneous snapshot of the spray pattern at two rotational regimes. Three different regions are significantly magnified as insets. The inset (a) shows the KH–RT surface instabilities near the bell cup rim that is caused by a small-scale vortex structure. These instabilities are formed at higher rotational speeds ($\omega_{Bell} = 50kRPM$) clearly, contrarily at low rotational speeds that the spray line is almost smooth. This inset also indicates the disintegration procedure of the droplets. The mechanisms of the KH–RT instability obtain larger droplets, typically larger than inside of the spray cone layer. The rebounded droplets from the surface of the target are crawled with a torus shape vortex. The size of this torus can achieve a larger size at low rotational speeds ($\omega_{Bell} = 25kRPM$) in comparison with the higher rotational speed, in which the spray hits the target with higher velocity and sticks on it without large rebounding. In the outside of the toroid-shape air vortex, we may witness on intensifies contain the overspray phenomenon at $\omega_{Bell} = 25kRPM$.

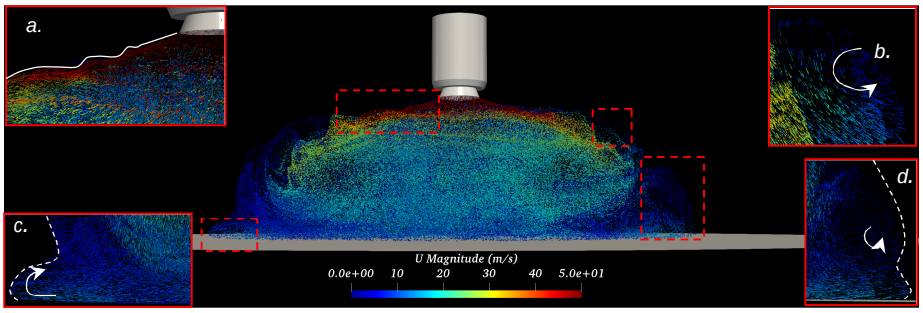

$\omega_{Bell} = 55kRPM$, $SF_{Droplet} = 200$, $SF_{Droplet} - sub\ frames = 400$, $t = 42ms$

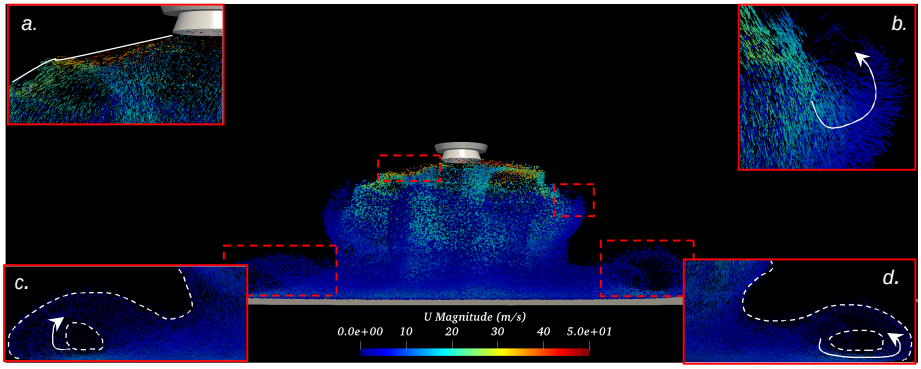

$\omega_{Bell} = 25kRPM$, $SF_{Droplet} = 100$, $SF_{Droplet} - sub\ frames = 200$, $t = 42ms$

Figure 3.12: 3D views of the spray pattern for two different ω_{Bell}. Inset frames illustrate magnified views of (a) mechanism of instabilities (b) Overspray flow (c-d) rebounded torus-shaped droplet.

The film thickness in the simulation of the coating process can be computed after the striking and spreading of the droplets over the workpiece. The operational condition effect on the constructed film pattern, uniformity and thickness will be discussed in Figs. 3.13 and 3.14. As visualized in these figures, the film pattern on the workpiece distinctly depends on the values of the ω_{Bell} and d_{cup}. The outer ring (white dash line) that covered with very thin thickness is the same in almost all cases with the same bell cup diameter, but the inner ring pattern has a structural difference in various cases. The numerical results indicated a non-asymmetric and non-homogeneous deposition circular structure, where the thickness of the deposition diminishes sharply to have almost no deposition around the center of the workpiece and far from the center. Higher bell cup rotational speed is produced a more uniform film pattern and a larger region of the film, consistent with the experimental results. A lower deposition film thickness at the central area of the body for the $d_{cup} = 65mm$ can be realized (As shown in Fig. 3.14). But in the case with $d_{cup} = 50mm$ this thickness due to the higher mass injections, caused by the vortical structure, is increased in the mentioned region. The diameter of the high thick film ring is highly increased by changing the head of the sprayer, with an increase in its diameter from 50 mm to 65 mm.

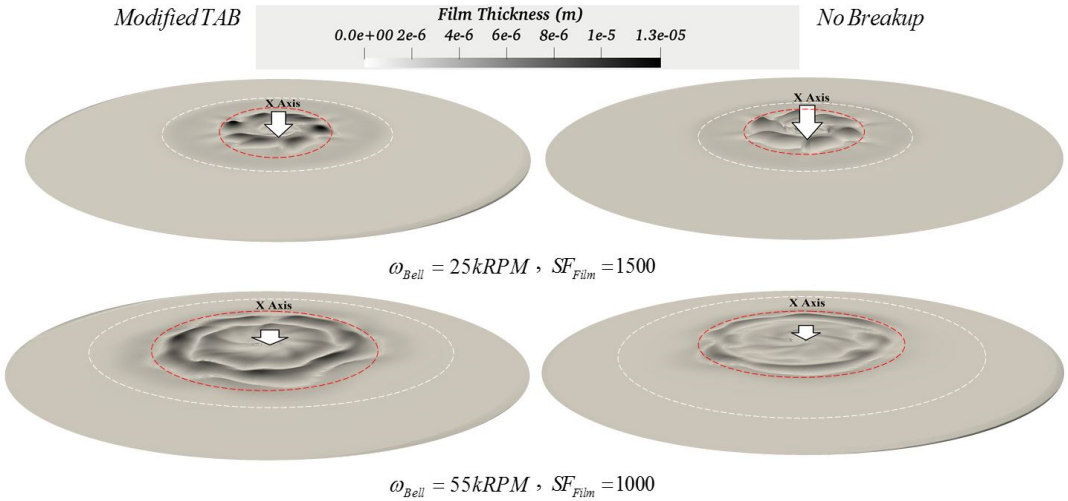

Figure 3.13: Visualization of 3D paint film wetted area on the target surface for different ω_{Bell}.

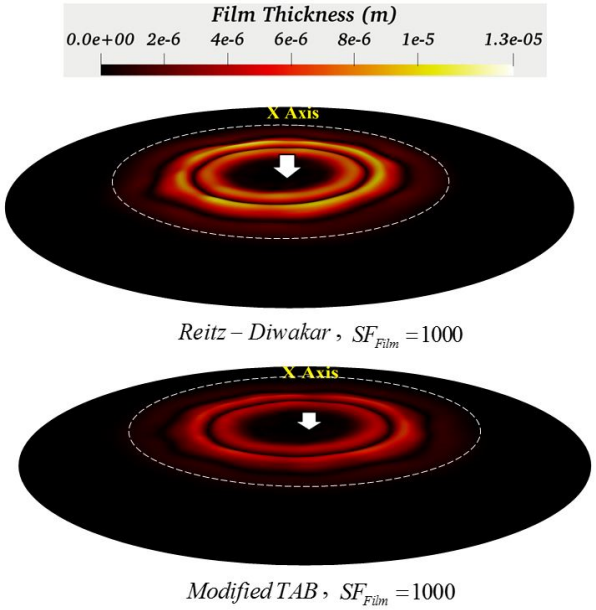

Figure 3.14: 3D paint film displaying on the workpiece surface for $d_{cup} = 65mm$ ($\omega_{Bell} = 40kRPM$).

In Figs. 3.15 and 3.16, the paint flux distribution in the radial direction of the workpiece surface is plotted for various operational conditions in order to consider their effect on the film-build. All levels of the rotational speed are produced a specific peak at roughly $r \approx 2.5R_{Bell}$, due to no droplet landing exactly on the round disk target, beyond the mentioned region. The peak in the film thickness distribution is shifted outward the center becomes flattened and the plum of the spray film pattern is more extended and becomes wider when we increase the ω_{Bell}. Larger droplets, because of their higher momentum, separate from the annular jet air stream. The overall distribution of the droplet size is skewed into the small and mid-range size, striking the workpiece more distant from the centerline. The film distribution of the droplets for the

different breakup model is almost identical. A slight difference is due to the changing in the hitting behavior and trajectory of the droplets because of the change in the prediction of their size by the breakup model. Fig. 3.16 shows that in the higher diameter of the sprayer, there are lower values but a more uniform pattern for the maximum paint film thickness.

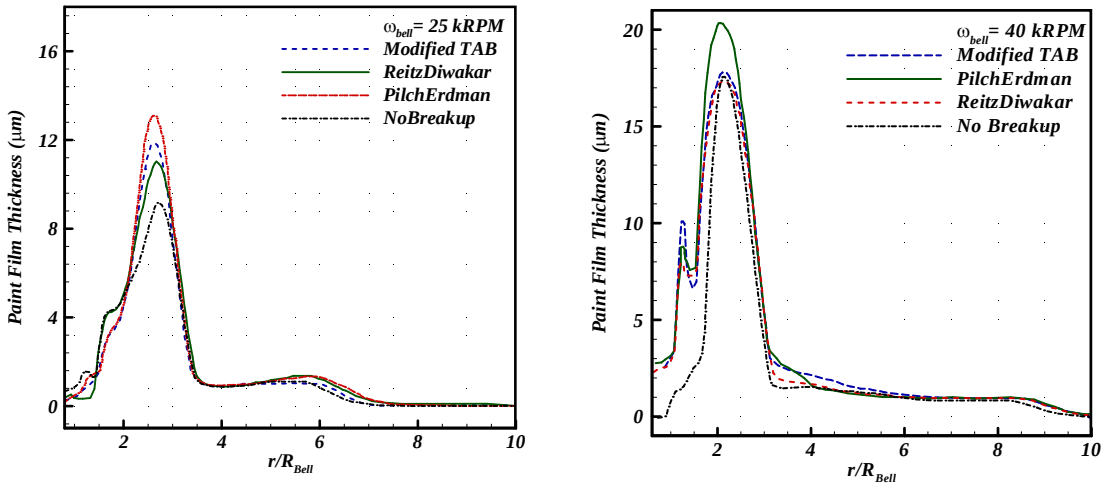

Figure 3.15: Paint film thickness distribution for different breakup model and ω_{Bell}.

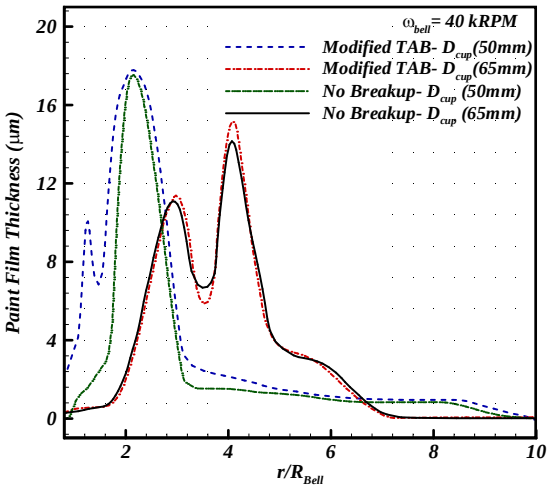

Figure 3.16: Thickness deposition of the paint droplets along the target surface for various d_{cup}.

From the frames in Fig. 3.17, it is visible that the pattern angle of the sprayed droplet close to the bell edge decrease from 64.3°, at $150\,norm.\,l/\min$ shaping airflow rate to 60.65°, at $300\,norm.\,l/\min$, and then to 57.7° at $500\,norm.\,l/\min$. The shaping airflow is not so effective in changing the spray angle and pattern in the area close to the bell cup rim. But the importance of this airflow is that it makes the outside toroid-shape air vortex more powerful. It causes to have better control on the sprayed droplet by means of these vortical structures.

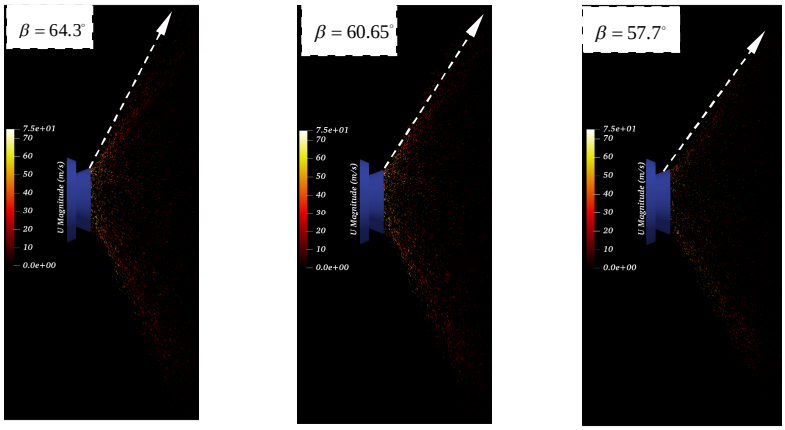

$\dot{m}_{air} = 150 norm.\ \mathrm{l/min}$ $\dot{m}_{air} = 300 norm.\ \mathrm{l/min}$ $\dot{m}_{air} = 500 norm.\ \mathrm{l/min}$

Figure 3.17: Changing of the shaping airflow rate at fixed bell cup rotational speed ($\omega_{Bell} = 10 kRPM$, $t = 20 ms$, $SF_{Droplet} = 20$).

Figure 3.18-3.20 illustrates the mean velocity contour with streamlines of airflow, which is visualized by using the Line integral convolution (LIC) approach (Stalling and Hege, 1997). The inner recirculation zone length (L_{rz}) is considered as the longitudinal distance from the sprayer to the location of the stagnation point on the axis that is produced by the mechanisms of the vortex breakdown (as shown in Fig. 3.18). By increasing the rotational speed, the recirculation zone length enlarges and the position of the attachment point, where the mean axial centerline velocity reaches to maximum values, moves upstream similarly to what was observed in reference Stevenin et al. (2015). The values of L_{rz} can enlarge several times more than the bell diameter, for high ω_{Bell}, and that can be large enough to reach the workpiece surface in the real industrial conditions.

The dimensionless inner recirculation length (L_{rz}/d_{cup}) for a rotational speed of 25, 40 and 55 kRPM is measured as a 1.64, 2.07 and 2.38, respectively. In the current flow around the ERBS, with high turbulent intensity and velocity values, the pattern of the flow is more controlled by the rotational speed levels compared with the injected shaping airflow. These analyses provide valuable data about the airflow for designing the new ERBS generation in order to have higher efficiency. By evolving the flow, the toroidal vortex in high values of ω_{Bell} and d_{cup} will enlarge enough into the workpiece surface (Figs. 3.18 and 3.19). For the higher rotational speed in Fig. 3.19, the vortex breakdown mechanisms result in multiply small-scale vortex structure that is recognized as the same that is observed in reference Stevenin et al. (2015). Figure 3.20 indicates the velocity magnitude contour with regard to the vortex growing structures. The center position of the inner and outer recirculation zone is indicated by the line in this figure. As visualized in the frames of Fig. 3.20, the recirculation zone downstream of the spraying flow is fully characterized and reaches a self-similarity condition.

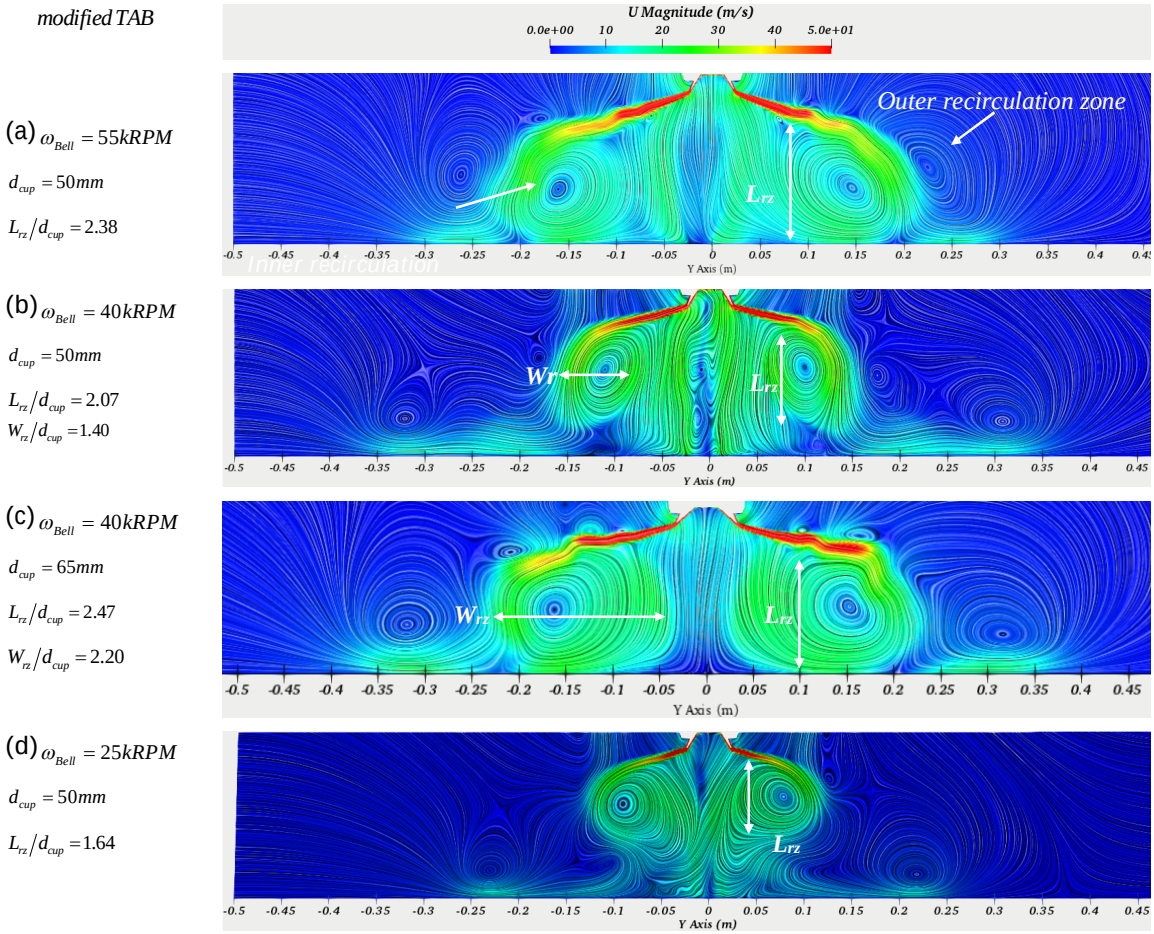

Figure 3.18: Velocity magnitude contour (m/s) with the streamline pattern, which is visualized by the LIC (Line Integral Convolution) method in different ω_{Bell} and d_{cup}.

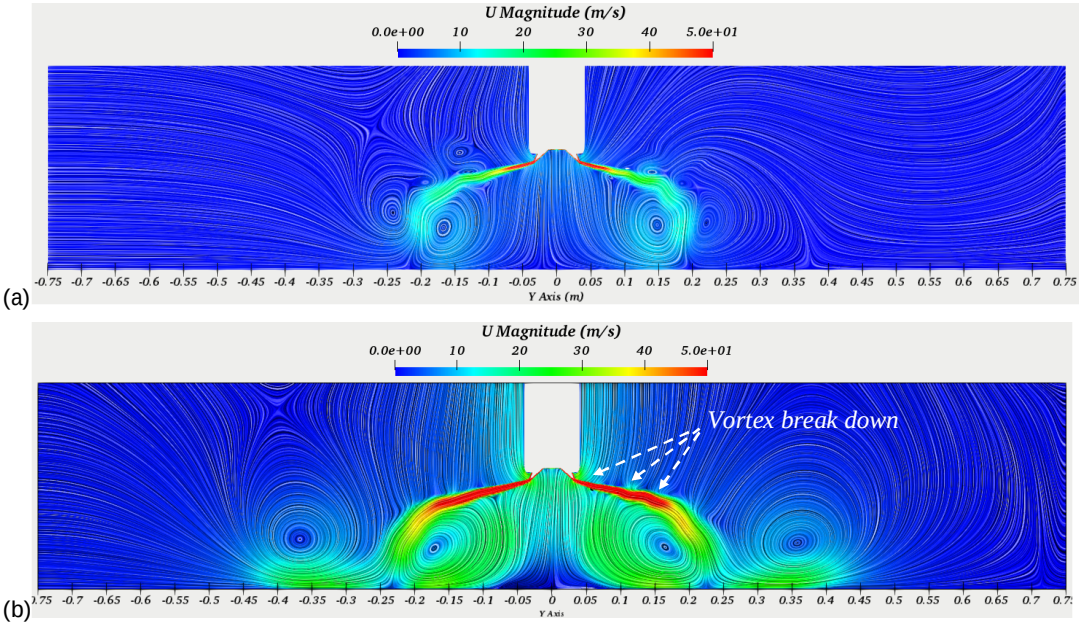

Figure 3.19: Shows the developed velocity contour with streamline in the ERBS with $d_{cup} = 65mm$, *modified TAB*, (a) $\omega_{Bell} = 20kRPM$ (b) $\omega_{Bell} = 50kRPM$.

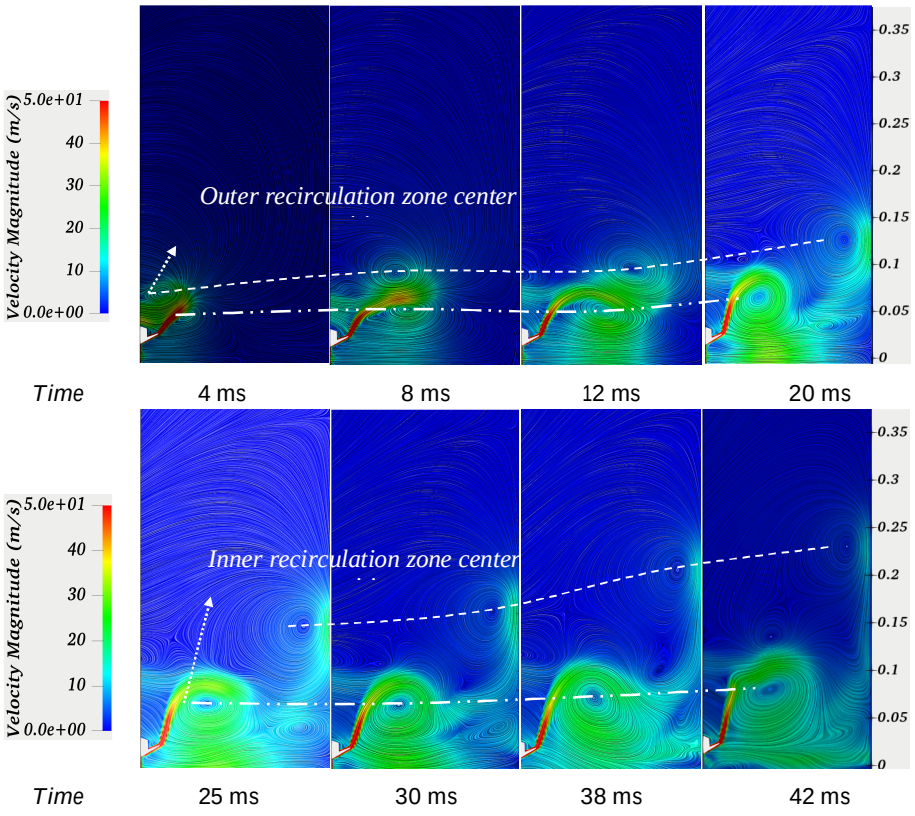

Figure 3.20: Periodical time evolution of the electrostatic spraying pattern ($d_{cup} = 50mm$, $modified TAB$, $\omega_{Bell} = 25 kRPM$).

Figure 3.21 shows the radial profile of the mean velocity evolution for different rotational speeds as a function of the breakup model. At $\omega_{Bell} = 55kRPM$ the mean velocity increases dramatically, by way of example U_{mean} is roughly 100 m/s. For a lower ω_{Bell} the air velocity that is reported by using a different breakup model presents almost the same behaviors. But, at a higher ω_{Bell} the effect of the droplet number and their size on the airflow velocity is more noticed.

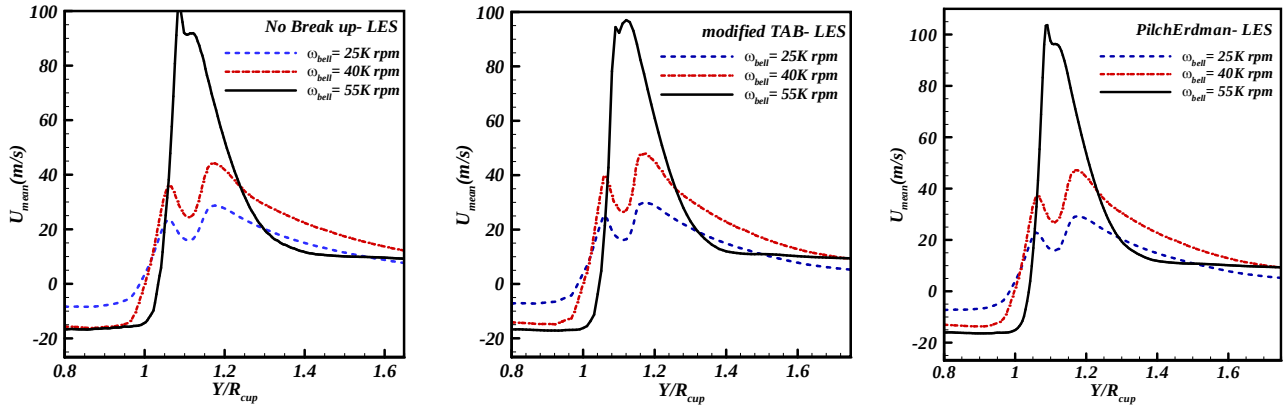

Figure 3.21: Radial mean velocity profiles for various breakup models and ω_{Bell} in the turbulent boundary layer close to the cup rim.

The numerical investigation inside the bell cup of the sprayer is very important because it cannot be observed easily in experimental studies. In this section, the qualitative information about the paint droplet breakup mechanisms and injection distribution is described exactly inside the rotary bell cup. Droplets have been colored by their velocity quantitatively and are showing different patterns by using different breakup models. In regards to the observations of the droplets in the frames of Fig. 3.22, the regular rotational pattern and the gradual increase in the velocity of the particle are apparently visible. Multiple breakups of the particles are happening in the area from the paint nozzle into the bell cup rim. First, the direct formation of the unstable droplets occurs near the nozzle with the patterns of ligament shape based on the Rosin-Rammler distribution model and next after the breaking up of the particles, they eventually explode into a small fairly uniform size, which are thrown from the bell cup surface. At the higher rotational speed the breakup phenomenon happens faster and the particles disintegrate into a smaller size. Also, utilizing the electrical potential for the bell surface creates a repelling force on the charged particles that changes the atomization pattern and also produces a smaller droplet size. The number and angle of the ligament shape particles are increasing with the growth of the rotational speed. The consideration of the internal initial paint flow indicates that the liquid droplets emerge from the nozzle and form a larger ligament, which breakup into larger droplets at $\omega_{Bell} = 25kRPM$. In contrast, at $\omega_{Bell} = 55kRPM$ few ligaments are formed that breakup into very small droplets.

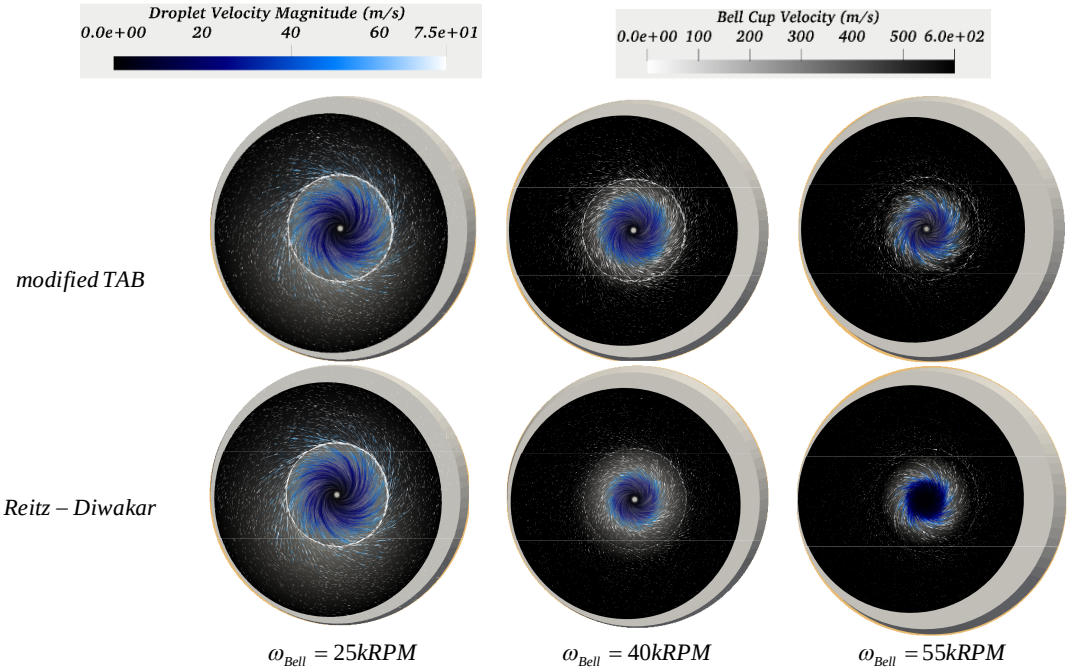

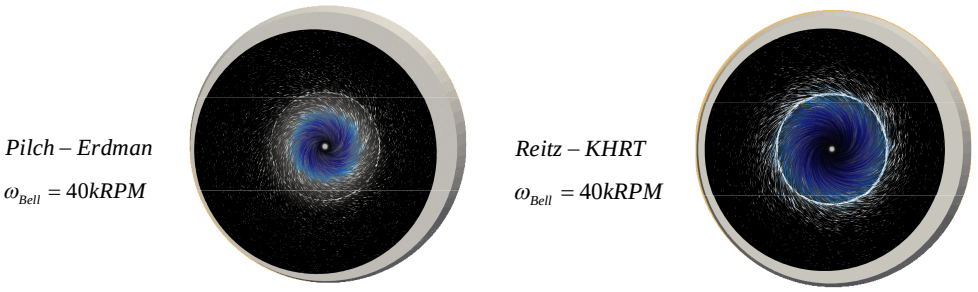

Figure 3.22: 3D visualization of the droplet trajectory, exactly over the bell cup surface that is valued by their velocity magnitude ($SF_{Droplet} = 40$, $t = 3ms$).

The size of the constructed paint particles is a function of the bell cup diameter, rotational speed, electrostatic charge and paint flow rate. The distribution of the particle size in Fig. 3.23 is showing that the droplet hydraulic diameter, as well as the overall mass, decreases with the growth of the rotational speed. The distribution indicates that the particles have a bimodal size, including an area near the nozzle with a high ratio in size increasing and also approximately constant size distribution with a slight increase in the region outside far away from the cup edge.

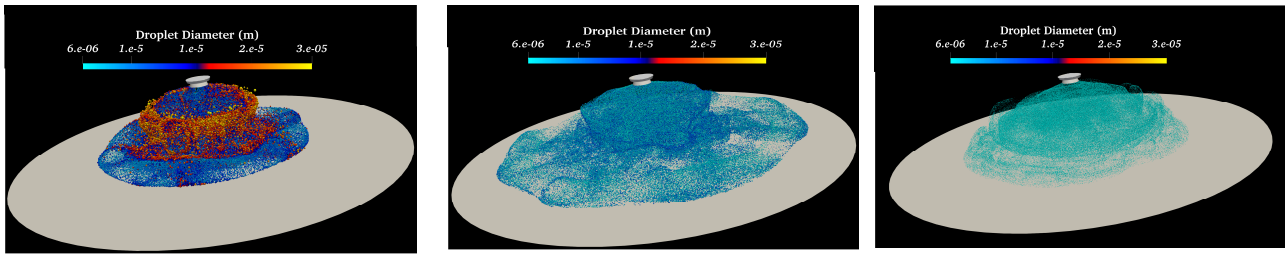

$\omega_{Bell} = 25kRPM$ $\omega_{Bell} = 40kRPM$ $\omega_{Bell} = 55kRPM$

Figure 3.23: (a) The size distribution of the particle at different rotational speeds (b) ($Modified\ TAB$, $SF_{Droplet} = 40$, $t = 40ms$).

Figures 3.24-3.27 present quantitatively the histograms of the diameter and velocity of the droplets for the various operational conditions. The distribution of the liquid particle diameter after their disintegration procedure, the so-called paint droplets breaking up process, is indicated in Fig. 3.24. Figure 3.24 (a) shows that by increasing the rotational speed in the modified TAB model, from 25 to 55 kRPM, the values of diameter, in the range of the maximum number, decrease significantly from 14.4 μm to 7.53 μm. This value, for the middle case of a rotational speed of 40 kRPM is 11.89 μm. Also, it can be identified that for the same values of the paint flow rate, the number of particles at higher rotational speed (55 kRPM), for example in the maximum range, is 2.5 million, that is not comparable with the lower rotational speed, 1.2 and 0.5 million for 40 and 25 kRPM, respectively. The particle diameter covers a larger range in the lower rotational speed and has a parabolic trend with a uniform slope. Increasing the rotational speed leads to a significant decrease in Sauter Mean Diameter (SMD) and obtained smaller droplets. The results of the current numerical study with the modified TAB showed that the higher rotational speeds ($\omega_{Bell} = 55kRPM$) resulted in 54% reducing droplet SMD compare to $\omega_{Bell} = 40kRPM$. The same trends ($\approx 51\%$) also observed among the $\omega_{Bell} = 40kRPM$ and

$\omega_{Bell} = 25kRPM$. In the Pilch-Erdman model, unlike the modified TAB model, most of the droplets are in the small range of the droplet, 17.5, 12.05 and 8.96 µm for a rotational speed of 25, 40 and 55 kRPM, respectively. The number of droplets in the mentioned ranges are 2.22, 2.03 and 2.7 million, respectively. Figure 3.24 (frame c) compares four various different models of the breaking of the droplets. Pilch-Erdman model predicts a larger droplet size with higher values of the SMD as compared to the two other models that are almost in the same range. For the reason of this overestimation, it can be stated that the concept of a maximum stable diameter droplet (Eq. 3.8) merely puts an upper limit on the largest droplet size possible. The comparison between the particle diameters by using various cup diameters (50 mm and 65 mm) shows that by increasing the cup diameter, the number of smaller droplets grows and inversely their diameter is decreased and the droplet size changes to smaller ones (as shown in Fig. 3.25). In other words, the uniformity of the droplets decreased. Figure 3.26 presents the velocity magnitude of all droplets in the computational domain. The maximum values of the velocity magnitude of the droplets, for higher rotational speed, increase dramatically. The range of velocity for the high percentage of particles at different ω_{Bell} is almost the same ($\approx\geq 250m/s$). Figure 3.27 shows the velocity magnitude of almost all droplets for the $d_{cup} = 65mm$ is higher than $d_{cup} = 50mm$. Also, the velocity of a few particles in the region where the overspray happens for $d_{cup} = 65mm$ is much more than $d_{cup} = 50mm$.

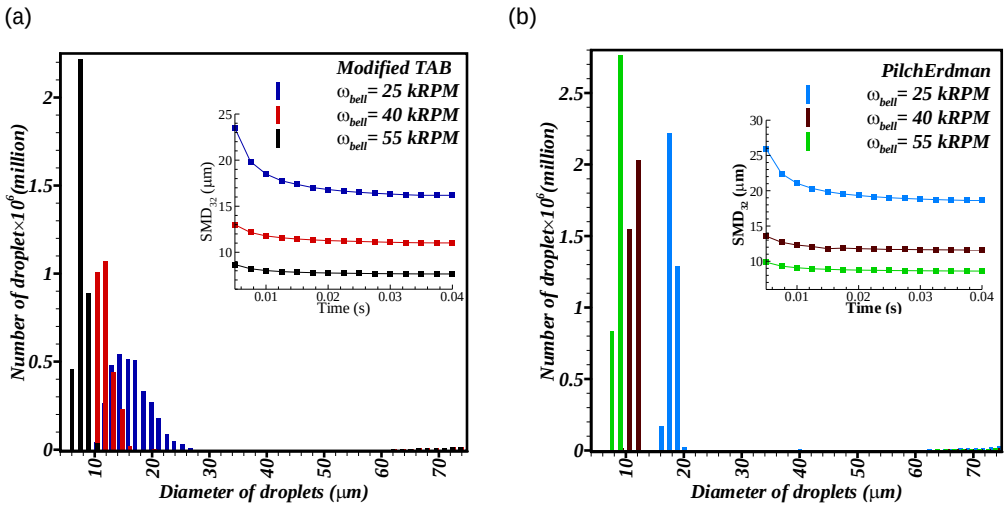

(c)

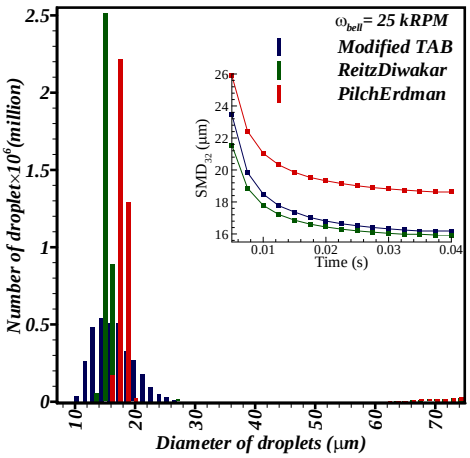

Figure 3.24: Sprayed droplet size distribution in the computational domain.

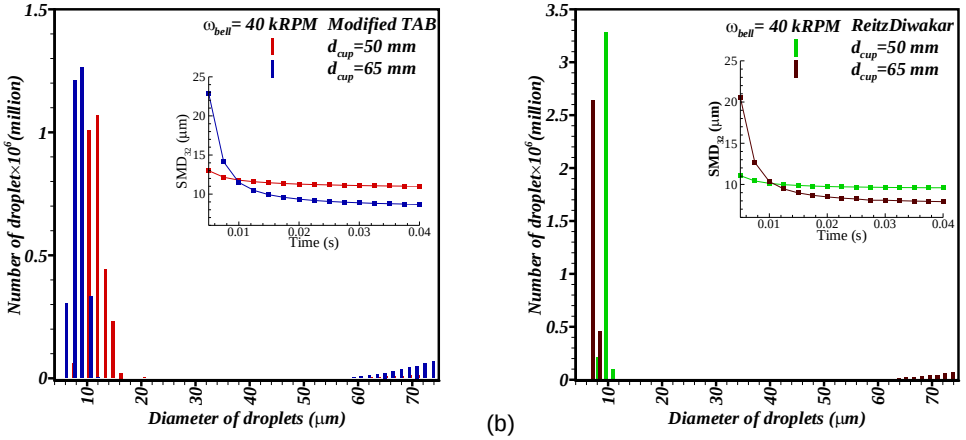

(a) (b)

Figure 3.25: Sprayed droplet size distribution in the computational domain for the various bell cup diameter: (a) $d_{cup} = 50mm$ (b) $d_{cup} = 65mm$.

a) (b) (c)

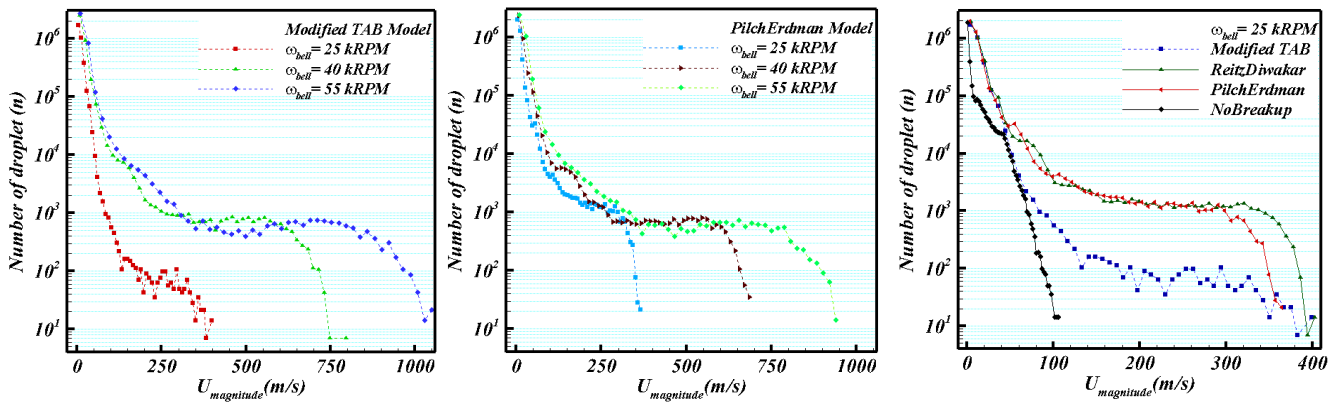

Figure 3.26: The x-axis in the plots indicates the droplet velocity magnitude and the y-axis shows the number of the droplet, which is located in the computational domain.

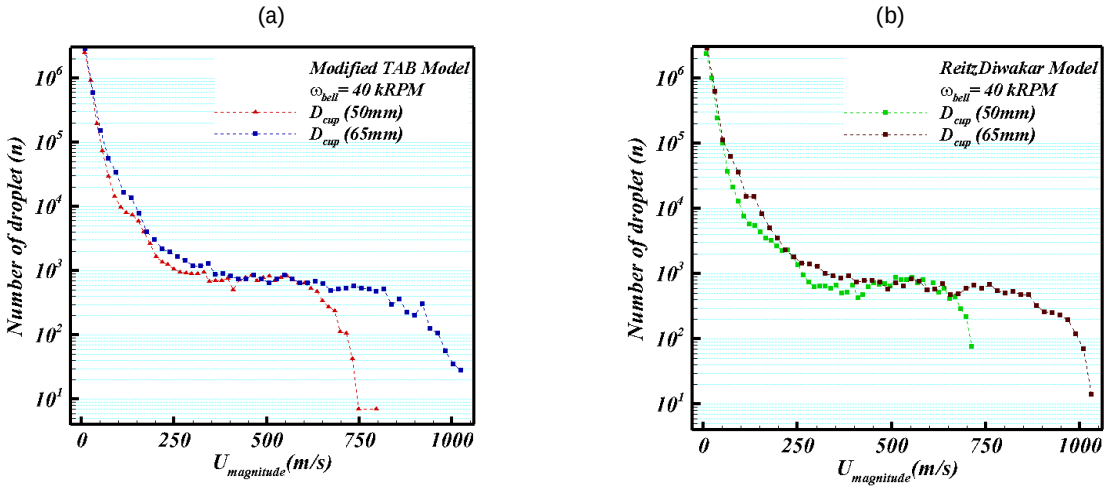

Figure 3.27: Sprayed droplet velocity magnitude distribution on the computational domain for the various bell cup diameters: (a) $d_{cup} = 50mm$ (b) $d_{cup} = 65mm$.

The resulting mean air velocity contour near the bell cup rim toward the outside is depicted in Fig. 3.28. For low rotational speeds ($\omega_{Bell} = 10kRPM$), the air velocity injected from the nozzles affect the air velocity and its pattern, for instance, it reaches 35 m/s and 10 m/s for $\dot{m}_{air} = 500$ and $\dot{m}_{air} = 150$, respectively (Fig. 3.28 (a)). Also, Fig. 3.28 (b) shows changes in the droplet pattern due to various breakup models, but this does not have an obvious impact on the airflow velocity distribution.

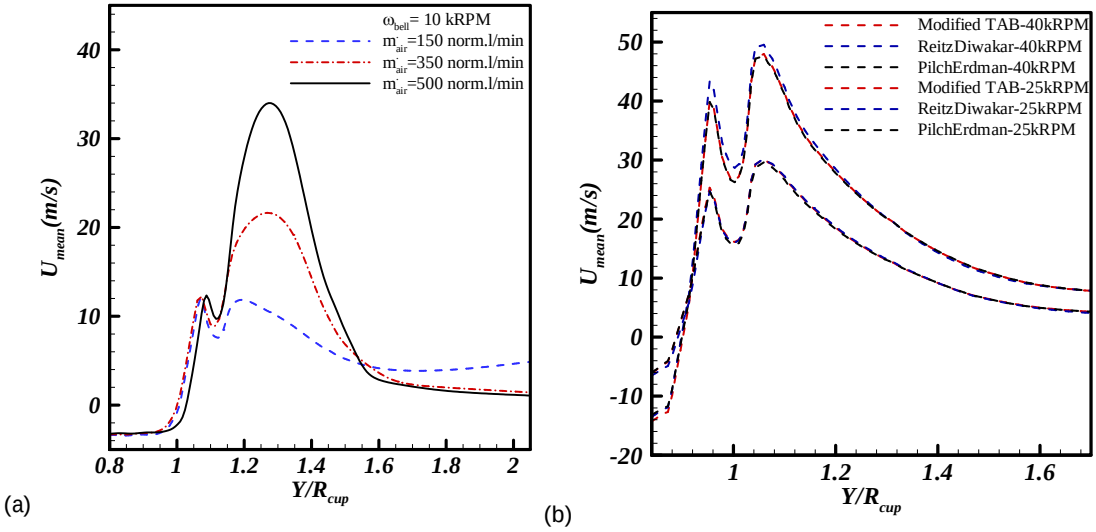

(a) (b)

Figure 3.28: Compared mean velocity near the bell cup rim (a) various airflow rates. (b) different breakup model.

In order to investigate the effect of the d_{cup} and ω_{Bell} on the vortical structure, the Q-criterion Iso-surface of the LES results is visualized in Fig. 3.29. Results indicate that the vortical structure has a similarity to the spray pattern because the injected droplets after separation from the bell cup surface lose their momentum and trace the vortex motion. In $d_{cup} = 50mm$, three vortex tubes

are formed, but in $d_{cup} = 65mm$ the inner conical layer has been removed and two large tubes are constructed. At a higher d_{cup}, a sizable outer layer almost reaches the target surface and it is a thick uniform circular shape and without any distortion. But at lower values of d_{cup}, a smaller vortex tube with a non-uniform surface is visible. By changing the rotational speed, the same behavior for the vortices has been observed, with just different sizes. By changing the ω_{Bell}, we can have an important tool to control the droplets that reach the target and also the area which is covered by the paint film. By examining the two-dimensional Q-Criterion contour, one area of Q-Criterion with negative values is visible between the two regions with high Q-Criterion values.

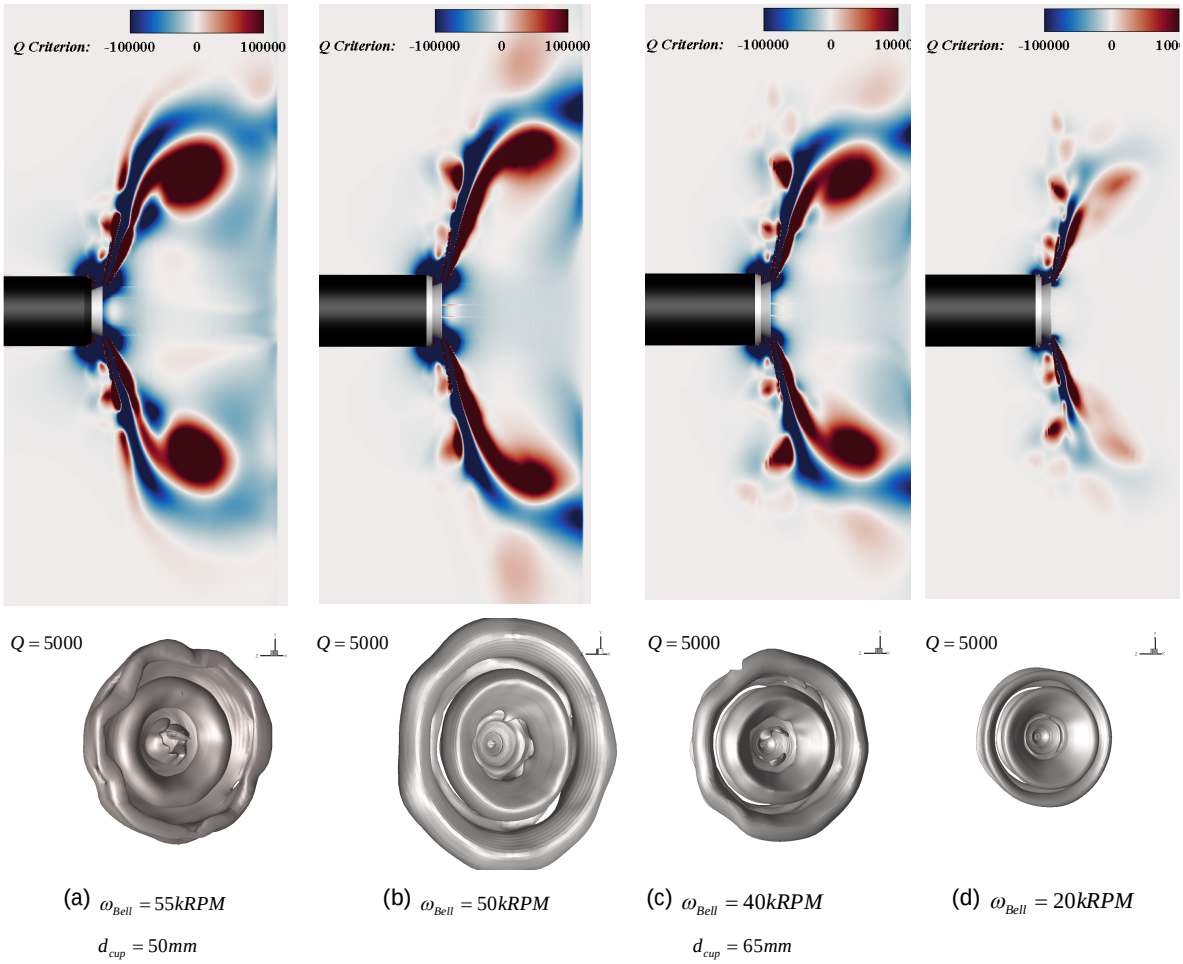

Figure 3.29: Q-criterion visualization of the vortical structures (by using mean velocity)($t = 42ms$): effect of rotational speed (b, c, d) and bell diameter (a,b).

3.5. Conclusions

In the current study, the main goal is to introduce a better understanding of the electrostatic spraying behavior in the ERBS, especially the mechanisms of the droplet breakup process. In doing so, a base code within the OpenFOAM framework (OpenFOAM, 2019) is developed and

expanded to capture the paint film distribution on the target body and also computed the effect of the electric field on the injected droplets. In addition, the present work pursues a detailed investigation about the impact of the modified breakup model on the spray distribution. The concept of dynamic airflow and droplet interaction is deeply investigated. The operating parameters are unified against a broad range of operating conditions. Parameters like the rotational speed, the bell cup diameter and voltage are combined parametrically.

A summary of the most important physical outcomes from the current simulation can be listed as follow:

(1) It is proved that the breakup model has a small effect on overall spray shape, but its effect on the diameter of the distribution of the droplets and SMD is more obvious, e.g., the modified TAB, Reitz-Diwakar and Pilch-Erdman predicted mean SMD values of 13.6, 12.9 and 15.9 μm , respectively, for the $\omega_{Bell} = 40kRPM$ during the spraying cycle.

(2) Although from point of view the vortical structures, the bottom-most and top-most, outside of the bell cup and target surface locations, respectively, the spray pattern is experienced the highest value of the vortical region. For moderate ω_{Bell}, the wake forms an inner recirculation area, whose length is in the order of 2.0 bell-cup diameter. An unfavorable overspray region occurs in higher rotational speed, which is the source of the negative force.

(3) At a constant rotating speed, the higher spray angle is obtained in lower shaping air and higher voltage.

(4) The shaping airflow from the nozzles is not so effective in changing the spray angle close to the bell, but it makes the outside toroid-shape air vortex more powerful and controls the spray distribution.

(5) The results of the modified TAB showed that the higher rotational speeds ($\omega_{Bell} = 55kRPM$) resulted in 54% reducing droplet mean SMD compare to $\omega_{Bell} = 40kRPM$. The same trends ($\approx 51\%$) also observed for the $\omega_{Bell} = 40kRPM$ and $\omega_{Bell} = 25kRPM$.

(6) The observations of the paint droplets inside the bell cup indicate a regular rotational pattern, gradual velocity increase and multiple breakups of them.

Chapter 4

Analysis of droplets charge and size distribution in the electrostatic coating process [3]

Abstract

This study presents a numerical performance evaluation of the electrostatic rotary bell sprayer (ERBS) with a particular focus on droplet charge, electric field, ambient conditions and through the implementation of a high-voltage control-ring field pattern effect into the fully turbulent airflow and by including the atomized droplets discrete phase. The simulation shows that the inclusion of droplet charging and electric field coupling, with different parametric values, significantly impacts the atomized droplet distribution over the spray plume and the deposition rate. This analysis was conducted using a three dimensional (3D) Eulerian-Lagrangian model to describe the two-phase spraying flow by extending the base OpenFOAM package. The procedure includes an unsteady compressible Navier-Stokes solver combined with a Large Eddy Simulation (LES) approach to model turbulence effects on the air flowfield. This is coupled to the spray dynamics by including; droplet trajectory tracking, wall film dynamics and electric field charge. The approach is further extended to include the evaporation phenomenon and the transport of its products. Compared to a conventional ERBS, herein, we provide an in-depth analysis of the fluid dynamic characteristics around the ERBS with a control-ring field pattern for vorticity, velocity and electrical fields. The results indicate that the control-ring operation improves the performance and transfer efficiency (TE) of the ERBS, and it also helps to harmonize the direction of the charged paint droplets. For the first time, finding a balance between the effect of the inside bell cup surface and control-ring voltage and charged droplet has been conducted.

4.1. Introduction

Electrostatically charged coating systems effectively increase transfer efficiency (TE) during a shorter process time. The coating process via high-speed rotary bell atomizer is become a key

[3] Based on the work published in the Journal of Physics of Fluids, https://aip.scitation.org/doi/10.1063/5.0041021, 33(3), 2021,
and, SAE International Journal of Advances and Current Practices in Mobility, https://doi.org/10.4271/2021-01-0022.

painting technology, especially in the automotive industries. It involves three main sub-processes: the paint droplets atomization, the transportation and the film formation processes due to their deposition on the target. The use of electrostatic rotary bell sprayer (ERBS) leads to a superior coating performance, material cost reduction, decrement of the environment's destructive impacts, and constructed a uniform film thickness with a high-quality (Akafuah et al., 2016). The atomization process includes two parts of the primary and secondary breakup procedures. The Euler–Euler and Euler–Lagrange approaches have been used previously for modeling the two-phase coating flow. During the past decades, some numerical and experimental works have also been conducted on the coating process in ERBS, but those are mainly focused on the electrical charge process (Guettler et al., 2020; Pendar and Páscoa, 2020a; Viti et al., 2008; Ellwood and Braslaw, 1998), droplet size, disintegration, transport, or mapping procedure (Gödeke et al., 2020; Darwish Ahmad et al., 2019; O'Rourke and Amsden, 2000). Some of these works have also studied the shaping airflow effect on the atomization procedure (Darwish Ahmad et al., 2018; Stevenin et al., 2015).

Numerical simulation of the coating application processes using ERBSs need to be implemented and continuously enhanced, in order to optimize the coating process parameters and reduce the material cost. Knowledge about material properties and application parameters is a fundamental aspect that must be considered by car manufacturers. The accurate implementation of the electric field is a crucial issue in an electrostatic spray simulation, to correctly capture the flow details. Some of the more recently published numerical investigations on the electrostatic effect on the paint particles during coating are the ones of Domnick et al. (2005), Ye et al. (2005), Colbert (2007), Toljic et al. (2011), Osman and Adamiak (2016).

The charge to mass ratio of individual particles is one of the main controlling parameters of the paint spray pattern during electrostatic coating. Ellwood and Braslaw (1998) offered a numerical insight into the spraying mechanisms using rotary bell atomizers to describe the charged droplets' distribution. Higashiyama et al. (1999) compared the diameter and distribution of the atomized charged and uncharged droplet shower from an airless nozzle. They showed that the charged droplet spread more broadly because of the repulsion force, and also there is no substantial difference in the distribution pattern for different droplet ranges. Im et al. (2001) illustrated that adequate electric field implementation in combination with a high shaping air flow rate significantly improves the coating efficiency, but the rotational speed is the dominant parameter. Im et al. (2004) demonstrated that the spray pattern is very sensitive to the charge to mass ratio, as was computed using their electrostatic spray code. Toljic et al. (2011) compared different values for the charge to mass ratio, for various droplet sizes, and also their influence on the particle movement trajectory and its distribution, and these have shown a remarkable impact on the film thickness. They concluded that by increasing the droplet surface charge value up to 1 mC/kg produced a significant increment on the transfer efficiency. Instead of using the primary breakup model, Osman et al. (2015b) ejected different droplet size ranges with the specified electrical charges from the presumed multiple injection points in the rotary bell sprayer and tried various cases and then compared the data with their experimental results. They assumed that all the droplets have the same surface charge-to-mass ratio, for instance,

equal to 1 mC/kg for the case with droplets by an average diameter of 35 μm. Subbotin and Semenov (2018) generated a bulk charge by the corona discharge due to a high electric field and described the conductive liquid behavior when experiencing high voltage. Colbert (2007) described the practical droplet charging process during the electrostatic coating in the relevant industries. Also, the effect of paint viscosity on the constructed film pattern was examined. As our literature review indicates, along with the numerical method developed, there is also the need to understand the charging process better.

The heat transfer and droplet evaporation during the electrostatic spraying process in the ERBS are not considered in detail in the previous studies. Still, as our literature survey shows, there are a few studies considering the effect of evaporation, i.e., Shrimpton and Laoonual (2006) and Arumugham-Achari et al. (2015). Brentjes et al. (2020) who investigated the role of the electric charge in the spraying process transfer efficiency, with a focus on evaporation and the transport of evaporation products. Their result indicates a notable growth in the cooling rate and an almost double spray transfer efficiency in the presence of the electric field charge.

An important parameter in estimating the droplet trajectory in an electrostatic spraying cloud simulation is the assumed initial distribution of the injected droplet size from the paint nozzle. Numerous works dealing with the high-speed rotary bell atomizer (Ellwood et al., 2014; Liu et al., 1998; Frost, 1981; Hinze and Milborn, 1950) have considered the droplet size by changing the bell cup rotational speed and the volumetric paint flow rate. They consistently confirmed the reduction of the droplet size by growing the rotational speed, while its increase by enhancing the volumetric paint flow rate, albeit less pronounced. The electric field's effect on the droplet size during the spraying process has remained ambiguous; that is why it will be considered in the present work in great detail. Darwish et al. (2019) explained the size distribution of the droplets by applying a three-dimensional mapping style for a rotary bell spray without an electrostatic field. They stated that the droplet size was increased in the vicinity of the cup, and the droplet size became more uniform by enlarging the lateral distance. Ahmed and Yousef (2012) explained the effect of the parametric change of the non-dimensional parameters, such as Weber number, Reynolds number and flow coefficient effect on the Sauter mean diameter (D_{32}). Wilson et al. (2018) visualized the ligament and droplet formation around an ERBS. Their experimental results showed that the higher rotational speeds reduced the droplets' Sauter Mean Diameters (SMD) and ligament size by 22.3% and 26.8%, respectively. Oswald et al. (2019) demonstrated that the elongational resistance flow influences the disintegration process in the bell atomizer. However, the sprayed droplets' size distribution is almost not affected by the alteration that is mentioned above. The complex nature of the droplet size estimation during the numerical spraying stimulation is still a challenging ongoing research topic.

The disintegration procedure on the surface of the rotary bell cup is divided into the film, ligament and droplet formation (Hinze and Milborn, 1950). A massive amount of experimental studies, as in Liu et al. (2012) and Ahmed and Youssef (2014), have investigated the transition between the different modes on a rotary bell cup. Shen et al. (2019) reported the droplet disintegration process and the non-Newtonian fluid behavior that is injected into the orifice and bell surface as an input paint high-speed rotary atomizer. However, just very few numerical

studies, like Shen et al. (2017), have considered the paint droplets primary breakup procedure through an ERBS full three-dimensional (3D) computational framework. Saha et al. (2012) investigated the breakup modes of water emanating from hollow cone nozzles that are induced by pressure-swirling. The primary and secondary breakup of liquid films were considered precisely.

The present contribution deals with the numerical investigation of the liquid atomization process using a commercial high-speed ERBS with a high-voltage control-ring. Here we introduce and optimize an appropriate application parameter to increase TE and prevent overspray during the electrostatic spraying, especially by providing a deeper understanding of the influence of the electric field and droplet charge. The first set of results considers the charge of the droplet, and applied voltage, in the case with and without a high-voltage control-ring around the sprayer, in association with a high-voltage bell cup surface. The second part focuses on the size distribution, and collision, of the droplets during the primary and secondary breakup process during the coating, and their effect on the coating transfer efficiency and film formation. In addition, the influence of ambient conditions on the spray evaporating is also presented in detail.

4.2. Governing equations: Paint film formula

The numerical formulations of this study consider both an Eulerian (continuous airflow and electric field) and Lagrangian (discrete paint droplet phase) model that we will now describe in more detail. In the airflow simulation, the compressible Navier-Stokes equations are used here, as is explained in detail in chapter 2. A Large Eddy Simulation (LES) model is retained by using a “one equation eddy viscosity model” (OEEVM) subgrid-scale method to simulate the turbulence effects of the current high-Reynolds flow (Pendar and Roohi, 2018).

The electric field is produced by the voltage applied to the ERBS’s surface and also by the high-voltage control-ring. The space charge is governed by a Poisson equation, as is described in detail in chapter 2.

4.2.1. Discrete paint droplets phase: two-way coupling

The trajectory of each Lagrangian electrically charged paint droplet is tracked individually throughout the computational domain by integrating the force balance and solving the differential equations. These describe the evolution of mass, velocity, temperature, and position. The droplet discrete phase is coupled with the airflow via source terms in mass, momentum and energy equations.

4.2.1.1 Evolution of mass

The droplet mass evolution is also considered when computing the mass source terms in the bulk carrier fluid phase and when updating the droplet pressure equation. The droplet mass (m_p) evolution is expressed via the following conservation form equation:

$$\frac{dm_p}{dt} = -\frac{Sh}{3Sc}\frac{m_p}{\tau_p}\xi_M \quad . \tag{4.1}$$

In which Sc , Sh , ζ_M and $\tau_p = \rho_p d_p^2 / (18\mu)$ are the Schmidt number, Sherwood number, a potential function driving the evaporation and the particle relaxation time, respectively.

4.2.1.2 Evolution of momentum

The droplet's velocity evolution is computed by applying Newton's second law of motion. The mathematical formulation of the forces that affect the droplet motion, e.g., Stokes drag, gravity, electrical and added mass force, can be found in detail in chapter 2.

4.2.1.3 Evolution of energy

The droplet temperature evolution is computed by the following enthalpy-based energy equation.

$$\frac{dH_p}{dt} = A_p(\dot{q_{con\upsilon}} + \dot{q_{abs}} - \dot{q_{em}}) \quad . \tag{4.2}$$

The particle enthalpy (H_p) change is equal to the sum of the convection heat transfer ($q_{con\upsilon}$), radiation heat transfer (q_{abs}) and negative values of the emitted radiation heat (q_{em}). Eq. (4.2) can then be expressed as a function of the temperature of the particle (T_p):

$$m_p c_p \frac{dT_p}{dt} = A_p(\mathrm{h}\,(\mathrm{T}_f - \mathrm{T}_p) + \dot{q_{abs}} - \varsigma\varepsilon\,\mathrm{T}_p^4) \,. \tag{4.3}$$

Where c_p , A_p , ς , h , I and ε are the particle specific heat capacity, the droplet surface, Boltzmann constant, heat transfer coefficient, and radiation intensity and emissivity, respectively. Ranz and Marshall heat transfer approach (Ranz and Marshall, 1952) is here used to evaluate a single paint droplet's mass due to the evaporation process. The heat transfer coefficient (h) is derived as a function of the Nusselt number and the droplet diameter ($h = N_{uk}/d_p = (2 + 0.6\sqrt{\mathrm{Re}}\,\mathrm{Pr}^{1/3})\kappa/d_p$).

4.2.1.4 Evolution of breakup process

Breakup modeling is one of the most critical procedures in the spraying simulation that is divided into primary and secondary breakup. In the primary breakup process, the droplet size

distribution is determined by using the Rosin-Rammler distribution model ($Y_d = \exp(-d/\bar{d})^n$). Here, the modified TAB breakup model is applied to predict the size of the paint droplet after the decomposition, as a secondary breakup procedure that can be found in detail in chapter 2.

4.2.2. Liquid paint film equations

4.2.2.1. Mass conservation equation of film

The mass conservation formulation is as follow:

$$\frac{\partial(\rho\delta)}{\partial t} + \frac{\partial}{\partial x_j}(\rho U_j \delta) = S_\delta \ . \tag{4.4}$$

Where, U_j and δ are the mean film velocity and the height of the film, respectively. The mass source term results from the impingement of the liquid droplets on the film surface ($S_{\delta,imp}$) and is also due to the evaporation of the film ($S_{\delta,eva}$) that is represented by $S_\delta = S_{\delta,imp} + S_{\delta,\mathrm{eva}}$. The impingement source ($S_{\delta,imp}$), is defined as the mass accumulation over a surface area for a given amount of time.

$$S_{\delta,imp} = \sum_i m_{imp,i} \Big/ A\Delta t \ . \tag{4.5}$$

The amount of mass impinging on any given surface is computed via interfacing with the Lagrangian particle tracking in the continuous phase. Note that the source term due to evaporation ($S_{\delta,eva}$) will be inserted into the pressure equation for the gas phase and also into the equation for the spices transport.

4.2.2.2. Momentum conservation equation of film

The equation for the momentum is expressed as follows:

$$\frac{\partial(\rho\delta U)}{\partial t} + \frac{\partial}{\partial x_j}(\rho U_i U_j \delta) = -\delta\frac{\partial p}{\partial x_i} + \tau + S_{U\delta} = -\delta\frac{\partial}{\partial x_i}(-\rho x_i g_i \delta - \sigma\frac{\partial\delta}{\partial x_i \partial x_i} + p_g) + \rho\delta g_{ti} - \mu\frac{3U_i}{\delta} + \tau_\theta + S_{U\delta} \tag{4.6}$$

Here, τ, p and $S_{U\delta}$ represent stress like components of the forces acting on the film, pressure and the effect of the impinging droplet, respectively. The pressure contribution is divided into capillary impact ($p_\sigma = -\sigma\frac{\partial\delta}{\partial x_i \partial x_i}$), hydrostatic contribution ($p_P = -\rho x_i g_i \delta$), and the surrounding gas's influence (p_g). The τ parameter is divided into the wall sear stress ($\tau_\omega = -\mu\frac{3U_i}{\delta}$), the gravitational force tangential to the wall ($\tau_t = \rho\delta g_{ti}$) and the contact line force contribution (τ_θ).

4.2.2.3. Energy conservation equation of film

The energy equation is given by;

$$\frac{\partial(\rho\delta h)}{\partial t}+\frac{\partial}{\partial x_j}(\rho U_j\delta h)=S_{h\delta}\ . \tag{4.7}$$

Here, h is the mean film enthalpy. The impact of the impinging droplets ($S_{h\delta,imp}$) and the evaporation of the film ($S_{h\delta,eva}$) effects into the energy equation are represented by $S_{h\delta}=S_{h\delta,imp}+S_{h\delta,eva}$.

4.2.3. Film thickness equation

The film thickness equation is computed by inserting the discrete momentum equation into the equation of the continuity. By using the discrete momentum equation (Eq. 4.4), the relation obtained for the U_p is inserted into the continuity equation and, as such;

$$\rho U_P\delta=\rho\left[H[U]\frac{1}{A_P}-\frac{1}{A_P}\delta\nabla(\underbrace{-\rho g_i x_i}_{P_P}\delta-\underbrace{\sigma\nabla\nabla\delta+p_g}_{P_u})+\frac{1}{A_P}\rho\delta g_t\right]\delta\ . \tag{4.8}$$

The operator $H[\mathrm{U}]$ conveys the contributions of the viscous shear, particle impingement, and the contact angle effect. The continuity equation is given as follows by inserting into Eq. (4.8):

$$\frac{\partial(\rho\delta)}{\partial t}+\rho\nabla.\left(\left[\frac{H[U]}{A_P}-\frac{\delta^2}{A_P}\nabla P_P-\frac{\delta P_p}{A_P}\nabla\delta-\frac{\delta}{A_P}\nabla P_u+\frac{\delta}{A_P}\rho g_t\right]\delta\right)=S_\delta\ . \tag{4.9}$$

4.3. Simulation setup

Fig. 4.1 (a) is a schematic representation of the electrostatic spray deposition process by means of an ERBS. Paint flow is stationary added through a small orifice in the center of the rotary bell cup. A robust axial force towards the workpiece deflects the paint particle movement's direction, which is produced by high-pressure shaping airflow that exhausts from ninety air nozzles. This shaping airflow modifies the spray pattern to ensure an axial flow towards the target with only low over spraying. Due to the rotary bell cup's high rotational speed and centrifugal force generation, the paint ligaments are formed and stretched radially on the inner surface of the bell cup. Then, these ligaments are disintegrated at the bell rim due to the high values of the relative velocity between the gaseous and liquid phases. The charged particles are driven towards the target by applying an electric force through an electric field among the high-voltage bell cup with the surrounding control-ring and workpiece.

Fig. 4.1 (b) indicates the typical automotive spray coating application. The procedure can be divided into the following distinguishable steps:

(a) The droplets atomization that is generated due to the film breakup over the rotary cup surface.

(b) High-speed shaping air jets, which impinge to the droplets and provide an extra momentum to direct them toward the workpiece.

(c) Charging of the atomized paint droplets by induction—connecting the cup and head of the ERBS to an electrical power supplier, and by corona— by placing a high-voltage control-ring field pattern around the sprayer, to increase the TE.

(d) A 3-D injection of the turbulent airflow from the upper section of the spray booth to control the over-sprayed flow and direct the droplets.

(e) Evaporation occurrence whenever the paint particle and film are exposed to the booth airflow.

(f) The paint droplets and film breakup process during the charged particles travel from the cup to the target and over the cup surface.

(g) The overspray phenomenon happens; due to the atomized droplet in the vicinity of the sprayer or close to the target that occurs due to the bounce-back of the droplets after hitting.

(h) Deposition on the target surface, the rate of this process depends on the droplets incidence angle, velocity, charge, and surface tension and wettability.

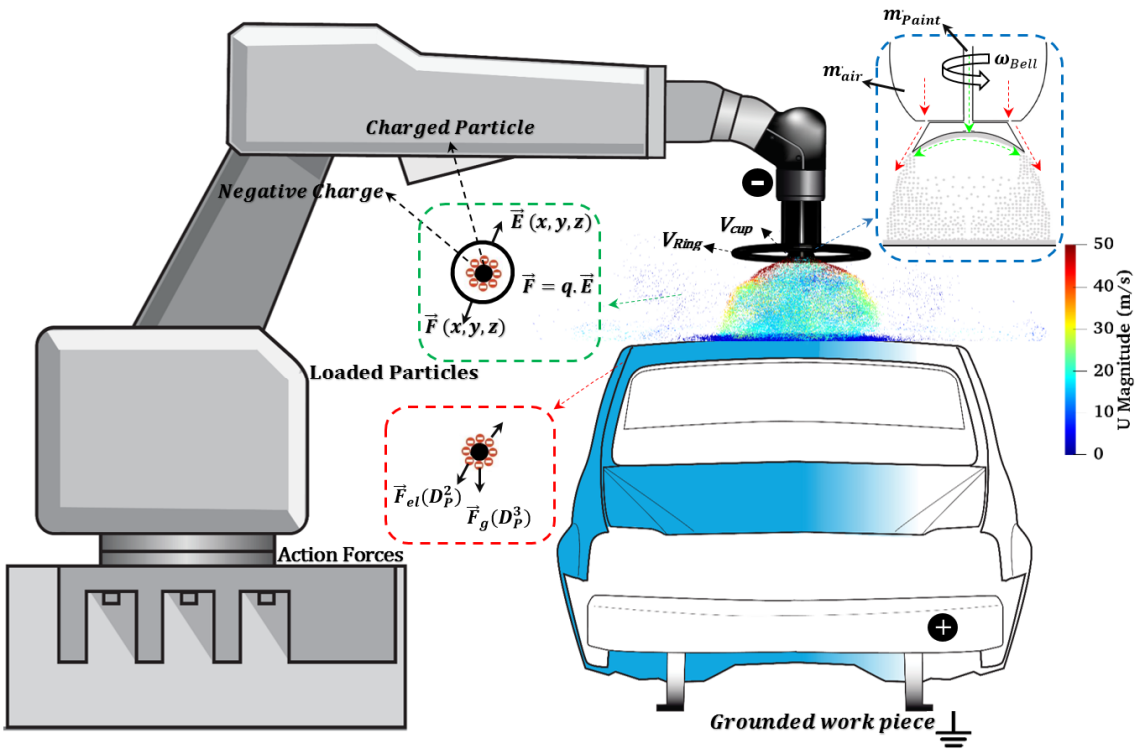

(a)

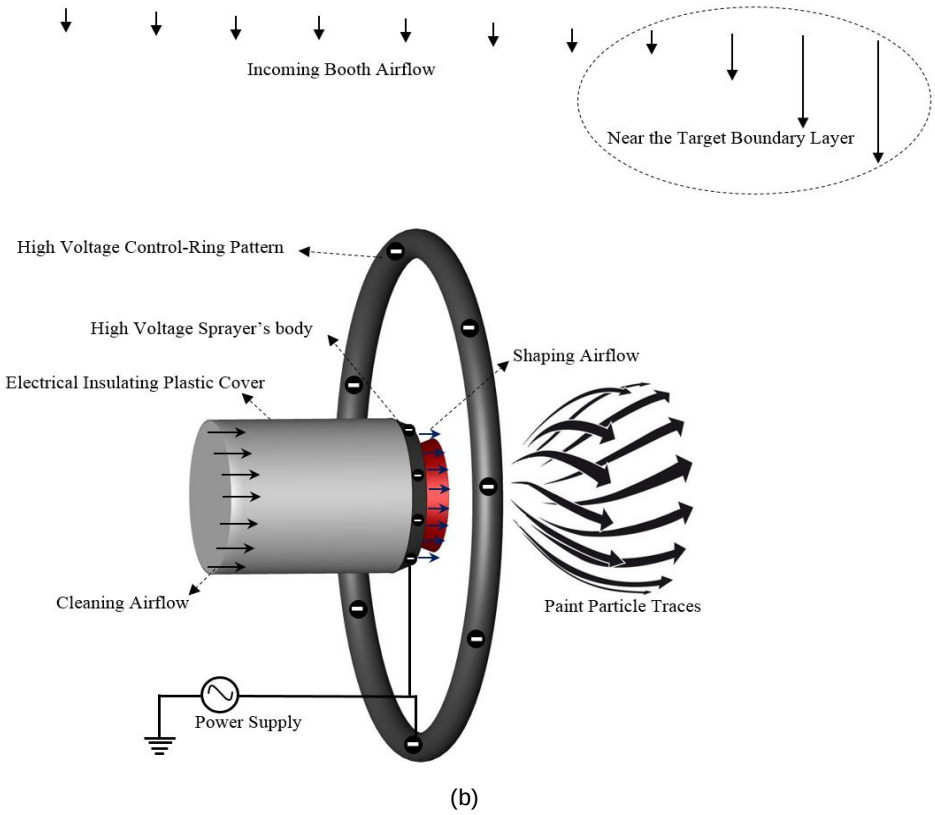

(b)

Figure 4.1: (a) Schematic representation of the electrostatic spray deposition process; (b) Schematic view of the automotive spray coating process, droplet atomization, induction and corona charging procedure.

An ERBS that was designed, developed, and is commercialized by SAMES (SAMES Technology, 2019) is depicted in Fig. 4.2. This is the ERBS that will be simulated and considered in this study using the OpenFOAM framework. A remarkable effort was focused on implementing a suitable turbulence model, as described in section 2. To obtain a proper time step, in order to ensure high accuracy results and simulation convergence, the maximum Courant number value is kept below 0.45 and a 5 $\times 10^{-8}$ s time step is then used. This value ensures that a sufficiently small period is used when capturing the details of the initial phenomenon that occurs in the ERBS. We verified that lower values of the Courant number do not change the simulation results. For all term computations, an upwind discretization scheme that yields a second-order spatial accuracy is used with a convergence target of 1×10^{-6}. The residuals of pressure and velocity reach around 10^{-8} and 10^{-9}, respectively. By examining the turbulent kinetic energy (TKE) power spectrum density (PSD) at a position close to the rim of the ERBS, the presence of the Kolmogorov power law-decay ($f^{-5/3}$) indicates the statistical scaling accuracy to evaluate the flow field inertial scales. Fig. 4.3 explains the dimensions of the computational domain and ERBS, and also the applied boundary conditions. In this study, an ERBS with a bell cup diameter of 65 mm is placed at the center of the cylindrical computational domain. The top boundary is modeled using the velocity inlet ($V = 0.3\ ms^{-1}$) condition, whereas all other sides of the computation domain are set to be at a stable atmospheric condition. The ERBS's surface, ring, and target are set as a no-slip

wall condition. Also, a moving wall boundary condition was set for the high-speed rotary bell of the sprayer. A specific value of potential ($\Phi = V_0$) is determined for the bell cup, ring and the retaining collar with the stainless steel material. The values of the potential in all other boundaries are set as $\Phi = 0$, as depicted in Fig. 4.3. The round boundary is set as a circle with a diameter of 40D, while the front and back are set as 15D and 25D away from the surface of the rotary bell cup, respectively, to ensure that the flow becomes fully developed.

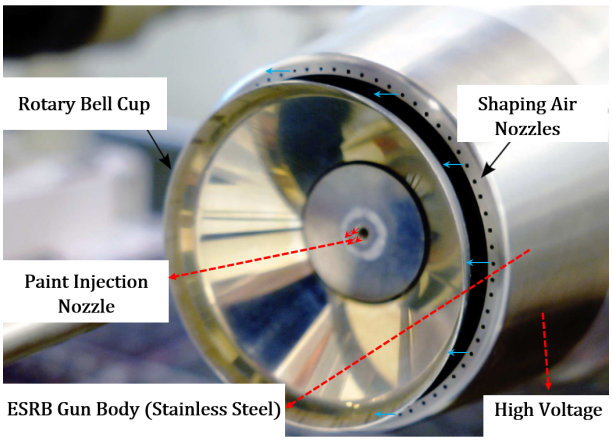

Figure 4.2: The PPH 308 high-speed ERBS photograph that was provided by SAMES-KREMLIN (Stevenin et al., 2015; SAMES Technology 2019).

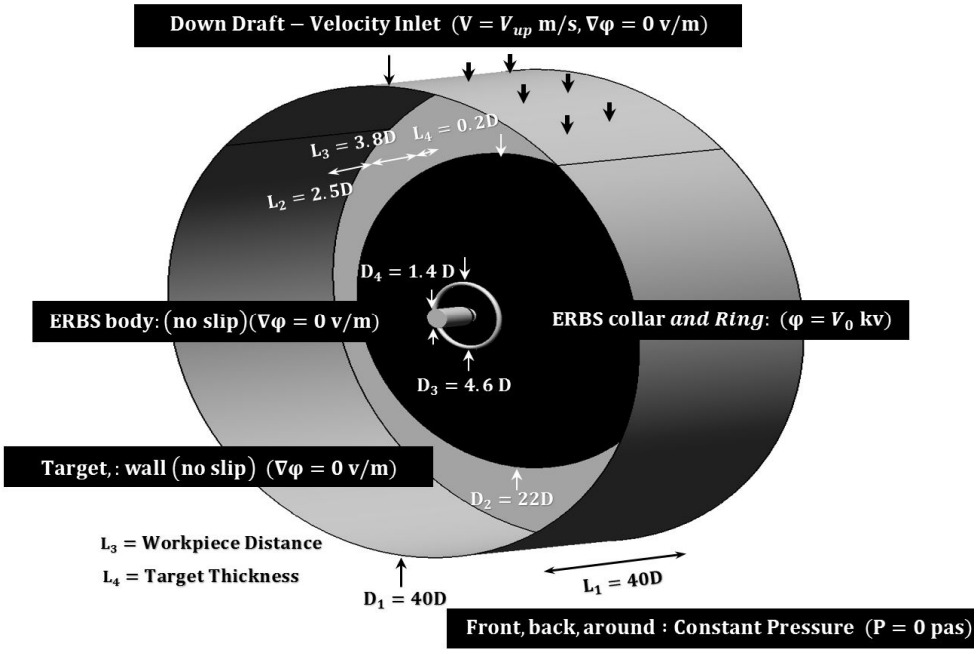

(a)

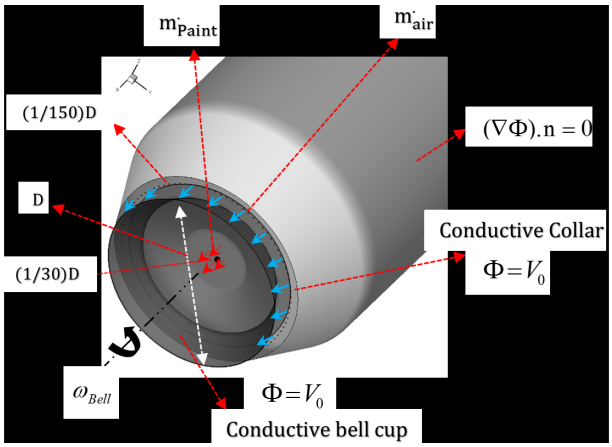

(b)

Figure 4.3: Detailed visualization of the computational domain dimension and the flow field boundary conditions: (a) overall computational domain; (b) close to the bell cup surface of the ERBS.

Fig. 4.4 displays a three-dimensional rendering of the sprayer structure, with the existence of the equipotential lines that demonstrate the constant voltage level in the computational domain, within a distance of 0.25 m from the nozzle of the sprayer to the target. In this area, a powerful electric force with dense electrical equipotential lines significantly accelerates the transfer process of droplets. At a scope outside of 0.25 m, the sparse electrical equipotential lines with very low electrical force values are visible, inducing a small effect on the droplets. The electric field's strength is inversely proportional to the distance from the ERBS, which is correlated with a greater spacing of equipotential lines in the weaker electric field strength regions. The use of a high-voltage control-ring that creates a field pattern around the ERBS is a novelty proposed in the present research (Fig. 4.4 (a)). This is to increase the efficiency of the electric field force on the atomized charged droplets that are to be transferred towards the target; as a result, the transfer efficiency (TE) increase that will be discussed in detail in the following section.

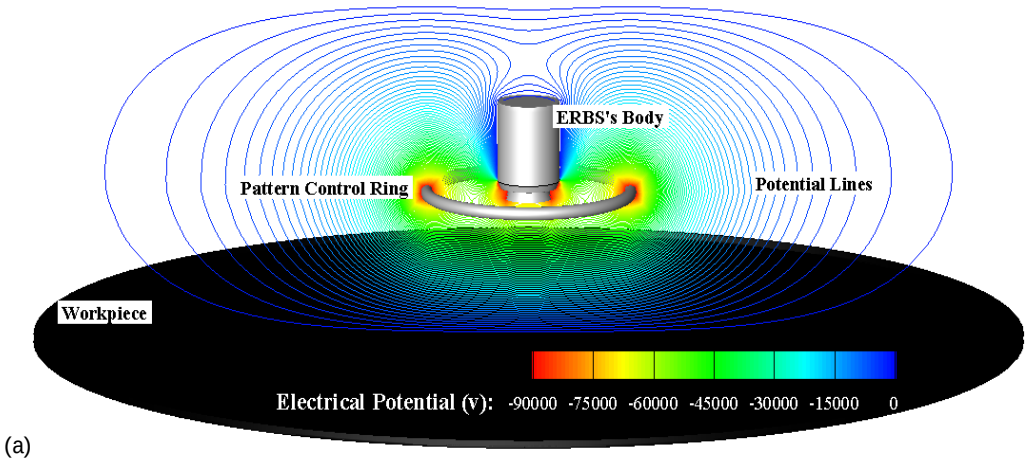

(a)

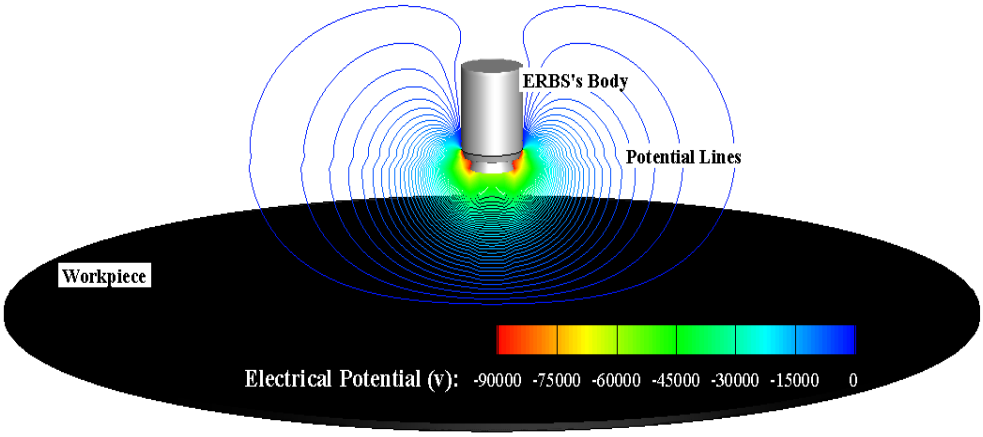

(b)

Figure 4.4: Visual representation of the electrostatic equipotential lines distribution around ERBS (a) with a surround control ring field pattern (b) without a spray control-ring.

A comprehensive representation of a computational grid for case (a) with and (b) without the spray control-ring is displayed in Fig. 4.5. The computational domain is produced with a fully structured quadrilateral mesh that is contained in a prism layer with a height of around 1.4×10^{-4} at solid boundaries. This height supports a y^+ value of less than 0.35 to accurately solve the boundary layer and capture the mechanisms of the high-Reynolds turbulent flow. The dimensionless wall distance is defined as ($y^+ = (u_\tau . \Delta y)/\upsilon$), where u_τ, Δy and υ are the friction velocity, the nearest distance to the solid wall surface and the kinematic viscosity, respectively. The domain is decomposed into a smaller sub-section to obtain more control over the grid size of the regions with a higher gradient, particularly near the sprayer. In order to perform a mesh independence study, three meshes with resolutions varying from coarse (5.5 million), medium (8.5 million) and fine (13.5 million) were generated with an $y^+ < 0.5$ in all three grids to capture the boundary layers adequately. Based on the evaluation of these three different grid sizes in our

previous study chapter 2, and by comparing with available numerical data and experimental results for the same simulation conditions, we concluded that a simulation using the medium mesh with an overall account of 8.5 million cells is adequate. Also, a mesh sensitivity study is conducted by considering the Kolmogorov power law-decay ($f^{-5/3}$) that also shows that the medium mesh is appropriate for the current turbulent flow regime. The total computational cost, in terms of simulation time, for the case when there is a control-ring pattern surrounding the ERBS, and for a voltage of -40 kV, is 774 hours when using 60 processor cores. Table 4.1 shows the parameters that are changed in the different cases for the current simulation. For simplicity water is used as the paint surrogate, a similar approach can be seen in Darwish Ahmad et al. (2019) and Viti et al. (2008), and a flat panel is used as the target surface. The atomized droplets are being broken during the spraying process and present a non-uniform distribution in what relates to the droplet diameter. Thus, the average computation of droplet size is relevant. For this goal, the Sauter mean diameter (SMD_{32}) (Eq. 4.10) is employed, defined as the diameter of a sphere that has the same volume to surface area ratio as a particle of interest.

$$\frac{D_{32}}{6}=\frac{V_m}{A_m}=\frac{\sum_{i=1}^{n}\frac{4}{3}\pi(d_p/2)^3}{\sum_{i=1}^{n}4\pi(d_p/2)^2}=\frac{\sum_{i=1}^{n}(d_p/2)^3}{\sum_{i=1}^{n}3(d_p/2)^2} \tag{4.10}$$

Table 4.1: Variable parameters in Electrostatic spraying simulation.

Constant (Units) (Symbol)	Range Explored
Bell-cup Rotational speed (RPM)(ω_{bell})	$10-55$
Cup voltage (kV) (φ_0)	$0-90$
Target voltage (kV) (φ)	0
Bell diameter (mm) (D)	65
Air viscosity(kg/m³/s) (μ)	1.8×10^{-5}
Air density(kg/m³) (ρ_{air})	1.225
Airflow rate (norm. l/min) ($\dot{m}_{air}$)	$150-500$
Paint density(kg/m³) (ρ_P)	998
Paint flow rate(ml/min)($\dot{m}_{paint}$)	$200-400$
Paint droplet size(µm)(D_p)	$5-75$
Charge-to-mass ratio(mC/kg) (ρ_m^q)	$-(0.5-6)$
Target distance (m) (L)	0.25

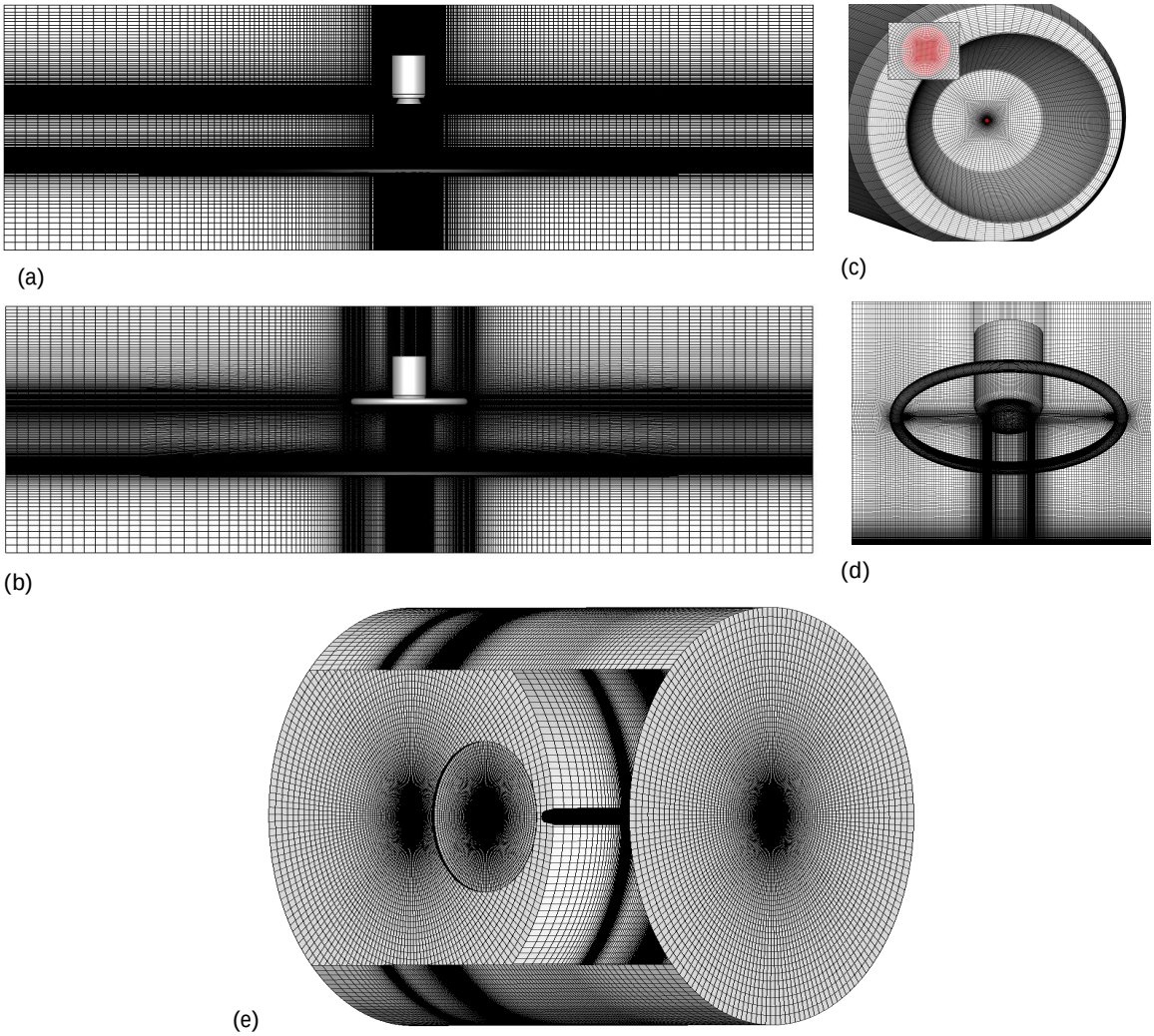

Figure 4.5: Illustration of grid distribution around the sprayer with and without the high voltage control-ring (a-e).

We will now demonstrate the proposed numerical solution's accuracy by comparing different experimental results with our work for the same operational conditions. In Fig. 4.6 (a), the shaping air flow subtended angle of our result is compared with the experimental results of Darwish Ahmad et al. (2018). The numerical angle is here 134.76° and is very close to the experimental one of 136° for the $\omega_{bell} = 50\,kRPM$. Fig. 4.6 (b) compares the computed velocity values, close to the rotary cup, with experimental data (Stevenin et al., 2015), and also an accurate prediction is observed. Fig. 4.7 (a) shows atomized paint droplets that are compared with the experimental result of Darwish Ahmad et al. (2018) obtained via an infrared thermographic flow visualization (IRFV) method, at a similar operational conditions. As the figure shows, the radial instabilities and the curvature of the spray plume, which was observed experimentally, are here appropriately captured. Fig. 4.7 (b) compares the current numerical result and the one of Shen et al. (2019) experimental snapshots in the paint film formation,

including its spiral distribution on the bell surface. An appropriate qualitative agreement is observed for the film distribution.

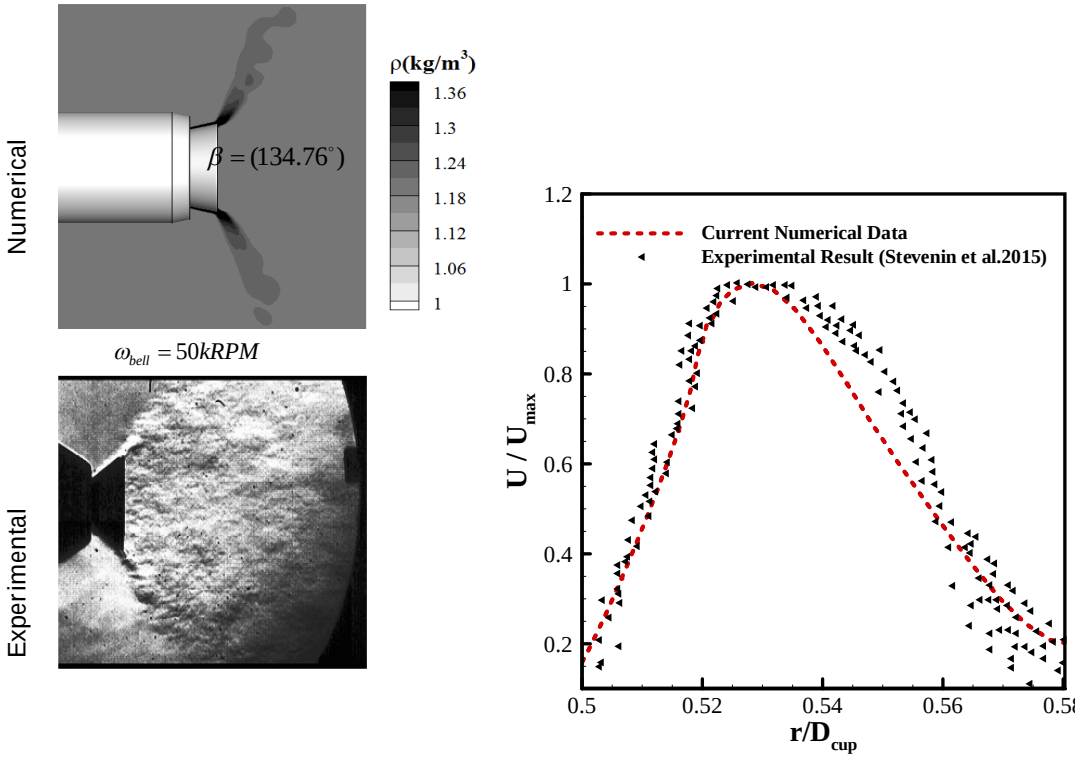

(a) $\dot{m}_{paint} = 0.1LPM$ (b)

Figure 4.6: Comparison of the airflow: (a) angle (Darwish Ahmad et al. 2018) (b) longitudinal velocity (Stevenin et al., 2015).

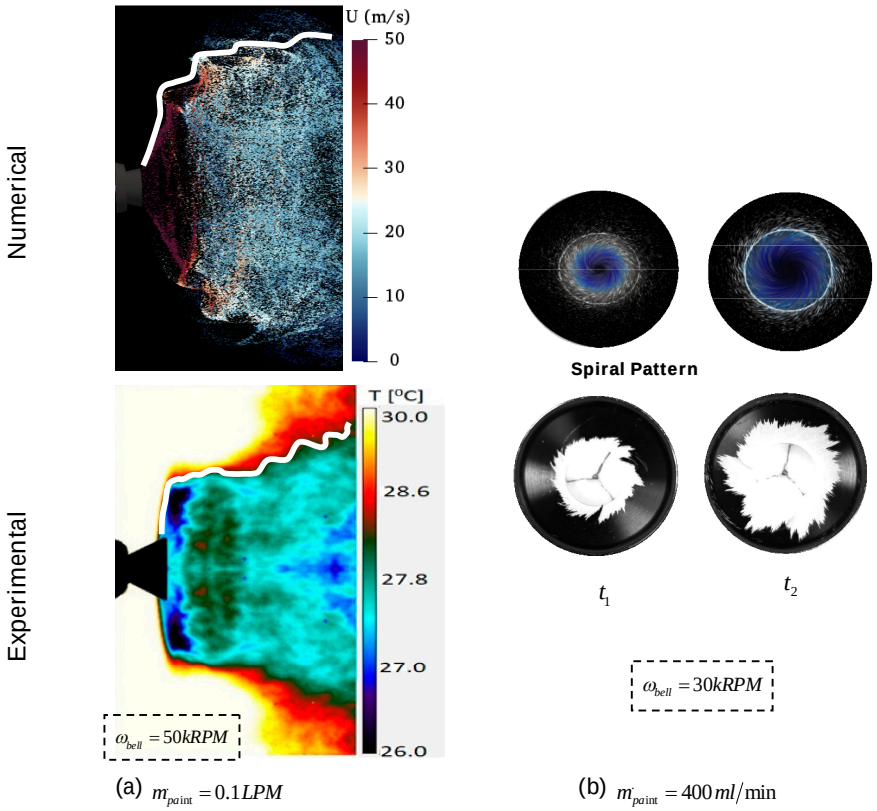

Figure 4.7: Comparison of the current numerical results with experimental data: (a) atomized droplet distribution (Darwish Ahmad et al. 2018) (b) paint film propagation (Shen et al., 2019).

4.4. Results and Discussion

The description of the time evolution of the droplet generation, deviation and trajectory behavior during a single complete coating process cycle is presented briefly in this section. Near the rotary cup surface, the larger paint droplets are flung further away from the ERBS before the aerodynamic drag force overcomes their initial high momentum, while the downward airflow immediately captures the very smaller paint particles. The presence of high-gradient turbulence flow, in combination with the droplet charge contribution to the electrostatic potential field, causes a high level of randomization in the droplets' trajectory. Near the stagnation point at the target surface, the droplets' trajectory behavior depends on their size is divided into two different paths. A large number of particles, due to the electrical force in combination with their momentum, deviate from the streamlines and move toward the target with a higher load near the center point. On the other side, some finer paint droplets are carried by the airflow streamline and form the overspray mass of droplets. This procedure will be discussed more in-depth in the following.

Here we consider the improvement that is provided by the charged droplets spraying by the ERBS with the presence of the high-voltage control-ring in comparison with the conventional

sprayers. As indicated in Fig. 4.8, there is a noticeable effect when using the control-ring field pattern around the ERBS. The spray plume shoulder curve and angle become narrower, due to a larger electric force, and this changes the droplet velocity produced by the presence of the control-ring. Also, the constructed spray plume diameter is smaller for the case with a control-ring field pattern ($L_2 > L_1$). The electrical force affecting the droplets in the vicinity of the ring is enough to guide more directly the workpiece's spray plume. The presence of the control-ring results in a more uniform coating thickness in a smaller area. In case b, the lower strength of the electric field, close to the applicator and target, exerts a smaller force on the charged droplet, and allows them to travel farther, producing overspray and a crawled rebounded torus-shaped. Also, the electric charge affects the droplet breakup process, in addition to the demonstrated significant change in the spray pattern.

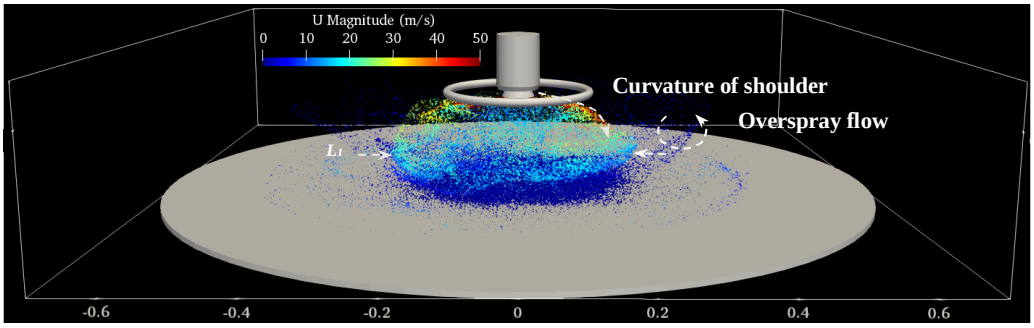

(a)

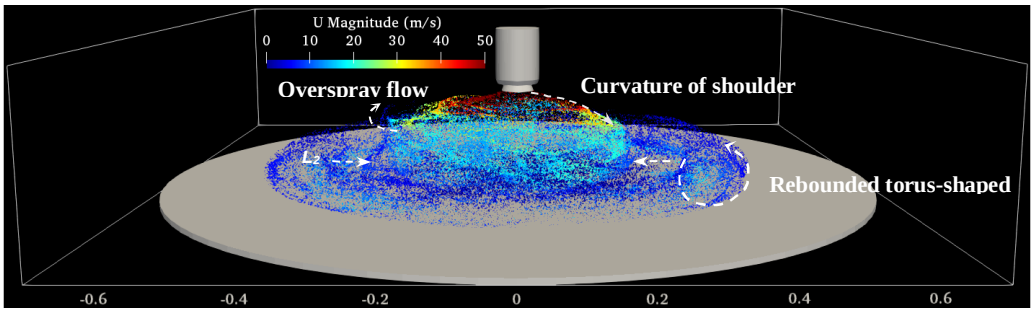

(b)

Figure 4.8: Comparison of the paint spray plume field (a) with and (b) without the presence of a control-ring field pattern. ($V_{cup} = -40kV$, $V_{Ring} = -40kV$, $\rho_m^q = -0.5mC/kg$, $\omega_{Bell} = 30kRPM$, $SF_{Droplet} = 200$, $t = 70ms$)

Fig. 4.9 illustrates 3D views of the sprayed droplets that are colored by their velocity, during the coating by the ERBS, with the presence of a control-ring field pattern for a broad range of voltages. The results predicted with the presence of the potential and electrostatic fields that are generated by the high-voltage surface and control-ring field pattern of the ERBS indicate a narrower spray plume and that more particles penetrate with larger velocity. At the same simulation time in different frames, at the higher absolute values of the negative voltage, the number of the paint particles that stick on the target is considerably more eminent and denser. In the case where the control-ring has a maximum voltage value of $V_{Ring} = -90kV$, the amount of

the droplets in the overspray and the rebounded torus shape vortex from the target is meager, and the painting reaches to the maximum transfer efficiency. Although the covered area is small in case (a), a higher density and better uniformity are obtained, this means a smaller number of droplets are wasted. In the mid-range voltage value for the control-ring ($V_{Ring} = -40kV$) and the surface ($V_{cup} = -40kV$), a higher amount of overspray is observed. However, the techniques of electrostatic painting with control-ring allow car manufacturers to reduce paint consumption, enabling them to optimize car paint operations, but the energy consumption (electric energy) is also an important factor to be considered. Therefore, although the maximum values of the voltage ($V_{Ring} = -90kV$) result in higher TE (as shown in Tab. 4.2), moderate voltage ($V_{Ring} = -40kV$) values have better efficiencies by consuming less paint and electric energy and by producing acceptable paint film with larger TE. In the zero value of the voltage, the number of droplets in the crawled rebounded torus shape vortex is significantly higher in comparison to the other cases that existing a voltage. Fig. 4.9 (e) shows that, without using a control-ring, a larger value of the torus shape vortex and an overspray flow are observed, if we compare to a similar case with the presence of ring (Fig. 4.9 (b)). As a result, the spray field pattern developed dramatically, by increasing the absolute value of negative voltage in the control-ring, and more uniform paint is obtained.

Table 4.2 reports the transfer efficiency values for the cases mentioned in Fig. 4.9 and 4.10. The transfer efficiency (TE) formula is computed as $\mathrm{TE} = (m_f - m_i) \times 100 / m_{out}$, where m_i, m_{out}, m_f are the initial sample mass, the paint exiting mass of the nozzle, during spraying, and the sample mass after coating and drying.

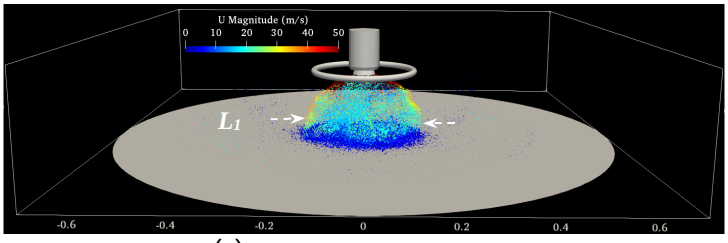

(a) $V_{Ring} = -90kV$, $V_{cup} = -40kV$

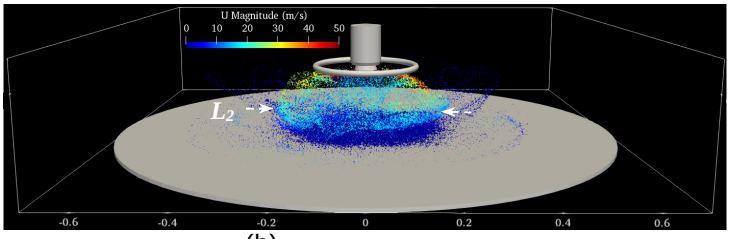

(b) $V_{Ring} = -40kV$, $V_{cup} = -40kV$

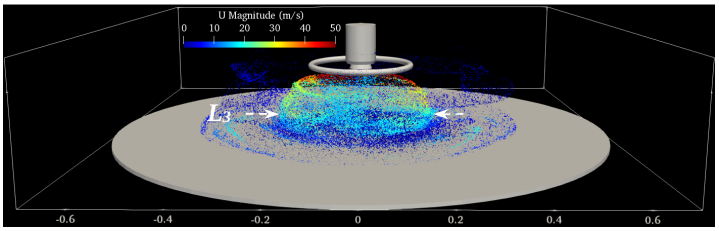

(c) $V_{Ring} = -20kV$, $V_{cup} = -40kV$

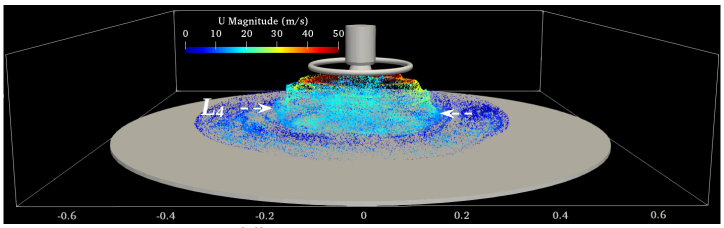

(d) $V_{Ring} = 0kV$, $V_{cup} = 0kV$

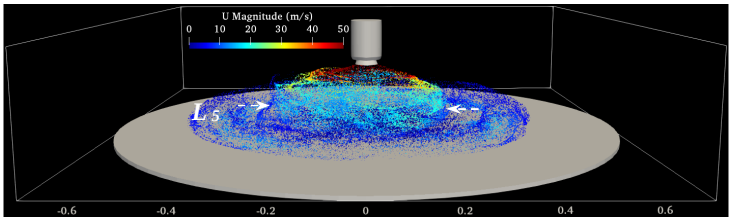

(e) $V_{cup} = -40kV$

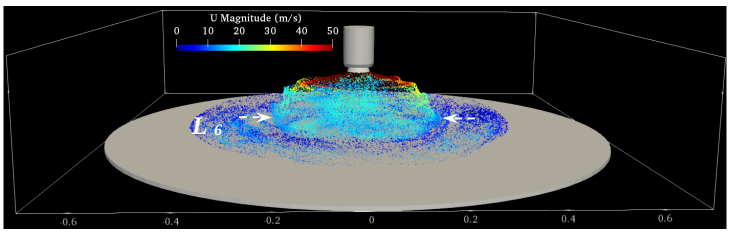

(f) $V_{cup} = 0kV$

Figure 4.9: 3D views of the paint spray field pattern for different voltages in the case in which the control-ring is present (a-f) ($\rho_m^q = -0.5mC/kg$, $\omega_{Bell} = 30kRPM$, $SF_{Droplet} = 200$, $t = 80ms$).

Here, the effect of changing the value assumed for the droplets charge (ρ_m^q), from a value of $\rho_m^q = -0.5 mC/kg$ (like around $q = -3.3\times10^{-14} C$ for the droplet size of $D_p = 25\mu m$) to $\rho_m^q = -6 mC/kg$ ($q = -2.0\times10^{-13} C$ for the droplet size of $D_p = 25\mu m$) has been examined. The atomized charged droplets, during the coating process, are affected by the local generated electric field, with the high-voltage control-ring and the sprayer between the ERBS and the target. The values of ρ_m^q have a considerable effect on the electrostatic spray plume formation and particle deposition. Our outcome shows that the charge in the range of $\rho_m^q \le -1.75 mC/kg$ is too high and do not allow the atomized paint to spray properly and causing dripping. As Fig. 4.10 indicates, droplets with weaker values of charge in face of the electric field allow some droplets to move towards the rear part of the pattern-field control-ring, due to the random action of large turbulent fluctuations. It can be clearly noted that the smaller droplets, with higher charge values, are more likely to be repelled through the cloud of space charges. In $\rho_m^q = -1 mC/kg$ the droplet pattern and film shape have an irregular and non-uniform distribution when compared to $\rho_m^q = -0.5 mC/kg$ (Fig. 4.10). The finding shows that the transfer efficiency (TE) increases as the exponent of the radius decreases or as the average charge to the mass ratio increases (as shown in Tab. 4.2). The last column in Tab. 4.2 indicates the coated area for the different operational conditions being presented in Fig. 4.9 and 4.10.

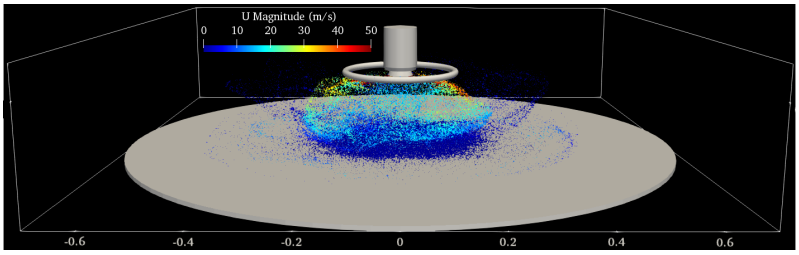

(a) $\rho_m^q = -0.5 mC/kg$

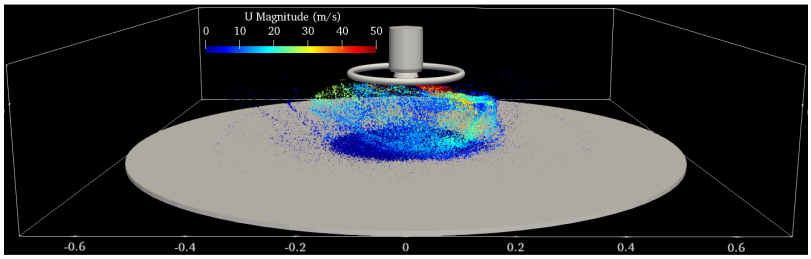

(b) $\rho_m^q = -1 mC/kg$

Figure 4.10: Comparison of different charge to mass ratio (ρ_m^q) for the atomized droplet (a, b).
($V_{Ring} = -40 kV$, $V_{cup} = -40 kV$, $t = 70 ms$, $\omega_{Bell} = 30 kRPM$, $SF_{Droplet} = 200$)

Table 4.2: Overall values of the Transfer efficiency (TE) for different cases.

$\omega_{Bell} = 30kRPM$	$\rho_m^q(mC/kg)$	Simulation condition $V_{Ring}(KV)$	Simulation condition $V_{cup}(KV)$	Transfer efficiency (TE)%	Coated area (m^2)
With Control-Ring	–0.5	-90	-40	80.78	0.053
		-40	-40	79.1	0.080
		-20	-40	77.40	0.094
		-20	-20	75.10	0.097
		0	0	49.10	0.110
	–1	-40	-40	82.78	0.066
Without Control-Ring	–0.5	-	-40	71.69	0.0824
		-	-20	64.28	0.099
		-	0	48.68	0.110

The longitudinal cross-sectional axial velocity contours of the airflow in the presence of streamlines (Line Integral Convolution (LIC) method) during the electrostatic spraying are shown in Fig. 4.11, for different operating absolute values of negative voltage. The airflow is accelerated near the surface of the bell cup and the central axis, and the velocity of the axial airflow can reach a maximum of $U_{X\,Max} = 179 ms^{-1}$. The airflow velocity decreases dramatically in the blocked area inside the rotary bell sprayer, and the axial flow direction is changed. Turbulence presence causes randomization in droplets' trajectory so that the flow pattern is not symmetric and the droplets, even with the same characteristics, do not follow the same path. The inner (V_1) and outer (V_2) vortices are depicted in the frames of Fig. 4.11. For the various values of absolute negative voltage that were examined the structure of the vortices has almost the same pattern, but the length of the recirculation zones is different. As shown in Fig. 4.11, by increasing the absolute values of the negative voltage, the recirculation zone length is reduced and the position of the attachment point, where the mean axial centerline velocity reaches to maximum values, moves upstream.

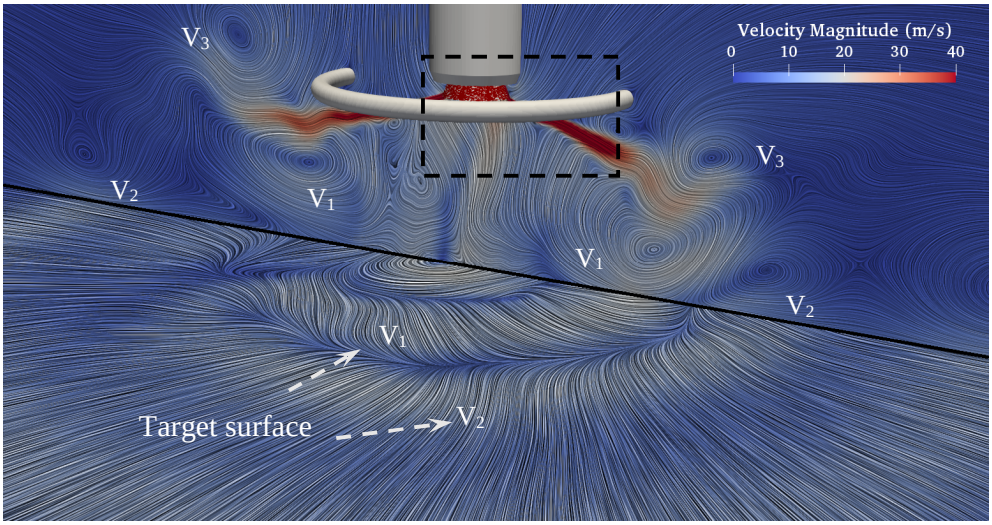

(a)

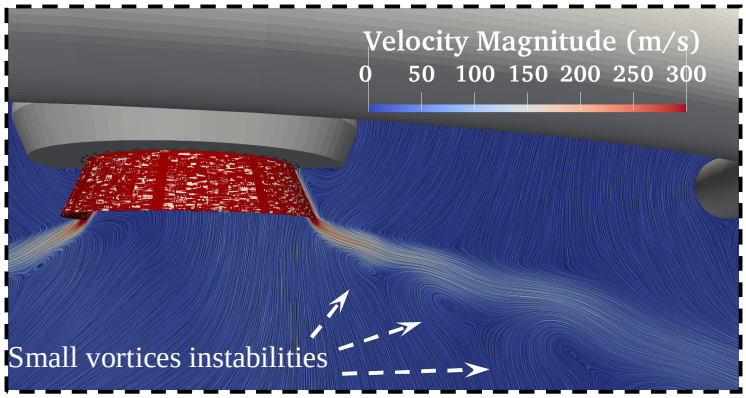

(b)

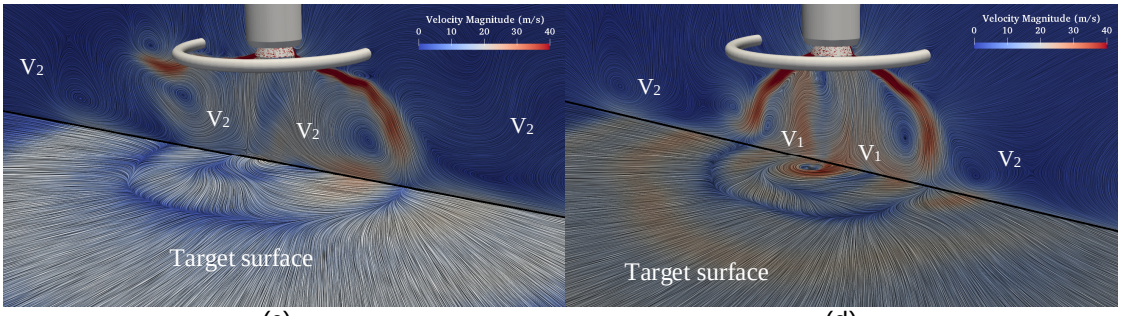

(c) (d)

Figure 4.11: (a) Flow velocity magnitude contour with streamline over the distance between the ERBS an target. (b) close-up vie near the rotary bell cup and control-ring surface ($\rho_m^q = 0.5 mC/kg$, $V_{Ring} = -40 kV$, $V_{cup} = -40 kV$, $\omega_{Bell} = 30 kRPM$, $SF_{Droplet} = 200$), (c) $V = -20 kV$, (d) $V = -90 kV$.

In Fig. 4.12 the coating deposition profile is shown for what corresponds to various voltage values of the bell cup and control-ring, and correspondingly different charged values of the droplets. All levels of voltage in these cases, under the presence of the control-ring pattern surrounding the ERBS, indicate a thick film deposition around the central axis of the workpiece; however, a small deposition is produced in the aforementioned area by using the conventional ERBS. Generally, the absolute values of negative voltage between the ERBS and target, especially when adding the control-ring, the most larger droplets inside the spray plume gain a higher driving force and sufficient power to disobey the inner vortex pattern and hit the central area of a hypothetical cylinder. Each of the deposition profile shows two peak thickness near the range of $d \approx 3R_{Bell}$ to $d \approx 4R_{Bell}$. These peaks draw a sinusoidal shape pattern with a trough in the deposition profile. In terms of the physics of fluids, the reason of this small trough is a change in the inner and outer vortex pattern direction for the spray curtain near the workpiece (V_1 and V_2 in Fig. 4.11). In other words, this position is the separation boundary point of those two mentioned vortexes. By increasing the absolute values of negative voltage, the paint film profile reaches a larger value and the constructed paint film's width becomes narrower. The most significant effect of implementing the spray control-ring field pattern around the ERBS is visible in the construction of the film deposition. For instance, at voltage values of $V = -40 KV$, the maximum film thickness reaches from $13 \mu m$ to $17 \mu m$, in the case without and with the use

of control-ring, respectively. During the painting process, when the constructed paint film's uniformity on the body surface is an important priority, applying higher values of the voltage is preferred. But, if the cost drives the painting procedure, applying smaller voltage values is less costly to operate, and is therefore suggested.

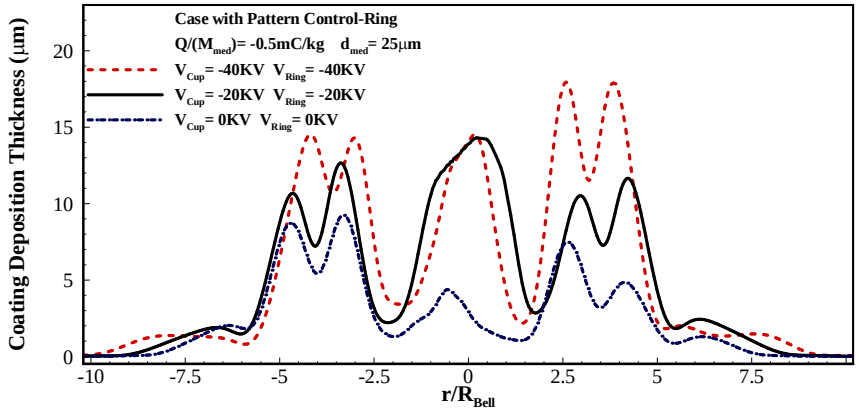

(a)

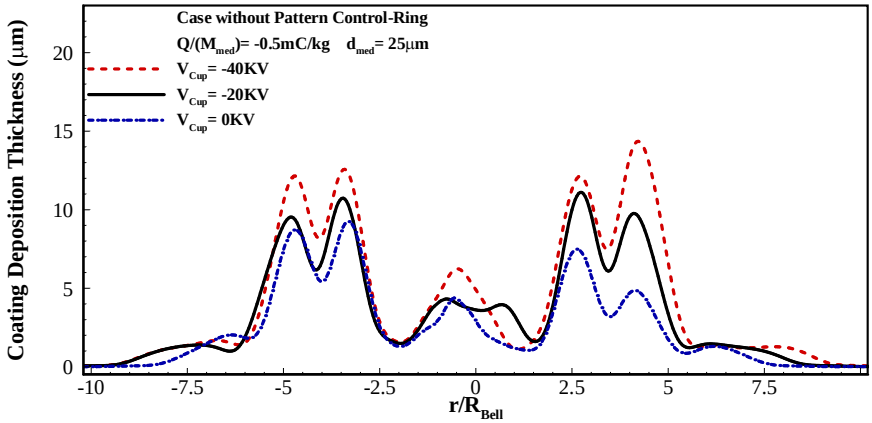

(b)

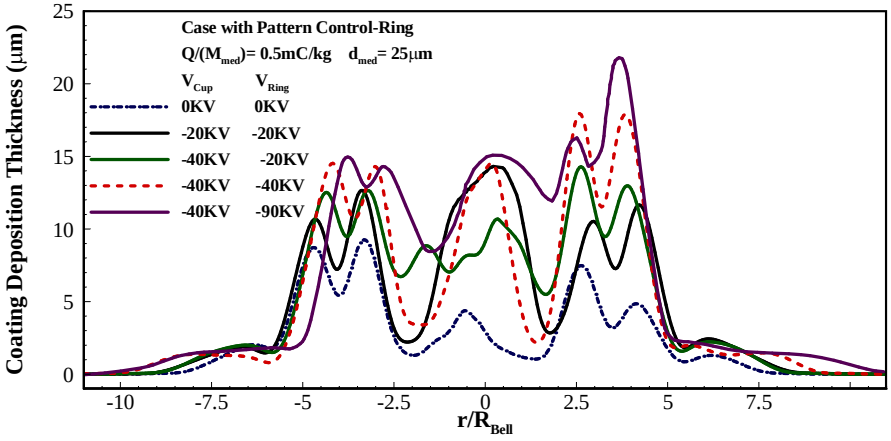

(c)

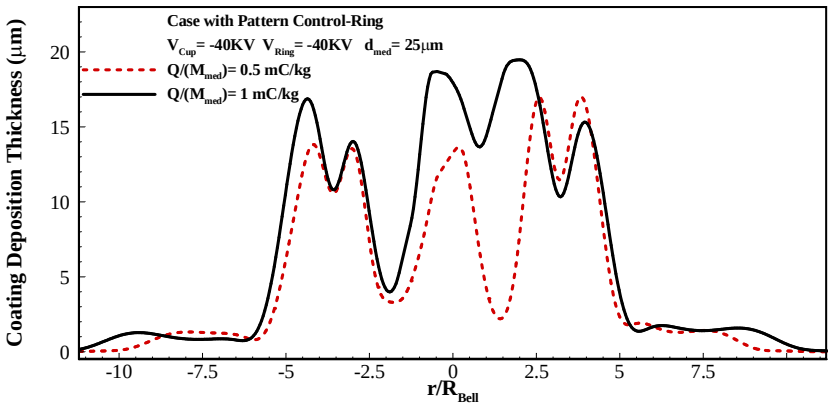

(d)

Figure 4.12: Bell-cup and control-ring voltage effect on the coating deposition pattern (a-c). Droplet charge values effect on the paint deposition distribution (d).

In Fig. 4.13 we analyze the influence of the droplet size distribution on; (a) a paint droplet sticks on the target (Hits) and forming a paint film or, (b) is missed and over-sprayed (Misses). Unlike the initial size distribution of atomized droplets that is exponential, the droplet size distribution pattern for the "Hits" group is Gaussian. Due to the disintegration, breakup, and evaporation process between the bell cup surface and the target, the droplet size distribution values for the "Hits" group are smaller than the initial size distribution. The “Misses” group of droplets exhibits a bimodal pattern, with two peaks in droplet size distribution. Droplets with lower diameter are dominated by their drag force and lack the mass needed to break free from the air vortex stream (Fig. 4.13 (d) P_1), swept away to the exhaust vent. This phenomena is responsible for the presence of the first peak. The second peak, with a larger size range distribution, is related to the droplets with a higher momentum that pass through the spray curtain. This most often occurs near the target surface. Due to the long-distance range of these droplets when reaching the surface, they lack the velocity to penetrate the high-speed airflow stream that occurs along the target surface. As a result, these paint droplets are also being swept near the workpiece (Fig. 4.13 (d) P_2).

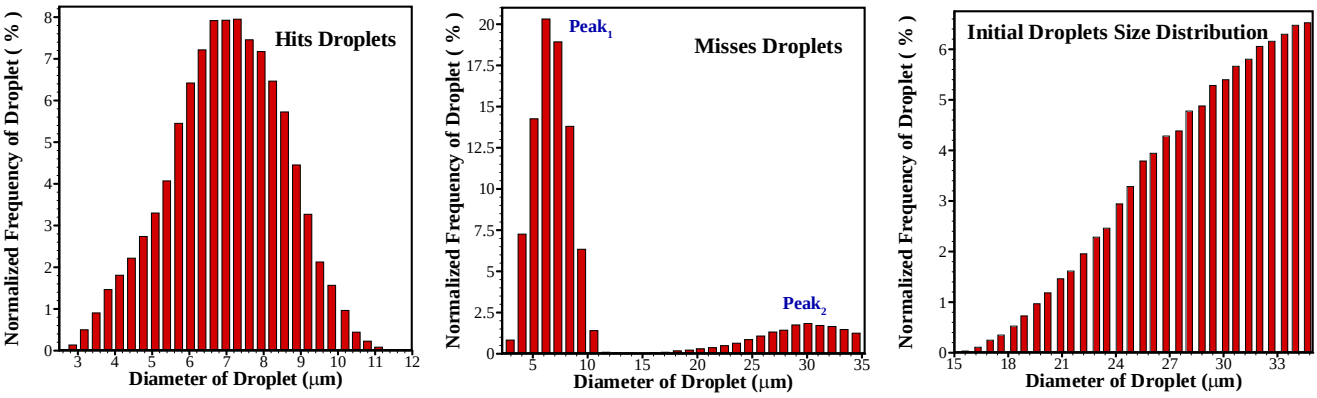

(a) (b) (c)

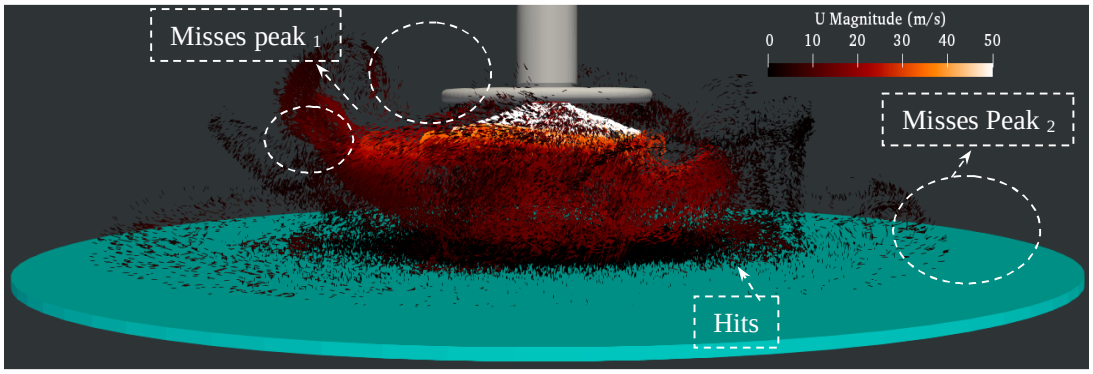

(e)

Figure 4.13: Droplet size distribution: (a) striking on the workpiece (b) missing the goal surface (c) initial size. (e) Position of these droplet over the domain.

The following vorticity transport equation is considered to clearly describe the connection between the paint droplet spray shape and the vortical flow structure:

$$\frac{D\omega}{Dt} = (\vec{\omega}\cdot\nabla)\vec{V} - \vec{\omega}\,(\nabla\cdot\vec{V}) + \frac{\nabla\rho\times\nabla p}{\rho^2} + (\upsilon+\upsilon_t)\nabla^2\vec{\omega} \tag{4.11}$$

Where $D\omega/Dt$ denote the rate of change of vorticity and the terms on the right-hand side denote the vortex stretching term $(\vec{\omega}\cdot\nabla)\vec{V}$, i.e., the stretching caused by the velocity gradients, the vortex dilatation term $-\vec{\omega}\,(\nabla\cdot\vec{V})$, i.e., the volumetric expansion or contraction in the flow that is proportional to the divergence of the velocity, the baroclinic torque $\frac{\nabla\rho\times\nabla p}{\rho^2}$, i.e., the misaligned density and pressure gradients and the viscous diffusion $(\upsilon+\upsilon_t)\nabla^2\vec{\omega}$, which is very small in high Reynolds number flows. All contours in Fig. 4.14 are plotted in five planes around the ERBS with and without the control-ring. The control-ring presence in conjunction with the droplet spraying induces a more considerable amount of vorticity in the flow field. In the contour of the vorticity magnitude (Fig. 4.14 (a)), inner and outer circular vorticity is larger in the case with a control-ring. Also, an irregular pattern of low-power vortices is formed around and above the control-ring. The vorticity production is restricted to inside and around the spray plume regions and is observed small in the other areas of the spraying computational domain. The vorticity dilatation (Fig. 4.14 (b)) due to the large volumetric expansions, especially inside the plume and near the target, spanned across the aforementioned area, with a considerable magnitude. In the current case, the vortex stretching magnitude is remarkable, because of the velocity gradient, can be seen mainly close to the rotary bell cup, being a little bit smaller than the vorticity dilatation. The vorticity stretching is continued even at farther distances away from the body and ring sprayer.

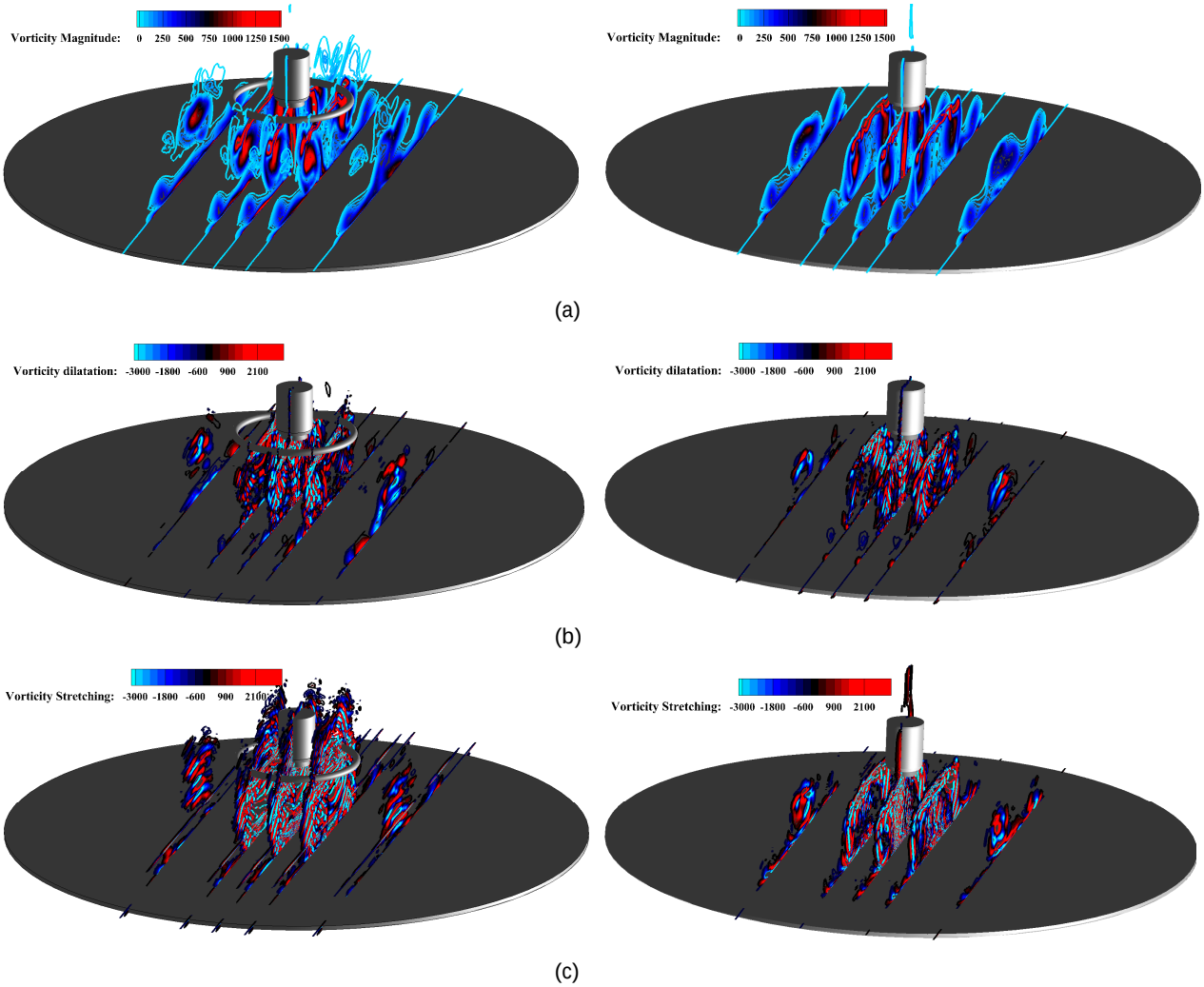

Figure 4.14: Distributions of the (a) vorticity magnitude, (b) vortex dilatation term, (c) vortex stretching term. ERBS with control-ring (left frames) and without control-ring (right frames). ($\rho_m^q = -0.5 mC/kg$, $V_{Ring} = -40 kV$, $V_{cup} = -40 kV$, $\omega_{Bell} = 30 kRPM$)

The film deposition pattern varied significantly across different voltage and charge density ranges. For $-40kV \le V \le -50kV$ and $\rho_m^q = -1.75 mC/kg$, the film deposition on the target achieves the maximum values of $A \approx 0.125 m^2$. The coated area is dramatically reduced by exceeding the voltage above $V_{Ring} \ge -60 kV$ and to larger values of the deposition density that are obtained at the center of this area. As shown in Fig. 4.15 for film distribution, for the $-20kV \le V_{cup} \le -40kV$, the paint deposition density is lower at the central areas. When the value of the voltage is set in the range of $-40kV \le V_{cup} \le -60kV$, the paint film deposition pattern becomes quite uniform and has moderate deposition values. The electrostatic spray atomization is more efficient in this situation.

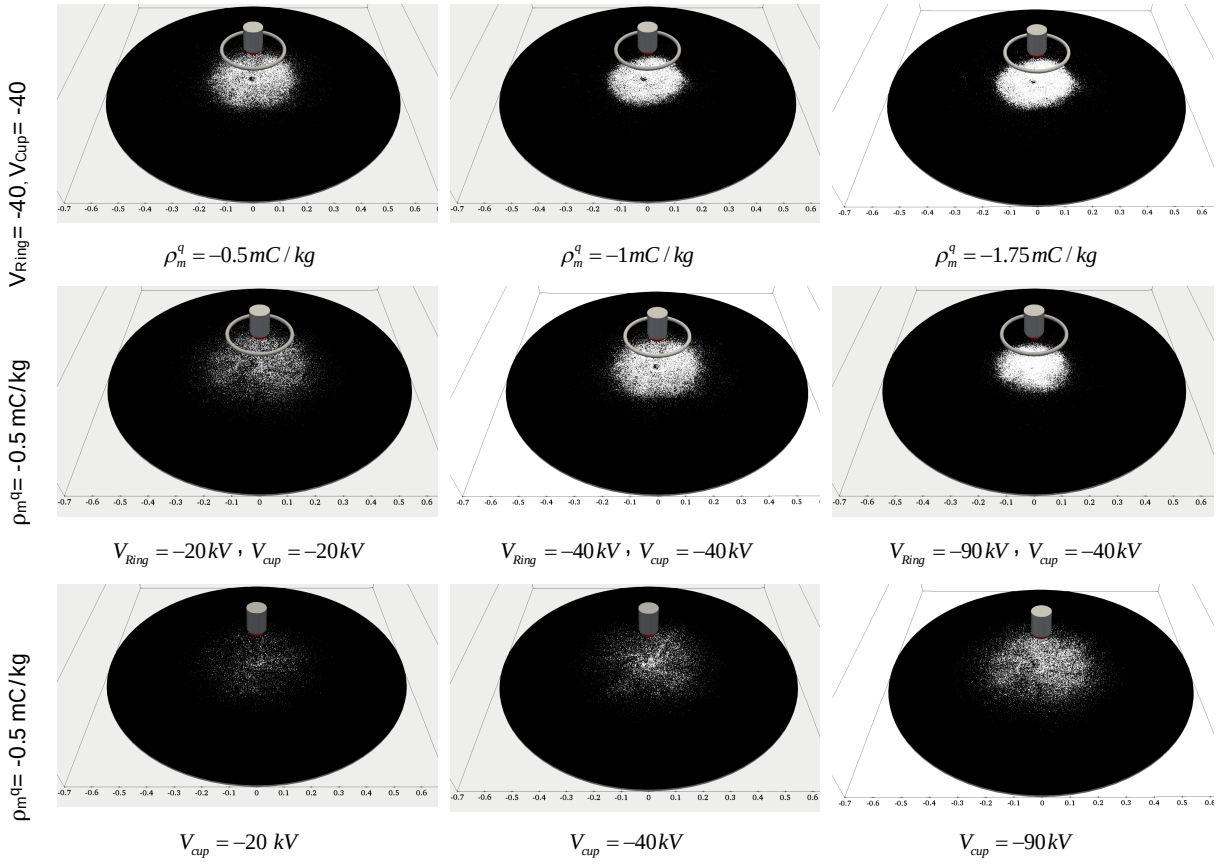

Figure 4.15: Deposited droplets pattern illustration on the target under different operating voltages and droplet charge ($\omega_{Bell} = 30kRPM$, $SF_{Droplet} = 200$).

The temperature of the atomized droplets along the spray plume and the airflow field along the vertical cross-section of the domain are examined in Fig. 4.16 and Fig. 4.17, respectively. The evaporating effects of the atomized droplet cause cooling of the surrounding air and result in a colder spray plume, especially in the cylinder region on the plume's central area. The temperature distribution of the spray plume is observed as being almost the same in all implemented cases of this work, since the cooling strongly depends on the evaporation that occurs before the saturation. Since the temperature of the air inlet, atomized paint and the target are all equal, then all the observed cooling near the target and the bell cup is fully attributed to the evaporation and rotational speed (ω_{bell}), respectively. Droplet collision on the target causes a significant temperature difference on its distribution (see Fig. 4.16 (b)). As Fig. 4.16 (c) exhibits, evaporative cooling happens immediately after the spray solution's existence inside the rotary cup. Fig. 4.18 shows the density of the atomized droplet during the coating.

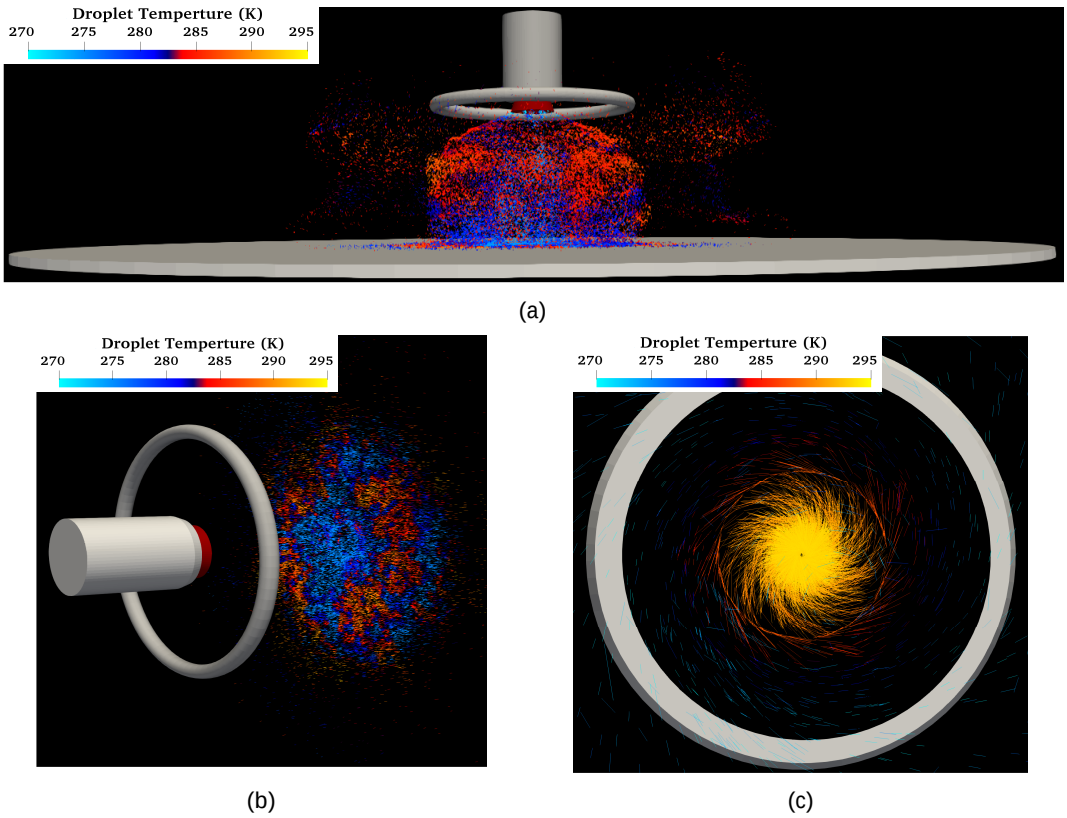

Figure 4.16: Droplet surface temperature (a) active droplets as a spray plum, (b) deposited droplets on the target surface, (c) inside the rotary bell cup.

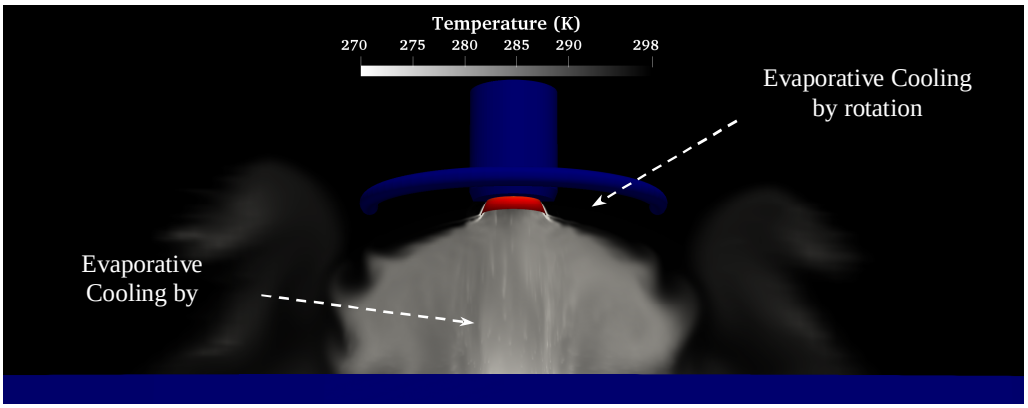

Figure 4.17: Airflow temperature visualization on the vertical cross-section of the domain during the coating process.

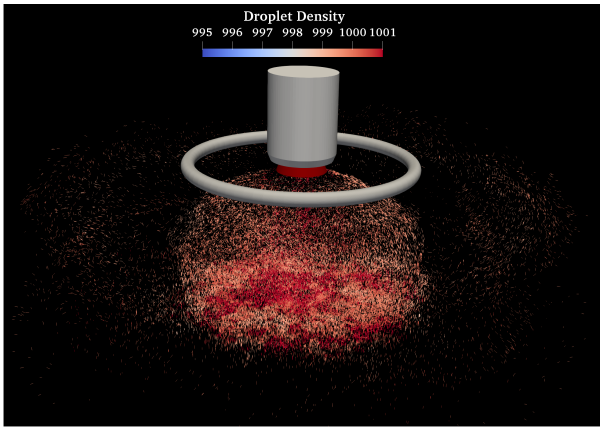

(a)

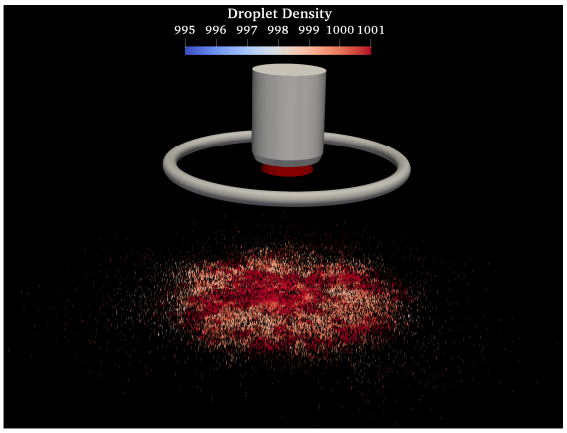

(b)

Figure 4.18: Densities of the atomized droplets during the coating: (a) spray-plume; (b) deposited droplet.

Figs. 4.19 and 4.20 discus about the constructed film after droplet hitting, sticking and spreading all over the target under various charges and voltages, with and without the presence of the control-ring, respectively. For better visualization, we magnified the film pattern on the target. The paint film deposition pattern on the workpiece indicates two concentric, non-homogeneous, high deposition rate rings. Under the presence of a large electrical voltage and droplet charge value, it is visible that a higher number of droplets start to divert from the flow path at the center regions of the paint film, near the stagnation point of the droplets. Paint droplets, particularly heavier ones, due to the guidance of the electrostatic force together with the momentum, are landing closes to the central point. The finer droplets are carried away by the air stream pattern. For the ERBS coating, most sprayed paint droplets hit the target with a transfer efficiency (TE) at least above 76.1% (as discussed in Tab. 4.2). The TE values are also affected by the various parameters.

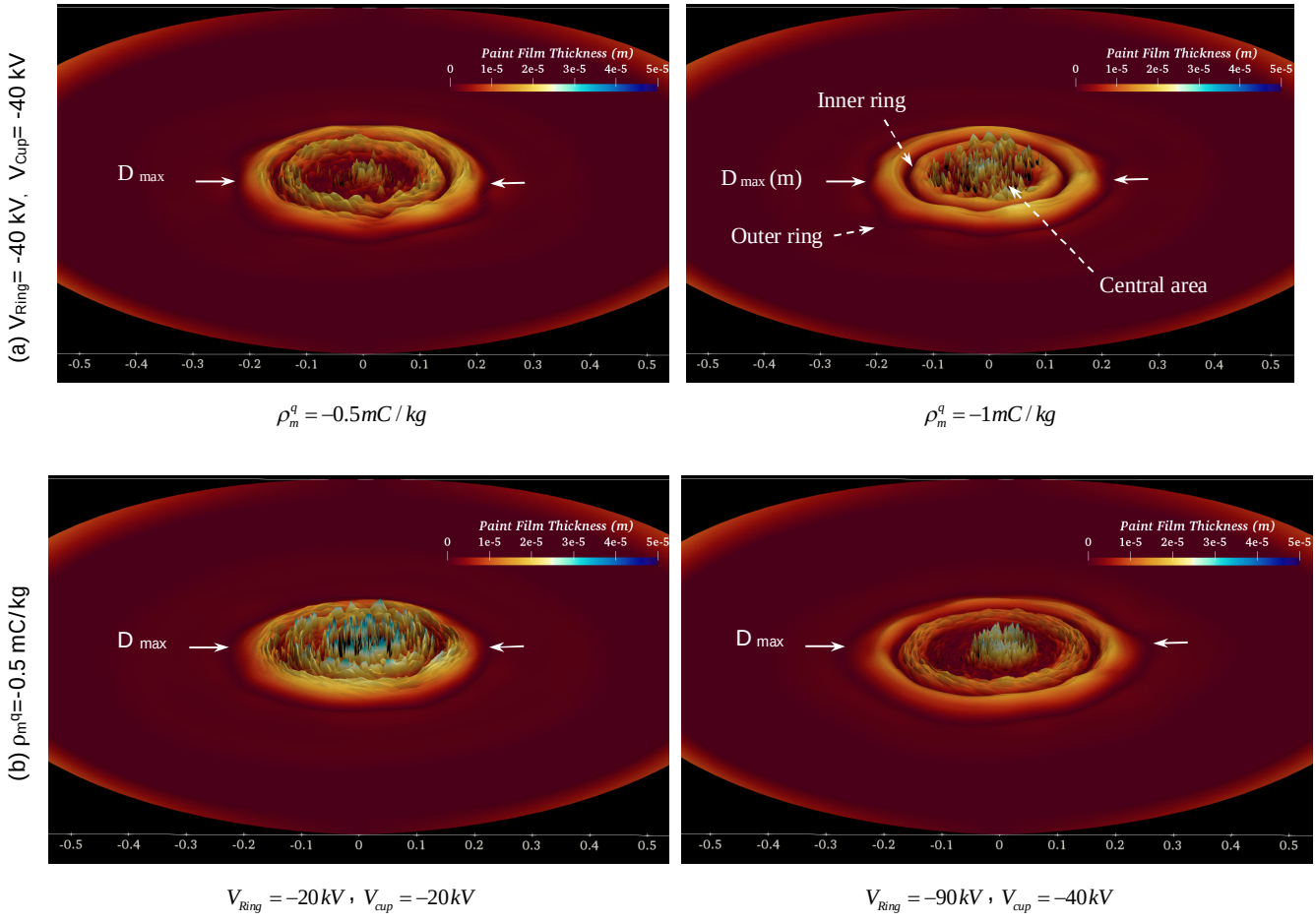

Figure 4.19: 3D paint film pattern visualization on the target, produced by the ERBS, with the control-ring field pattern for various: (a) droplet charges and (b) operating voltages.

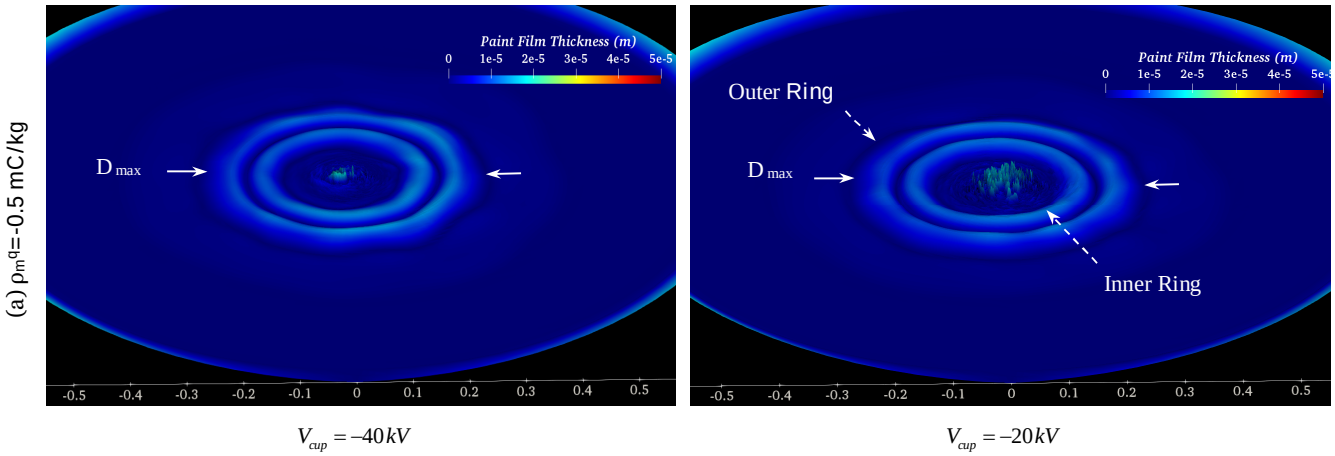

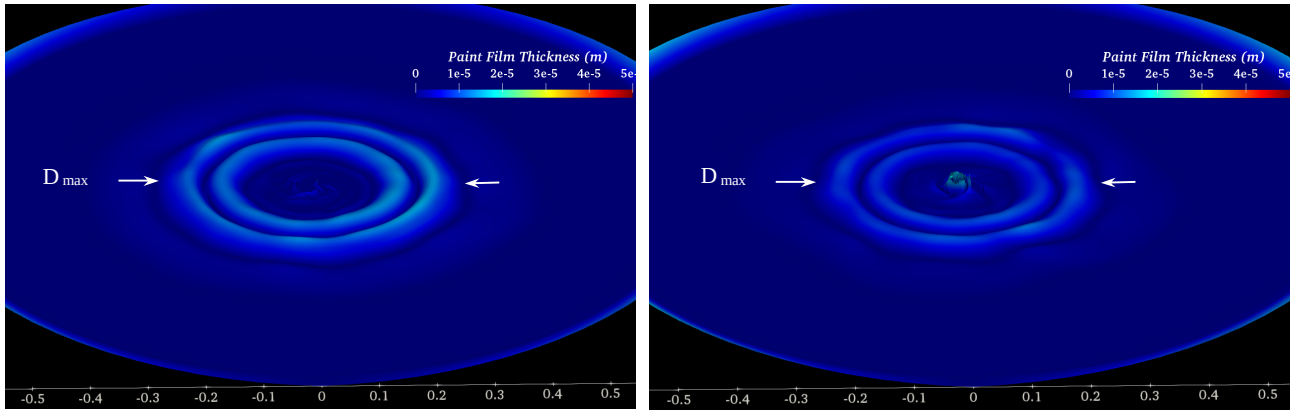

Initial Droplet size ($D_{average} = 75\mu m\ D_{\max} = 150\mu m\ D_{\min} = 15\mu m$)

Initial Droplet size ($D_{average} = 25\mu m\ D_{\max} = 35\mu m\ D_{\min} = 15\mu m$)

Figure 4.20: 3D deposition of the coating film produced by the conventional ERBS for different: (a) operating voltages; (b) initial droplet sizes.

As a pivotal factor in evaluating the paint film quality, the droplet size distribution formed during the electrostatic spray coating depends on the operating voltage. A discrete quantity, the probability density function of the electrostatic spraying paint particle size distribution, on the overall computational domain, under the different operating voltages, is illustrated in Fig. 4.21. Also, for easier understanding, the distribution of droplets colored by their size is presented in Fig. 4.23. For lower absolute values of negative voltage, the particle size distribution shows a bimodal form with an overall large droplet size distribution. The decrease in droplet size can be assumed to occur when higher voltages are applied, since this allows to easily overcome the surface tension of the droplets in comparison to lower voltage cases, thus causing a production of smaller initial size droplets. In this low electrostatic voltage value, due to insufficient breaking the atomization is not adequate. The paint particles are almost completely broken and the spraying efficiency increases by exceeding the operating absolute values of negative voltage higher than -40 kV. The droplet size, in the form of probability density function, exhibits a normal distribution that is consistent with the practical applications. The peak of the size distribution, corresponding to the droplet diameter, is reduced to the range of $5-7\mu m$. Therefore, due to the droplet breakup acceleration and their atomizing speed, we may conclude that electrostatic spraying around -40 kV achieves a higher transfer efficiency and spraying uniformity focused effect, and the electrostatic operating voltage can usually be selected within this voltage range.

Based on results of our numerical simulation, a growing voltage causes a slight increment in Sauter Mean Diameter (SMD_{32}) (as shown in Fig. 4.22). Higher voltages correspond to larger droplets, which deposit closer to the target center.

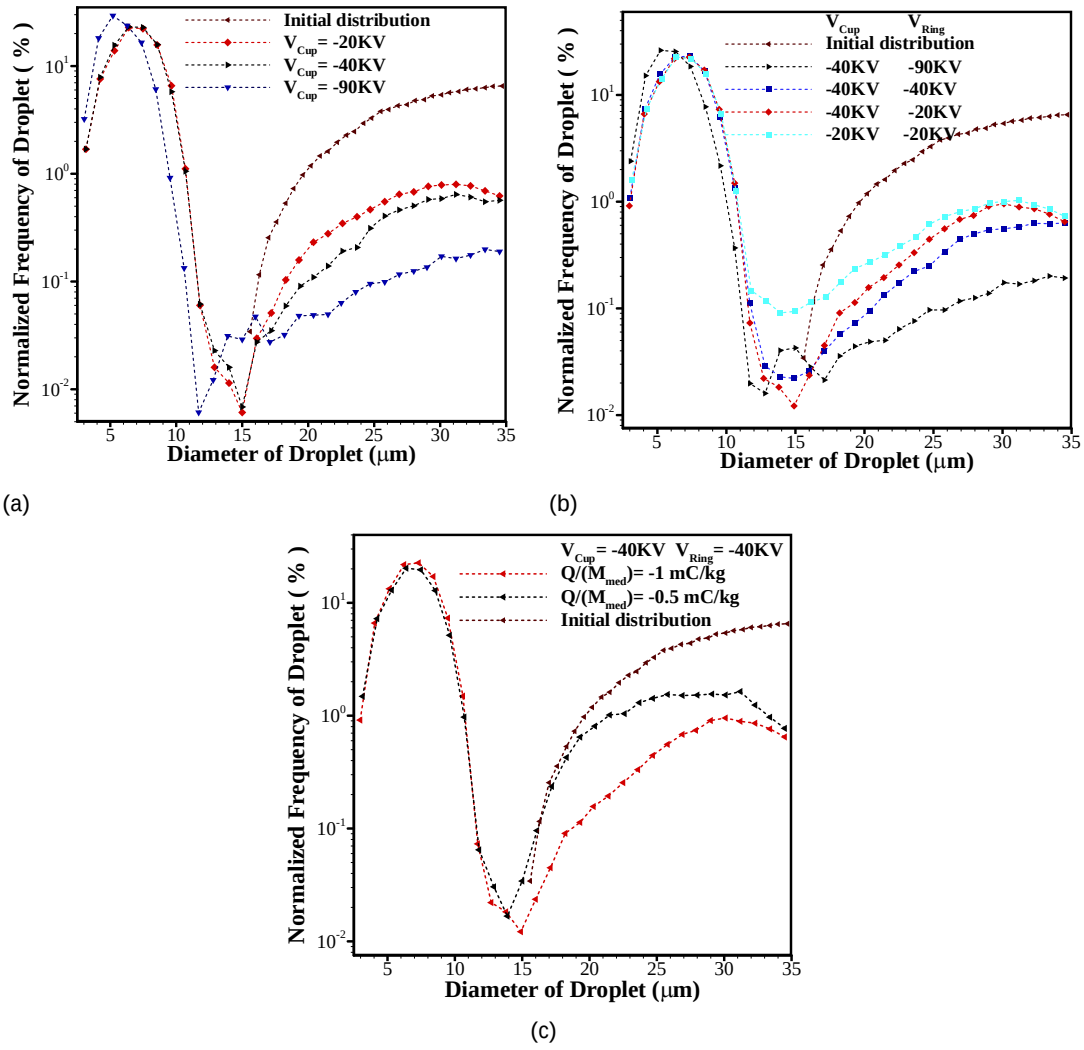

Figure 4.21: Paint droplet size distribution under various voltages (a, b) and charge values (c).

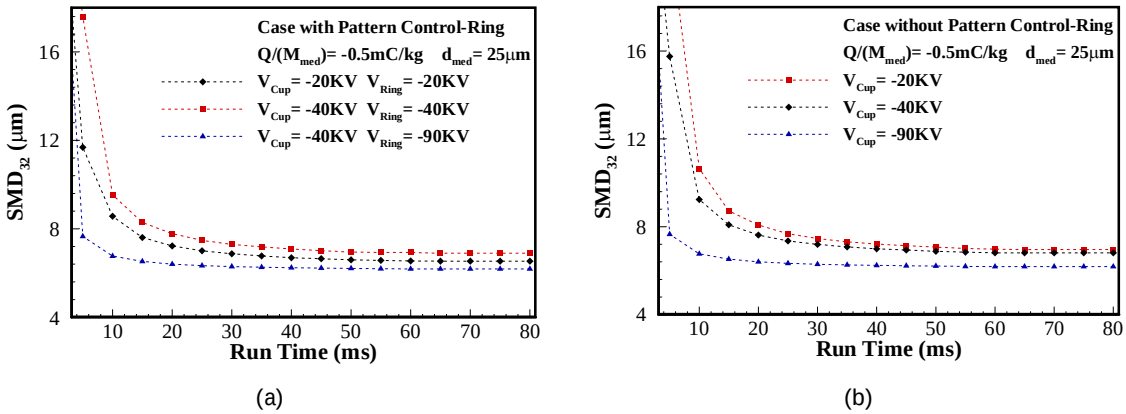

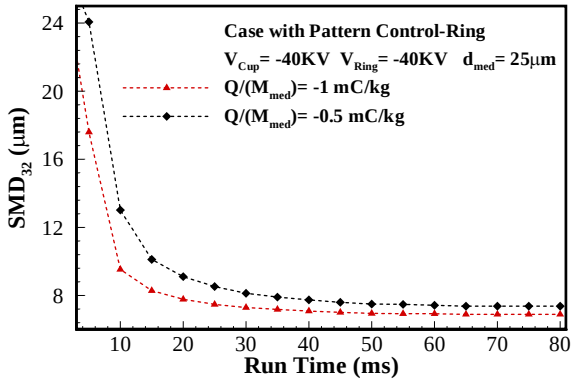

(c)

Figure 4.22: Sauter Mean Diameter (SMD_{32}) values at different: (a) bell-cup voltage; (b) control ring voltages and; (c) droplet charge values.

The droplet size produced during the electrostatic coating is mainly a function of the electric voltage, droplet charge, rotational speed and paint flow rate. The interaction of charged droplet size and position with the electrical field is illustrated in Fig. 4.23. The particle size distribution shows that the droplet diameter slightly reduces with the growth of the bell cup, control-ring voltage, and droplet charge. It must be noted that the effect of voltage on the droplet size distribution when compare with the rotational speed that was discussed in detail in chapter 3, is negligible. The results indicate that the shower of the charged droplets remain almost a hollow cone, and the larger size of the injected droplets exists around the outer region.

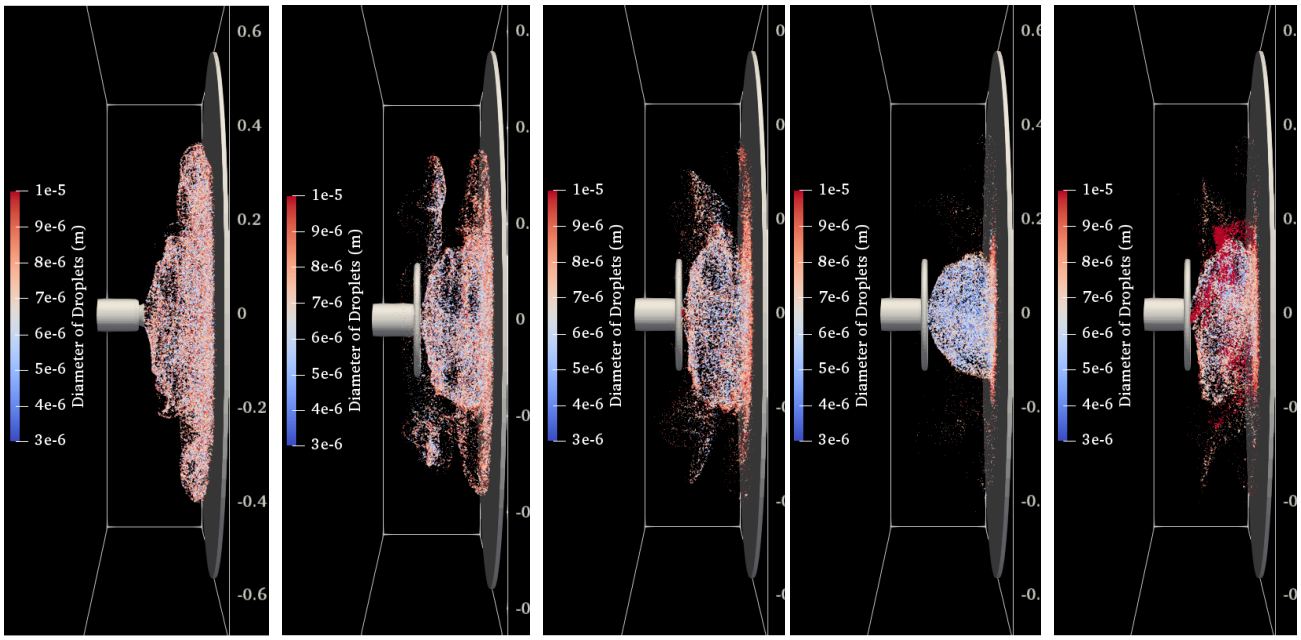

$V_{cup} = -40\,kV$ | $V_{Ring} = -20\,kV$, $V_{cup} = -20\,kV$ | $V_{Ring} = -40\,kV$, $V_{cup} = -40\,kV$ | $V_{Ring} = -90\,kV$, $V_{cup} = -40\,kV$ | $V_{Ring} = -40\,kV$, $V_{cup} = -40\,kV$

$\rho_m^q = -0.5\,mC/kg$ | $\rho_m^q = -1\,mC/kg$

Figure 4.23: Particle trajectories colored by their size at different voltage and charges.

4.5. Conclusion

A comprehensive numerical study of an ERBS has been conducted for different operational conditions. In doing so, a base code within the OpenFOAM framework is developed to capture the atomized charged droplet trajectory and paint film formation on the target. Here the focus is on flow physics by investigating the effect of the droplet size distribution, the applied voltage, and the ambient condition on the temporal evolution of the spray pattern. This work provides a thorough insight for the spraying industries on how to achieve higher transfer efficiency (TE) by manipulating the different operating parameters. According to the present simulation, the following conclusions have been drawn as the most important outcomes:

1- It is proved that using a high-voltage control-ring with the ERBS has a noticeable improvement on the overall spray plum pattern and film, e.g., producing a more uniform film, lower unfavorable overspray and a crawled rebounded torus shape, a narrower plum and more penetrations at higher velocities.

2- Although growing the control-ring voltage from -20 kV to -90 kV causes more paint droplet to stick on the workpiece, and produces a more eminent and dense film, but it has associated costs of larger energy consumption, therefore the moderate voltage of -40 KV is more efficient.

3- By adding a control-ring around the ERBS, the value of TE is enhanced by around 10 % (from 71.7% to 79.1%) when using a moderate voltage of -40 KV.

4- The values of ρ_m^q have a considerable effect on the atomized droplets. Results indicate that spraying with $\rho_m^q \approx -1 mC/kg$ allows to obtained the maximum values for the TE reaching 82.78%. Higher values of the negative charge ($\rho_m^q \leq -1.75 mC/kg$) have a negative effect on the TE value.

5- The deposition film profile shows a peak with a small sinusoidal pattern that is produced due to inner and outer vortex separation. Upon increasing voltage, and using the control-ring, the film profile reached a larger amount and became narrower.

6- By analyzing the droplet size distribution, it is shown that the values of voltage and charge are not so effective on the droplet size changing as much as the bell cup rotational speed and the paint flow rate. The particle size distribution slightly reduces with the growth of the voltage and charge droplet.

Chapter 5

Other useful applications of the implemented code: (I) Investigation of aerosol dispersion in the indoor work environment and (II) Numerical Investigation of Plasma Actuator Effects on Flow Control over a Three-dimensional Airfoil with a Sinusoidal Leading Edge [4]

Abstract

In the current chapter, some other useful applications of the implemented code are presented briefly. First, the modified spraying part of the code is used to precisely simulate the trajectory of the saliva droplets as an atomized droplets during sneezing, coughing, or even exhaling. Second, the implemend electrical field that added to code (just in the continuous field, not spraying electrical field) is considered without injecting droplets to accurately simulate the plasma flow that created due to potential difference.

(I) Aerosol dispersion investigation: Violent respiratory diseases, i.e., coronavirus (COVID-19), spread through saliva in cough, sneeze or even exhale in the form of microbial pathogen micro-droplets. Therefore, here a comprehensive fully coupled Eulerian-Lagrangian method has been applied for infection control, thus leading to a deeper understanding of the saliva-disease-carrier droplets transmission mechanisms, and also of its trajectory tracking by using the OpenFOAM package. This model determines the droplet–air interactions, the breakup process, and turbulent dispersion forces on each micro-droplet that is expelled within the respiratory tract in a correct way. By examining a broad range of initial velocity, size distribution, injection angle of saliva micro-droplets, and mouth opening area, we predict the maximum opening area that can be driven by micro-droplets. One important contribution of this work is to present a correlation for the length and width of the overall direct maximum reach of the micro-droplets, driven by a wide range of mild cough to intense sneeze. Our results indicate that the movement of the expelled droplets is mainly influenced by their size, angle, velocity, and environmental factors. During virus crisis, like COVID-19, this study can be used to determine the "social distance" between individuals to avoid contamination, by inhaling or touching their bodies, due

[4] Based on the work published in the International Journal of Physics of Fluids, https://doi.org/10.1063/5.0018432, and, SAE International Journal of Advances and Current Practices in Mobility, https://doi.org/10.4271/2021-01-0016, and also paper to Journal of Wind Engineering & Industrial Aerodynamics (Under Review).

to these saliva-disease-carrier droplets in sneezing, at various social distance positions like face-to-face, meeting standing, and near an equipment. The safe distance must be increased to around 4m during a sneeze. By wearing a face mask, and by bending the head during a sneeze as a protective action, we can reduce the contamination area to one-third and three-quarters, respectively. Furthermore, the dispersion of the film of the expelled saliva micro-droplets, and the spatial relationship between the subjects, that affects the airflow inside the room, are also analyzed in detail.

(II) The impetus of the present bio-inspired work is to investigate the impact of simultaneously using wavy leading-edge (WLE) airfoil in combination with curved multi dielectric barrier discharge (DBD) plasma actuator as passive and active flow control, respectively, to improve the performance of the wing, particularly at stall conditions. The distinction of produced frequency, noise signals, on the other hand, an acoustic effect of using WLE and DBD plasma actuators together are analyzed precisely. Two designed DBD plasma actuators are located at the $x/C = 3\%$ and $x/C = 30\%$ of the NACA 63$_4$-021 airfoil with sinusoidal WLE having a wavelength of 25% and an amplitude of 5% of the mean chord length and straight-leading-edge (SLE). We used a large eddy simulation (LES) turbulence model to solve the flow at considered chord-based Reynolds numbers and across a variety of angles of attack (AoA).
Here, detailed analyses of flow mechanisms at pre-stall and post-stall AoA, i.e., dynamic control of unsteady flow separation, 3D vortical structure and induced trains of vortices, aerodynamic forces, velocity variation, and spanwise flow, are addressed. The momentum transfer between the main flow and the boundary layer was improved by the induced trains of vortices due to the plasma actuators and the formed streamwise counter-rotating pairs of vortices over tubercle in WLE cases. Also, the continuous wavelet transforms (CWT) and fast Fourier transforms (FFT) methods are used to investigate the induced plasma flow spectral content under the influence of WLE and SLE geometries. Optimized flow control using DBD plasma actuators for the WLE airfoil resulted in less massive flow separation, faster turbulent transition and robust earlier flow reattachment. Also, this modification is very beneficial in increasing efficiency and decrease the noise for low Reynolds number operational conditions on wings and blade turbines.

5.1. Introduction

5.1.1. Aerosol dispersion investigation

A considerable number of respiratory infectious diseases like coronavirus, severe acute respiratory syndrome (SARS), Spanish flu (H1N1) and influenza are transmitted among humans through micro-droplets and airborne routes, endangering their lives (WHO, 2002). In 2019-2020, the coronavirus epidemic reached more than ten million infections and is known as the twenty-first century's most pandemic disease. In our modern world, infectious respiratory diseases like COVID-19 would cause many deaths, economic losses, and social disruption (Li et al., 2020). A deeper understanding of the dispersion and transmission mechanisms of saliva-disease-carrier droplets during our respiratory activity like, sneeze and cough, is needed to

control these infectious pandemics. Understand more about aerosolization and virus spreading is an essential issue for carrying out preventive measures such as social distancing, indoor ventilation and face masks wearing. Respiratory infectious diseases can be transmitted through direct contact with the expelled micro-droplets (Leder and Newman, 2005) or by indirect connections that occur when the micro-droplets have been deposited on the surface (Chao et al., 2008). Yan et al. (2018) concluded that the flu virus can be transmitted through emanated droplet during talking, or even by breathing. While the transmission mechanisms are still under debate, it is commonly accepted that respiratory droplet transmission induces a continued circulation of the influenza virus among individuals (Richard et al., 2020). Beans (2020) confirmed that SARS-CoV-2 can be spread via aerosolized droplets emitted by exhaling patients, although they noted that they've not be able to confirm if the coronavirus found in ambient air is a viable way to infect humans.

Following a brief introduction to the respiratory infectious diseases, we report thematically studies on the size distribution of saliva micro-droplet during different respiratory activity. Then, some relevant research will be explained in detail. Finally, the overall feature of the current study will be presented.

The findings indicate that the deposition and dispersion mechanisms of the expelled micro-droplets by patients are incredibly dependent on the droplet size (Chao et al., 2008; Wan et al., 2007). A substantial part of literature consideres the micro-droplet size distribution of expiratory and saliva in sneeze (Buckland and Tyrrell, 1964; Duguid, 1946), cough (Johnson and Morawska, 2009), talking (Xie et al., 2009; Chao et al., 2007) and breathing (Holmgren et al., 2010; Haslbeck et al., 2010; Almstrand et al., 2010). They confirmed that in various circumstances, the size distribution of micro-droplets is entirely different. Han et al. (2013) reported significant inconsistent values for the sneeze micro-droplet size in comparison with other previous studies. As a reason for these differences, they mentioned common problems that occur in earlier works like the effects of evaporation, the impact of the measuring method, and the experimental equipment error.

The turbulent flow mechanisms created during sneezing are considerably different from other respiratory processes and result in a very large size of the micro-droplets (Johnson and Morawska, 2009), i.e., the size of the micro-droplet in a sneeze is around eighteen times larger than cough (Gerone et al., 1966). Also, the velocity of the airflow that is exhaled by sneeze is higher than on cough or breath (Gupta et al., 2009; Gao and Niu, 2006). Studies of the sneeze micro-droplet size are still rare up to now. Xie et al. (2009) and Dbouk and Drikakis (2020a) discussed the micro-droplet size and mass during the conversation, cough, and sneeze. They corrected the size distribution of micro-droplets in line with the above-aforementioned work of Han et al. (2013), since they had noticed that it was underestimated in previous research work.

COVID-19 infections transfer at a faster rate due to the higher viral load in the respiratory tract of hosts, during breathing and social activities (Bai et al. 2020, Li et al., 2020). The lack of knowledge is evident in guidelines about the social distance and face mask-wearing (Elegant, 2020), mostly supported on outdated research (Asadi et al. 2020; Bourouiba 2020).

Dbouk and Drikakis (2020a) analyzed numerically the effect of wind speeds on the social distancing during the human cough. They found that the saliva droplets travel up to 6 m at a wind speed of 15 kmh^{-1} and a social distance of 2 m is not appropriate for outdoor environments. Blocken et al. (2020) studied COVID-19 virus spreading patterns in human subjects movement, like running and cycling, under external wind effects. They propose that larger social distances ($d \geq 1.5m$) must be preserved throughout the external activities. Bourouiba et al. (2014) described violent expiratory fluid dynamics of sneeze and cough. They predicted the pathogen range and introduced the fall out model. Zhao et al. (2005) reported a numerical analysis for droplet distribution during the sneezing process. They confirmed that droplets traveled longer distances during sneezing than breathing, and this poses an increased risk of human body SARS infection. Bhardwaj et al. (2020) investigated the drying time of respiratory droplets expelled from an infected COVID-19 person by evaluating droplet contact angle, volume, temperature and environmental humidity. They predicted that drying time is a crucial factor when infecting another subject, a diffusion limited evaporation approach for a sessile droplet on a partially wetted surface was implemented. Zhu et al. (2006) demonstrated that the transport characteristics of the saliva droplets, due to coughing in a calm indoor atmosphere are able to change with their size and can travel further than 2m. They further observed that the inertia and gravity of droplets with $d_p \leq 30\mu m$ in diameter is negligible. They found that droplets with size between $d_p = 50 - 200\mu m$ and $d_p \geq 300\mu m$ are significantly affected by gravity and inertia. Wan and Chao (2007) investigated the importance of the ventilation system on the infection risks by expiratory droplets. They revealed that unidirectional-upward and single-side–floor ventilation systems are more useful to mitigate the effect of small and large droplet distribution, respectively. Dbouk and Drikakis (2020b) studied the fluid dynamics of respiratory droplets induced by a mild incident of coughing around a face mask filter. They investigated the interaction modes, i.e., rebound, stick and penetration of saliva droplets onto the fibrous porous of the mask. They found that the travel distance of droplets by wearing a mask is about half of the distance when on naked face, and this distance becomes larger during incremental cough cycles. The LES approach is suitable for capturing flow features and for analyzing the internal flow principle, which is used in the current work (Roohi et al., 2016; Kolahan et al., 2019; Pendar and Roohi, 2015).

In our study and by using the OpenFOAM package, we modelled the size, velocity and spatial distribution of the expelled micro-droplet through sneezing and coughing. These findings are useful for effective prevention of infectious droplet-borne and airborne diseases, in particular coronavirus (COVID-19), by identifying the transmission processes in different places such as hospitals.

5.1.2. Flow control with DBD plasma actuators

Several passive and active flow control strategies have been used during the last few decades to improve performance by manipulating flow, i.e., advance/delay transition, enhancing/suppressing turbulence, or avoiding separation (Duvigneau and Visonneau, 2006;

Yagiz et al. 2012; Abdollahzadeh et al. 2018). Lift enhancement, noise removal, drag decrement, and optimization of the heat transfer can be listed as an example of benefits of utilizing these techniques (Harouni, 2014). The passive flow control methods mainly entail local vehicles' geometric modification with no auxiliary power demand; on the other hand, the active flow control systems can be turned on or off as needed and are more versatile.

Following, we present a review of literature on active flow control by implementing dielectric barrier discharge (DBD) plasma actuators, and then for the passive flow control with utilizing sinusoidal wavy leading edge (WLE) over airfoils.

The DBD plasma actuators, between various active flow control techniques have been become increasingly popular due to their unique advantages, i.e., fully electrical equipment, lack of mechanical components, fast-acting response times, wide frequency bandwidths, light weight, cheap cost of manufacturing, being entirely surface mounted of the vehicle without requiring complicated ducting, cavities or holes and low consumption of energy (Cho and Shyy, 2011; Ilieva et al. 2012; Morgado et al. 2015; Abdollahzadeh et al. 2016).

The use of high-voltage AC kilovolts at a frequency of kHz between the upper and lower electrodes of the DBD plasma actuator, which are separated by a dielectric material, ionized the air around the upper electrode, resulting in the formation of plasma. The charged species collision in weakly ionized plasma with neutral air molecules, momentum is transferred to the latter, resulting in a near-surface jet flow with velocity in the order of several meters per second over the embedded electrode (Moreau, 2007). On the initiation of the DBD plasma actuator, a generated starting vortex convects along the wall and leads to creation of a laminar wall jet (Jukes et al., 2006). As a result, the interaction of this jet with the external flow, i.e., energization of the boundary layer in continuous actuation mode or the natural airflow instability excitation in burst actuation mode.

Yu and Zheng (2020) offered a detailed flow resolution under DBD plasma forcing, utilizing alternating current (AC) and nanosecond (NS) over a pitching airfoil. Comparing the AC and NS plasma actuators' performances revealed that both achieve appropriate control authority for the moderate Reynolds flow. However, at high Reynolds flow, AC DBD has a small effect on the flow, whereas NS DBD achieves considerable success in aerodynamic forces improvement.

Implementing plasma actuators for controlling dynamic stalls, as an important cause of negative effect in engineering practice, has been an ongoing research topic in the past decades. Post and Corke (2004) analyzed the flow over an airfoil in a stall and post-stall regimes while using plasma actuators for flow control. They mentioned that the actuator's reattached flow resulted in significant suction-pressure recovery and drag reduction, resulting in a 400 % rise in the lift to drag ratio. After a while, they used continuous and pulsed AC plasma actuators to control dynamic stall over a periodically oscillating NACA 0015 airfoil with a Reynolds number of $Re = 7.6\times 10^4$. They found that AC plasma actuation can improve lift-cycle hysteresis and boost cycle-integrated lift (Post and Corke, 2006). Benard et al. (2009) examined the influence of the steady and unsteady plasma actuation over the airfoil. Their findings showed an improvement in aerodynamic forces, lift and drag coefficients, while the frequency resembles natural vortex frequency. Akansu et al. (2013) manipulated the separation of the flow around a NACA0015

airfoil by using four DBD plasma actuators at a low Reynolds number regimes. Several parameters, such as dielectric thickness, applied voltage amplitude and unsteady actuation had been considered in their experimental investigation.

According to a recent study by Guoqiang et al. (2019), AC plasma actuation results in a slight delay in the stall angle and a 7.1% increase in the lift coefficient for flow over a pitching S809 airfoil. They highlighted that AC DBD has a low induced jet velocity, limiting the device's application in a high-speed flow regime. They mentioned the best control authority occurs at the U_∞ = 10 ms^{-1} freestream velocity.

Based on general knowledge, DBD that includes ionic winds has broad range of applications, especially in aeronautics. The distinction of produced frequency, noise signals, and acoustic effects during the DBD plasma actuator's implementation in various operating conditions is an important factor in discriminating the flow, which is often ignored, and there are very few relevant investigations. Zhang et al. (2021) investigated the created acoustic streaming flow by DBD associated with induced ultrasound, utilizing particle image velocimetry. Their analysis of the pressure field, obtained from the highly sensitive microphone, revealed that the acoustic characteristics are divided into three stages of streamer discharge period, glow discharge period, and discharge quenching period in each cycle. Sato et al. (2020) performed large-eddy simulations of separated airfoil flows with control by a DBD plasma actuator over a broad range of Reynolds numbers to cover most of the conditions. They mentioned that the high burst frequency ($F^+ \simeq O\,(10)$) leads to early reattachment of flow due to turbulent transition promotion. Patel et al. (2008) reported that the optimum frequency of unsteady actuation is equal to $F^+ = 1$ ($F^+ = F_\beta C / U_\infty$). To obtain this optimum frequency, the actuator's voltage is changed until to when a sudden growth occurs in the lift coefficient. Mitsuo et al. (2013) showed that the unsteady plasma actuation frequency is one of the most critical factors in flow control authority. Their work indicated a frequency value of $F^+ \approx 0.5$, as an optimum burst modulation frequency. But, the experimental results of Sidorenko et al. (2007) conducted an optimum frequency for both burst modes of actuation and pulsed voltage around $F^+ = 2.6 - 14$. Wu et al. (2019) considered the mechanism and effect of the burst mode actuation in plasma flow, particularly the trains of vortices shed by this burst mode. Their results showed that the separation flow control under $F^+ = 10$ is the most effective, and the maximum reattachment of separated flow happens.

To improve the efficiency of plasma actuators usage, parameter optimization can be useful to achieve higher performances. Chernyshev et al. (2016) proposed a new design of multi DBD plasma actuators for flow control and boundary layer flow modification over a lengthy surface. Erfani et al. (2013) presented a new design for DBD plasma actuators with multi-encapsulated DBD electrodes to achieve higher velocities to generate more momentum. According to Tsubakino et al. (2007), the position of the plasma actuator has a substantial impact on the ability of flow control ability. Abdollahzadeh et al. (2012) shown that fixing the plasma actuator before the separation point, provides the best efficiency for flow control. The voltage waveform pattern has an impressive effect on the electric discharge and generated trust by the DBD

plasma actuators (Kotsonis and Ghaemi, 2012; Kimura et al., 2013). Zheng et al. (2016) described the generated repetitive vortices train moving downward and flow separation control by a DBD plasma actuator over airfoils near the stall or post-stall angle of attack. They considered the process of the flow control at a high Reynolds number of 4.63×10^5, at different actuation frequencies.

Chen et al. (2021) provided a new approach on separation control using the high-fidelity body force field with Drift-Diffusion (D-D) approach in an alternating voltage range of 7 kV to 20 kV. They employed LES to investigate the induced flow by DBD in quiescent air and over a stalled airfoil.

The concept of using a wavy leading edge (WLE) airfoil as an adequate passive control approach is inspired by the pectoral flippers of a humpback whale that enhanced its moving maneuverability. Using the WLE reduced the turbulence interaction and instability noise and eliminated the laminar separation bubble (LSB) over the airfoil (Chen et al., 2021). Miklosovic et al. (2004; 2007) studied the 3D bio-inspired wing with tubercled leading edge, based on the idealized flipper of humpback whale and compared with straight ones, for the first time. They observed that the stall angle was 40% delayed, maximum lift increased by 6 % and the drag values are significantly reduced by using the tubercled airfoil. Their finding attracts the attention of many researchers to work on this concept by considering the tubercled wing with different wavelength and amplitude in various Reynolds and angle of attack.

5.2. Governing Equations

5.2.1. Governing Equations for aerosol dispersion investigation

5.2.1.1. Continuous phase

For the carrier bulk multiphase flow, the mathematical formulations include a continuous and discrete phase. The compressible Navier-Stokes equations, in conjunction with a large eddy simulation (LES) turbulence model, are applied for modeling the flowfield. The continuity and momentum equations used in the LES model with Favre-averaging operation are defined as follows:

$$\frac{\partial \rho}{\partial t} + \frac{\partial (\rho \overline{u_j})}{\partial x_j} = 0, \tag{5.1}$$

$$\frac{\partial (\bar{\rho}\,\bar{\mathrm{u}}_j)}{\partial t} + \frac{\partial (\bar{\rho}\,\bar{\mathrm{u}}_i \bar{\mathrm{u}}_j)}{\partial x_j} = -\frac{\partial \bar{p}}{\partial x_i} + \frac{\partial \bar{\sigma}_{ij}}{\partial x_j} - \frac{\partial \tau_{ij}}{\partial x_j} + S. \tag{5.2}$$

S is used to denote other forces, such as surface tension and gravity, that are acting on the fluid. The subgrid-scale (SGS) stress tensor (τ_{ij}) is modeled by employing an eddy-viscosity approach.

$$\tau_{ij} \approx \rho(\overline{u_i u_j} - \overline{u_i}\,\overline{u_j}) \;,\; \tau_{ij} = \frac{2}{3}\overline{\rho k} I - 2\mu_k \overline{S_{ij}}, \tag{5.3}$$

$$\overline{S_{ij}} = \frac{1}{2}\left(\frac{\partial \overline{u_i}}{\partial x_j} + \frac{\partial \overline{u_j}}{\partial x_i}\right). \tag{5.4}$$

Here S_{ij} is defined as a rate-of-strain tensor for the resolved scale. We employed the "one equation eddy viscosity model" (OEEVM) subgrid-scale (SGS) in the current work. To obtain the turbulent kinetic energy (K), the OEEVM is solved as follow:

$$\partial\left(\overline{\rho} k\right) + \nabla.\left(\overline{\rho} k \tilde{u}\right) = -\tau_{ij}.\overline{\mathrm{S}_{ij}} + \nabla.(\mu_k \nabla \mathrm{k}) + \overline{\rho}\varepsilon, \tag{5.5}$$

$$\varepsilon = c_\varepsilon k^{3/2} / \Delta. \tag{5.6}$$

The SGS turbulent viscosity, μ_k, is calculated from:

$$\mu_{\mathrm{k}} = c_k \overline{\rho} \Delta \sqrt{k}, \tag{5.7}$$

, Here C_ε and C_k are set as 1.048 and 0.094 in the present implementation. The governing equations that are used in the current study are mentioned in detail in chapter 2. The saliva micro-droplets have interaction with the injected respiratory airflow, from the mouth, and with the ambient airflow.

5.2.1.2 Discrete Phase

The discrete phase that refers to the processes of dispersion of saliva droplets throughout the computational domain is solved as a series of differential equations using a Lagrangian approach. Through these differential equations, we compute the velocity, mass, and position of each individual droplet in each time step. The following equation for the saliva micro-droplet trajectory considers the effect of gravity, Stokes drag, added-mass force, and pressure variation:

$$m_p \frac{\partial \vec{u}_p}{\partial t} = \vec{F}_G + \vec{F}_D + \vec{F}_M + \vec{F}_P = (\rho_P - \rho_f) V_P \vec{g} + \frac{3}{4} C_d \frac{\rho_f}{\rho_P} \frac{m_P}{2R_P} \left|(\vec{u}_f - \vec{u}_P)\right| (\vec{u}_f - \vec{u}_P) + \frac{\rho_f V_P}{2} \frac{\partial(\vec{u}_f - \vec{u}_p)}{\partial t} + V_P \nabla P \tag{5.8}$$

Here $\vec{u}_p$ and $\vec{u}_f$ are the saliva particle and fluid velocity vector, respectively. Also, ρ_f and ρ_p are the air and particles density, V_p, R_P and m_p are the volume, radius, and the mass of the saliva particles, respectively. The values of the drag coefficient C_D, which depend on the droplet's Reynolds number, is given by:

$$C_D = \begin{cases} 24/\mathrm{Re}_P, & if \quad \mathrm{Re}_P < 1 \\ (24/\mathrm{Re}_P)(1+0.5\,\mathrm{Re}_P^{0.687}), & if \quad 1 \le \mathrm{Re}_P \le 1000 \\ 0.44, & if \quad \mathrm{Re}_P > 1000 \end{cases} \tag{5.9}$$

$$\text{Where} \qquad \mathrm{Re}_p = \frac{2\mathrm{R_p}\left|\vec{u}_f - \vec{u}_p\right|\rho_f}{\mu_f}, \tag{5.10}$$

Here $\vec{\mu}_f$ is the fluid viscosity. The final expression of Eq. (5.8) is written as follow:

$$\frac{\partial \vec{u}_p}{\partial t}\left(1+\frac{\rho_f}{2\rho_p}\right) = \frac{3}{4}\frac{C_d}{2\mathrm{R_p}}\frac{\rho_f}{\rho_p}\left|\vec{u}_f - \vec{u}_p\right|(\vec{u}_f - \vec{u}_p) + \left(1-\frac{\rho_f}{\rho_p}\right)\vec{g} + \frac{\rho_f}{2\rho_p}\frac{\partial \vec{u}_f}{\partial t} + \frac{\nabla P}{\rho_p}. \tag{5.11}$$

Disease transmission by larger saliva-disease-carrier droplets is certainly more probable, as mentioned in reference (Wells et al., 2019). The droplet size distribution droplets is an important factor because of its strong effect on the travel distances; and subsequently it influences on the infection risk (Xie et al., 2009). The breakup approach is one of the most important sub-models to be considered during the coughing simulation. The primary breakup process in the current work is implemented through the Rosin-Rammler approach. This procedure in a person's mouth is modeled by seeding different ranges of droplet radii, by invoking a presumed probability density function (PDF). In OpenFOAM the Rosing-Rammler PDF is expressed as:

$$f(r) = \frac{q\,r^{q-1}}{\bar{r}^{q}}\exp\left[-\left(\frac{r}{\bar{r}}\right)^{q}\right] \tag{5.12}$$

Where q and $\bar{r}$ are the exponential factors and average radius, respectively, that are based on the saliva injection flow rate as an input parameter for the considered seeding droplet $N_{droplet}$. An exponential factor is set as $q = 2.56$ in this work. The average radius ($\bar{r}$) of the droplet is reported in Tab. 5.2 (a). The modified TAB breakup model (Tanner et al., 1997), which is a developed version of the original TAB model, is applied as a secondary breakup model. In this model, there is a proportional relation between the droplet number and its rate of production. Also, the balance of energy among parent and produced droplets results in an expression for the velocity component of the newly produced droplet. Here, Ranz and Marshall (1952) heat transfer model is used to evaluate the reduction of saliva droplet mass due to evaporation. Then, the temperature of the droplets is computed by solving energy and enthalpy equations, which are presented in detail in reference Dbouk and Drikakis (2020a). Here, the developed trajectory collision model (Nordin, 2001), which is available in the OpenFOAM code is implemented. The model considers the droplet local interaction procedure with the mask, which is used here, as is also explained in Dbouk and Drikakis (2020b). Penetration, rebound and stick interaction modes are a function of the maximum droplet diameter, Weber, and Laplace number, respectively, all of them happen during this phenomenon.

5.2.2. Governing Equations for flow control with DBD plasma actuators

To model the influence of the plasma actuation, a new term (F_{Plasma}) included into the momentum equation of Navier–Stokes system. Filtered momentum and continuity equations that are used in the LES method, under the effect of the mentioned body force, are given as follow:

$$\frac{\partial \rho}{\partial t} + \frac{\partial (\rho \bar{u}_j)}{\partial x_j} = 0, \tag{5.13}$$

$$\frac{\partial (\bar{\rho}\,\bar{\mathrm{u}}_j)}{\partial t} + \frac{\partial (\bar{\rho}\,\bar{\mathrm{u}}_i \bar{\mathrm{u}}_j)}{\partial x_j} = -\frac{\partial \bar{p}}{\partial x_i} + \frac{\partial \bar{\sigma}_{ij}}{\partial x_j} - \frac{\partial \tau_{ij}}{\partial x_j} + F_{Plasma} + S. \tag{5.14}$$

We used the “one equation eddy viscosity model” (OEEVM) subgrid-scale in this study. The equations of the implemented LES turbulence model are provided in detail in (Pendar et al., 2020). The external electrodynamics body force generated by the plasma actuator that is mentioned in Eq. (5.14) is given by:

$$\vec{F}_{Plasma} = \rho_C \vec{E}\,. \tag{5.15}$$

The Maxwell equations for a quasi-steady plasma are given as follows:

$$\nabla \cdot (\varepsilon_0 \varepsilon_r E) = \rho_C\,,\ \nabla \times E = 0\,. \tag{5.16}$$

The electrical field can be drive from the scalar potential gradient:

$$\nabla \cdot (\varepsilon_r \nabla \phi) = -\rho_C \big/ \varepsilon_0\,,\ (E = -\nabla \phi). \tag{5.17}$$

Since the gas particles are weakly ionized, the potential can be decoupled into two parts (Bouchmal, 2011),

$$\Phi = \bar{\varphi} + \phi, \tag{5.18}$$

The potential are computed as follows:

$$\nabla \cdot (\varepsilon_r \nabla \phi) = 0, \tag{5.19}$$

$$\frac{\rho_C}{\varepsilon_0} \approx -\frac{1}{\lambda_d^2}\bar{\varphi} \tag{5.20}$$

An equation for the charge density by using Eqs. 5.17 and 5.20 is written as:

$$\nabla.(\varepsilon_r \nabla\rho_C) = \frac{\rho_C}{\lambda_d^2}, \tag{5.21}$$

The values of the Debye length is estimated based on the introduced relation by Bouchmal (Bouchmal, 2011):

$$\lambda_d = 0.2(0.15\times10^{-6}V_{pp} - 7.42\times10^{-4}), \tag{5.22}$$

Here, a Gaussian distribution is considered for the charge density based on the experimental observations:

$$\rho_{C,\omega}(t) = \rho_C^{\max} G(x) f(t), \tag{5.23}$$

$$G(x) = \exp\left[-\frac{(x-\eta)^2}{2\sigma^2}\right] \tag{5.24}$$

Finally, we applied the following for the calculation of $\rho_C^{\max}$:

$$\rho_C^{\max} = 2 f C_{eq} \frac{(V_{pa} - V_{bd})}{f_{corr}\lambda_d}, \tag{5.25}$$

$$f_{corr} = \frac{1}{2}\sqrt{2\pi}\frac{\sigma}{l_p}\left[erf(\frac{1}{2}\frac{\eta\sqrt{2}}{\sigma}) + erf(\frac{1}{2}\frac{\sqrt{2}(l_p-\eta)}{\sigma})\right],\ \vec{E} = E_0\vec{E}^*,\ E_0 = \frac{(V_{pa}-V_{bd})}{l_p}. \tag{5.26}$$

In this work also, the continuous wavelet transforms (CWT) and fast Fourier transforms (FFT) methods are implemented for processing the obtained data. The CWT method is based on the transform time-based function to wavelets that give a time-frequency representation of a signal that specifies the position of frequencies at various times. The continuous wavelet transformation of a function f(t) is conveyed as follow:

$$\langle f(t), \psi_{a,b}(t)\rangle = \frac{1}{|a|^{1/2}}\int_{-\infty}^{\infty} f(t)\psi^*(\frac{t-b}{a})dt, \tag{5.27}$$

Here a, b and ψ(t) are scale (a > 0), time of translational and mother wavelet, respectively. The FFT method disintegrates the time-series data to the frequencies, which influence it. The Fourier transformation of a function x(t) is conveyed as follow:

$$X(f) = \int_{-\infty}^{\infty} x(t) e^{-2j\pi ft} dt \tag{5.28}$$

More details about the CWT and FFT methods can be found in detail in Kolahan et al. (2019).

5.3. Numerical setup

5.3.1. Numerical simulation methodology for aerosol dispersion investigation

In the current study, we examined various configurations of full-scale polluted persons and exposed individuals, or equipment, at different lateral distances. The distances for the following cases were selected to assess the suggested social distance by the CDC and WHO during normal activities of the subjects (CDC 2020; WHO 2020). Figure 5.1 displays the computed computational domain in combination with all dimensions and boundary conditions. A full-scale room with the dimensions of X×Y×Z= 4m×3m×3m is used as an indoor environment for the current simulation. This room is ventilated via an air conditioner on the ceiling and a window and door on the side wall. A polluted person is shown in a fixed position compared to another person or equipment in other locations:

Case (a): The position near the table (L= 0.75 m)

Case (b): Face to face position (L= 2 m)

Case (c): Meeting standing position ($\alpha^{\circ} = 45$ and L=1.5 m)

Case (d): Face mask wearing by the polluting person at case (a) (L= 0.75 m)

Case (e): A polluting person standing outside the room and just the mouth is stitched onto the side wall and sneezing inside the room.

Face mask tight-fitting is a critical factor that affects the mask performance. As indicated in Fig. 5.1 (d), the minimum and maximum distance between the mask and face are here considered 4 mm and 11 mm, respectively. We set the temperature of the human's mouth and environment at the 34°C and 20°C, respectively. The polluting person's mouth altitude from the floor is considered about 1.6 m. The expelled saliva's initial total mass is estimated to be 15 mg. Here, the saliva is considered as a Newtonian fluid with a density of 998 kgm^{-3}; however, it is certainly a more complex fluid. We applied a constant inlet velocity boundary condition for the polluting person's mouth, window, and air conditioner with a turbulence intensity of 20% in the specified direction. The velocity of the respiratory airflow and saliva micro-droplets that are injected from the mouth is varied between 6.3- 22.3 ms^{-1}, typical of various statistically representative cough and sneeze, as reported in experimental data of Chao et al. (2009). The air conditioner and window induce an airflow with velocities set at 0.6 ms^{-1} and 0.2 ms^{-1}, respectively. At the exhaust door, an outlet pressure boundary condition is used. We defined all remaining boundaries (human bodies, other walls, floor) as a no-slip wall boundary condition, applying wall functions to implement the turbulent boundary layer properly.

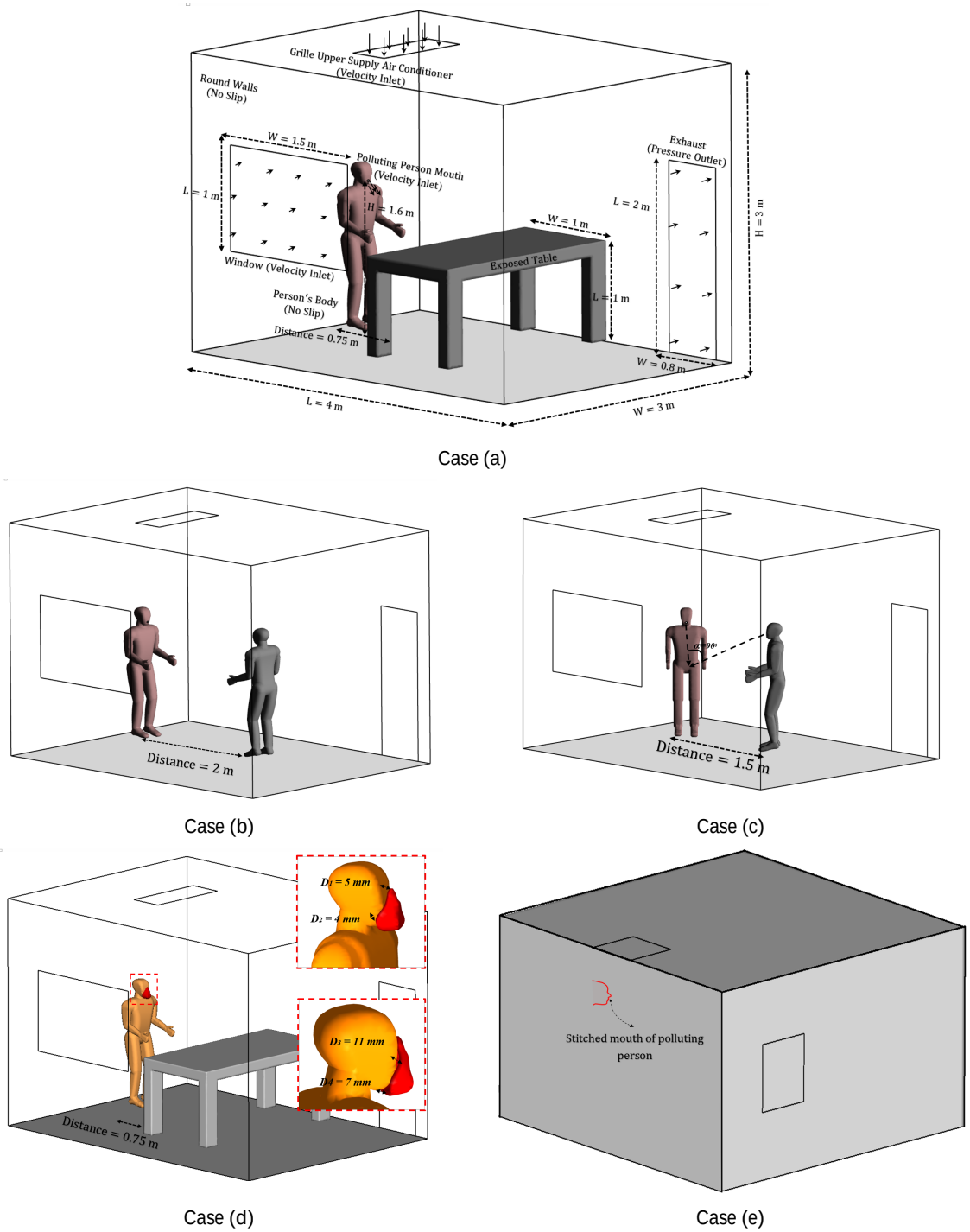

Figure 5.1: The computational domain dimensions and boundary conditions. Case (a) subject facing a table at 0.75 m distance. Case (b) face to face position at 2 m distance. Case (c) meeting position at 1.5 m distance. Case (d) subject facing a table while wearing a face mask. Case (e) subject standing close to the side wall.

Fig. 5.2 shows the three dimensional (3D) computational grid that we used in our simulation with a total cell number of 5.1×10^6 (Medium Grid). We generated a mesh comprising tetrahedral, non-uniform, and unstructured cells because of the complex geometry of the human body. Table 5.1 presents the quality of three different grids, e.g., maximum skewness, aspect

ratio, and boundary layer size. The grid size is progressively increased outward of the body surface, where the variations of flow are proportionally small. Since the accuracy of results strongly depends on the mesh size, a dense mesh near the head and, especially around the mask region, is used. This method helps to save the computational cost by decreasing the total cell numbers for the present complex geometry. The applied computational grid shows a high resolution, in particular close to the body surface and on mouth-print, around 1.9 millimeters that is coarsened in the outward direction with a ratio of 1.15. The selection of this grid size has been conducted based on analyzing the fluid velocity (U_f). Fig. 5.3 compares the velocity magnitude profile, sampled at a vertical line close to the mouth with the coarse, medium, and fine grid.

Table 5.1: Element description of the coarse, medium, and fine grid for the "face to face" case.

Description	Fine Grid	Medium Grid	Coarse Grid
Total element number	6842897	5123271	2234562
Boundary layer element size	1.5 mm	1.9 mm	3.8 mm
Volume element size	1.2-15 mm	1.4-19 mm	3.2-38 mm
Maximum aspect ratio	23.3	26.6	37.2
Maximum cell skewness	0.972	0.938	0.915

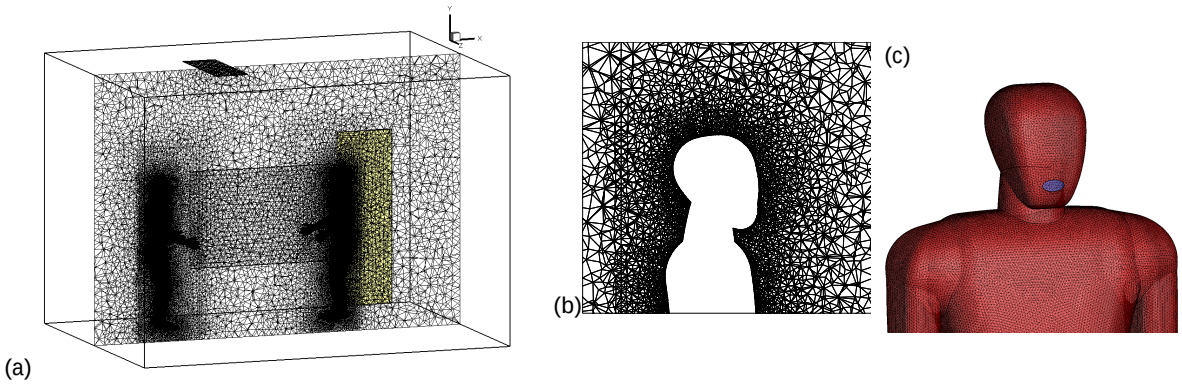

Figure 5.2: Computational grid with specific refinement near the mouth. The total cell count is about 5.1×10^6 cells.

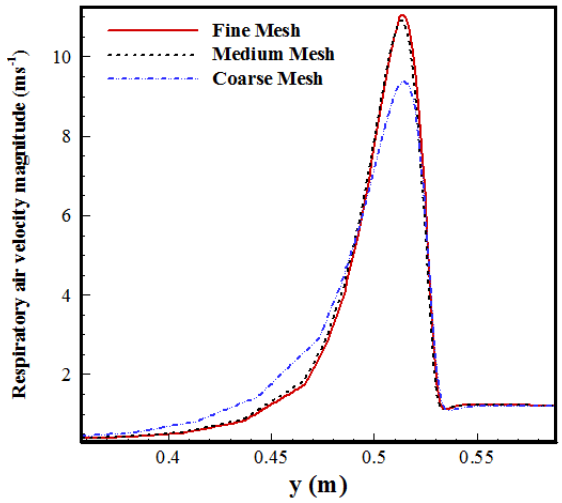

Figure 5.3: Velocity magnitude compared between coarse, medium, and fine grid near the mouth distance of 0.03 m near the mouth).

Table 5.2 presents the distribution of saliva micro-droplets produced using the Rosin-Rammler method with a minimum, average, and maximum diameter, in accordance with the approximately equivalent range of values used in Blocken et al. (2020), Han et al. (2013) and Dbouk and Drikakis (2020a). Based on the experimental results (Han et al. 2013), one single sneeze can produce more than O (10^4) saliva droplets, and we considered the same range in our numerical simulation. Han et al. (2013) considered the forward velocity for a sneeze and cough as 20 ms^{-1} and 10 ms^{-1}, respectively. Wells (1934) estimated that about 100 µm is the critical size, which can be recognized as a boundary between large and small droplets. Also, various cases are considered with a broad range of coughing/sneezing horizontal angle and mouth printed areas in the present simulations (Tab. 5.2 (b)). Our simulation is implemented under the framework of the open-source Computational Fluid Dynamics (CFD) code "OpenFOAM" (Jasak, 2009). Second-order schemes are used in discretizing the momentum and continuity equations. For pressure-velocity coupling, the PIMPLE algorithm is used (Pendar and Roohi, 2018).

Table 5.2: The various situations considered: (a) Data for the distribution of micro-droplet diameters and sneezing initial velocity comparisons ($\theta_{inj} = 33^{\circ}$, $Mouth\,area = 314\,mm^2$).

Bin	$d_{average}[\mu m]$	$d_{min}[\mu m]$	$d_{max}[\mu m]$	$\Delta V_{Initial}[ms^{-1}] = 1 ms^{-1}$
Case (1-8)	90	40	980	6.3-14.3
Case (9-16)	140	40	980	6.3-14.3
Case (17-24)	190	40	980	6.3-14.3
Case (26-32)	240	40	980	6.3-14.3
Case (33-40)	290	40	980	6.3-14.3
Case (41-48)	340	40	980	6.3-14.3
Case (49-56)	390	40	980	6.3-14.3
Case (57-64)	440	40	980	6.3-14.3
Case (65-72)	490	40	980	6.3-14.3
Case (73-80)	540	40	980	6.3-14.3

(b) Comparison of injection angle and mouth area for different cases.

Bin	θ_{inj}	$Mouth\,area\ [mm^2]$	$d_{average}[\mu m]$	$d_{min}[\mu m]$	$d_{max}[\mu m]$	$V_{Initial}[ms^{-1}]$
Case (1-4)	$3^\circ - 43^\circ (\Delta\theta_{inj} = 10^\circ)$	314	290	40	980	8.3
Case (5-8)	33°	170, 314, 490, 700	90	40	980	14.3

5.3.2. Numerical procedure for flow control with DBD plasma actuators

In this study, the implemented 3D airfoil geometry has a section of NACA 63_4–021 profile with an average chord length of 0.1 m. Two different geometry with a straight leading edge (SLE) and sinusoidal wavy leading edge (WLE) has been considered, as shown in Fig. 5.6. The NACA 63_4–021 profile is chosen to construct the bioinspired humpback whale (Megaptera novaeangliae) pectoral flipper cross section (see Fig. 5.4 (c, d)). Humpback whales have sinusoidal bumps with a scalloped appearance on their flippers (see Fig. 5.4 (a, b)) that change the fluid flow over these wing-like flippers as vortex generators maintaining the flow attached at higher AoA (Fish and Battle, 1995). The test case is placed at the center of the computational domain like wind tunnel, which has a 0.30 m square cross-section under the atmospheric conditions, as remarked in reference Johari et al. (2007). The mean chord-based Reynolds number is set at 0.5×10^5, which corresponds to freestream velocity of $U_\infty = 7.0\,ms^{-1}$ and turbulence intensity of $TI \approx 0.6\,\%$.

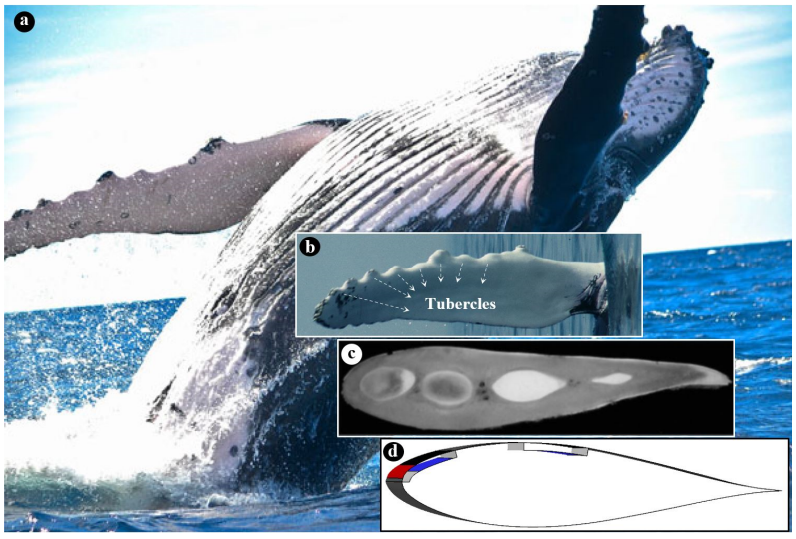

Figure 5.4: Comparison between the cross-section of humpback whale pectoral flipper and NACA 634-021 profile: (a) Flippers on a humpback whale, Photo by Sho Hatakeyama (Hrynuk and Bohl, 2020), (b) Scalloped pattern of tubercles, (c) cross-section of the flipper, (d) NACA 634-021 profile.

The angle of attack (AOA) was set at range of $\alpha = 12^{\circ} - 18^{\circ}$. The PIMPLE algorithm is used to solve the pressure–velocity coupling, as detailed in reference Pendar and Roohi (2018). Incorporating the time-varying plasma body force to the N–S equations and solving by a high-order scheme accuracy in discretizing equations term is implemented. During the simulating procedure, the time step size is kept at around 10^{-5} s. The dimensions of the simulated computational domain and the employed boundary conditions are shown in Fig. 5.5.

The utilized 3D structure quadrilateral grid of the NACA 63_4-021 airfoil with a WLE and SLE is shown in various viewpoints in Fig. 5.6. Overall views, Z-axis views, WLE, and SLE close-up views of the airfoil are included in the frames. To more precisely represent the characteristics of the small-scale turbulence mechanisms, the LES turbulence technique requires finer mesh resolution, especially near the surface of the airfoil. We tried to obtain isotropic grids with a meager expansion factor. The grid sizes at the airfoil surface are well refined, particularly around the position of DBD plasma actuators, where velocity gradients and flow interactions are greater and plasma jet flow is formed. The mean expansion factors values are around 1.025 and 1.015 in the wall-normal and chordwise direction, respectively, around the airfoil.

Table 5.3 compares various grid sizes of a WLE lifting surface with an amplitude of $h_{LE}/c_{ref} = 0.05$ and a wavelength of $\lambda_{LE}/c_{ref} = 0.25$. The measurement was implemented by monitoring the pressure fields around the lower and upper airfoil surfaces. The values measured for average lift ($C_L = Lift/0.5\rho \times U_{\infty}^2 \times C \times Span$) and drag ($C_D = Drag/0.5\rho \times U_{\infty}^2 \times C \times Span$) coefficients when the plasma actuators are turn off are compared for the same operational conditions ($\alpha = 12^{\circ}$) with the experimental data that is reported in reference Johari et al. (2007). It is observable that with growing cell number the difference between the coefficient values becomes negligible and close to the experimental data. Also, the minimum values of pressure coefficients ($C_P = P/0.5\rho \times U_{\infty}^2$) was examined in this case. The results of grids 3 and 4 are almost the same. Accordingly, we used grid 3 for our simulation. To correctly solve the boundary layers and expected flow separation phenomenon, in this case with the LES turbulence model, the condition of $\Delta y^+ \sim 1$ along the airfoil surface needs to be satisfied. For grid 3, the mean values of Δx^+, Δy^+ and Δz^+ are 3.42, 1.35 and 18.1, respectively. Also, the minimum values of Δx^+ and Δy^+ are 0.573 and 0.21, respectively.

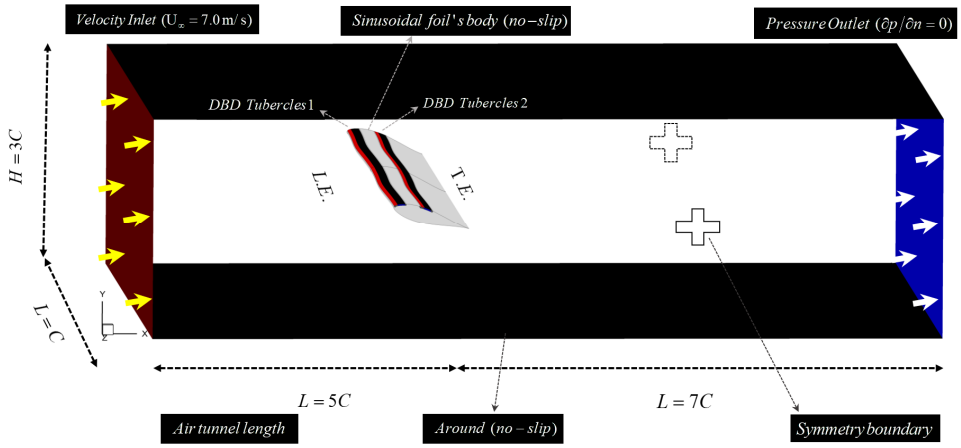

Figure 5.5: Three dimensional views of the overall computational domain with dimensions and boundary conditions.

Table 5.3: Considering the effect of four different grid resolutions used for a grid dependence test based on the WLE case on the average lift and drag coefficients.

$\alpha = 12^\circ$ ($h_{LE}/c_{ref} = 0.05$, $\lambda_{LE}/c_{ref} = 0.25$)	Nodes (million)	Present work			Johari et al. (2007)	
		C_L	C_D	Min C_P	C_L	C_D
Grid 1 (Coarse)	3.4	0.854	0.122	-2.126	0.915	0.098
Grid 2 (Medium1)	5.7	0.890	0.114	-2.204		
Grid 3 (Medium2)	8.1	0.911	0.106	-2.439		
Grid 4 (Fine)	10.6	0.913	0.104	-2.487		

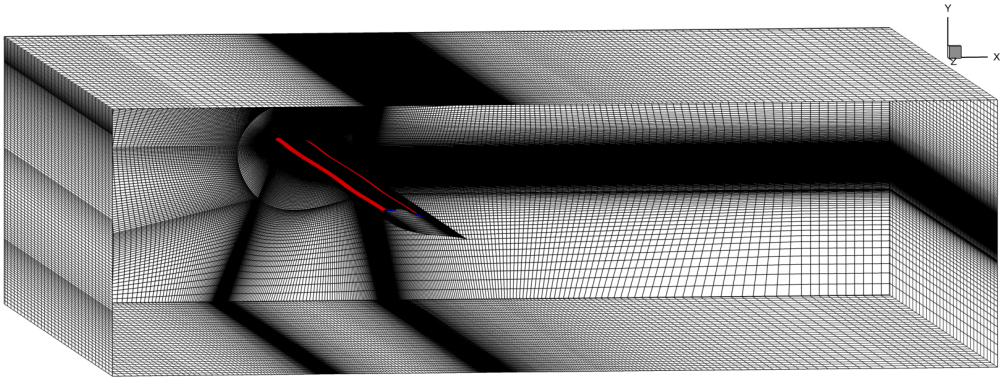

(a) overall view of the computational domain

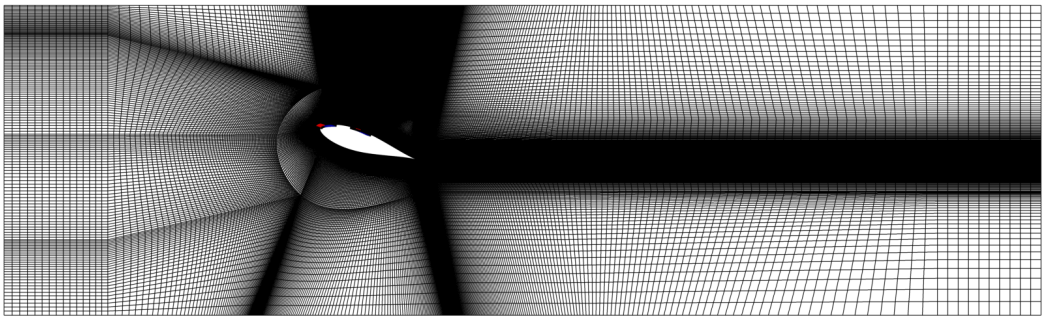

(b) Z-axis view

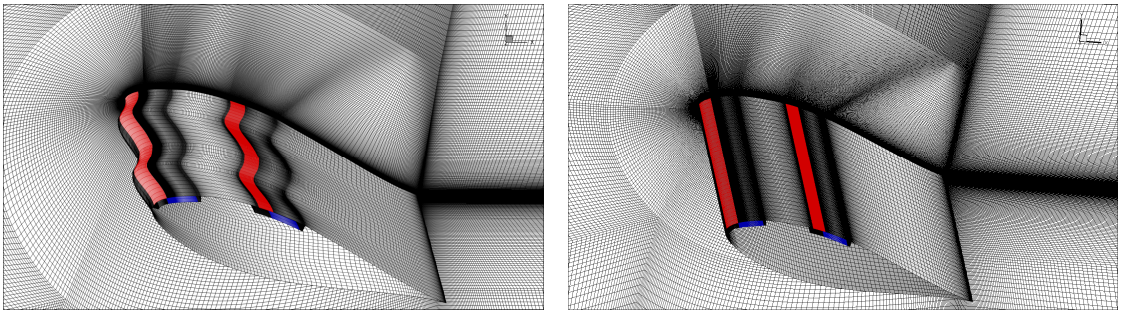

(c) WLE airfoil with DBDs Close-up view (d) SLE airfoil with DBDs Close-up view

Figure 5.6: Three-dimensional computational grid created around the NACA 63_4-021 airfoil. The colored area indicates the fine resolution zone with the presence of the DBD plasma actuators.

Figure 5.7 (a) shows a schematic illustration of the designed electrodes and dielectric layer structure. Two plasma actuators with a sinusoidal pattern for WLE airfoil are mounted at $x/C = 3\%$ and $x/C = 30\%$ from the leading edge for the flow controlling. Each plasma actuator comprises of a pair of electrodes, exposed and embedded electrode with the length of $L_{expose} = 0.05C$ and $L_{embedded} = 0.1C$, respectively, with no overlap. It is assumed that the certain thickness of electrodes are $D = 70\,\mu m$. A layer of dielectric material with a thickness of $t = 0.04C$ and a dielectric permittivity of $\varepsilon = 4\varepsilon_{\circ}$ separates these electrodes. The alternating current (AC) actuators as a momentum-based active control technique are driven by sinusoidal signals of voltage with peak-to-peak ranging from a few to tens kilovolts (kV), frequency from a few to tens kilohertz (kHz). Also, Fig. 5.7 (b) shows the corresponding boundary conditions.

Figure 5.7 (c, d), for the validation purpose, the accuracy of the numerical procedure and the employed solver were evaluated around the SLE and WLE airfoils. The computed results for the lift and drag coefficients around the baseline 63_4-021 airfoil and WLE foils with wavelengths of 50% and amplitudes of 5% and 25% of the mean chord length at Re=1.83×10^5 are compared with the experimental data reported by Johari et al. (2007). A suitable agreement between our

computational results and available experimental data shows the appropriateness in predicting the considered turbulent flow.

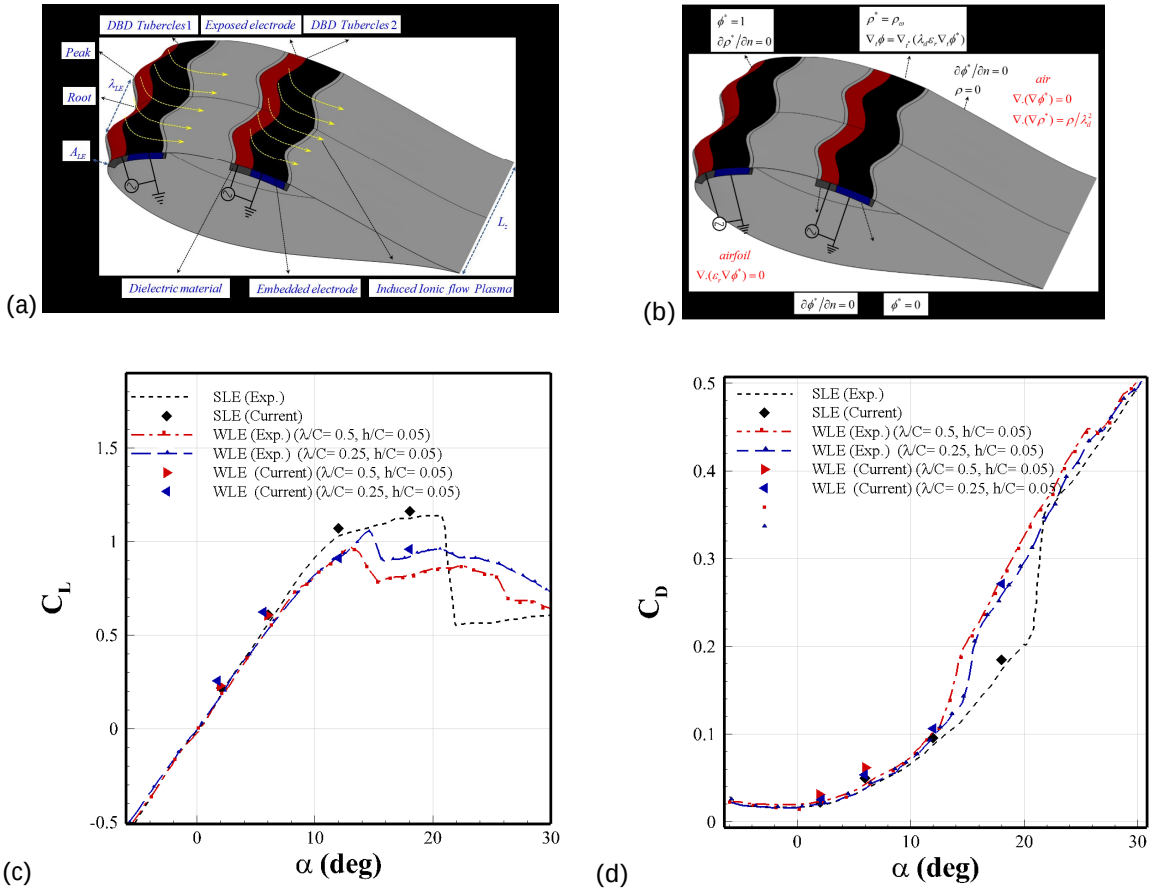

Figure 5.7: (a) Schematic configuration of two DBD plasma actuators over WLE airfoil ($h_{LE}/c_{ref}=0.05$, $\lambda_{LE}/c_{ref}=0.25$, $\alpha=18^{\circ}$), and (b) the corresponding boundary conditions. Comparison of the (c) lift coefficient, and (d) drag coefficient with the experimental data of Johari et al. (2007).

Figure 5.8 (a) illustrates contour of the normalized body force magnitude in the region above the embedded electrode that is decreasing in the direction of the wall jet. This distribution is based on the Suzen et al. (2005) model implemented in the current simulation. The non-dimensional chordwise length and vertical width of the region are $l/C=0.125$ and $w/C=0.042$ for the case with $Re=0.5\times10^5$. Also, the dimensionless electric potential distribution in the air and electric zones are depicted in Fig. 5.8 (b). The electric potential near the exposed and embedded electrodes approaches a maximum and zero value, respectively.

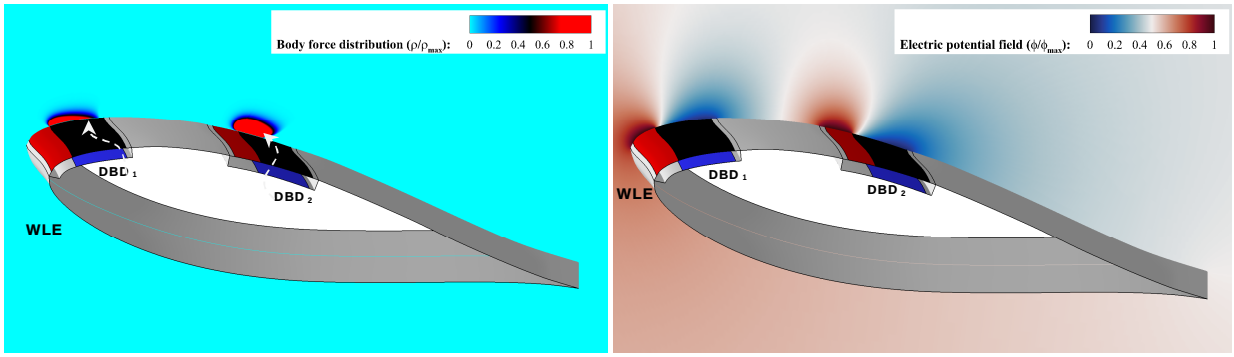

Figure 5.8: The distribution of the normalized (a) body force, and (b) electric potential produced by the DBD plasma actuators ($V_{\max} = 16\,kV$, $f = 20\,kHz$).

5.4. Results and discussion

5.4.1. Results of aerosol dispersion

Our numerical study revealed how saliva micro-droplets, during coughs and sneezes, can be dispersed in turbulent clouds, precisely the same as in the real condition. We simulate dynamic mechanisms of saliva micro-droplets using the initial parameters, i.e., initial velocity ($V_{Initial}$), initial size distribution (D_p), horizontal injection angle (θ_{Inj}) of the micro-droplets, mouth area and cloud opening angle (θ_{out}), this is performed according to the reported in the experimental literature. Also, the transport of these micro-droplets over a farther distance from the mouth depends on the conditions of the indoor environment, like complex recirculatory flows of ventilation systems.

Coronavirus transmission occurs in three ways: (a) Direct transfer of large droplets expelled at high momentum to the receiver's conjunctive, mouth or nose (b) Physical contact with droplets deposited on the surface and subsequent absorption to the nasal mucosa of the receiver (c) Inhalation by the recipient of expiratory ejected aerosolized droplet nuclei (Mittal et al. 2020). The suggested social distancing by the Centers for Disease Control (CDC) and World Health Organization (WHO) is around 3–6 feet (0.9 - 1.8 m) (CDC 2020; WHO 2020). The turbulent jet generated with the violent sneeze is spread at a Reynolds number O (10^4) (Bourouiba et al. 2014). Competition between gravity, inertia, drag and environmental forces determines the fate of saliva droplets.

Fig. 5.9 shows the saliva micro-droplets kinematics for a complete sneezing cycle, from the mouth to floor, for various social positions. This evolution involves the dispersion, breakup and deposition process of the saliva droplets during sneezing. At first, the droplets expelled from the mouth are mostly affected by the inertia force and are moving along the direction of the initial velocity (Frame a). These droplets, at first, travel a long distance (0 to 16 ms). Following the development of a conical jet near the mouth, the droplets entertained a vortical flow (Frame b).

The droplet velocity, with a maximum value of 14 ms^{-1}, drop-down gradually when they depart from the mouth. In this time, the inertia force gradually decreases and the gravity force control the larger droplets, while drag and Brownian forces control smaller droplets (Frame c). The velocity of the droplets decreases to 2 ms^{-1} after about 16 ms. Therefore, larger droplets immediately fell on the floor and smaller ones stay fluctuate and take a lot of time to reach the ground (16 ms to 1s). Frame (d) shows the virus-laden droplet deposition of the host's respiratory mucosa in the final stage of transmission. As any virus is able to survive on a surface for hours (Van Doremalen et al. 2020), these droplets are important for the analysis of contaminated surfaces. Larger droplets reach a larger distance and may influence the infection's intensity and progression. Shorter people are at higher risk since their faces are located on the falling region of the micro-droplet trajectory. The inlet airflow of the air conditioner and window changes the normal path of the low-velocity droplets having a smaller diameter. It increases the flow vortices and intensifies the Brownian movement (Frame c).

In case (I) ($L = 2m$), "face to face", the droplets are deposited at a horizontal distance of more than $\approx 2.8\ m$ away from the mouth. These droplets passed through the opposite person in the area below the chest area. They cannot reach the face of the opposite individual and just can be deposited on the clothes or shoes. In case (II) ($L = 0.75m$), "person near the table", the droplets pass entirely over the table, and it is shown that the considered distance is not safe at all. A larger portion of the table surface is polluted due to hitting by the droplets at a high speed of 4 ms^{-1}. Finally, in case (III) ($L = 1.5m$), "meeting position", the deposition pattern revealed that the preferred length could be considered as a safe distance. For proper visualization of the spatial distribution and deposition of the saliva droplets, their size is magnified by the scale factor of $SF_{Droplet} = 15$.

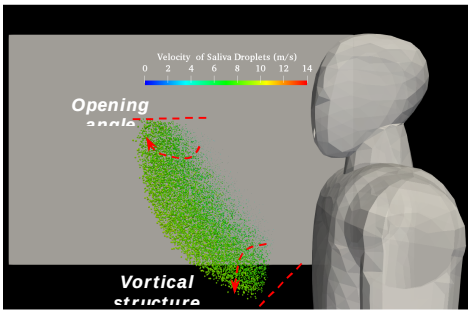

(a) $t = 0.06$ (s)

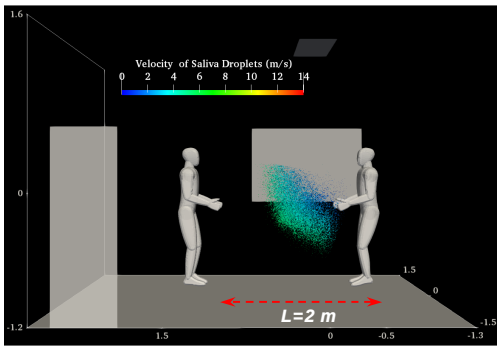

(b) $t = 0.16$ (s)

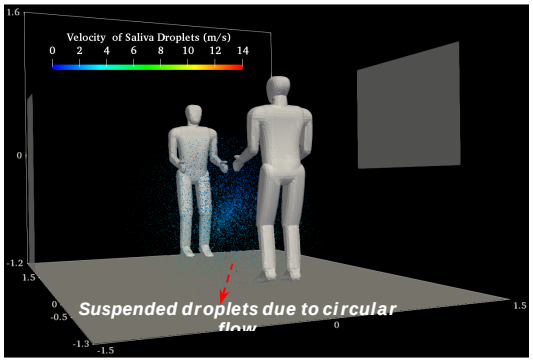

(c) $t = 0.3$ (s)

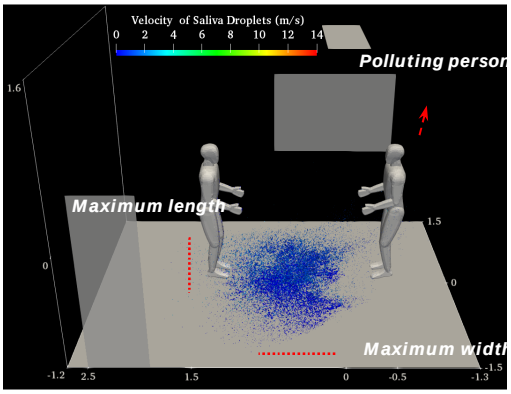

(d) $t = 1$ (s)

Case (I): Face-to-Face

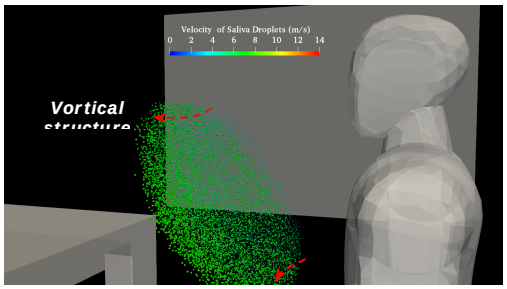

(a) $t = 0.06$ (s)

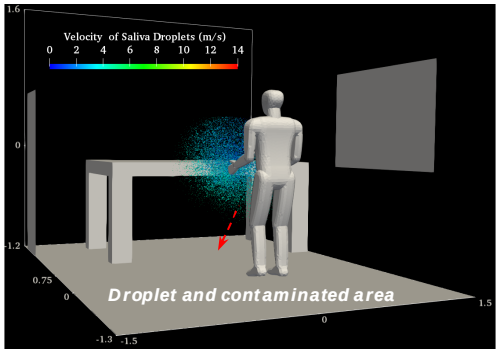

(b) $t = 0.16$ (s)

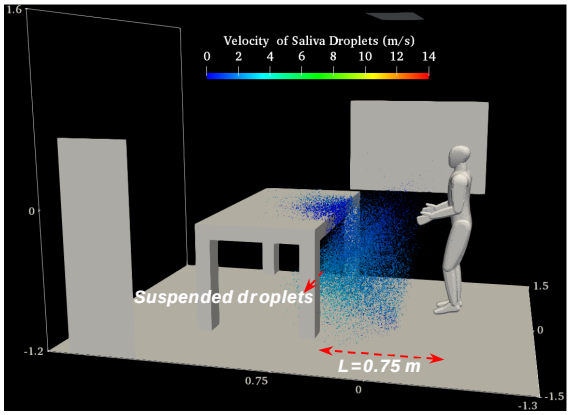

(c) $t = 0.4$ (s)

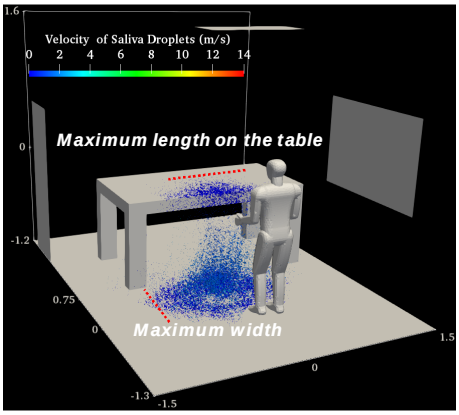

(d) $t = 1$ (s)

Case (II): Near the table

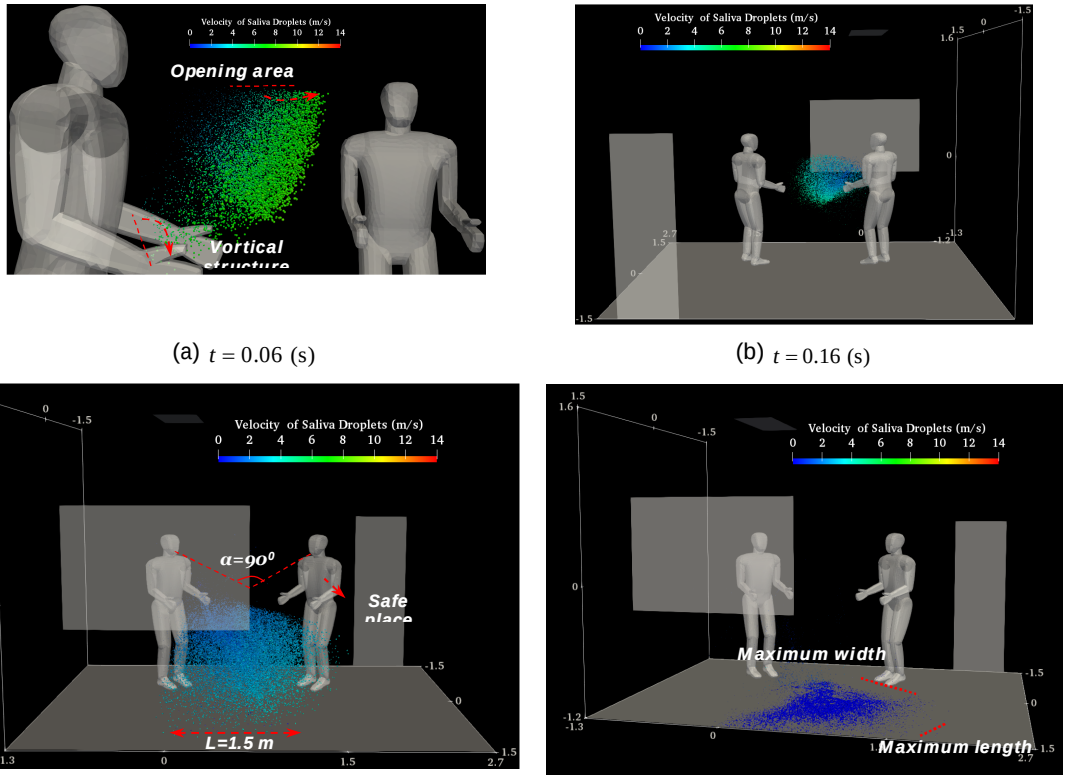

(a) $t = 0.06$ (s)

(b) $t = 0.16$ (s)

(c) $t = 0.3$ (s)

(d) $t = 1$ (s)

Case (III): Meeting standing

Figure 5.9: A human sneeze: Kinematic visualization of the expelled saliva disease-carrier droplets for cases: (I) Face-to-Face (II) Meeting standing (III) Near the table; (a) t=0.06 s, (b) t=0.16 s, (c) t=0.3 s, (d) t=1 s. (The initial velocity, the total mass, diameter, scale factor and the number of the saliva are $V_{Initial} = 14.3 ms^{-1}$, $m_{Saliva} = 15 mg$, $D_{average} = 360\,\mu m$, $D_{\min} = 10\,\mu m$, $D_{\max} = 980\,\mu m$, $SF_{Droplet} = 15$ and $N_{Saliva} = 95000$, respectively).

Figure 5.10 indicates the saliva droplets distribution, which are colored according to their size in the same condition also in Fig. 5.9. Due to the breakup process, disintegration and evaporation phenomenon, the values of Sauter Mean Diameter (SMD) decrease from $D_{32} = 307\,\mu m$ to $D_{32} = 205\,\mu m$. Larger droplets, with a diameter larger than the critical size ($D_{droplet} \approx \geq 100\,\mu\mathrm{m}$), are deposited on the floor or equipment farther and faster by overcoming the inertia and gravity forces on the aerodynamic drag force, before evaporation, but the smaller ones remain airborne and may be transported through the airflow (Frame c and d). The vortical dynamic cloud has a minor effect on the larger droplet size, but circular flow suspends the droplets with medium and small size. Various saliva droplet kinematic phenomena such as elongation, rotation, and drift are shown in Fig. 5.10. The saliva droplets are advected in the airflow direction with a slight rotation in the clockwise direction. A few number of droplets disintegrate into a very small size due to the breakup process and these droplets quickly evaporate. Small droplets, drifting due to their lower effective momentum, became sustainable (Frame c). This research shows that the recommended 6 feet (2 m) safe distance isn't reliable. For all cases, droplets take about 0.3 s to fall and cross under the human waist.

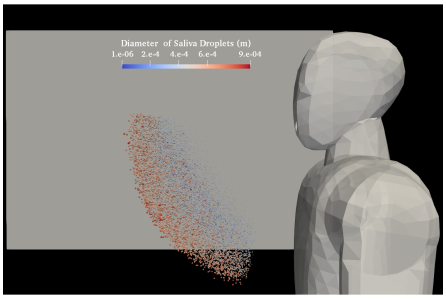

(a) $t = 0.06$ (s)

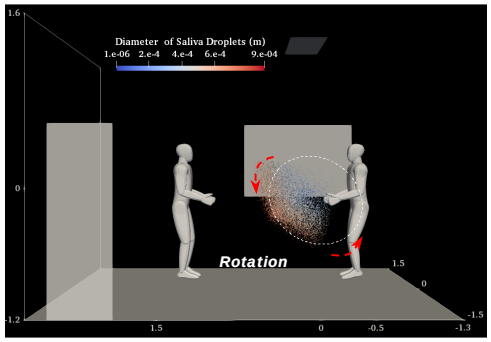

(b) $t = 0.16$ (s)

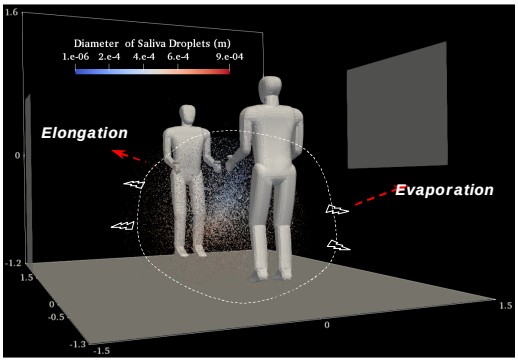

(c) $t = 0.3$ (s)

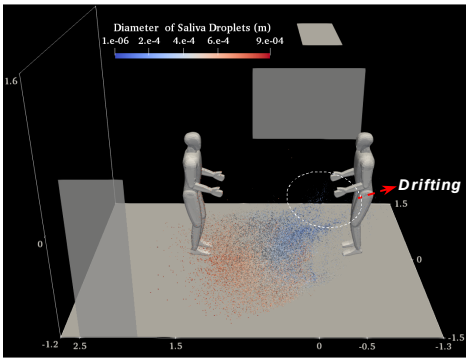

(d) $t = 1$ (s)

Case (I): Face-to-Face.

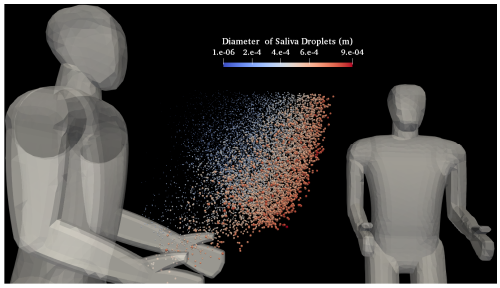

(a) $t = 0.06$ (s)

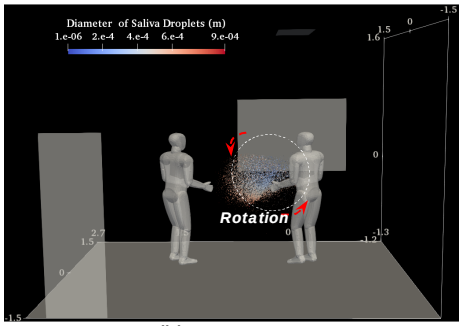

(b) $t = 0.16$ (s)

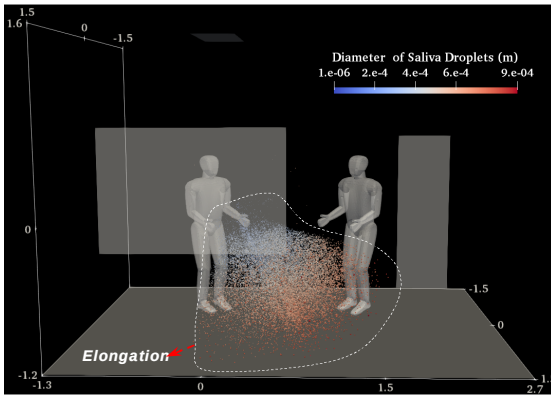

(c) $t = 0.3$ (s)

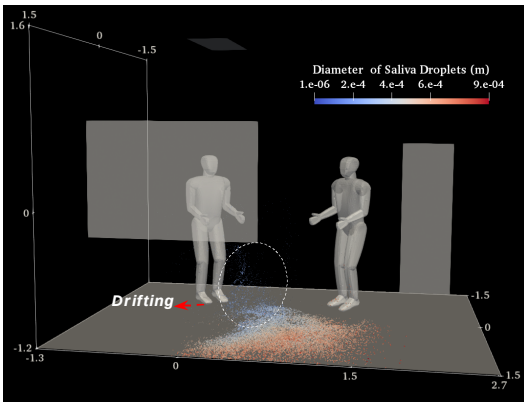

(d) $t = 1$ (s)

Case (II): Meeting standing.

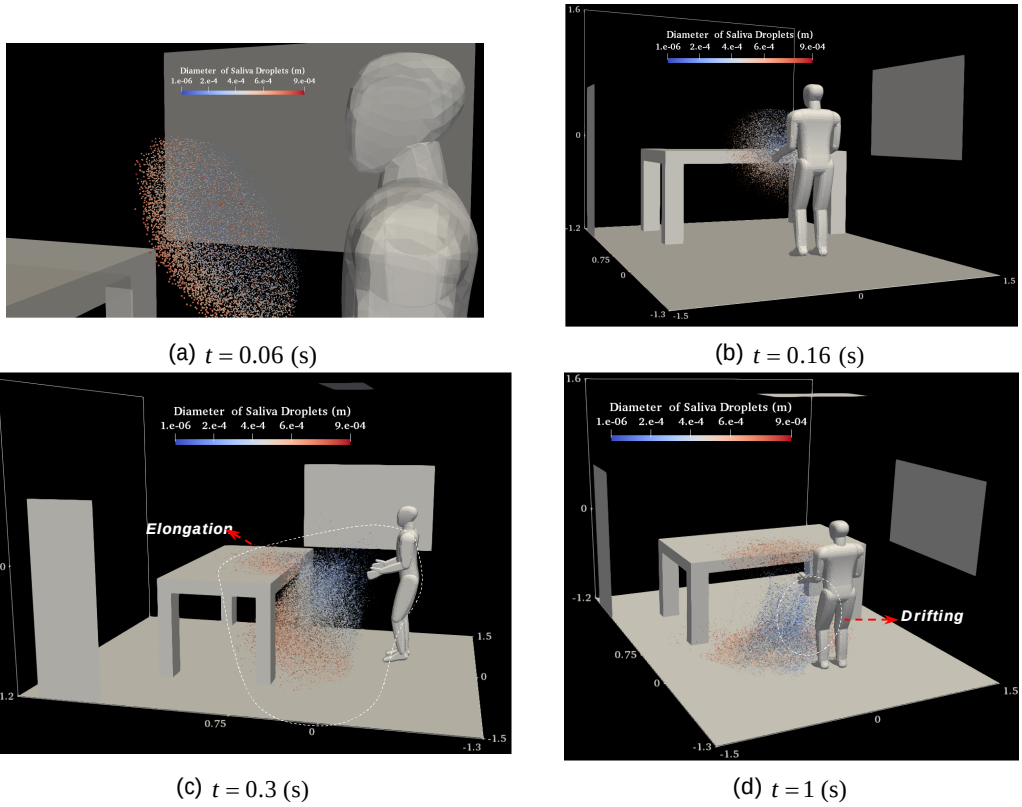

(a) $t = 0.06$ (s) (b) $t = 0.16$ (s)

(c) $t = 0.3$ (s) (d) $t = 1$ (s)

Case (III): Near the table.

Figure 5.10: A human sneeze: Saliva disease-carrier droplets diameter distribution for diverse cases: (I) Face-to-Face (II) Meeting standing (III) Near the table; (a) t=0.06 s, (b) t=0.16 s, (c) t=0.3 s, (d) t=1 s. (Same operational conditions as Fig. 5.9).

Figure 5.11 compares the flowfield of saliva droplets for two cases with different sneezing ranges and for a different social position: hard sneeze ($V_{Initial} = 14.3 ms^{-1}$) (red color contour) and normal sneeze ($V_{Initial} = 6.5 ms^{-1}$) (blue color contour) at $t = 1s$. It is obvious that the contaminated area, especially the maximum polluted length, due to differences in inertial force is completely different. As it is shown, the number of drifted and suspended saliva droplets at about 0.6 m above the floor during a normal sneeze is higher than for a hard sneeze since the aerodynamic drag force can easily overcome the inertia and gravity forces. Droplets did not exceed 1 m away from the mouth during a normal sneeze.

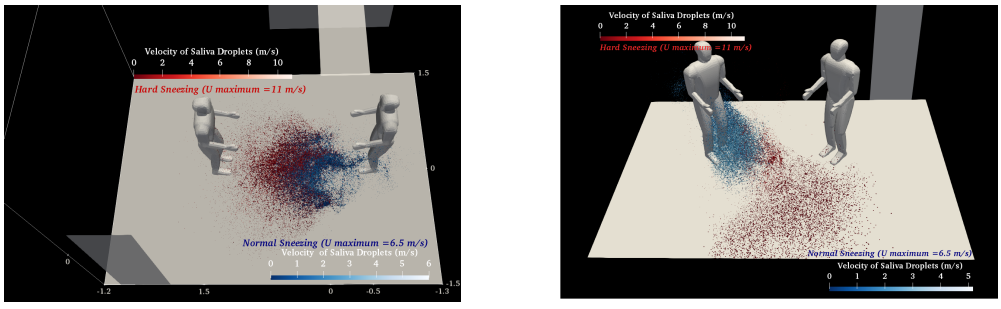

(a) (b)

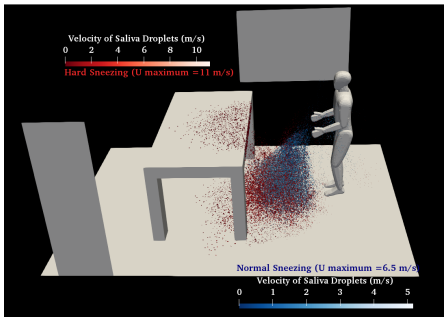

(c)

Figure 5.11: Comparison of the velocity distribution of saliva droplets for two different sneezes: normal ($V_{Initial} = 6.5 ms^{-1}$) (blue droplets) and hard ($V_{Initial} = 14.3 ms^{-1}$) (red droplets); (a) face-to-face position. (b) meeting standing position. (c) near the table position.

The maximum horizontal traveled distance of the droplet transmission route is an important factor. Figure 5.12 shows the pattern of micro-droplets deposition for a wide range of initial size distribution and velocity, which is scaled to be visible with naked eyes. In this figure, the maximum deposition area has been assessed precisely. The first frames of each part show a size distribution of droplets that is estimated according to the Rosin-Rammler approach, resulting in various sizes $D_{Average} = 90–540\ (\mu m)$. The pattern of deposition has clearly changed for various range of droplet sizes. For $D_{Average} \geq 390\ (\mu m)$ they have almost elliptical forms albeit with different sizes. The deposition patterns in these size range clearly demonstrates that the effects of gravity and inertia forces are dominant and the influence of the flow field is largely diminished. By reducing the size distribution, for example $D_{Average} \leq 190\ (\mu m)$, this pattern becomes chaotic, especially for higher initial velocity values that have a disordered pattern with a more elongated shape. The micro-droplets, due to an environmental situation, such as a window or air conditioner inlet flow, have changes in their normal direction before reaching the fall out length. It confirms that through the decreasing of the size distribution of droplets, the role of the inertia and gravity forces in determining their trajectory is declining, and the aerodynamic drag force and environmental conditions have a stronger influence. The droplet settling at a farther distance, on the floor, for larger size and long-lived micro-droplets, is settling at a very low speed of around 0.06 ms^{-1}.

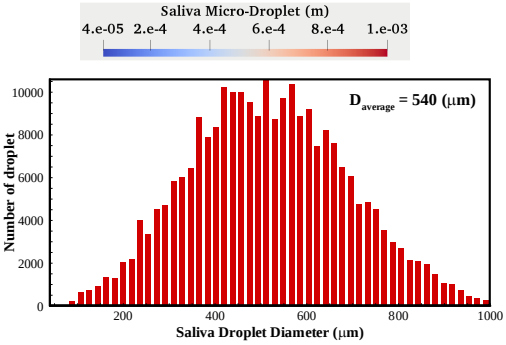

(a) $D_{Average} = 540\ (\mu m)$, $D_{Min} = 40\ (\mu m)$,

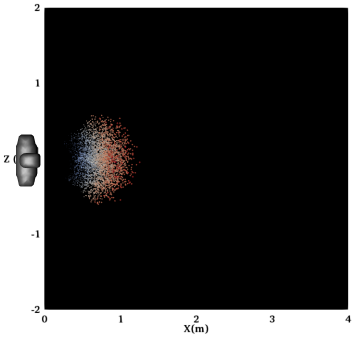

Case (1): $V_{Initial} = 6.3\ (ms^{-1})$

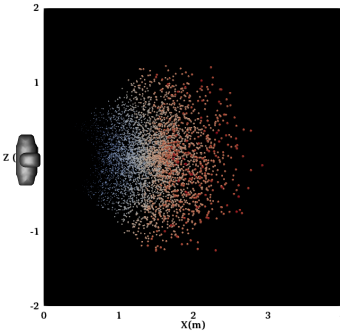

Case (2): $V_{Initial} = 10.3\ (ms^{-1})$

$D_{Max} = 980\ (\mu m)$

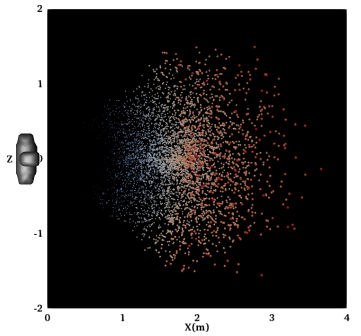

Case (3): $V_{Initial} = 14.3\ (ms^{-1})$

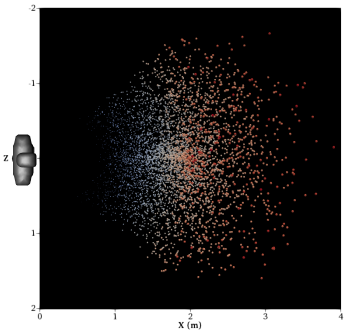

Case (4): $V_{Initial} = 18.3\ (ms^{-1})$

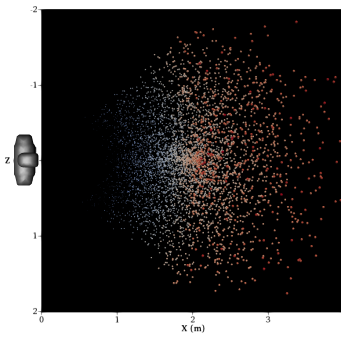

Case (5): $V_{Initial} = 22.3\ (ms^{-1})$

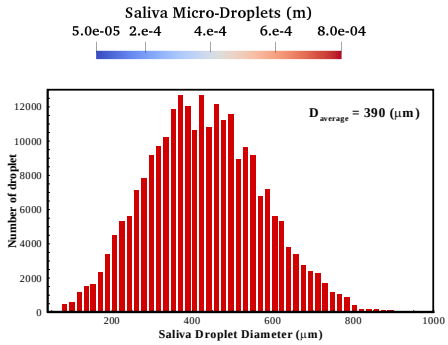

(b) $D_{Average} = 390\ (\mu m)$, $D_{Min} = 40\ (\mu m)$, $D_{Max} = 980\ (\mu m)$

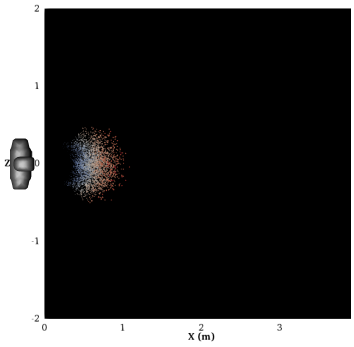

Case (1): $V_{Initial} = 6.3\ (ms^{-1})$

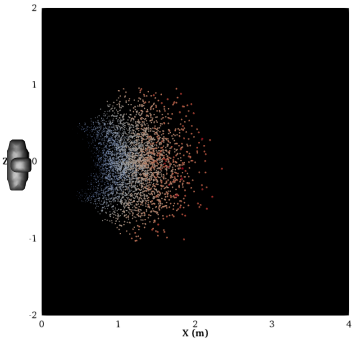

Case (2): $V_{Initial} = 10.3\ (ms^{-1})$

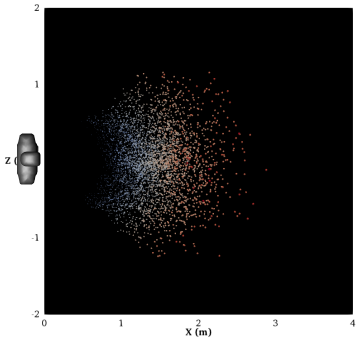

Case (3): $V_{Initial} = 14.3\ (ms^{-1})$

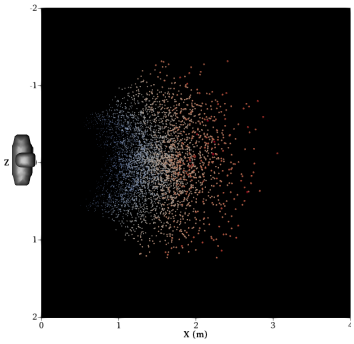

Case (4): $V_{Initial} = 18.3\ (ms^{-1})$

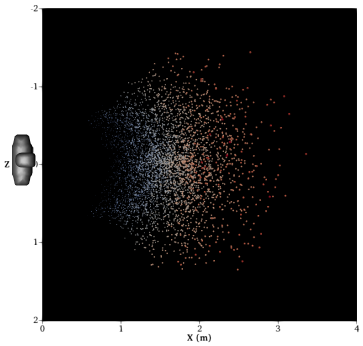

Case (5): $V_{Initial} = 22.3\ (ms^{-1})$

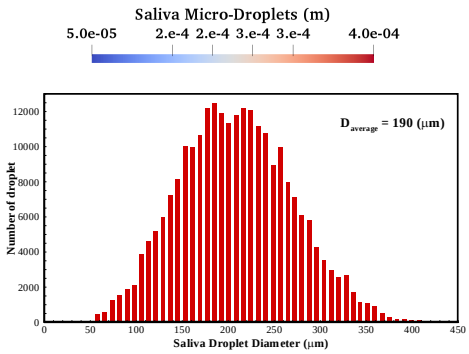

(c) $D_{Average} = 190\ (\mu m)$, $D_{Min} = 40\ (\mu m)$, $D_{Max} = 980\ (\mu m)$

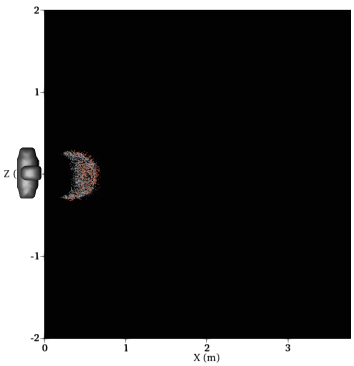

Case (1): $V_{Initial} = 6.3\ (ms^{-1})$

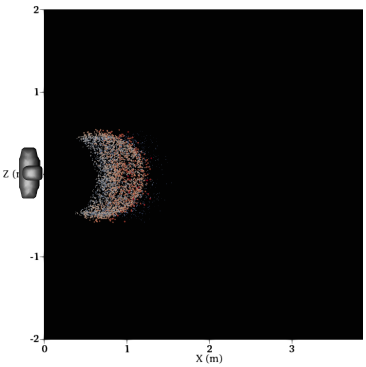

Case (2): $V_{Initial} = 10.3\ (ms^{-1})$

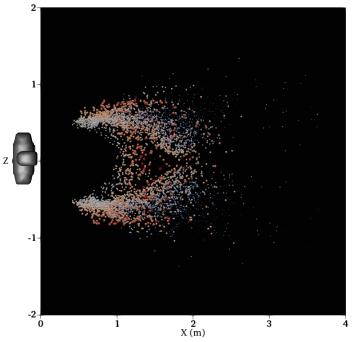

Case (3): $V_{Initial} = 14.3\ (\mathrm{ms}^{-1})$

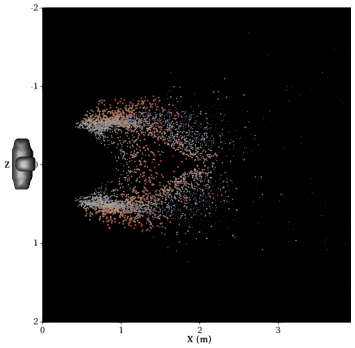

Case (4): $V_{Initial} = 18.3\ (\mathrm{ms}^{-1})$

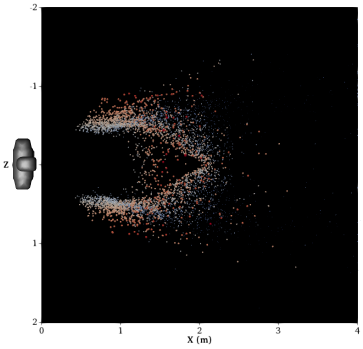

Case (5): $V_{Initial} = 22.3\ (\mathrm{ms}^{-1})$

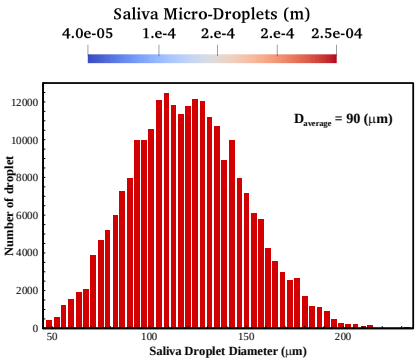

(d) $D_{Average} = 90\ (\mu\mathrm{m})$, $D_{Min} = 40\ (\mu\mathrm{m})$, $D_{Max} = 980\ (\mu\mathrm{m})$

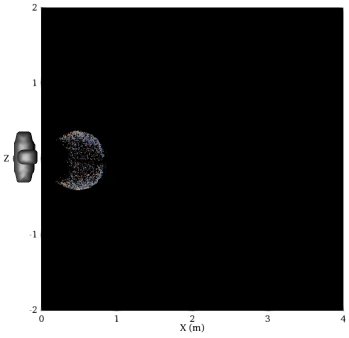

Case (1): $V_{Initial} = 6.3\ (\mathrm{ms}^{-1})$

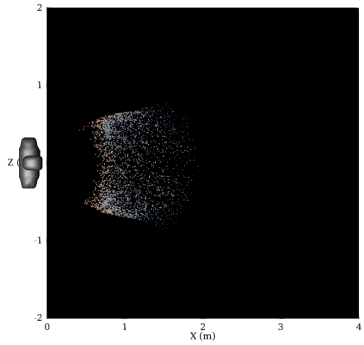

Case (2): $V_{Initial} = 10.3\ (\mathrm{ms}^{-1})$

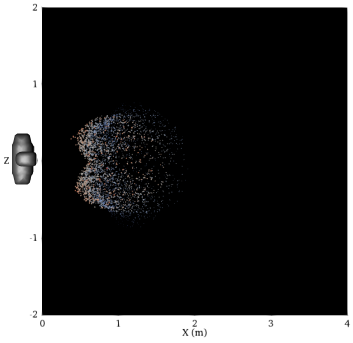

Case (3): $V_{Initial} = 14.3\ (\mathrm{ms}^{-1})$

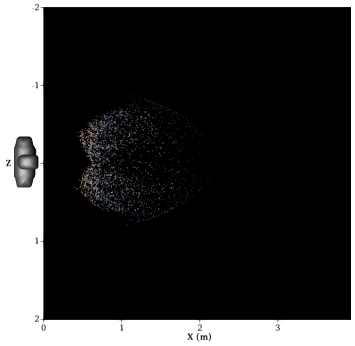

Case (4): $V_{Initial} = 18.3\ (\mathrm{ms}^{-1})$

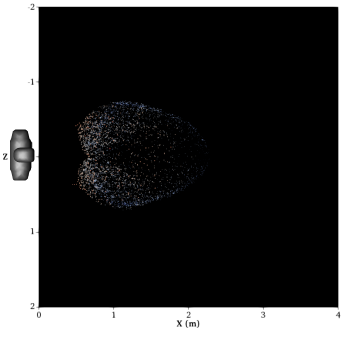

Case (5): $V_{Initial} = 22.3\ (\mathrm{ms}^{-1})$

Figure 5.12: The deposition pattern of micro-droplets of saliva under various operating conditions: (a) $D_{Average} = 540\ (\mu\mathrm{m})$ (b) $D_{Average} = 390\ (\mu\mathrm{m})$ (c) $D_{Average} = 190\ (\mu\mathrm{m})$ (d) $D_{Average} = 90\ (\mu\mathrm{m})$.

Figure 5.13 displays several temporal consecutive patterns of saliva droplet distribution, which are described by their size for a complete period. A significant portion of space is exposed to pollution during the case (I) ($V_{Initial} = 14.3\ \mathrm{ms}^{-1}$). This figure also highlights the impact of the environmental parameters, in comparison to the cases in Fig. 5.9, and for different described phenomena, such as drifting, elongation, disintegration, evaporation, and rotations. By assessing the droplet diameter distribution here, and as discussed in Figs. 5.10 and 5.12 above, it can be concluded that the effect of the gravity and inertia force on the small saliva droplets ($D_{droplet} \approx\leq 40\,\mu\mathrm{m}$) as compared to the influence of the indoor airflow is negligible. Also, medium

($50 \approx\leq D_{droplet} \approx\leq 150\,\mu\mathrm{m}$) and large ($D_{droplet} \approx\geq 200\,\mu\mathrm{m}$) sizes are more affected by the gravity and inertia force, respectively.

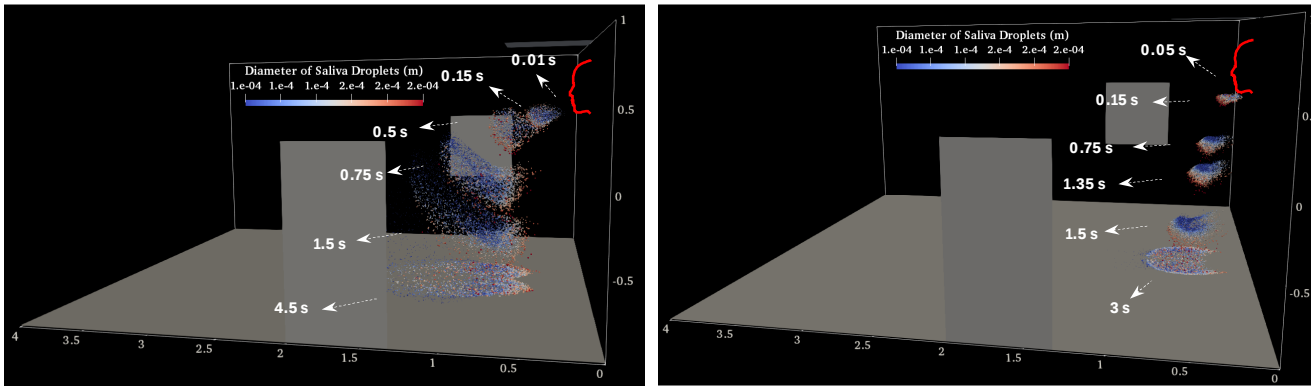

(a) (b)

Figure 5.13: Time evolution of the transport processes of saliva droplets as a function of their diameter during a human sneeze ($D_{Average} = 90\,\mu\mathrm{m}$): (a) $V_{Initial} = 14.3\ \mathrm{ms}^{-1}$, (b) $V_{Initial} = 6.3\ \mathrm{ms}^{-1}$.

As it was mentioned in the literature reviews about micro-droplet dynamics, face mask-wearing is a common effective way for mitigating the respiratory infections. Other methods, such as hand washing, fogging machines, ventilation, and consideration of social distancing are also beneficial (as is mentioned in Figs. 5.9 and 5.10). Figure 5.14 provides a schematic representation of the leakage trajectory of saliva droplets across the facial mask. There are three distinct types of local interaction between the saliva droplets and the mask, which can be named rebound/splash, stick and penetration. A limited number of droplets escape from any opening area due to increasing pressure and velocity originating on the turbulent jet during cough, rebound, or splash. Therefore, face mask tight-fitting is a critical factor that affects mask performance, as indicated in Fig. 5.14. The bulk of droplets, particularly the larger ones, stick to the fibrous layers of the mask. A few particles with a very small size, lower than the critical droplet diameter, leak from the cover and penetrate. This critical diameter is based on the mask microstructure, varies between 27.19 μm and 146.6 μm as reported by Leonas and Jones (2003). Porosity, roughness, and fibrous microstructure can be counted as elements of mask microstructure (Dbouk and Drikakis, 2020b).

In the present simulations, based on the considered initial size distribution of droplets, the number of the penetrated droplets can be ignored, as compared to the total droplet number that is expelled from the mouth. Figure 5.10 shows that the face mask can prevent airborne pathogens from spreading. 'Forward driven droplet' protection by filtering and trapping virus-laden is almost entirely successful, but 'outward driven droplet' protection is not so effective, particularly around the edges of the mask and surrounding. The velocity of the large particles which are able to transmit the coronavirus is not significant enough to pass from the mask during sneezing ($V_{Initial} = 14.3\ \mathrm{ms}^{-1}$).

The saliva micro-droplets rebound and escape from any opening area, especially the pores under the mask (a) and the area above the nose (b) during the hard sneeze (as shown in Fig. 5.15 (I)).

During the high rate of sneezing, the droplets scattering region is limited to a sphere with a diameter of around 0.6 m when wearing the face mask instead of traveling the distance of 3.5 m in the naked face case. Figure 5.15 (II) shows the size values for micro-droplets during a sneeze while wearing a face mask. The scattering of the droplets indicates that the droplet size is considerably reduced as compared to the case without using a mask (Fig. 5.10 (case (III))). Sauter Mean Diameter (SMD) is decreased from $D_{32} = 205\,\mu m$ to $D_{32} = 155\,\mu m$ for the case with and without using a mask, respectively, in the time $t = 1s$ after sneezing. The sticking of droplets onto the mask surface and their breaking up can be considered as the main reason for this reduction.

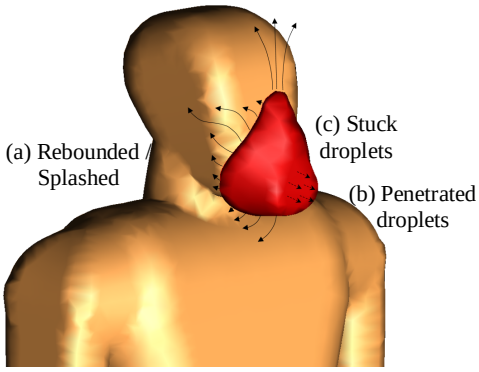

Figure 5.14: Different modes of interaction between the mask and droplets.

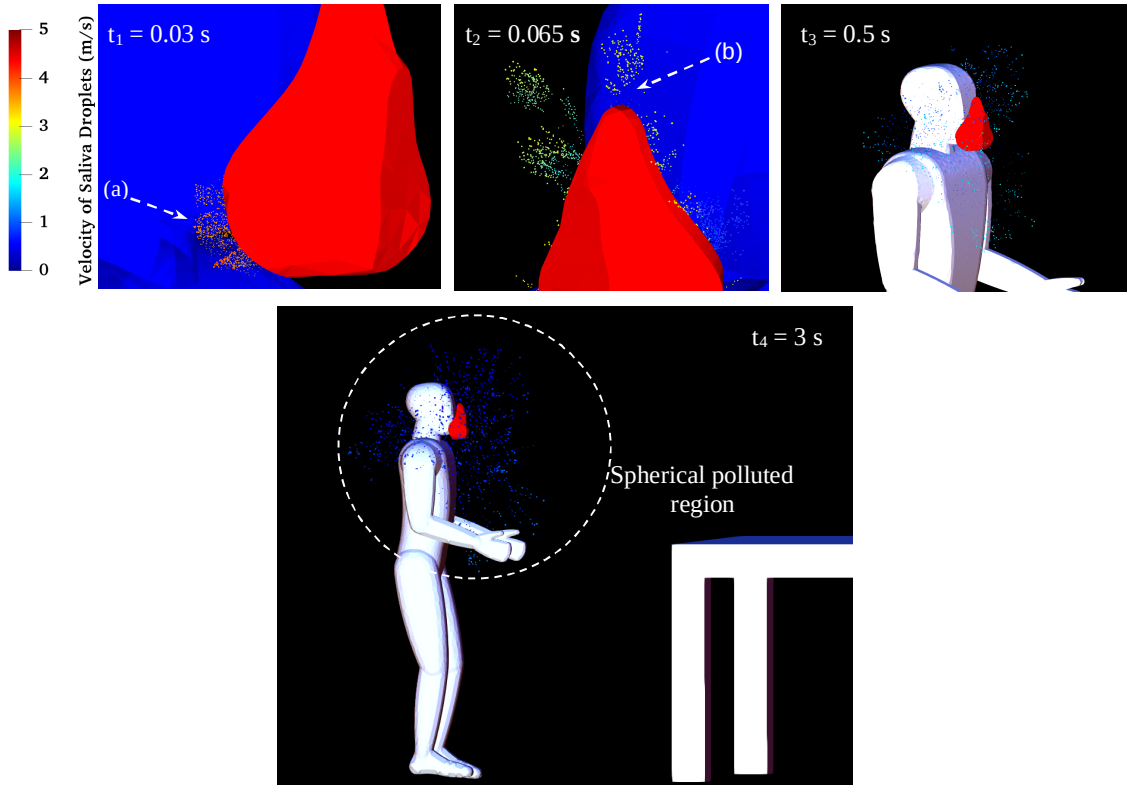

(II)

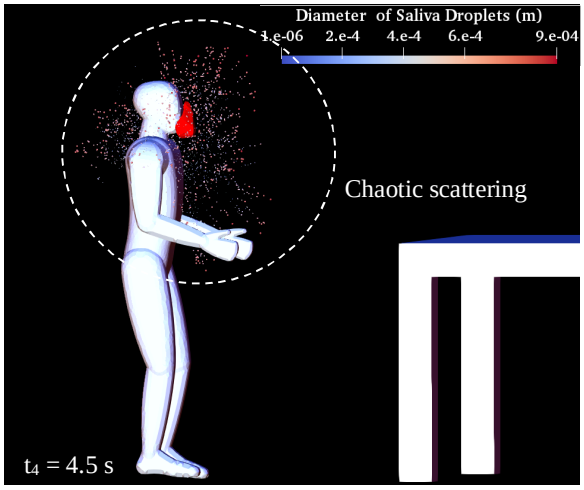

Figure 5.15: Sneeze over one cycle with mask: (I) Saliva droplet velocity (II) diameter ($D_{average} = 360\,\mu m$, $V_{Initial} = 14.3\ \mathrm{ms}^{-1}$).

The dispersion in the sneezing process is affected by the air–mucous, fragmentation of the liquid droplets and the turbulence of the jet, especially close to the mouth. Figure 5.16 reveals the airflow with velocity streamlines tracing being visualized by LIC (Line Integral Convolution) model. The vortical structure grows exactly near the mouth, like a source of the infected person, and moves away from the head. The micro-droplet speed exceeds the mean circular air velocity of the vortices, and these vortices affect the patterns of the suspended micro-droplets. Two apparent kinks emitted from the mouth affect the flow streamlines (air outlet combined with droplets), having an important effect on the micro-droplets trajectory of the sneeze saliva. A circular changing pattern within the droplet cloud is obvious, and has been shown with a pair of arrows during the passing time. Vortex 3, which is caused by the air conditioner, has an effect on the overall flow pattern of sneeze and can control it.

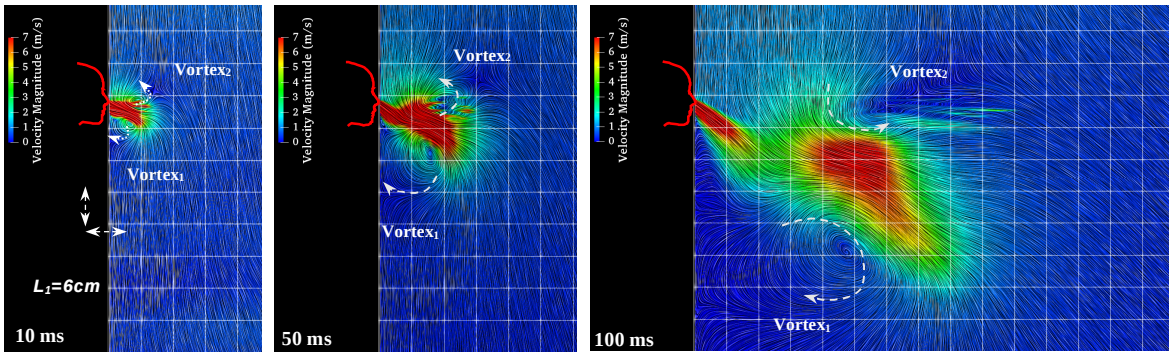

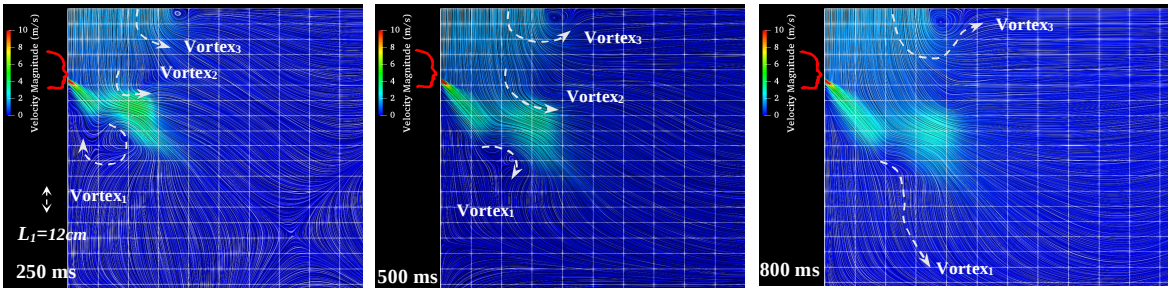

Figure 5.16: The interaction between the two phases of gas (air) and fluid (saliva). The arrows illustrate the apparent circulation within the cloud.

The penetrated liquid traveling distance is a significant factor that defines the maximum distance reached by saliva droplets. Figure 5.17 compares the saliva droplets maximum fall out length and width, on other words contamination distances, for a broad range of initial velocities from $V_{Initial} = 6.3 - 14.3\ \mathrm{ms}^{-1}$ and for a wide range of micro-droplet distribution in size ($D_{mean} = 90 - 540\,\mu m$). Figure 5.17 (a) shows that the maximum fall out distance considerably depends on the combination of the average droplet size distribution and initial velocity of a sneeze. The maximum length and width of the sneeze cloud reaches almost 3.5 m and 1.5 m, respectively, at the $V_{Initial} = 14.3\ \mathrm{ms}^{-1}$ and $D_{mean} = 540\,\mu m$. However, the maximum length and width of sneeze at the same initial velocity, but at a smaller average size of $D_{mean} = 140\,\mu m$, are 1.5 m and 0.73 m, respectively. At the normal sneeze velocities $V_{Initial} = 6.3\,\mathrm{ms}^{-1}$, the maximum fall out length and width for the average size of $D_{mean} = 140\,\mu m$ and $D_{mean} = 540\,\mu m$ decline to 1.27 m, 0.71 m, and 0.87, 0.36, respectively. It is obvious that the cloud size and its dynamics play an important role in the maximum contamination area of micro-droplets and significantly affects infection risk indoor. This figure reveals that larger droplets carry a larger number of small viruses and pose increased potential risk of airborne propagation disease, exceeding a safe social distance of 2 m during the roughly mild sneeze.

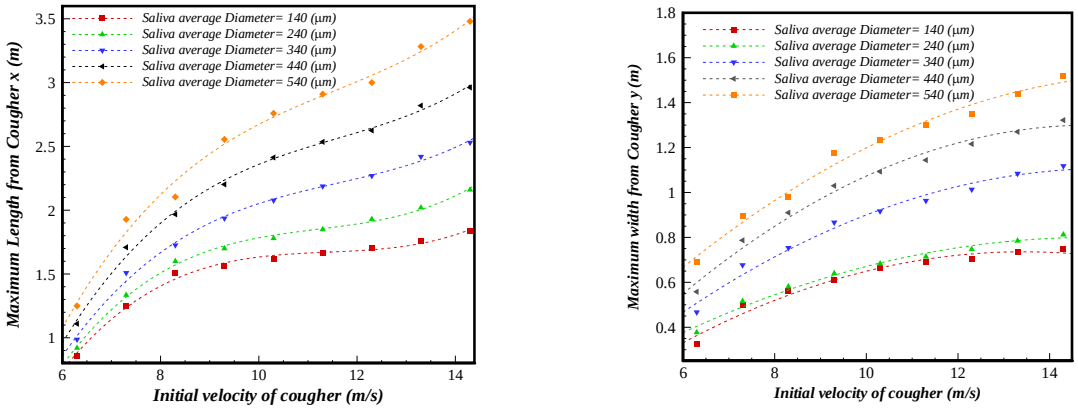

Figure 5.17: The maximum fall out distance, contamination risk distances, for a broad range of droplet size and velocity ($D_{mean} = 90 - 540\,\mu m$, $V_{Initial} = 6.3 - 14.3\ ms^{-1}$): maximum (a) length (b) width ($\theta_{inj} = 33^{\circ}$, $Mouth\,area = 314\,mm^2$).

Based on the numerical simulation of around 45 multiple sneezes, with different operational conditions, we deduced polynomial correlations for the maximum length and width of sneezes as follows:

$$L_{\max} = aV_{Initial}{}^{3} - bV_{Initial}{}^{2} + cV_{Initial} - c_0 \tag{5.29}$$

$$W_{\max} = -aV_{Initial}{}^{2} + bV_{Initial} - c_0 \tag{5.30}$$

Although many parameters are effective in extracting the maximum fall out correlation, herein, we considered these parameters as constant in order to evaluate the effect of the two main parameters; initial velocity and size distribution of droplets. The coefficient of the above polynomial formulation is provided in Tab. 5.4.

Table 5.4: Coefficients of polynomial equation for the deposited saliva droplet area for maximum length and width.

(a) maximum length

D_{mean} (µm)	a	b	c	c_0
140	0.0056	0.191	2.180	6.69
240	0.0058	0.196	2.239	6.68
340	0.0050	0.172	2.085	6.51
440	0.0056	0.193	2.350	7.39
540	0.0058	0.201	2.476	7.80

(b) maximum width

D_{mean} (µm)	a	b	c_0
140	0.0073	0.199	0.586
240	0.0053	0.158	0.384
340	0.0074	0.227	0.629
440	0.0095	0.283	0.807
540	0.0077	0.256	0.595

Figure 5.18 depicts the mean velocity of the micro-droplets distribution during a sneeze decay with time from a human mouth. The velocity of micro-droplets, of the varying size range ($D_{mean} = 90 - 540\,\mu m$) is herein measured, and the results are entirely different in terms of fall out time. It can be noticed that the droplets of larger size ($D_{mean} = 490\,\mu m$) hit the floor in less than 1s due to higher inertia and gravity and their overall velocity reaches almost zero. However, due to the Brownian movement, drifting and environmental influence, the smaller size distribution of droplets ($D_{mean} = 90\,\mu m$) has not lost all of their velocity, as described before.

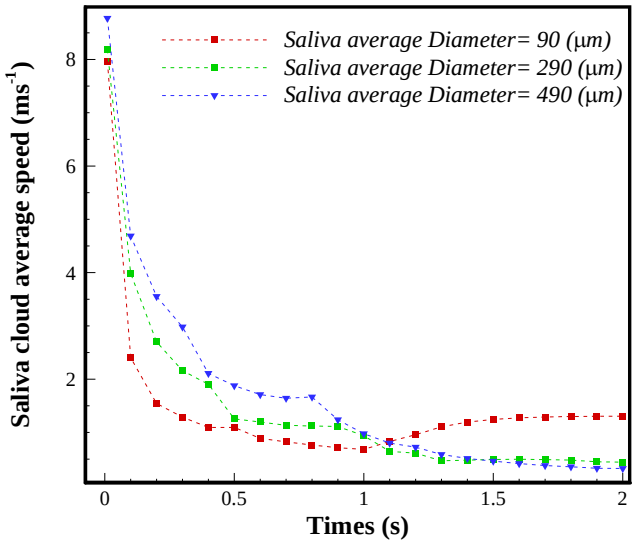

Figure 5.18: The velocity of the sprayed cloud during a sneeze as compared with various diameters, for a different time, from expelling to fall out ($V_{Initial} = 11.3\ ms^{-1}$).

Figure 5.19 shows the effect of various horizontal injection angles ($\theta^{\circ}_{Injection}$=3°–43°) at a specific sneeze ($V_{Initial} = 14.3\ ms^{-1}$, $D_{mean} = 90\mu m$) that comes out from a polluting person's mouth. As a protective action to avoid the spread of respiratory diseases, such as coronavirus, it is advisable to bend the head during sneezing. In other words, the infected distance declines considerably by increasing the injection angle. The maximum polluted distance drops around 22 % from 2.2 m to 1.8 m for sneeze injection angles of 3° and 43°, respectively. Also, the start point of the contaminated area, from the sneezer's mouth, declines from 0.57 m to 0.32 m for the 3° and 43° angles, respectively. However, the maximum width of the contaminated area, as the angle of injection grows, increases slightly (due to higher sneeze power), but it is not as much important as the maximum length in the spreading of the respiratory disease.

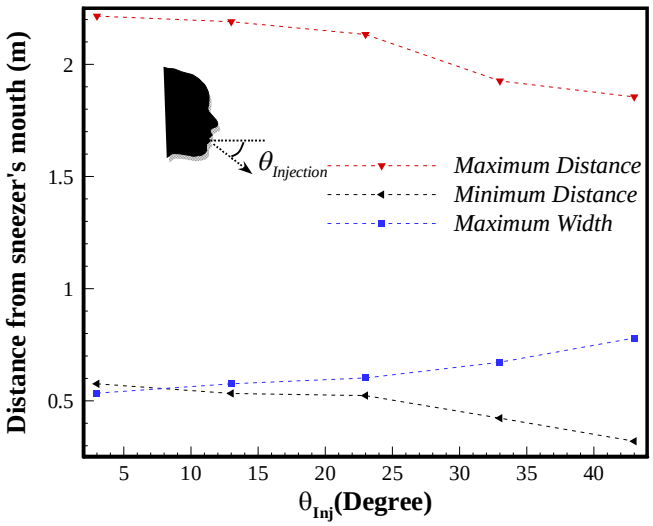

Figure 5.19: Comparison of various injection angles for a specific sneeze ($V_{Initial} = 14.3\ ms^{-1}, D_{mean} = 90\mu m$).

Figure 5.20 demonstrates the impact of different mouth area during one particular sneeze. For a similar power of sneeze, various people, with different mouth area, may produce a completely different contaminated area. If one individual continues to open his mouth and the elliptical area of the mouth expands from 170 to 700 mm^2, the maximum distance that saliva micro-droplet may travel is reduced from 2 m to 0.9 m, respectively.

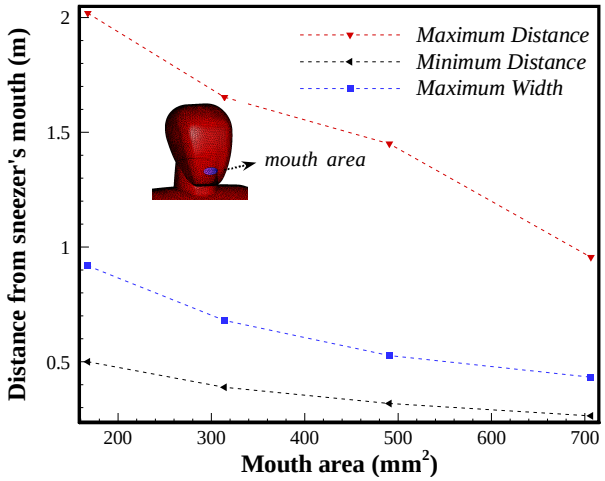

Figure 5.20: Comparison of various mouth area for a specific sneeze ($V_{Initial} = 8.3\ ms^{-1}$, $D_{mean} = 290 \mu m$).

5.4.2. Results of flow control with DBDPA

This section is structured as follows. The pressure coefficient and the aerodynamic forces coefficient are analyzed precisely for the modified cases. Then, the data is analyzed utilizing CWT and FFT methods to investigate the flow spectrum and noise content. Finally, the dynamic control of unsteady flow separation, reattachment, turbulent transition, 3D vortical structures and induced vortices are investigated for all various considered cases in detail.

Figure 5.21 shows the mean pressure coefficient along the surface of the airfoil for various cases at two different angles of attack of α=12° and 18°. In Fig. 5.21 (a) and (b), cases with one and two DBD plasma actuators in the WLE airfoil compared with the case without plasma actuator. Consequent to the presence of DBD along the surface of the airfoil, the low-pressure area on the suction side becomes larger, which leads to an improvement in the aerodynamic coefficient, particularly growth in the lift coefficient. The mean pressure coefficient value illustrates much higher suction peaks near the leading edge for the case with 2DBD ($C_{pMean} = -2.20$) compare to the case with 1DBD ($C_{pMean} = -1.78$) and without plasma control ($C_{pMean} = -1.38$). The mentioned higher suction peak resulting from a shorter separation bubble and extension in the attached region, which leads to more aerodynamic improvement. After the peaks, the mean pressure

coefficient distribution starts to become flatten through the laminar-separation bubble, turbulent transition and reattachment. None of the pressures in various considered cases can recover the freestream pressure at the trailing edge due to the separated flow that is not fully suppressed at this point.

The mean pressure coefficient is slightly higher on the pressure side and somewhat lower on the suction side of the case with DBD than in the no active control situation, resulting in a lift improvement. Additionally, the separated flow being more attached in order to increase the lift and drag coefficients. The control effect trend shows that the separation bubble length becomes shorter and the flow reattachment happen earlier for the case with 2DBD and WLE that other cases. For the α=18°, the C_{pMean} distribution of the no-control case is almost flat towards the leading edge, indicating a considerable separation from the leading edge, compare to cases α=12°.

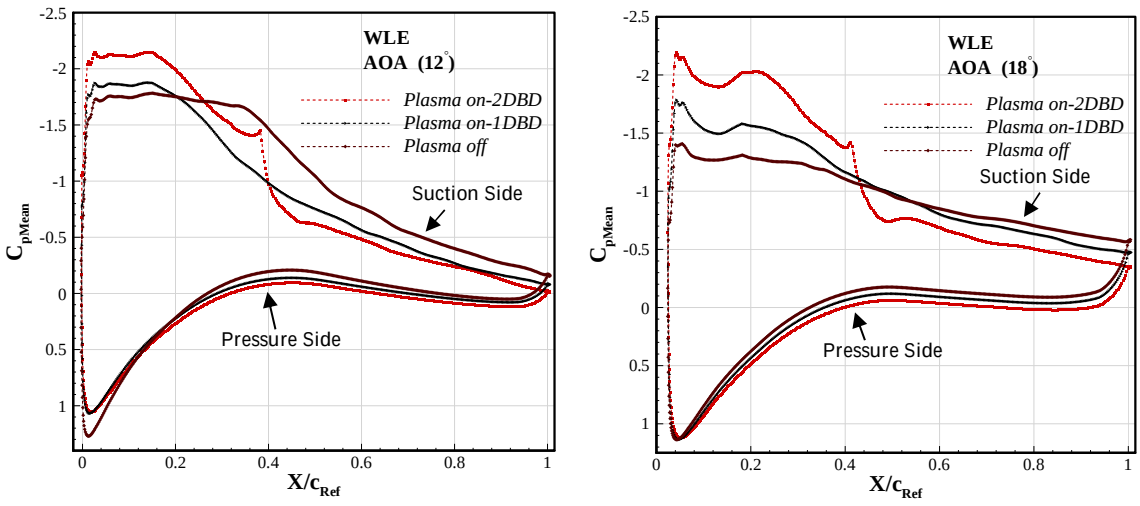

(a) (b)

Figure 5.21: Mean pressure coefficient distribution along the surface of the airfoil with and without the presence of DBD plasma actuators, cases with WLE: (a) α=12°, (b) α=18°.

Also, the C_{pMean} distributions in the case with WLE in combination with DBDs as passive and active flow control have a higher negative peak near the leading edge (plane in peak) compare to case with WLE with DBDs. Also, in Fig. 5.22 (a) and (b), the WLE and SLE cases with 2DBD plasma actuators are compared with each other. With the presence of the WLE, the flow is diverted towards the troughs as it passes over the tubercles. Resultantly, a considerable pressure gradient forms in the airfoil's spanwise direction and pressure immediately drops following the

trough. The effect of plasma is also is clearly visible. This proves the beneficial effect of spanwise and induced flow combination due to tubercles and DBDs, respectively. Following the negative peak in the leading-edge area, especially at the trough, pressure regions corresponding to a laminar separation bubble (LSB) are observed for these cases, which has a significantly higher effect with the presence of DBD. It is noted that the LSB length in the chordwise direction is higher in the AOA of 18°.

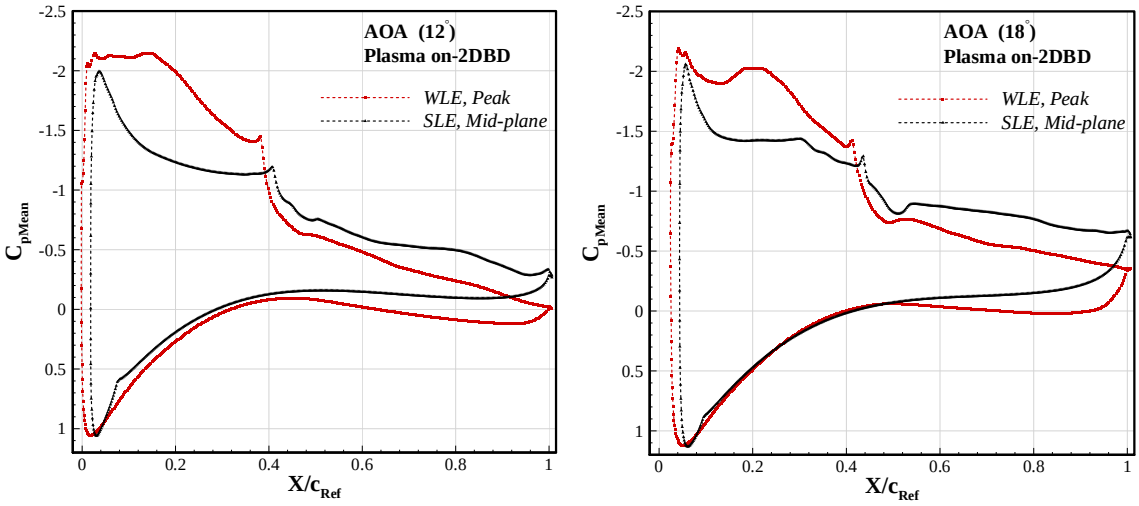

(a) (b)

Figure 5.22: Mean pressure coefficient distributions along the surface of the airfoil, comparison between the WLE (at peak) and SLE cases: (a) α=12°, (b) α=18°.

By comparing the mean pressure coefficients along the chord between the cases with and without DBDs with the presence of WLE in Fig. 5.23, it can be observed that the presence of the tubercle not only causes a sharp pressure decrease behind the trough but also causes a gradual drop decrease behind the peak. These drops are more intensive with the presence of the DBD plasma actuators compare to the case just with the WLE.

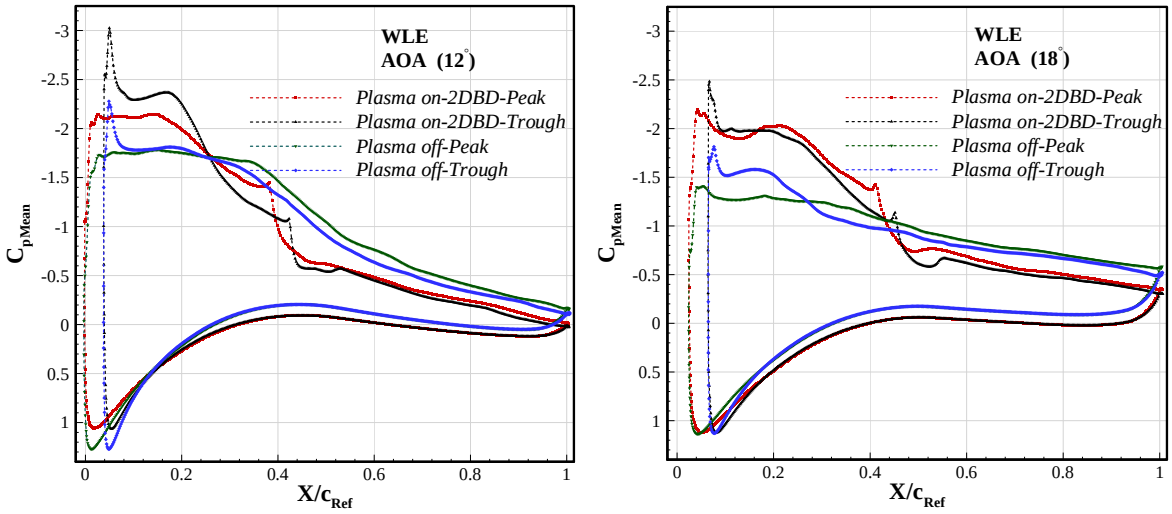

Figure 5.23: Comparison of mean pressure coefficients along the airfoil surface at the peak and trough of the WLE case, with and without presence of the DBDs: (a) α = 12°, (b) α = 18°.

Figure 5.24 illustrates the lift (C_L) and drag (C_D) coefficients temporal development for various considered cases in this study at $\mathrm{Re} = 0.5\times10^5$ and $AOA = 12^\circ$. The x-axis is plotted in non-dimensional time ($t^* = tU/C$), where U, C and t are the freestream velocity, chord length and flow time, respectively. The initial values of lift and drag coefficient vary significantly. Then, the values converge to the almost quasi-steady values, especially in the case with 2DBD plasma actuators due to the more separation suppression in comparison to other cases. Here, the data of the aerodynamic forces were averaged for the duration of $3 \le tU/C \le 16$, close to the flow reattachment transient duration that were reported by Sato et al. (2020) and Amitay and Glezer (2002).

The aerodynamic performance improves greatly in the case with 2DBD and WLE and only slightly in cases like 1DBD with SLE, in comparison to the cases with no flow control. Due to the flow control, fast and robust flow reattachment, stabilization, along with the increase/reduction of the lift/drag, respectively, are achieved.

For the case with 2DBD and WLE, the aerodynamic coefficients temporal oscillation cycles are significantly small, tend to be more stable in the average duration. The lower amplitude evidenced that the flow is continuously reattached and sucked up to the airfoil surface. On the other hand, the mentioned temporal unsteady fluctuations are remarkably large in the case without both active and passive flow control. These results demonstrate that the controlled flow, using the DBD plasma actuator and WLE, substantially reduced the amount of unsteady

temporal fluctuations at the periodic vortex shedding frequency, which arises from the separation of the leading-edge and is approximately steady in the aerodynamic performance terms. From Table 5.5, the averaged C_L and C_D for the 2DBD and WLE case are 0.75 and 0.160, which has the highest value among all the cases considered in this study. Comparison between WLE and SLE reveals that an increase in lift and a decrease in drag are obtained using the WLEs with DBD plasma actuator compared to the straight leading edge (SLE) case. The pair of counter-rotating streamwise vortices creation due to the WLE structure and their integration with the plasma jet by the DBDs significantly adjacent fully separated shear layers are discussed following. As has been discussed later, the improvement and degradation in aerodynamic performance is closely related to the leading-edge flow control mechanism in each case.

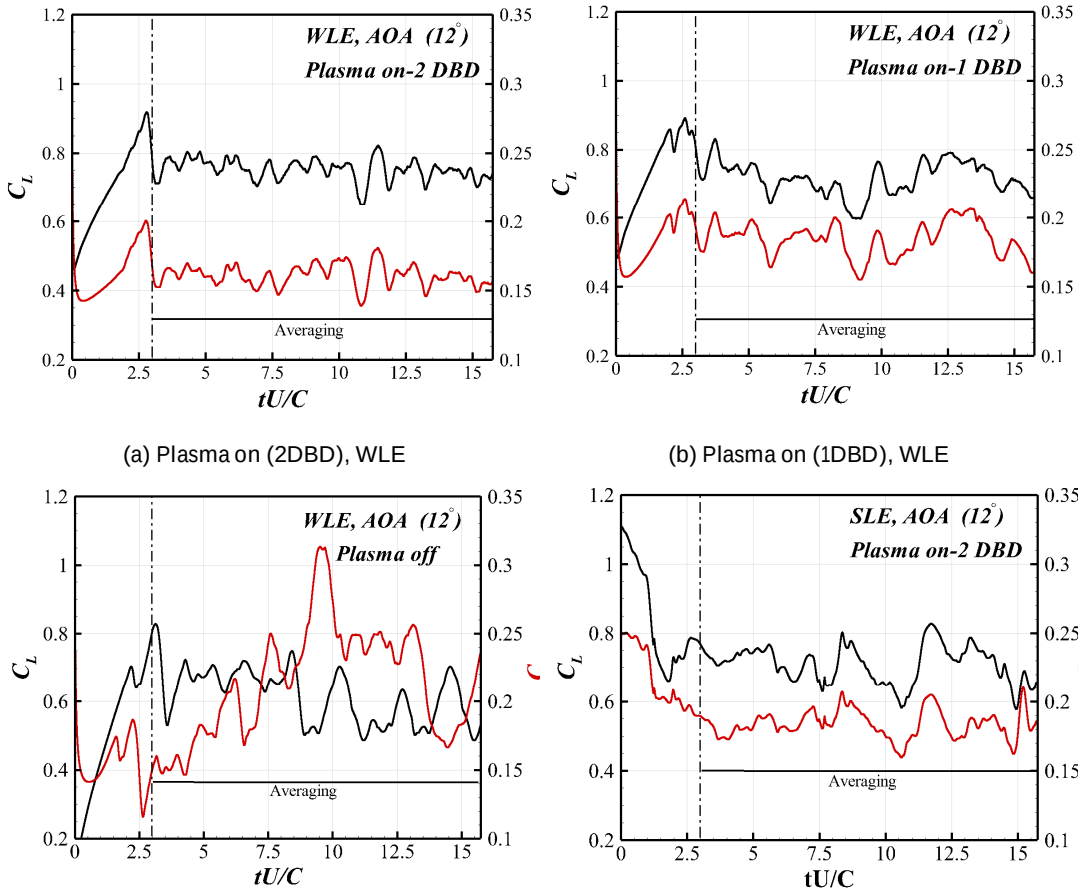

Figure 5.24: Time development of lift and drag coefficients at $\mathrm{Re} = 0.5\times10^5$ and $\alpha = 12^\circ$ for various cases. Solid black and red lines indicate lift and drag coefficients, respectively.

Table 5.5: Averaged lift and drag coefficients comparison for cases in Fig.5.24.

	averaged C_L	averaged C_D	C_L/C_D
Plasma on (2DBD), WLE	0.750	1.60E-01	4.68
Plasma on (1DBD), WLE	0.715	1.83E-01	3.91
Plasma off, WLE	0.685	2.12E-01	3.23
Plasma on (2DBD), SLE	0.740	1.80E-01	4.10

The power spectra of the instantaneous lift force in cases with the presence of the DBDs in the WLE and SLE airfoil proceed to compute in Fig. 5.25, and compared with the base case without any control. The output frequency is normalized by the freestream velocity (U_∞) and mean chord length (C_{mean}), giving a Strouhal number of $St = f\, C_{mean} \sin\alpha / U_\infty$. The acoustic streaming flow produced by the DBD plasma actuators in quiescent air can be observed in this figure. The associated scales seem to reasonably resemble Kolmogorov power-law decay ($f^{-5/3}$) scaling and can be judged that the turbulence spectrum and flow inertial subrange captured accurately.

For the case without active DBD flow control, for instance in $\alpha = 12^\circ$, there is a dominant frequency at $f \approx 31.4\,Hz$, which is typical of vortex shedding on bluff bodies. For the modified cases with DBD beside the WLE geometry, a broadband range of peaks is observed, for example, for 2DBD and WLE and $\alpha = 18^\circ$ from $f \approx 15.9\,Hz$ and tapers off around $f \approx 117.0\,Hz$. It can be concluded that the produced vortex shedding with the presence of DBDs is less coherent and contains broadband peak frequencies compare to being monochromatic or narrow peak in the PSD in the case just with the passive flow control with WLE. This broadband frequency is the prominent point of the power spectra in the case with DBD, which contains the notable energy that is produced utilizing the DBDs. With the absence of synchronization in the shedding and the consequences frequencies, the lower fluctuation amplitudes are observed, as discussed in Fig. 5.24. utilizing the DBD improves the flow separation, expedite the transitional process and earlier reattached the flow, and the produced frequencies effectually excite the natural unstable frequencies in the turbulent transition process and promote it.

It is found that the noise power spectrum instability shifts to broadband peak range with switching the case from the SLE to WLE. The reason is that the formation of the counter-rotating streamwise vortices between the tubercles by improving the momentum exchange, suppressing the instability noise. Also, it can be found that by growing the AOA, the instability noise leads to narrow peak from broadband hump in the considered cases with DBDs and WLE.

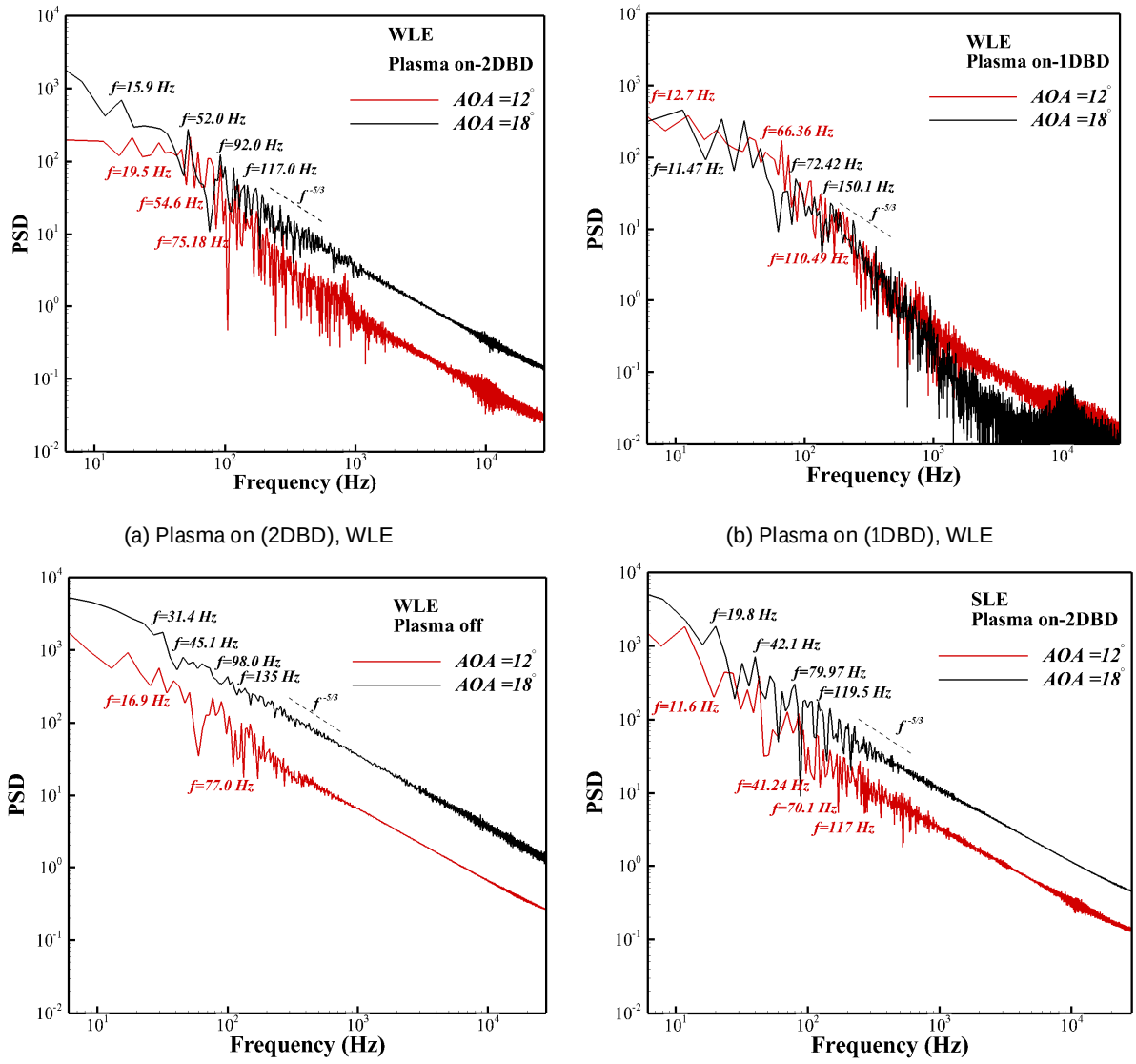

(a) Plasma on (2DBD), WLE

(b) Plasma on (1DBD), WLE

(c) Plasma off, WLE

(d) Plasma on (2DBD), SLE

Figure 5.25: Power spectral density (PSD) analysis of the measured aerodynamic forces at $\mathrm{Re} = 0.5\times10^5$. Solid red and black lines indicate $\alpha = 12^\circ$ and $\alpha = 18^\circ$, respectively.

Due to the unsteady nature of the plasma flow over the WLE airfoil, time consideration in the spectrum analysis is necessary. Signals have long-term low-frequency and short-term high-frequency components in the considered cases, as mentioned in Fig. 5.25. Thus, implementation of the wavelet analysis that produces accurate time resolution for high frequencies, as well as proper frequency resolution for low frequencies, can be so useful. The wavelet transform method is computed separately the signals various parts in the time dimension, unlike the Fourier transform analysis that produces the same transform for all times.

In Fig. 5.26 and 5.27, the continuous wavelet transform of the plasma flow and its effect on the flow fluctuations around the WLE and SLE airfoil is illustrated. The structure of the wavelet transform has a distinctively different pattern compare to each other by using SLE or WLE, with or without activation of the DBD plasma actuators. It can be found that compare to high range frequencies Strouhal numbers, lower Strouhal numbers, e.g., $St < 0.08$, have altitude (see Fig. 5.26 and 5.27). Moreover, based on Fig. 5.27, frequencies with a higher range that are indicated by D are damped rapidly in around $t = 0.125s$. Depends on the cases, lines with labels A to D are equivalent to the dominant frequencies that were evaluated in Fig. 5.25 by using the Fourier transform method. Another feature of the preceding contours is the positive slope of the lines, which shows the Strouhal numbers increment over time. Also, high frequencies are going to be damped with time.

Furthermore, the numbers 1 and 2, two peaks of line A in frames of Fig. 5.26 and 5.27, indicate the moments that one dominant separation type occure in our flow, as are shown in Fig. 5.28 to 5.30. According to the wavelet transform, by growing the AOA or using the SLE airfoil instead of WLE, the high-frequency cycles number is increased. By activation of both DBDs, the number of these cycles is decreased. Also, the damping duration of the high-frequency cycles is longer in higher AOA.

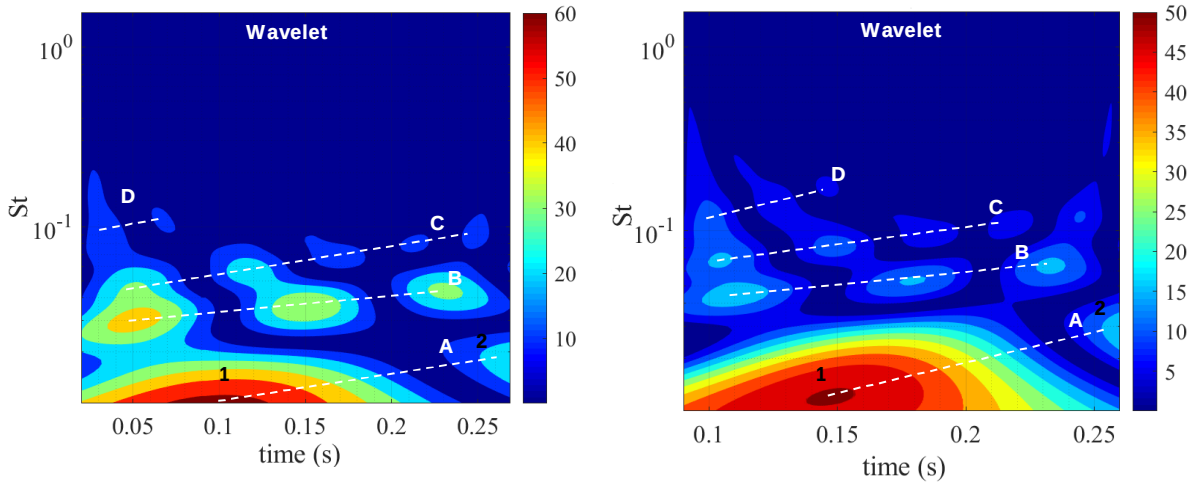

(a) Plasma on (2DBD), WLE

(b) Plasma on (1DBD), WLE

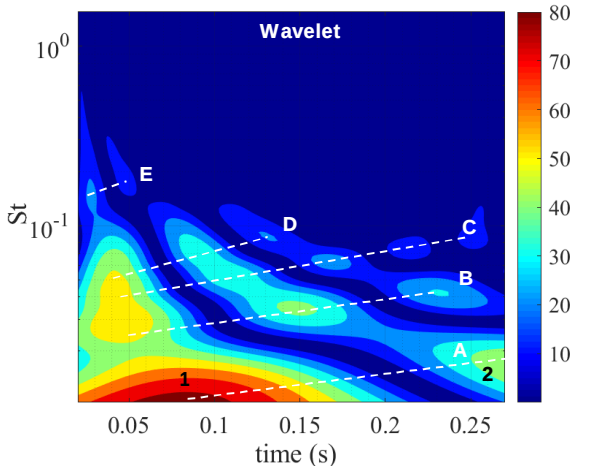

(c) Plasma off, WLE

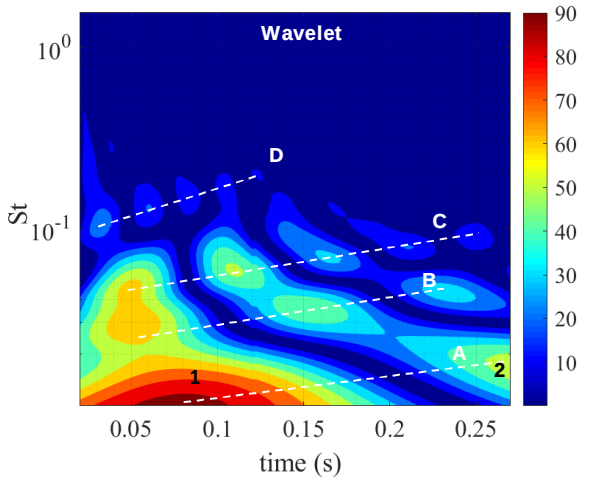

(d) Plasma on (2DBD), SLE

Figure 5.26: Wavelet transform analysis of plasma flow passing over the studied WLE and SLE airfoil at $\mathrm{Re} = 0.5\times10^{5}$, AOA=18˚.

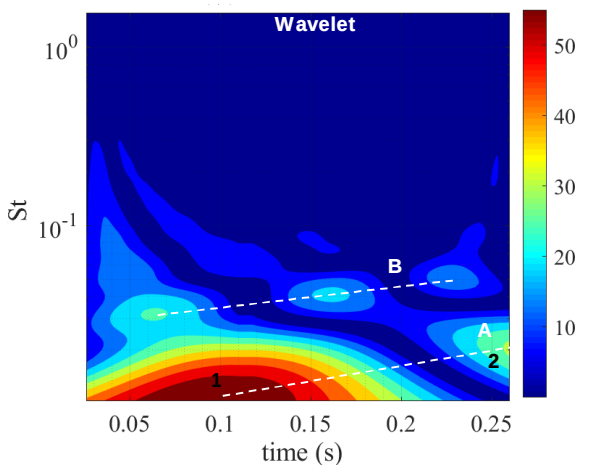

(a) Plasma on (2DBD), WLE

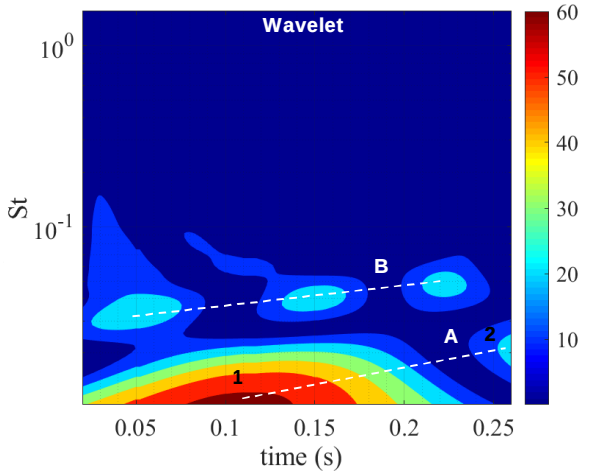

(b) Plasma on (1DBD), WLE

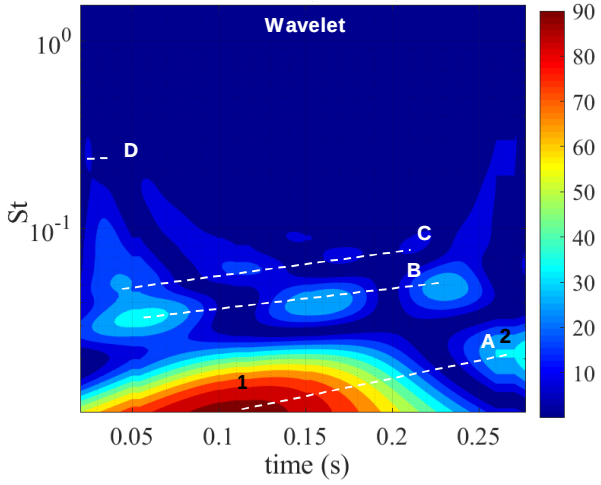

(c) Plasma off, WLE

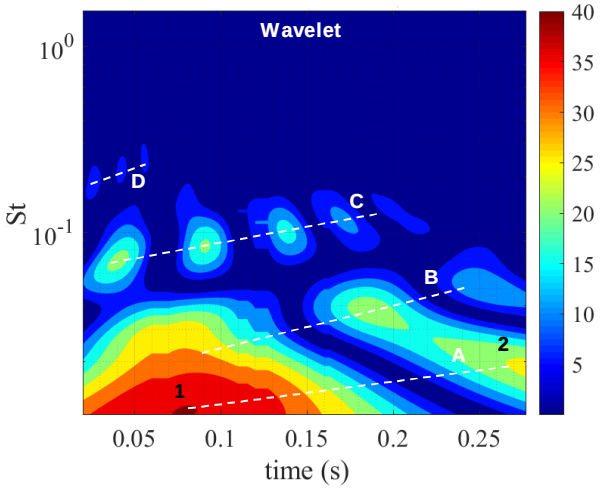

(d) Plasma on (2DBD), SLE

Figure 5.27: Wavelet transform contour of turbulence flow passing over the modified airfoil at $\mathrm{Re} = 0.5\times10^{5}$, AOA=12˚.

Figure 5.28 shows the isosurface of the zero time-averaged streamwise velocity for various cases considered in this study. This variation indicates the border between the separated and attached flow, because the flow direction reverses for the separated flow zone, resulting in a negative streamwise velocity value. The laminar separation bubble (LSB) that identified the formed low-pressure zone at the separation zone behind each trough also can be observed in the WLE cases. With the presence of DBDs the LSB volume becomes diminish significantly. Also, it can be found that the level of flow separation in the case of WLE and 2DBD is clearly suppressed and only in a small area near the trailing edge than in the SLE cases, especially when the plasma control is off. This is due to the combination of the induced flow near the locations of DBDs and the early development of LSBs near the wavy leading edge that prevents large flow separation. In the SLE case without DBDs, no LSBs are visible and significant areas of separation are identified, but with activation of two DBDs, the separation region is divided and diminished.

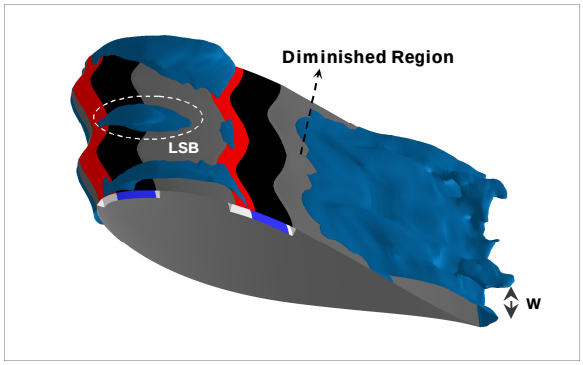

(a) Plasma on (2DBD), WLE

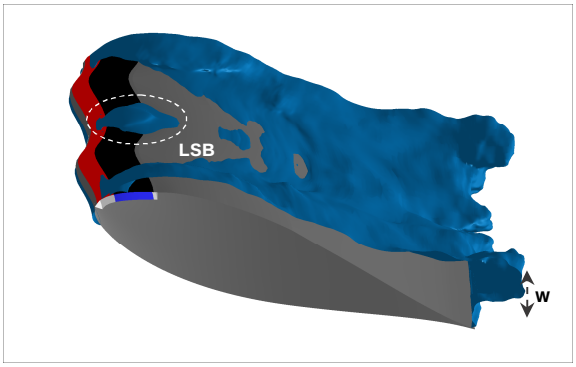

(b) Plasma on (1DBD), WLE

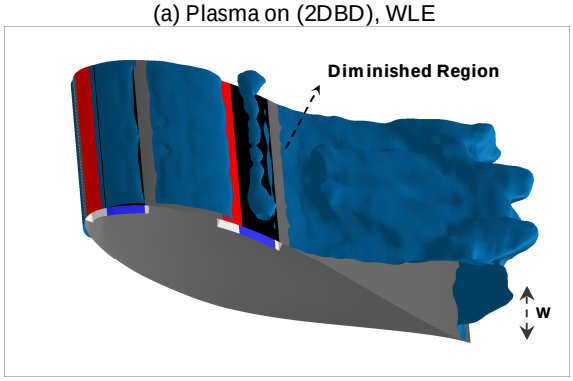

(c) Plasma on (2DBD), SLE

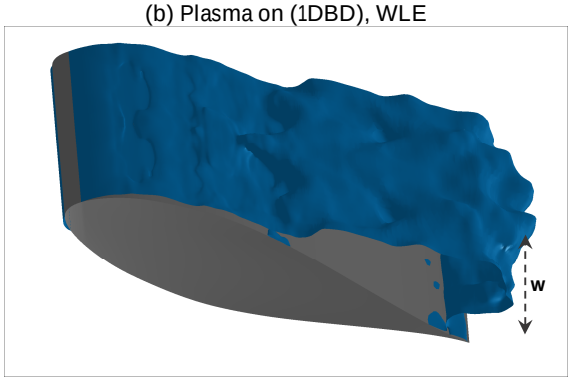

(d) Plasma off, SLE

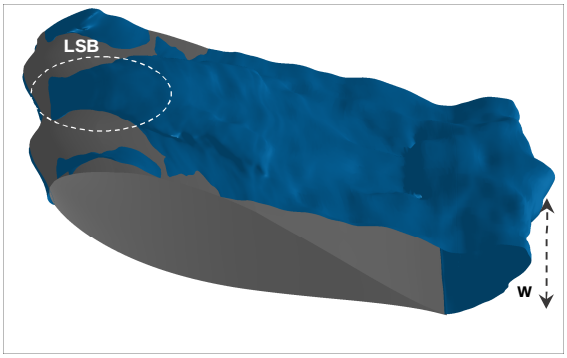

(e) Plasma off, WLE

Figure 5.28: The isosurface of zero streamwise velocity, showing flow separation, for the baseline and tubercled airfoil at AOA=18° and $\mathrm{Re} = 0.5\times10^{5}$, with and without plasma flow control.

Figures 5.29 to 5.31 show the time development of the spanwise vorticity for different geometry with WLE and SLE and different operational condition with activation of one or two DBD, at two various AOA ($\alpha = 12^{\circ}$ and 18°). In These figures, the plot at time t = T shows a fully stalled condition. As clearly illustrated in Fig. 5.29 and 5.30, the dynamics of the vortices are entirely different in various considered cases. These cases investigate which can achieve higher improvement by separation control between the active and passive control method. The LIC approach is used to visualize the vortices trains (VT) shed sequentially from the turbulent shear layer created by actuators. The use of the multi DBD plasma actuators with a sinusoidal wavy leading edge is able to split the original large-scale separation vortexes and broken them into a small-scale vortices series.

In the cases with plasma on (both DBD activation mode), the produced vortex and natural vortex shedding pairing occurs and then the momentum induction to the boundary layer happens and these vortices convect towards the trailing edge that leads to the separation suppression and lift increment by the negative vortex pressure, especially in the WLE case (see Figs. 5.29 to 5.32).

The large-scale spanwise vortices are not appeared in the lower AOA (12°) and fully detached (see Fig. 5.30). In the case with 2DBD and WLE, unlike the case with 1DBD, there was sufficiently injected momentum to the tangential direction along the WLE suction side and the flow separation reattachment was achieved under the induced wall jet flow effect. The effect of this flow for the lower angle of attack is more helpful (as shown in Fig. 5.30). The vortices trains shed by operation mode actuation, visualized with velocity streamline by the LIC approach, can break the main initial large-scale separation vortices into a succession of small-scale vortices,

which causes the separated flow reattachment. The vortices trains, which are not exist when the plasma is off (see Fig. 5.29), shed is improved the momentum transmission between the main flow and the boundary layer. This leads to the lift increments by vortex convection near the surface of the airfoil. In addition, a slight reduction in the drag coefficient is obtained by decreasing the separation bubble length. Also, it is observable with multiple DBD plasma actuators, the higher number of the vorticity trains can better improve the momentum transfer among the boundary layer and main flow. The altered separated shear layer has moved downstream and migrated away from the location of the plasma actuator. Plasma actuation improves the separation point, guides the separated region to the upper surface of the suction side, tends to attach to the surface, and makes it smaller, especially in the case of 2DBD.

Under the DBD plasma actuator operation on the WLE airfoil, the separated flow region becomes smaller (Fig. 5.28 and 5.29). Also, it can be found that the separated area significantly diminished when both DBDs are activated. As shown in Figs. 5.31 (label SP), a leading-edge separation happened in the SLE geometry when plasma is off.

By comparing the instantaneous streamline in Figs. 5.29 and 5.31, it can be found that the unsteady plasma actuation with the WLE succeeds in causing attachment of the flow separation to the airfoil compare to the SLE.

The contour maps of second invariant of the velocity gradient tensor (Q) are illustrated in Fig. 5.33 and 5.34, for different geometry with WLE and SLE and different operational condition with activation of one or two DBD, at two various AOA ($\alpha = 12^{\circ}$ and 18°). The Q is the criterion mostly used in the high turbulent flow for better extraction of the vortical structure. The induced spanwise vortices by the actuators can be clearly observed for all the cases with active control. It can be found that the vortices scales become finer and their density increases by using the DBD and WLE, particularly in the case of 2DBDs. These fine scale vortices produced by turbulent transition remarkably contribute to flow separation and reattachment, as discussed above in detail. These figures show that without plasma control, a leading-edge separation occurs in a large area. When plasma control is used, the separation region shrinks, but the flow around the airfoil still stays in a separated state.

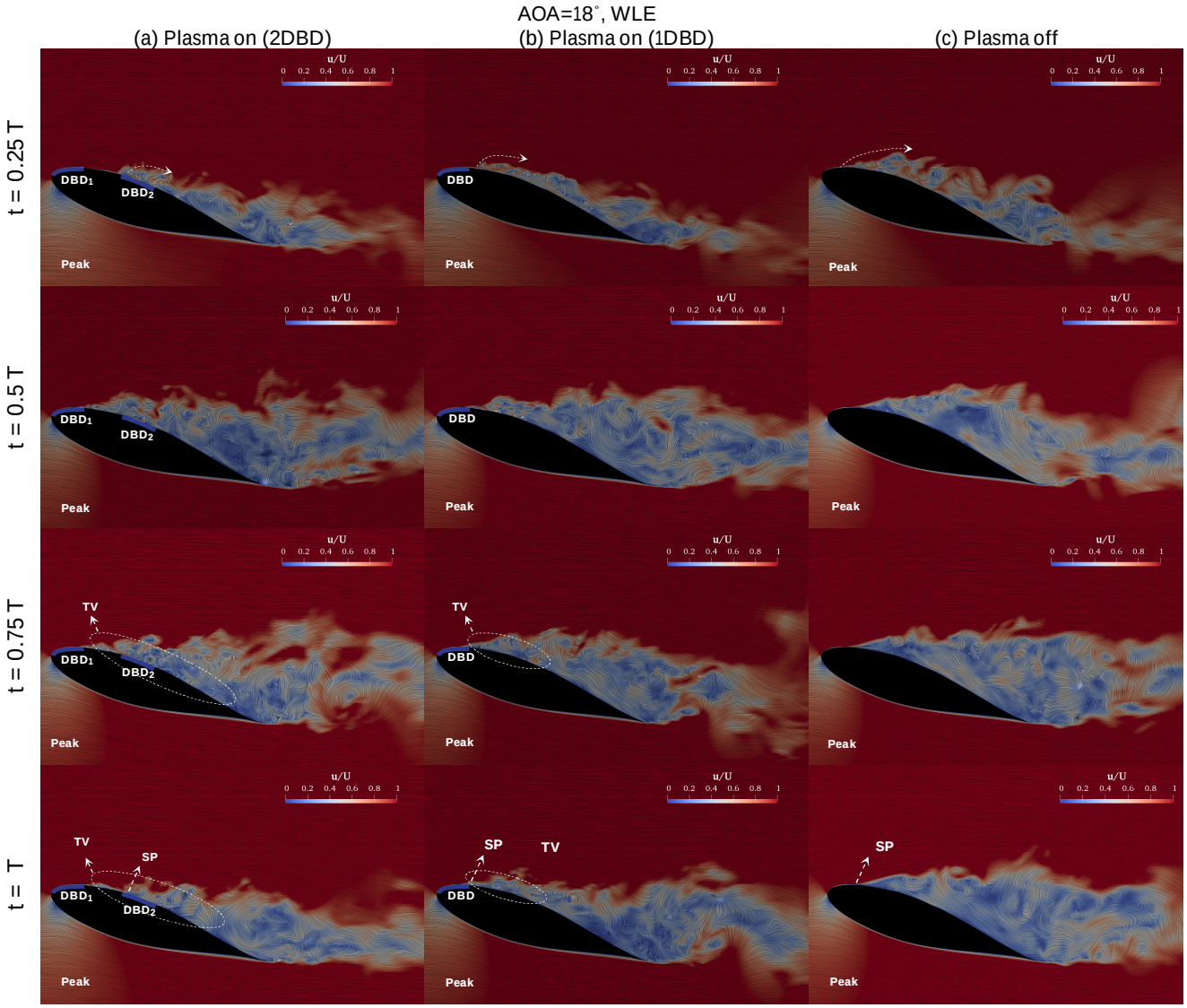

Figure 5.29: The contour of the normalized velocity magnitude with the presence of streamline pattern (visualized by the Line Integral Convolution (LIC) method) at AOA=18°, for the WLE (Peak) cases with plasma on (a) 2DBD (b) 1DBD and (c) plasma off. Each set of images shows 0.25T, 0.5T, 0.75T, and T in one typical cycle.

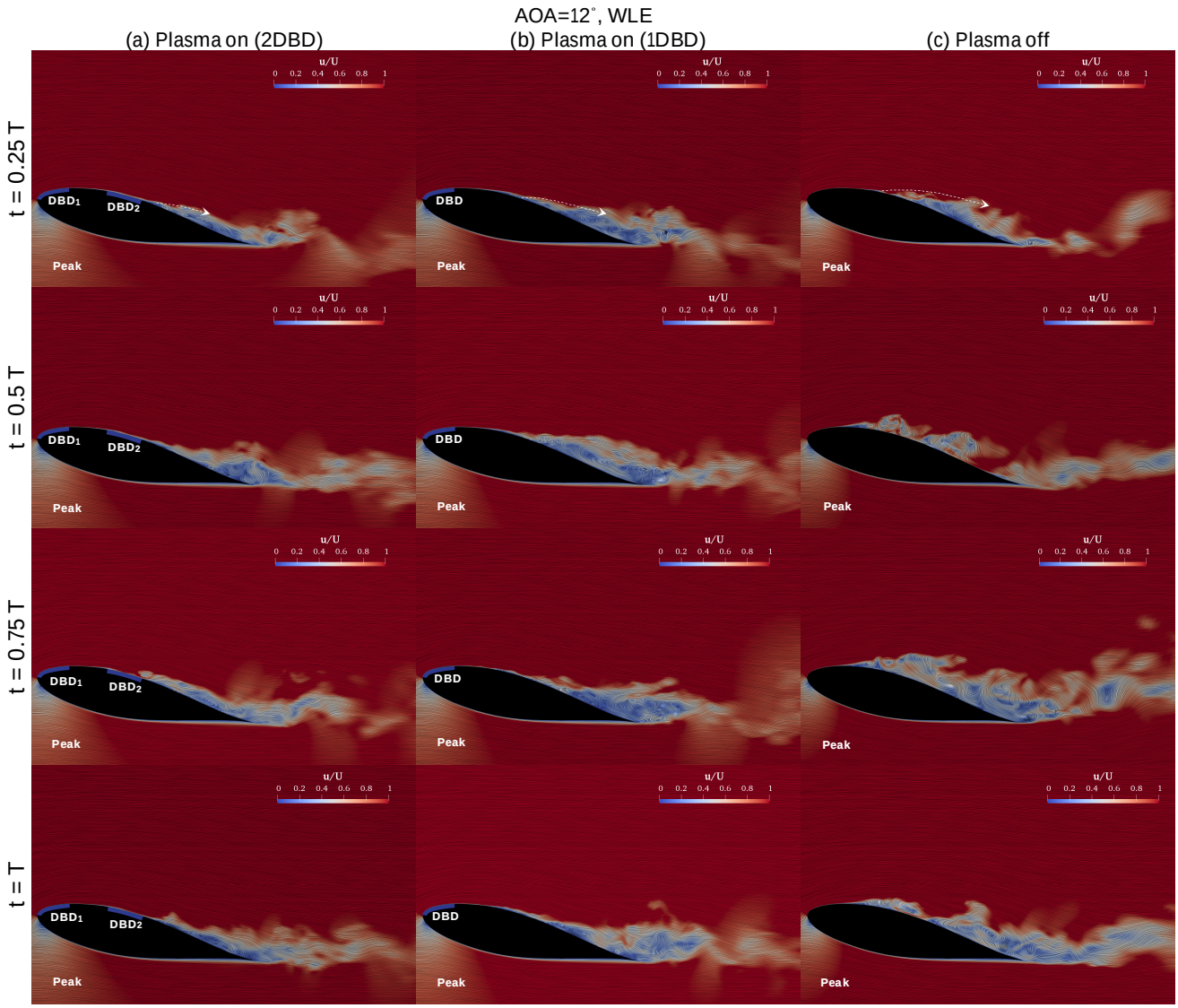

Figure 5.30: The visualization of the vortex structures with the LIC method on the contour of the velocity magnitude at AOA=12°, for the same operational condition of Fig. 5.28.

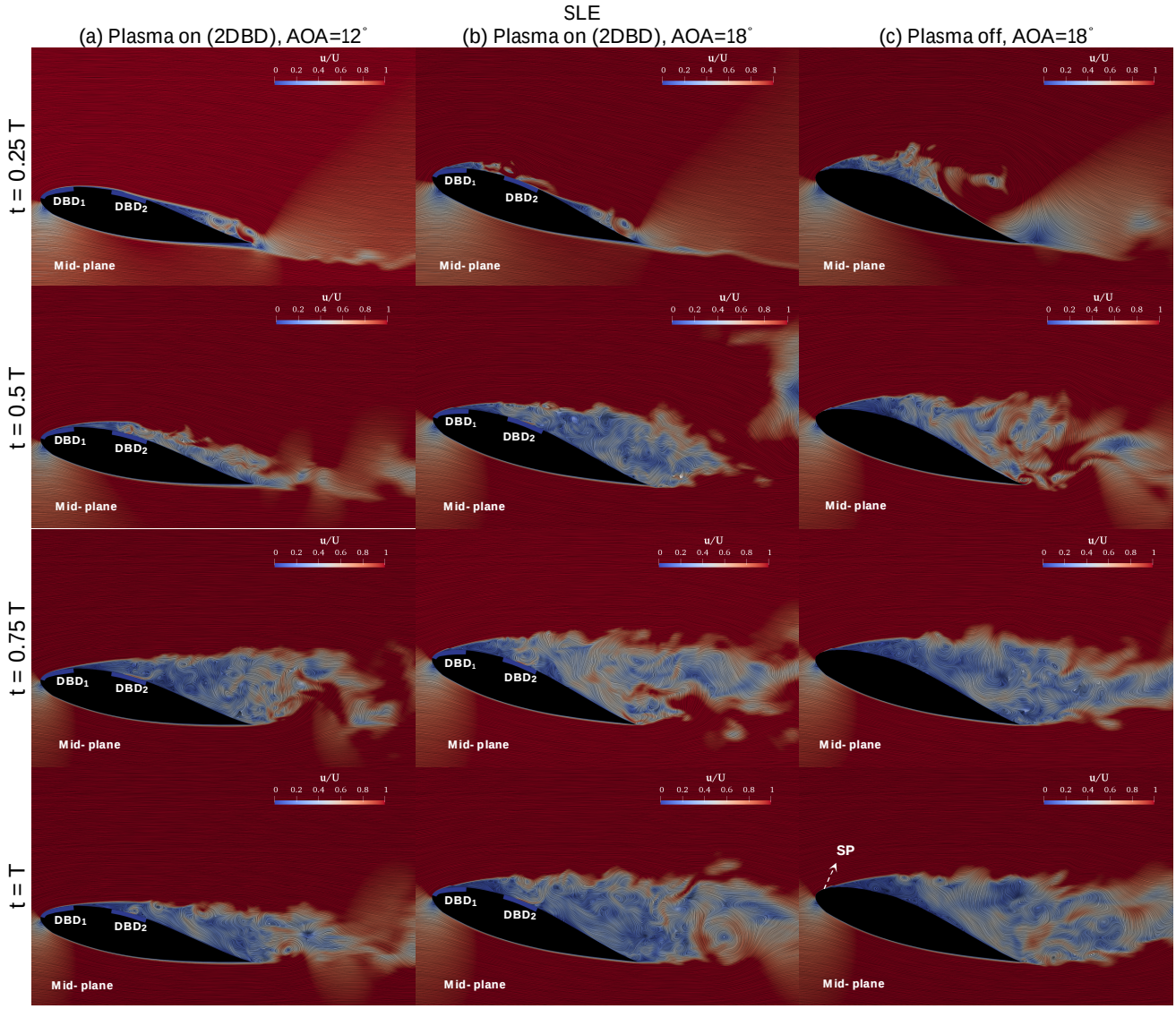

Figure 5.31: The contour of normalized velocity magnitude with visualization of streamline via LIC approach along 2D plane for the SLE cases (a) Plasma on (2DBD) AOA=12° (b) Plasma on (2DBD), AOA=18° (c) Plasma off, AOA=18°.

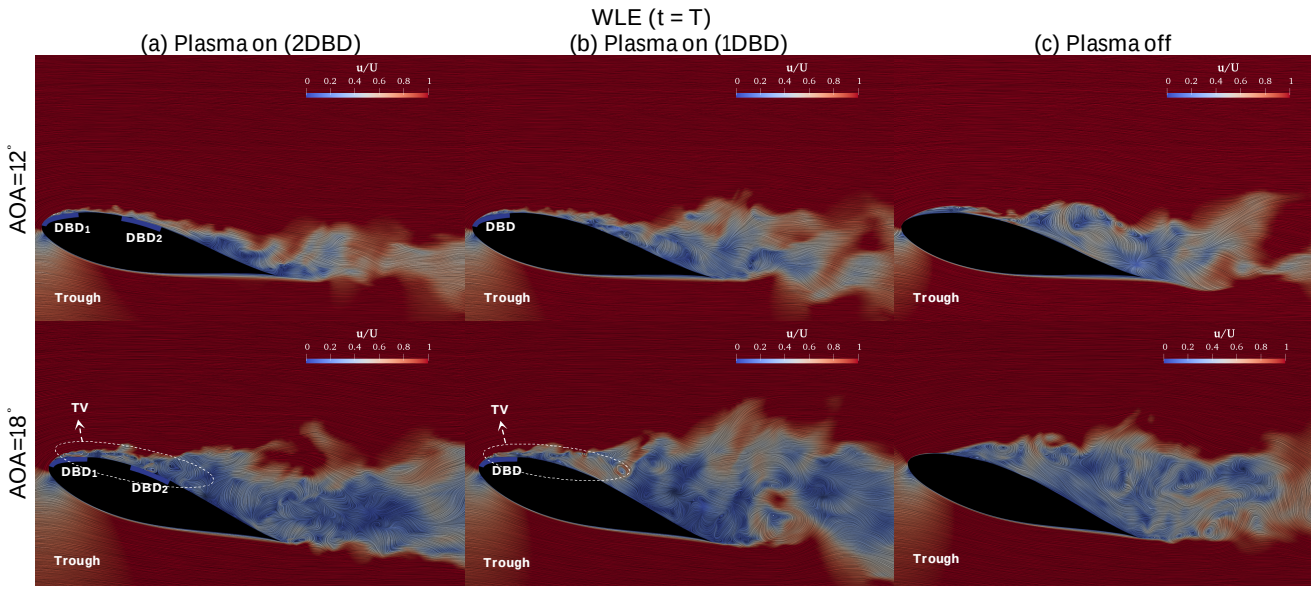

Figure 5.32: The contour of velocity magnitude contour with the streamline patterns at trough in the fully developed time of the flow, for the same operational condition of Fig. 5.28 and 5.29.

In the cases with WLE and DBD, the separated shear layer is clearly closer to the surface of the airfoil. To reduce the LSB near the leading edge, the actuator is located on the leading edge. From Figs. 5.33 and 5.34, compared to the case with no control, the LSB length is reduced and the suction peak becomes higher. This results from early reattachment of flow due to excitation with DBD that promotes turbulent transition of the LSB at the leading edge. Then, to excite the turbulent shear layer, the second actuator is positioned at the 30 % of chord length. The separated flow is suppressed (as shown in Fig. 5.28) by the sequential shedding of vortices from the turbulent separation shear layer that is induced by the actuation or natural vortex shedding. The spanwise vortices are shed sequentially from the turbulent shear layer as a result of the actuation. This leads to higher energy at the turbulent separation shear and excites the turbulent shear layer.

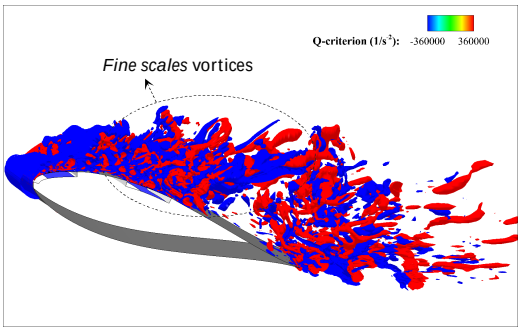

(a) Plasma on (2DBD), WLE, AOA=18°

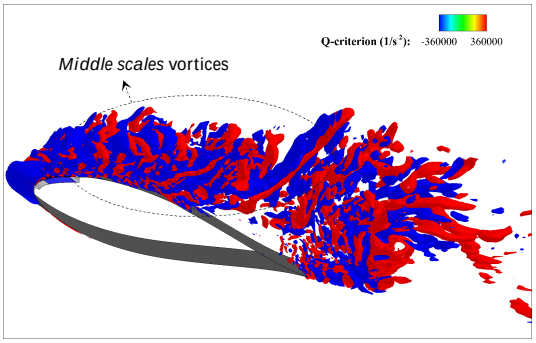

(b) Plasma on (1DBD), WLE, AOA=18°

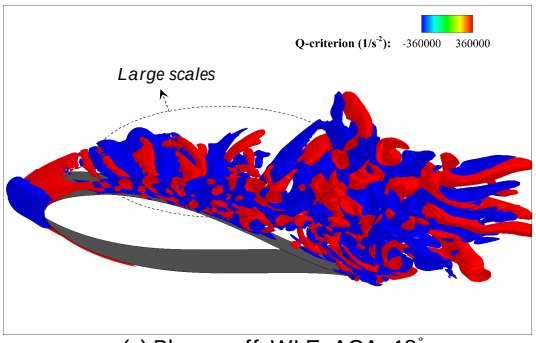

(c) Plasma off, WLE, AOA=18°

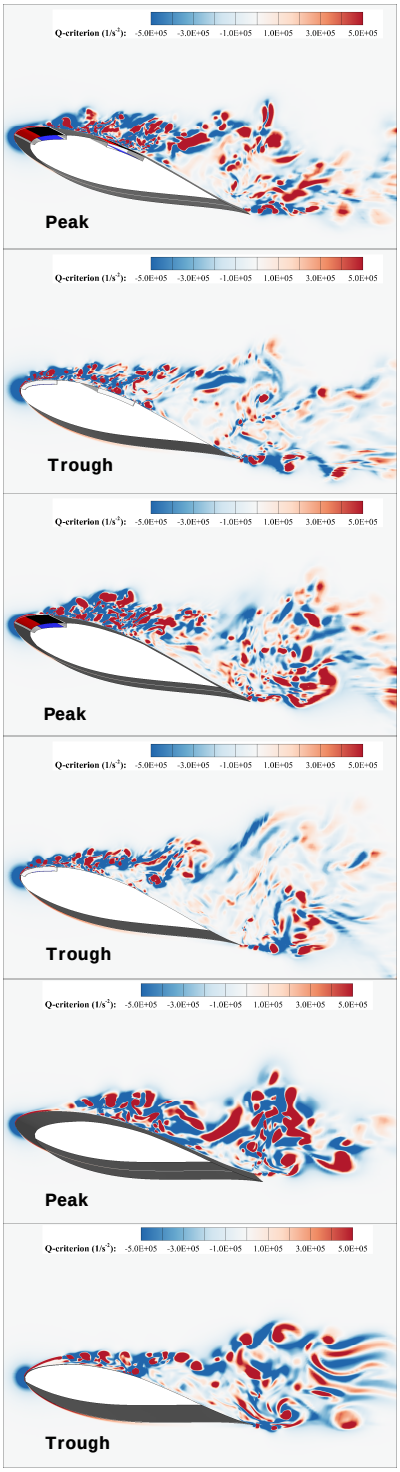

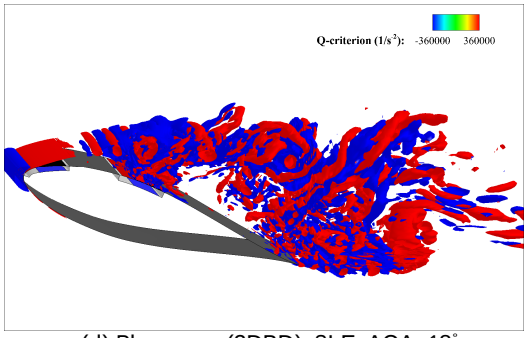

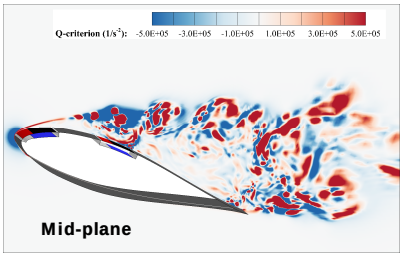

(d) Plasma on (2DBD), SLE, AOA=18°

Figure 5.33: The 3D iso-surfaces of second invariant of the velocity gradient tensor (Q) at $\mathrm{Re} = 0.5\times10^5$, AOA=18°, for the WLE cases with plasma on (a) 2DBD, (b) 1DBD, (c) plasma off and the SLE with plasma on (d) 2DBD (left frames). Besides, the planes at trough and peak are visualized (right frames).

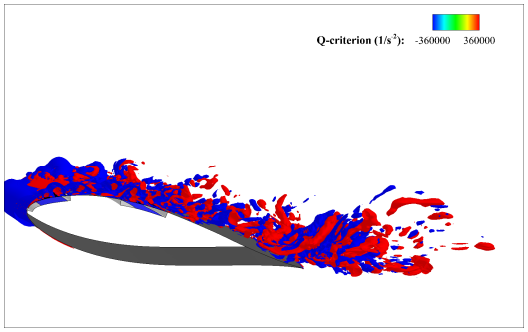

(a) Plasma on (2DBD), WLE, AOA=12°

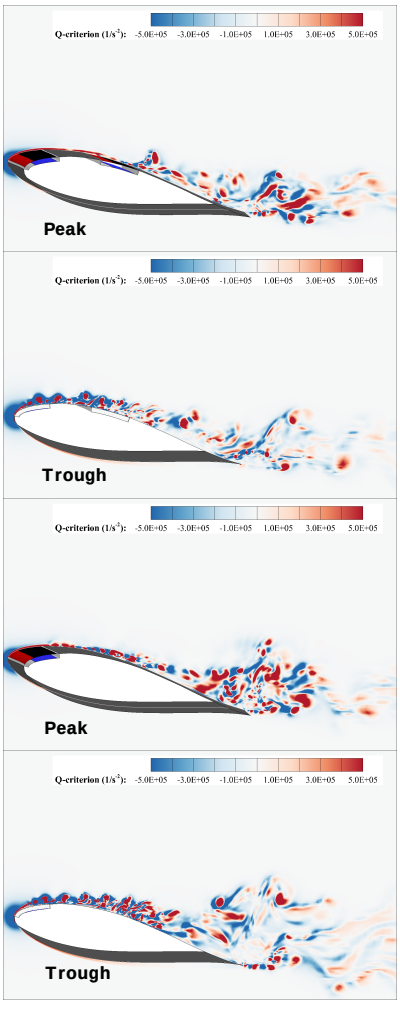

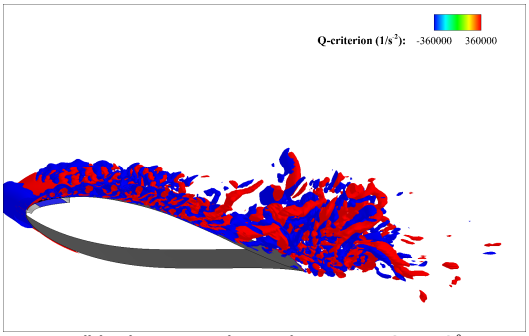

(b) Plasma on (1DBD), WLE, AOA=12°

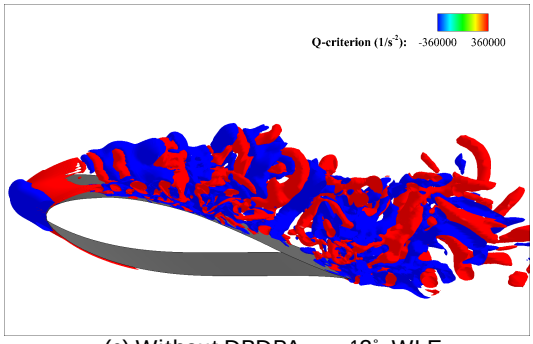

(c) Without DBDPA, α=12˚, WLE

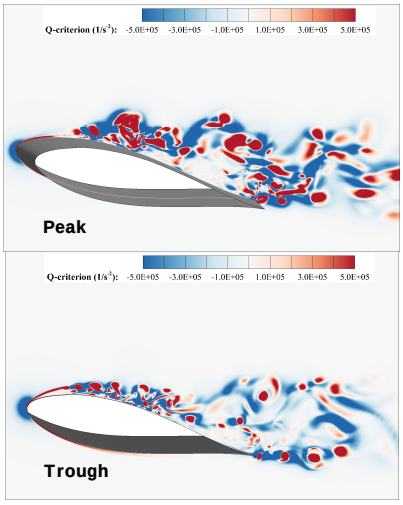

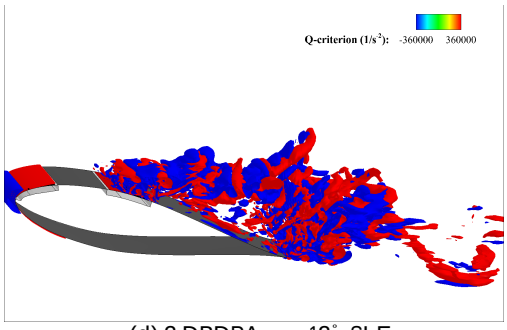

(d) 2 DBDPA, α=12˚, SLE

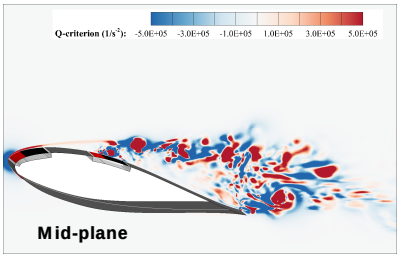

Figure 5.34: The 3D iso-surfaces of second invariant of the velocity gradient tensor (Q) at $\mathrm{Re} = 0.5\times10^5$, AOA=18˚, for the same operational condition of Fig. 5.31.

5.5. Conclusion

(I) Conclusion for Aerosol dispersion investigation: The main goal of the current work is to perform a detailed analysis of the transport characteristics and related fluid dynamics for saliva droplets occurring due to sneeze in an indoor environment. The following topics were discussed in detail: (a) Identifying the micro-droplet transmission mechanisms that are expelled during sneezing within the respiratory tract (b) Characterization of the expelled micro-droplet, including size distribution and velocity, in order to mimic the experimental conditions. (c) Compare the effect of the different size-range of micro-droplets, and its influence on the transmission routes and deposition pattern (d) Determine a safe settling area based on information from a hundred cases with various initial velocities ($V_{Initial}$), micro-droplet size distribution (D_P), injection angle (θ_{Inj}), and mouth opening area (e). By further quantifying external factors like air-conditioner, and the flow created by a window and a door in the room. (f) Considering various social distancing positions: face-to-face, meeting standing, and near an equipment.

The following remarkable findings can were identified:

1. We deduced polynomial correlations for the maximum length and width of the contaminated area by considering various sneeze conditions.

2. Sneezing at $V_{Initial} = 22.3\ ms^{-1}$, with an average size of $D_{mean} = 90\,\mu m$, caused the saliva droplets to be transported at a distance around 2.3 m, but larger droplets $D_{mean} = 540\,\mu m$ extended at an even larger length, of more than 4 m.

3. Evaluating various horizontal sneezing angles revealed that a full bending of our head, used as a protective action, reduces the droplets traveling distance by more than 22%.

4. The saliva droplet dispersion analysis confirmed that face mask-wearing, due to sneezing, is a very effective protective measure against the spreading of an infectious disease. With this, the maximum transmission area of the droplets is a sphere with a diameter of 0.6 m and this corresponds to about one-third of the distance a droplet traveled by a naked face.

5. Standing opposite to polluters, face to face is more susceptible to infection as compared to other positions. The full discharge of a hard sneeze, and its deposit on a surface, takes around 3 seconds.

6. The effect of gravity and inertia forces on small saliva droplets ($D_{droplet} \approx\leq 40\,\mu\mathrm{m}$), in comparison to the influence of the indoor airflow, is negligible. Medium ($50 \approx\leq D_{droplet} \approx\leq 150\,\mu\mathrm{m}$) and large ($D_{droplet} \approx\geq 200\,\mu\mathrm{m}$) size saliva droplets are more affected by the gravity and inertia forces, respectively.

7. Our results indicate that the 2 m social distance may not suffice, since it will depend on the environmental conditions. To improve safety this distance should be increased to around 4m.

8. During the sneeze of people with various mouth sizes the contamination area is different and can experience a 50 % increment.

9. The saliva droplet deposition pattern is extremely dependent on the initial size distribution that can be circular, elliptical and chaotic shape with a corresponding reduction of the size distribution, respectively.

10. Transportation of the saliva droplets is accelerated by the presence of turbulence in the mouth air jet. Also, appropriate ventilation can effectively control the direction of saliva-disease-carrier and provide a healthy indoor environment.

11. Shorter people are at higher risk of facial contact, since their faces are located on the trajectory of the falling micro-droplets.

(II) The current bioinspired study's objective is to investigate the ability of the optimal configuration, contains two curved DBD plasma actuators in combination with WLE airfoil, in flow control under different AOA. To analyze separation control and vortical structure, the WLE and SLE airfoils were examined as cases with single and double DBD actuators and compared to the case without DBD. Induction of the small-scale vortices by two plasma actuators at $x/C = 3\%$ and $x/C = 30\%$ over the WLE airfoil, greatly separation suppressions as a consequence of that, leads to the highest lift enhancement with appreciable reduction of lift fluctuation and hysteresis and earlier reattachment of the flow. This gives the WLE airfoils superiority over other SLE airfoils in the DBD applications. Wavelet and FFT analysis of the aerodynamic forces, as well as the second invariant of the velocity gradient tensor and LIC streamline contour analysis are employed to investigate the shedding structure, flow unsteady frequencies,

boundary layer, trains of vortices shed and separation layer instabilities. From frequency analysis, the natural unstable frequency is excited more by the presence of the DBDs, which is results in earlier reattachment due to faster turbulent transition.

Chapter 6

Electrostatic Sprayer Based on High-voltage Retractable Blades or High-voltage Adjustable Control Ring[5]

Abstract

This chapter is based on the submission of our patent which is presenting a novel electrostatic spraying mechanism for industrial coating with high rotary bell sprayer based on high-voltage retractable blades or high-voltage adjustable control ring.

6.1 Electrostatic Sprayer Based on Retractable Blades or Adjustable Control Ring System Definition

The present invention relates to an electrostatic spraying system with high rotary bell sprayer based on high-voltage retractable blades or high-voltage adjustable control ring. This invention has advantages such as higher coating transfer efficiency, reduction of losses of the liquid or mixture dispensed and less environmental impact.

The system comprises a rotary bell cup (1), a paint injection nozzle (2), a plurality of shaping air nozzles (3), stainless steel high-voltage gun body (4) and a grounded aluminum gun body (5). In one embodiment it comprises retractable blades constituted by stainless steel high-voltage retractable blades (6), mounted on the front side, and retractable blades insulating cover (7), mounted on their back side, and both of them (6) and (7) are fixed on retractable blades base holder (8) with an electrical insulating cover while, in another embodiment, it comprises a high-voltage adjustable control-ring (9), with a stainless steel pipe grip clamp body (10), a pipe grip clamp screw (11), a plurality of control-ring pin levels (12), a pipe grip clamp holder (13), a high-voltage adjustable control-ring base frame holder (14) on the gun body, a high-voltage adjustable control-ring frame holder (15) and a frame holders connector (16).

[5] Based on the work submitted as a patent, Electrostatic Sprayer Based on High-voltage Retractable Blades or High-voltage Adjustable Control Ring, Application Ref.: PAT 117317 L.

6.2. Description

6.2.1 Technical Domain

The present invention relates to an electrostatic sprayer which operates with high-voltage retractable blades or high-voltage adjustable control ring for improvement of the atomization process and increment the transfer efficiency of the liquid particles projection against target surfaces.

6.2.2 Summary

The present invention discloses an electrostatic sprayer capable of dispensing a liquid or mixture for coating, disinfection or pesticides application with improvement of the atomization process and increment the transfer efficiency. The electrostatic sprayer system comprises a rotary bell cup, at least a paint injection nozzle, a plurality of shaping air nozzles, a stainless-steel high voltage gun body and an aluminium zero voltage gun body. The electrostatic sprayer operates in two different embodiments. In one embodiment, it comprises retractable blades constituted by a front side stainless steel high-voltage retractable blades and a back side of high voltage retractable blades made of non-conductive cover which are operated in such a way that generate a more efficient pattern of the equipotential lines of the electric field in order to control the sprayed charge particles with a more desirable force in a forward direction, toward the target surface. In a second embodiment, the electrostatic sprayer comprises a high-voltage adjustable control-ring, with a stainless-steel pipe grip clamp body, a pipe grip clamp screw, a plurality of pin levels of high-voltage adjustable control-ring and a pipe grip clamp holder, in such a way that the diameter of the high voltage ring can be adjusted in order to intensify the influence of the electrostatic force and prevent the deviation of the atomized particles in the radial direction.

6.2.3 Prior Art

The invention described herein is based on an electrostatic sprayer which makes use of high-voltage retractable blades or adjustable high-voltage control ring to control the spray plum of the atomized particles and improve the transfer efficiency.

Prior art document, namely document WO 2009/012025 A2 (Seitz, 2009), discloses a coating device comprising a bell cup and a motor for rotating the bell cup. It includes also a conduit for feeding the coating material to the interior of the bell cup as the bell cup is rotated by the motor. In this device compressed air is coupled to the annular slot to generate and direct a first air stream at an exterior of the bell cup. Besides, it contains at least one additional opening coupled to the compressed air that generates and directs a second air stream to combine with the first air stream. The document WO 2004/041443 A2 (Wang, 2004) discloses a method and apparatus to improve the atomization and the deposition efficiency of liquid particles. For this purpose, it is used a spray gun with an electrode with high voltage placed at a position near to the spray gun that sprays the liquid by hydraulic pressure or by compressed air. The shape of the electrode is similar to the sprayer pattern and thus it can be constituted by a circular aperture electrode to

produce a circular cone spray or two linear electrodes, on each side of the flat spray, in such a way that the electric charges can be induced onto the majority of the liquid particles. The document WO 03/072263 A1 (Sumiyoshi, 2003) discloses an electrostatic spraying device configured to electrostatically charge and dispense a liquid from a supply to a point of dispersal. This electrostatic spraying device is constituted by a nozzle to disperse the liquid composition, a channel between the reservoir and the nozzle, a power source and a high voltage power supply, a high voltage electrode which electrostatically charges the liquid composition within the channel at a charging location and contains a portion disposed between the reservoir and the nozzle. Document US10464084 B2 (Nolte et al., 2019) discloses various exemplary illustrations for electrode assembly in an electrostatic atomizer and exemplary methods to use them for coating of workpieces by means of electrostatically supporting atomization, in particular by means of the electrostatic rotary atomization. The rotary atomizer with an electrode atomizer assembly comprises an electrode holding device for holding at least one electrode or a plurality of electrodes. The electrodes of this electrode assembly are provided to generate an electrostatic field which contributes to creating discharge currents flowing at least over a housing surface. The document US 10894262 B1 (Cooper, 2021) discloses an electrostatic sprayer system for dispensing and dispersing a liquid containing a spray compound. This system presents a spray dispersal feature that reduces the time that a spray cloud containing droplets remains suspended after spraying. The sprayer system includes a sprayer having a nozzle for charging, atomizing and spraying the liquid and charging and the spraying the air or a non-active liquid. The document US 7056387 B2 (van der Steur, 2006) discloses an apparatus and method for isolating an electrostatic sprayer from an electrically grounded target. This apparatus includes an electrostatic sprayer, which is a part of a manoeuvrable robot arm. This electrostatic sprayer has the capability of spraying a conductive coating liquid onto a workpiece. The coating liquid is supplied from a remote source of supplier through at least one distribution circuit associated to the sprayer. The document WO 2004/071670 A1 (Allen, 2004) discloses an electrostatic atomizer which comprises a channel through which a fluid passes, one or more orifices to allow the fluid to exit the atomizer and at least two electrodes in contact with the fluid. When the atomizer is operated, an appropriate potential is applied to the electrodes and the fluid particles are charged. The electrode contacting region with the fluid comprises a closely contiguous array of non-fibrous conductive elements forming an array of individual electrode points where the field generated by the atomizer is concentrated. The document US 2001/0032897 A1 (Shawpittman, 2001) discloses an electrostatic sprayer which makes use of a pulsating voltage that is obtaining by using a battery or generator as power supply coupled with a step-up transformer. The step-up transformer is located near the spray nozzle and the high voltage pulse is rectified and applied to the electrostatic electrode in order to electrify the spray that is jetted from the spray nozzle. Considering this arrangement, the high voltage is applied to the electrostatic electrode with a minimized loss. The document WO 2013/018477 A1 (Terebessy, 2001) discloses an electrostatic atomizer which includes a spray site, a spray electrode connected to the spray site, a reference electrode and a power supply. In this atomizer the spray electrode and the reference electrode are arranged in such a way that an electrical charge of the

content to be atomized is counterbalanced by production of at least equal amount of opposite electrical charge at the reference electrode. The aim of this invention is to provide an electrostatic atomizer which may be changed in terms of arrangement and configuration being uncomplicated and presenting low cost.

The previous documents disclose electrostatic sprayers or atomizers however the current devices still fail on controlling the trajectory of particles with various ranges or sizes and the generation of an efficient spray plum conduction remains problematic. None of the previous documents integrate high voltage retractable blades or high voltage adjustable control ring and also do not present any mechanism to control the electrostatic distribution in order to achieve higher authority over the trajectory of the particles. In the present document we disclose an electrostatic sprayer system that in one embodiment operates with high voltage retractable blades and in another embodiment operates with a high voltage adjustable control ring. The use of high voltage retractable blades or adjustable high voltage control ring allows to manipulate and control the electric field distribution, as well as the electrostatic equipotential lines, which will directly influence the atomization process and allow a better control over the atomized particles.

6.3. General description

Following unfavourable phenomenon like the overspray happening, low paint film quality, low values of transfer efficiency, excessive material consumption, and high environmental pollution during conventional coating methods, the development of the coating apparatus is a vital issue. Electrostatic sprayers, due to their superior spraying performance, have been developed rapidly during recent years and became a key coating technology. Electrostatically charge painting apparatuses effectively grow the coating transfer efficiency during a shorter process time. Using this generation of sprayer leads to a superior coating performance, high-quality uniform coatings, material cost reduction, uniform film thickness with a high-quality and decrement of the environment's destructive impacts. Electrostatic painting process via high-speed rotary bell sprayer is broadly used in industries, especially in the automotive coating industries. One of the critical issues with any paint spray pattern formation, due to an electrostatic rotary bell, is the ability to control the trajectories of paint particles with various ranges of sizes. While an apparent attempt has been directed during the years toward achieving more efficient results in conduction of the trajectory of the droplet but efficient spray plum conduction remains problematic. The smaller atomized droplets generally tend to be more influenced by produced electrostatic forces and shaping air and travel more directly toward the grounded target to be coated. The paint droplets with larger sizes are less affected by electrostatic forces and move higher outward of the sprayer's bell cup, as an oversprayed and deviated flow. By increasing the rotational speed of the rotary bell cup, the particle size will be reduced, so that electrostatic force can better control the droplets trajectory. Some particles with larger sizes deviate from the target that must be coated. The ceilings and walls of the automotive spray booth, coating robot arms and housings, and body of the sprayer gun can become coated with these stray particles. Other high mass paint droplets are moderately affected by electrostatic forces and shaping air.

The newly described and illustrated systems by this work tend to more incorporate atomized droplets, especially larger droplet size, into the main stream of the spray plume and formation the bulk of the pattern. It helps keep the surrounding areas clean, reduction of the material cost and decrease of the environmental pollution. Also, it tends to a superior coating overall transfer efficiency.

The electrostatic spraying involves three main sub-processes of (a) the film, ligament, and droplet generation inside the rotary bell cup, (b) transportation of the formed paint materials, and (c) paint film formation on the target. The invention described herein consists of a novel electric field generation system, which includes a unique high-voltage retractable blades design and an unique high-voltage adjustable control-ring design. These two complicated novel designs, assemblies to the electrostatic sprayer, are an adequate system for significant development of the transfer efficiency, making the coating process much more efficient.

Due to the high rotational speed of the rotary bell cup, up to 70 KRPM, the generated centrifugal force affects the injected liquid. Consequently, the film, ligament, and droplets are formed on the inner surface of the bell cup and stretched radially. Then these generated droplets are more disintegrated because of the remarkable relative velocity among the liquid and gaseous phases. Then, strong axial forces, which are produced by the electrostatic generated field and high-pressure shaping airflow, directed the droplets towards the target.

This invention introduces two different control systems to drive the charged atomized droplets towards the goal workpiece, based on generating a more efficient electric field between the rotary bell cup and the workpiece to more electric force affects the charged particles movement's direction. These technologies take advantage of the ionization of the airflow by a high-voltage with maximum absolute negative values of around -90 kV through a safety distance among the rotary bell cup and target, which can be used for intensely painting spray flow control. These electrostatic sprayers can operate in different depending operational conditions, for instance, the type of film pattern, pain material, workpieces shape. The integration of the three main forces of rotary bell cup rotational speed, the generated electrostatic force, and the injected shaping airflow affect the trajectory of paint droplets due to their locations and the charge values.

The technology introduced in this invention as a new class of the electrostatic sprayer, by generating the electric fields controller due to the high voltage adjustable control-ring or high voltage retractable blades, makes them versatile coating tool for the most demanding industrial finishing requirements, which is created a uniform paint distribution with the highest values of transfer efficiency. Both the disclosed embodiments of high-voltage adjustable control-ring and high-voltage retractable blades thus achieve more efficient paint spray pattern control, higher transfer efficiency with less liquid paint consumption, lower overspray phenomenon happening lead to cleaner surrounding environment and equipment, the ability to provide the narrower pattern with the smaller shoulder of the spray plum precisely in the area of the target that must be coated and less manual cleaning and the resulting downtime.

6.4. Description of the Drawings

In this part For better understanding of the present application, figures representing preferred embodiments are herein attached which, however, are not intended to limit the technique disclosed herein.

Figure 6.1: a) Represents a schematic of the coating system, applied to an electrostatic rotary atomizer, with a combination of high-voltage retractable blades, where:

1 – Rotary bell cup,

2 – Paint injection nozzle,

3 – Shaping air nozzles,

4 – Stainless steel high-voltage gun body,

5 – Grounded aluminium gun body,

6– Stainless steel high-voltage retractable blades,

7 – Retractable blades insulating cover,

8 – Retractable blades base holder.

b) Illustrates a schematic of the coating system, applied to a high-speed electrostatic rotary bell sprayer, with a combination of high-voltage adjustable control-ring, where:

9 – High-voltage adjustable control-ring,

10 – Pipe grip clamp body,

11 – Pipe grip clamp screw,

12 – Control-ring pin levels,

13 – Pipe grip clamp holder,

14 – Control-ring base frame holder,

15 – Control-ring frame holder,

16 – Frame holders connector.

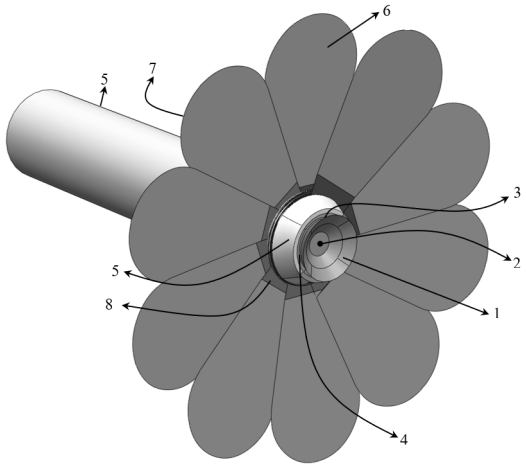

(a)

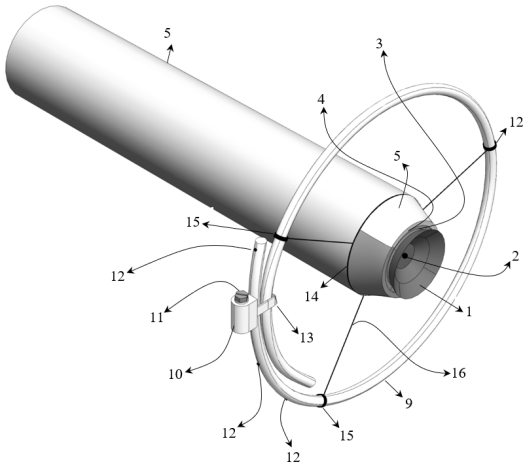

(b)

Figure 6. 1: Schematic representation of the electrostatic rotary atomizer, in combination with (a) the high-voltage retractable blades, and (b) high-voltage adjustable control-ring.

Figure 6.2: Represents a perspective view, from the front, of certain details of the apparatuses illustrated in Fig. 6.1;

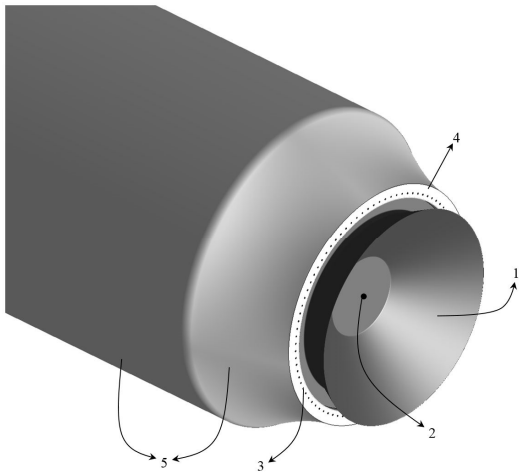

Figure 6. 2: Close-up view of the sprayer apparatus' head.

Figure 6.3: a) Illustrates a perspective view, from the front, in semi-closed mode of the apparatus illustrated in Fig. 6.1 (b); b) Illustrates a perspective view, from the front, in fully-closed mode of the apparatus illustrated in Fig. 6.1 (b);

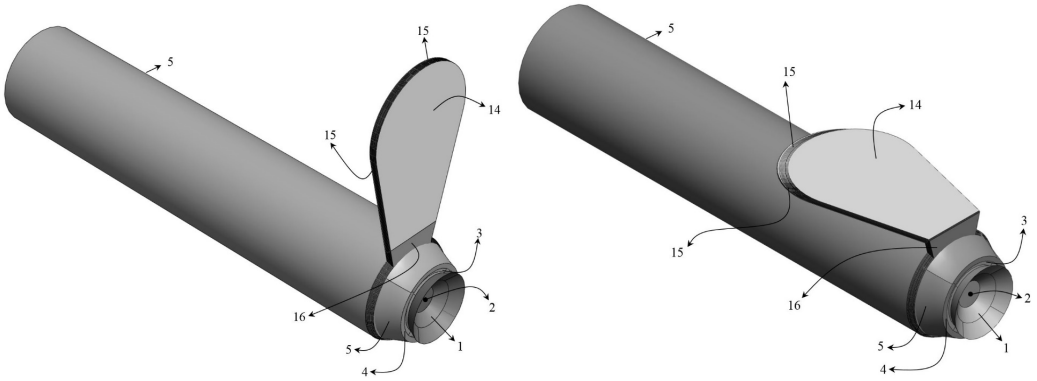

(a) (b)

Figure 6. 3: Perspective view of the electrostatic rotary atomizer with the high-voltage retractable blades in (a) semi-closed, (b) fully-closed, modes.

Figure 6.4: Representation of the electrostatic equipotential lines distribution around electrostatic sprayer due to different apparatus: (a) retractable high-voltage field pattern blades and sprayer head; (b) high-voltage adjustable control-ring and sprayer head; (c) high voltage head of the sprayer body.

In which (17) is the target surface and (18) is the equipotential lines distribution.

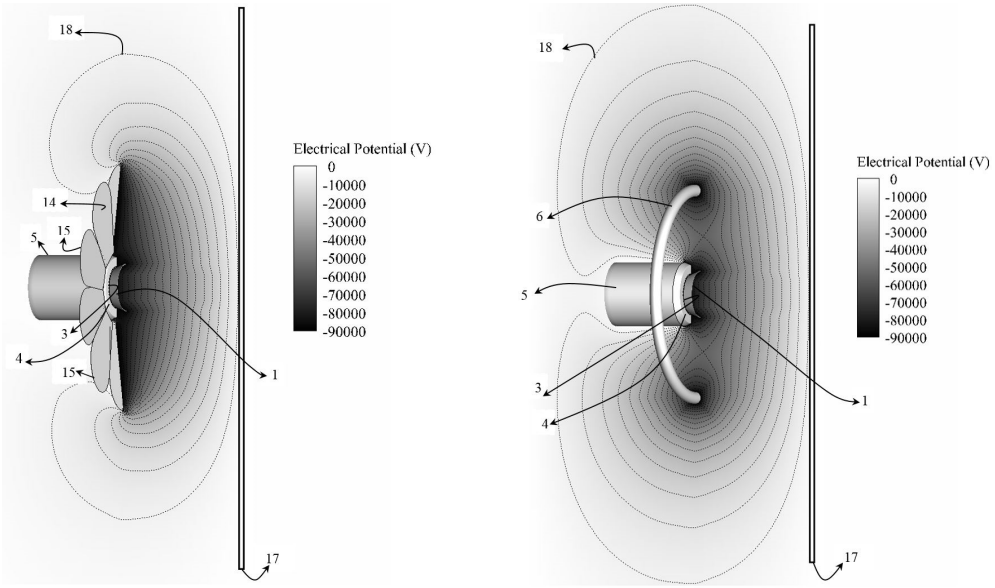

(a) (b)

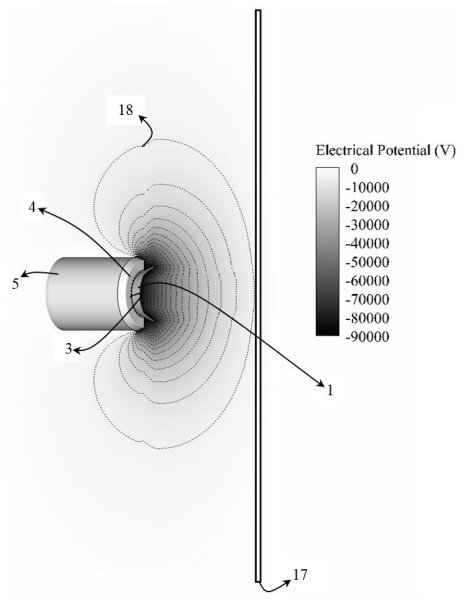

(c)

Figure 6. 4: Representation of the electrostatic equipotential lines distribution around sprayer with (a) high-voltage retractable blades, (b) high-voltage adjustable control-ring, and (c) typical ones.

Figure 6.5: Schematic representation of the new electrostatic sprayer applied on a standard automotive spray booth system, in which

17 – Target surface,

19 – Paint spray plume pattern,

20 – Floor grating,

21 – Air exhauster,

22 – Water pond,

23 – Flooded paint,

24 – Return sluice,

25 – Ground,

26 – Robotic equipment holder base,

27 – Inlet air supplier,

28 – Sliding rails,

29 – Paint booth control system,

30 – Paint booth monitoring system,

31 – Manual operator input,

32 – High voltage unit,

33 – Voltage converter,

34 – Air compressor,

35 – Paint container,

36 – Paint feeding conduit,

37 – High-pressure air conduit,

38 – High voltage cable.

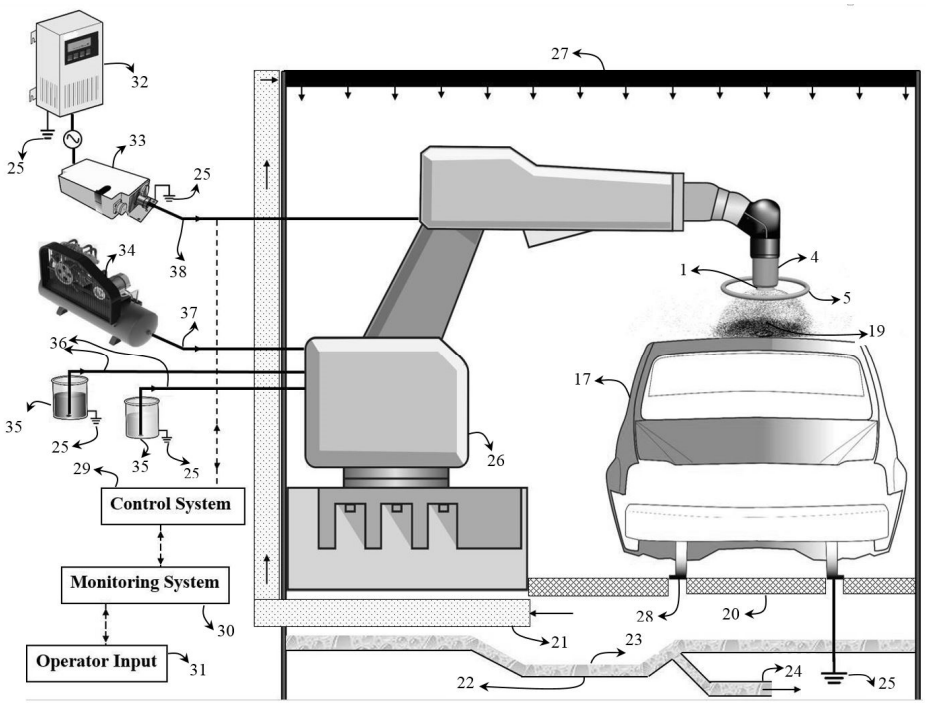

Figure 6. 5: Schematic representation of the new electrostatic sprayer in a standard automotive spray booth.

Figure 6.6: Illustrates the complicated pattern of the paint droplet trajectory schematically that can be divided into four various behaviours:

39 – Paint droplet toroid–shape vortex,

40 – Large size droplet trajectory,

41 – Small size droplet trajectory,

42 – Rebounded droplet from the target with the circular pattern,

43 – Over sprayed paint droplets near the spray plum shoulder.

44 – Motor.

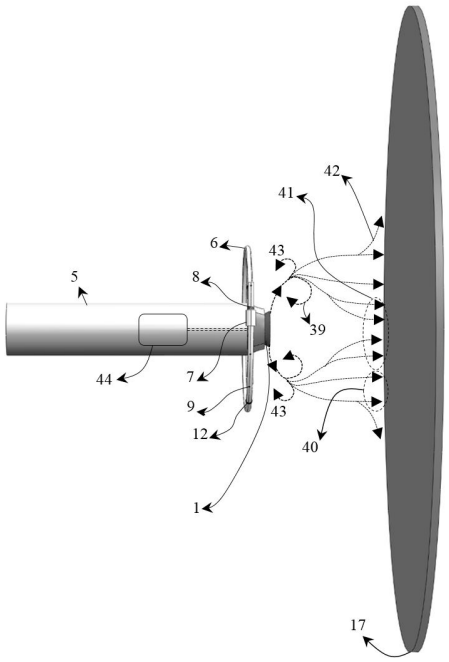

Figure 6. 6: Schematic pattern of the paint droplet trajectory around sprayer with high-voltage adjustable control-ring.

Figure 6.7: Indicates the complicated airflow pattern (visualized with the Line Integral Convolution (LIC) method) that can be divided into four main behaviours of:

45 – Inside toroid–shape air vortices,

46 – Outside toroid–shape air vortices in the spray plume shoulder,

47 – Shaping airflow stream,

48 – Outside toroid–shape air vortices near the target workpiece.

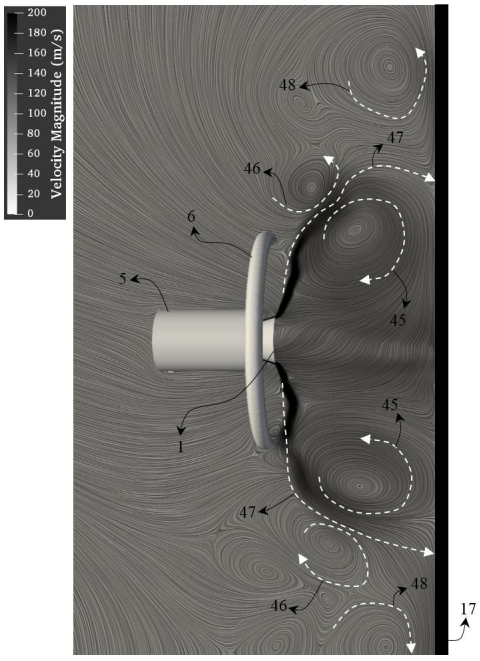

Figure 6. 7: Complicated airflow pattern (visualized with the Line Integral Convolution (LIC) method) around sprayer with high-voltage adjustable control-ring.

6.5. Matching numbers

(1): Rotary bell cup,
(2): Paint injection nozzle,
(3): Shaping air nozzles,
(4): Stainless steel high-voltage gun body,
(5): Grounded aluminium gun body,
(6): Stainless steel high-voltage retractable blades,
(7): Retractable blades insulating cover,
(8): Retractable blades base holder.
(9): High-voltage adjustable control-ring,
(10): Pipe grip clamp body,
(11): Pipe grip clamp screw,
(12): Control-ring pin levels,
(13): Pipe grip clamp holder,
(14): Control-ring base frame holder,
(15): Control-ring frame holder,
(16): Frame holders connector,
(17): Target surface.
(18): Equipotential lines distribution,
(19): Paint spray plume pattern,
(20): Floor grating,
(21): Air exhauster,
(22): Water pond,
(23): Flooded paint,
(24): Return sluice,
(25): Ground,
(26): Robotic equipment holder base,
(27): Inlet air supplier,
(28): Sliding rails,
(29): Paint booth control system,
(30): Paint booth monitoring system,
(31): Manual operator input,
(32): High voltage unit,
(33): Voltage converter,
(34): Air compressor,
(35): Paint container.
(36): Paint feeding conduit,
(37): High-pressure air conduit,
(38): High voltage cable,
(39): Paint droplet toroid–shape vortex,

(40): Large size droplet trajectory,
(41): Small size droplet trajectory,
(42): Rebounded droplet from the target with the circular pattern,
(43): Over sprayed paint droplets near the spray plum shoulder,
(44): Motor,
(45): Inside toroid–shape air vortices,
(46): Outside toroid–shape air vortices in the spray plume shoulder,
(47): Shaping airflow stream,
(48): Outside toroid–shape air vortices near the target workpiece.

6.6. Detailed Description

This invention comprises an electrostatic sprayer system with high voltage retractable blades or high voltage adjustable control ring. The embodiment illustrations are presented in Fig. 6.1 and are based on the concept of efficient external electrical charging that is produced by high-voltage retractable blades (6) or a high-voltage adjustable control ring (9) assembled with a grounded aluminium gun body (5). In both embodiments the electrostatic sprayer comprises a rotary bell cup (1) which rotates with high rotational speed and a paint injection nozzle (2) through which the paint particles or other type of particles (such as chemicals or pesticides) are injected. Rotary bell cups (1) with diameters of 35mm, 50 mm, and 65 mm can be used for different operating conditions. In addition, both embodiments comprise a plurality of shaping air nozzles (3) in order to produce the shaping air flow and a stainless-steel high-voltage gun body (4) coupled to the grounded aluminium gun body (5).

In one embodiment, represented in Fig. 6.1 (a), the system comprises retractable blades that are constituted by front side stainless steel high-voltage retractable blades (6) and back side retractable blades insulating cover (7) and are mounted in the system by means of a non-conductive retractable blades base holder (8). These retractable blades assembly is introduced to create an electrostatic field that contributes to generating discharge current flowing over a housing surface. Using high-voltage circular, retractable, detachable blades that are connected to the electrostatic atomizer body can be adapted for the respective purpose, for instance, painting in the external environment. In one embodiment, ten retractable blades with equal intervals (36˚) that are mounted on the retractable blades base holder (8) spaced radially outwardly with an angle of around 6˚ degrees compared to the axis perpendicular to the sprayer's axis. The front sides of high-voltage blades are made of conductive stainless-steel, and the back sides of high-voltage blades are covered with insulating material. The retractable blades maximum length and width in cross-section are 130.0 mm and 80.0 mm, respectively, equally circumferentially spaced at 36° intervals around the rotary bell cup (1) axis of rotation on the gun body.

In another embodiment, represented in Fig. 6.1(b), the system comprises a high-voltage adjustable control-ring (9) containing a stainless-steel pipe grip clamp body (10) with a pipe grip clamp screw (11) which allows to fasten the high voltage control ring in the different control-ring pin levels (12). This system allows the operation of the electrostatic sprayer system

for a wide range of high voltage control ring diameters. Besides, the system comprises a pipe grip clamp holder (13), a high voltage adjustable control-ring base frame holder (14) on the gun body, high-voltage adjustable control-ring frame holder (15) and a frame holders connector (16) that allow to fix and set the adjustable control ring system in the desired position.

The high-voltage adjustable control-ring assembly is provided to create an electrostatic field that contributes to generating discharge current flowing over a housing surface. By changing the levels of available four-pin that are placed on the body of the high-voltage adjustable control-ring (9), it is possible to provide a changeable electric field for the different operation of the atomizer, for example in which can be open to achieve a higher radius of electric filed in the condition with higher rotational speed or external painting or using compressed air.

Figure 6.2 shows in detail the geometry of the electrostatic sprayer, which includes a high-voltage rotary bell cup (1), a paint injection nozzle (2), a plurality of shaping air nozzles (3), a stainless-steel high-voltage gun body (4) and a grounded aluminium gun body.

Figure 6.3 shows the new electrostatic sprayer system with the blades retracted, in which (1) represents the rotary bell cup, (2) represents the paint injection nozzle, (3) represents a plurality of shaping air nozzles, (4) represents the stainless-steel high-voltage gun body and (5) represents the grounded aluminium gun body. As exemplified in Figure 6.3, the retractable blades constituted by front side stainless steel high-voltage retractable blades (6) and back side retractable blades insulating cover (7) are attached to the gun body by means of a non-conductive retractable blades base holder (8) and, accordingly with the operation conditions, they can be retracted and their influence on the electrostatic field is cancelled.

Fig. 6.4 shows the electrical potential and equipotential lines distribution for the different embodiments wherein (1) represents the bell cup, (3) represents a plurality of shaping air nozzles, (4) represents the stainless steel high-voltage gun body, (5) represents the grounded aluminium gun body, (9) represents the high-voltage adjustable control-ring, (6) represents the stainless steel high-voltage retractable blades, (7) represents the back side retractable blades insulating cover, (17) represents the grounded target surface and (18) represents the equipotential lines distribution. This figure illustrates the equipotential lines distribution (18) issuing from openings of the retractable blades base holder (8) or high-voltage adjustable control-ring (9) spread in the high range to reach the target surface (17). An appropriate relationship must be maintained among the discharged paint droplets from the bell cup edge and the electrostatic equipotential lines distribution band.

Suppose the electrostatic field distribution is too close to the rotary bell cup (1) (Fig. 6.4(C)). In that case, the equipotential lines with a high absolute value of negative voltage having a limited effect on the dispensed sprayed droplets. In the case with the help of high-voltage adjustable control-ring (9) or Stainless-steel high-voltage retractable blades (6), how narrower or wider paint spray plume is to be formed by determining higher or lower absolute values of the negative voltage and generated equipotential lines due to the high voltage unit (32).

By using high-voltage retractable blades (according to the comparison of frames (a) and (b) in Fig. 6.4, no gaps or voids are formed in the electric potential distribution issuing from the stainless-steel high-voltage retractable blades (6) and rotary bell cup (1) surface, owing to the

spacings between adjacent blades. Additionally, all other parameters being equal, the higher and closer values of voltage equipotential lines distribution (18) due to the high-voltage adjustable control-ring (9) or stainless-steel high-voltage retractable blades (6), especially the second ones, the lower paint droplets overspray and more particles stick on the target. Based on the portable high-voltage retractable blades assembly for an electrostatic atomizer body, the first and second electric potential areas that is produced by the blades and the rotary bell cup (1) fully expanded and entirely cover the region of the paint spray plume pattern (19). Based on the fixed high-voltage adjustable control-ring (9) assembly for an electrostatic atomizer body, the first and second electric potential areas that produced by the high-voltage adjustable control-ring (9) and rotary bell cup (1) does not entirely cover the paint spray plume pattern (19). Control-ring pin levels (12) allow to set the diameter of the high-voltage adjustable control-ring (9) remarkably influence the effective electrostatic equipotential lines distribution (18) that can be used in various operational conditions of coating.

The surface areas and length of the annulus stainless steel high-voltage retractable blades (6), their distance from the tip of the rotary bell cup (1), and their tilting angle that makes them closer to the surface of the rotary bell cup (1) significantly affect the electrostatic equipotential lines distribution (18) and thus the paint spray distribution. Of course, the generated annulus electrical potential pattern by stainless steel high-voltage retractable blades (6) or high-voltage adjustable control-ring (9) will keep charged sprayed droplets from too much extending outward the axis of the rotary bell cup (1) to reaches the grounded target surface (17).

Figure 6.5 shows the schematic representation of the application of the new electrostatic sprayer for automotive spray booth. Although in this figure it is represented the high voltage control ring embodiment, both embodiments can be implemented in this type of application. In this figure (1) represents the rotary bell cup, (4) represents the stainless-steel high-voltage gun body and (9) the high-voltage adjustable control-ring of the electrostatic sprayer which will atomize the paint particles and create a paint spray plume pattern (19) projected in the direction of grounded target surface (17), such as the surfaces of a vehicle chassis. The automotive structure is usually moved by means of sliding rails (28) mounted over a floor grating (20) that allows the excessive painting particles to be drained to the water pond (22), equipped with a return sluice (24), forming a flooded paint (23). During the painting process, the circulation of the air is performed trough an inlet air supplier (27) which exits from the air exhauster (21). In this figure (26) represents the robotic equipment holder base, which is connected to the paint booth control system (29) that controls the robotic arm in accordance with the paint booth monitoring system (30) and manual operator input (31). The high voltage needed to operate the electrostatic sprayer is produced by a high voltage unit (32) connected to a voltage converter (33) which converts the voltage and makes the connection between the low voltage from the control module and is connected to the electrostatic sprayer by means of a high voltage cable (38). The shaping air flow is generated by receiving the air from an air compressor (34) through a high-pressure air conduit (37) while the painting particles are provided from a paint container (35) connected to the sprayer trough a paint feeding conduit (36). The compressed high-pressure air is injected in ninety annular shaping air nozzles (3) (with an interval angle of 4°)

with equal intervals for generating and directing an artificial air stream just behind the bell cup edge. The target surface (17), the high voltage unit (32), the voltage converter (33) and the paint container (35) are connected to the ground (25).

Figure 6.6 schematically illustrates the complex pattern of the droplets trajectory. It is known that paint droplets are leaving the tip of a sprayer's rotary bell cup (1) with specific patterns that can be divided into four different behaviours: paint droplet toroid-shape vortex (39), large size droplet trajectory (40), small size droplet trajectory (41), rebounded droplet from the target with the circular pattern (42) and oversprayed paint droplets near the spray plume shoulder (43). By appropriately locating the high-voltage adjustable control ring (9) or stainless-steel high-voltage retractable blades (6) around the atomizing bell cup edge, one can increase or decrease the influence of the electrostatic force on the coating paint particles stream that distributed from edge bell cup edge. The longer painting droplets are in the more powerful electrostatic field, the higher the chances are of the painting particle's path (39, 40, 41,42 and 43) being affected and prevention from the deviation in the radial direction (39, 43) to a more desirable forward direction toward the body of the target (40, 41) by the electrostatic field.

Figure 6.7 illustrates the airflow pattern in operational mode which includes four main patterns: Inside toroid-shape air vortices (45), outside toroid-shape air vortices in the spray plume shoulder (46), shaping airflow stream (47)(blown air), and outside toroid-shape air vortices near the target workpiece (48). The airstream (47) that issues from the rotary bell cup (1) rotation, intensified by the high-pressure air coming out of the shaping air nozzles (3).

6.7. Application Examples

The present invention has various industrial applications such as automotive coating, disinfection of different types of places or application of pesticides in agriculture.

6.8. Claims

1. Electrostatic sprayer comprising at least a rotary bell cup, a paint injection nozzle for feeding the paint materials, a plurality of shaping air nozzles, a stainless stell high voltage gun body, a grounded aluminium gun body, a plurality of retractable blades constituted by a front side stainless steel high-voltage retractable blades and a back side retractable blades insulating cover, mounted on a retractable blades base holder wherein the retractable blades create an electric field, manipulate the equipotential lines distribution and control the electrostatic force that acts over the sprayed particles.
2. Electrostatic sprayer according to claim 1, wherein the rectractable blades can be substituted by a high-voltage adjustable control-ring, equipped with a pipe grip clamp body, a pipe grip clamp screw, a plurality of control-ring pin levels, a pipe grip clamp holder, a control-ring base frame holder, a control-ring frame holder and at least a frame holders connector, wherein the high voltage adjustable control ring creates an electric field, manipulates the equipotential lines distribution and controls the electrostatic force that acts over the sprayed particles.

3. Electrostatic sprayer system comprising the device described the previous claims, wherein the retractable blades are supplied with a negative DC voltage between -10kV and -90kV.
4. Electrostatic sprayer system according to claim 3, wherein the adjustable high voltage control ring operates with diameters in the range of 250mm to 325mm.
5. Electrostatic sprayer system according to claim 3, wherein the adjustable high voltage control ring is supplied by a negative DC voltage between -10kV and -90kV.
6. Electrostatic sprayer system according to claim 3, wherein the maximum length and width of the retractable blades are 130mm and 80mm, respectively.
7. Electrostatic sprayer system according to claim 3, wherein the retractable blades are equally circumferentially spaced at intervals of 36º around the rotation axis of the bell cup.
8. Electrostatic sprayer system according to claim 3, wherein the retractable blades are spaced radially outwardly with an angle of 6º.
9. Electrostatic sprayer system according to previous claims, wherein the diameter of the bell comprises a range of values between 35mm and 65mm.
10. Electrostatic sprayer system according to previous claims, wherein the rotary bell operates with rotational velocities up to 70 kRPM.

Electrostatic sprayer system according to previous claims, wherein the shaping airflow is produced by ninety annular shaping air nozzles with an interval angle of 4° generating and directing an artificial air stream on the bell cup edge.

Chapter 7

Final remarks, conclusions and future Work

7.1 Final Remarks and Conclusions

This thesis presents a comprehensive numerical performance evaluation of the electrostatic rotary bell sprayer (ERBS) with a particular focus on the mechanisms of the droplet primary and secondary breakup process, sprayed droplet size distribution, droplet charge, applied voltage, ambient conditions and examination of different operational conditions in the fully turbulent airflow and by including the atomized droplets discrete phase. This efficient algorithm contains spray dynamics, airflow, paint droplets tracking and an electrostatic effect to simulate atomization. This analysis was conducted using a three dimensional (3D) Eulerian-Lagrangian model to describe the two-phase spraying flow by extending the base code within the OpenFOAM framework (OpenFOAM, 2019). The procedure includes an unsteady compressible Navier-Stokes solver combined with a Large Eddy Simulation (LES) approach to model turbulence effects on the air flowfield. This is coupled to the spray dynamics by including; droplet trajectory tracking, wall film dynamics function and electric field charge. This work provides a thorough insight for the spraying industries on how to achieve higher transfer efficiency (TE) by manipulating the different operating parameters. The effect of operational parameters like bell rotational speed, shaping air and paint flow rate, electrical charge values and droplet distributions are considered precisely. This study reports a thorough analysis about the toroid-shaped vortex ring, air and paint particle evolution, vortex shedding, recirculation zone length, overspray phenomena, electrical voltage distribution, mean velocity, pressure, turbulent kinetic energy and velocity fluctuation. The simulation shows that the inclusion of droplet charging and electric field coupling, with different parametric values, significantly impacts the atomized droplet distribution over the spray plume and the deposition rate. As another useful application, and to show versatility, the available developed code successfully modeled the plasma flow that is created due to potential difference in a DBD was also used to predict the trajectory of saliva droplets as an atomized droplets during sneezing, coughing, or even exhaling.

A summary of the most important conclusions from the investigations of this thesis can be listed as follow:

1- Numerical results obtained in this study put forward a clear link between the shaping air flow rate and the rotation frequency on the aerodynamics and also provide valuable insights to design modern ERBS.

2- The observations of the paint droplets inside the bell cup indicate a regular rotational pattern, gradual velocity increase and multiple breakups of them.

3- The droplet size near the bell cup was increased noticeably, however, their radius becomes more uniform at a longer lateral distance.

4- The measured size of the droplets is controlled by increasing the bell rotational speed or decreasing the paint flow rate, in this case, promoting a reduction in droplet size.

5- The results indicate as dominant operating parameter the air-paint flow rate with voltage level deeply affecting the spray shape. The effect of the bell rotational speed in comparison with other parameters is dominant.

6- The paint spray distribution, shaping air flow subtended angle, computed velocity values, length of the recirculation area, potential fields, electrostatic fields, and paint film formation on the rotary bell cup obtained in the present work is validated against coating experimental results with suitable accuracy. The maximum difference between the current numerical results and experimental ones is less than 1.5 percent.

7- It is proved that using a proposed high-voltage control-ring with the ERBS has a noticeable improvement on the overall spray plum pattern and film, e.g., producing a more uniform film, lower unfavorable overspray and a crawled rebounded torus shape, a narrower plum and more penetrations at higher velocities.

8- Although growing the control-ring voltage from -20 kV to -90 kV causes more paint droplet to stick on the workpiece, and produces a more eminent and dense film, but it has associated costs of larger energy consumption, therefore the moderate voltage of -40 KV is more efficient.

9- By adding a control-ring around the ERBS, the value of TE is enhanced by around 10 % (from 71.7% to 79.1%) when using a moderate voltage of -40 KV.

10- The values of ρ_m^q have a considerable effect on the atomized droplets. Results indicate that spraying with $\rho_m^q \approx -1 mC/kg$ allows to obtained the maximum values for the TE reaching 82.78%. Higher values of the negative charge ($\rho_m^q \leq -1.75 mC/kg$) have a negative effect on the TE value.

11- The deposition film profile shows a peak with a small sinusoidal pattern that is produced due to inner and outer vortex separation. Upon increasing voltage, and using the control-ring, the film profile reached a larger amount and became narrower.

12- By analyzing the droplet size distribution, it is shown that the values of voltage and charge are not so effective on the droplet size changing as much as the bell cup rotational speed and the paint flow rate. The particle size distribution slightly reduces with the growth of the voltage and charge droplet.

13- It is proved that the breakup model has a small effect on the overall spray shape, but its effect on the diameter of the distribution of the droplets and SMD is more obvious, e.g.,

the modified TAB, Reitz-Diwakar and Pilch-Erdman predicted mean SMD values of 13.6, 12.9 and 15.9 μm , respectively, for the $\omega_{Bell} = 40kRPM$ during the spraying cycle.

14- The results of the modified TAB breakup model showed that the higher rotational speeds ($\omega_{Bell} = 55kRPM$) resulted in 54% reducing droplet mean SMD compare to $\omega_{Bell} = 40kRPM$. The same trends ($\approx 51\%$) also observed for the $\omega_{Bell} = 40kRPM$ and $\omega_{Bell} = 25kRPM$.

15- Although from point of view the vortical structures, the bottom-most and top-most, outside of the bell cup and target surface locations, respectively, the spray pattern is experiencing the highest value on the vortical region. For moderate ω_{Bell}, the wake forms an inner recirculation area, whose length on the order of 2.0 bell-cup diameter. An unfavorable overspray region occurs at higher rotational speed, which is the source of the negative force.

16- The distribution of the particle size is very sensitive to changes in the rotational speed. At a constant rotating speed, the higher spray angle is obtained in lower shaping air and higher voltage.

17- A more uniform distribution of the coating is obtained by growing this high-velocity shaping airflow, although the values of the transfer efficiency (TE) are reduced.

18- The shaping airflow from the nozzles is not so effective in changing the spray angle close to the bell, but it makes the outside toroid-shape air vortex more powerful and controls the spray distribution.

19- The numerical results describe exact values for the size, distribution, velocity and trajectory of the particles in ERBS, and these results are important for coating industries, in order to optimize their working conditions.

20- The model correctly predicts that the bell cup spin forces the paint particles to fall off from the bell surface towards the high-velocity airflow. This leads to new knowledge on flow physics for these devices.

21- We deduced polynomial correlations for the maximum length and width of the contaminated area by considering various sneeze conditions.

22- Evaluating various horizontal sneezing angles revealed that a full bending of our head, used as a protective action, reduces the droplets traveling distance by more than 22%.

23- The saliva droplet dispersion analysis confirmed that face mask-wearing, due to sneezing, is a very effective protective measure against the spreading of an infectious disease. With this, the maximum transmission area of the droplets is a sphere with a diameter of 0.6 m and this corresponds to about one-third of the distance a droplet traveled by a naked face.

24- The effect of gravity and inertia forces on small saliva droplets ($D_{droplet} \approx\leq 40\,\mu\mathrm{m}$), in comparison to the influence of the indoor airflow, is negligible. Medium ($50 \approx\leq D_{droplet} \approx\leq 150\,\mu\mathrm{m}$) and large ($D_{droplet} \approx\geq 200\,\mu\mathrm{m}$) size saliva droplets are more affected by the gravity and inertia forces, respectively.

25- During the sneeze of people with various mouth sizes the contamination area is different and can experience a 50 % increment.

26- Our results indicate that the 2 m social distance may not suffice, since it will depend on the environmental conditions. To improve safety this distance should be increased to around 4m.

27- Simulation results prove that plasma flow control using 2-DBDPA could significantly promote the lift coefficient and reduce the drag coefficient. Also, implementing the multi-DBDPAs are able to break the original large-scale separation vortexes and break into a series of small-scale vortices.

7.2 Recommendations for future work

There are some suggestions to improve the level of numerical simulations for future works in the area of the modeling of the electrostatic spray painting process:

1- The effect of target movement in one and two directions and the influence of using a full three-dimensional body of the product as a coating case study needs to be investigated.

2- Spraying various paint materials and examining their effect on the paint film pattern on the workpiece. Such testing would provide spray conditions that more closely represent those of industrial paint applications.

3- Incorporation of a second spray applicator need be studied. There is seldom a single electrostatic spray applicator operating in most industrial applications. An applicator is typically part of a sprayer bank that provides a curtain of charged, sprayed material to be coated on the target substrates. Investigation into the interaction effects of a multiple gun array would increase the usefulness of this model to industry.

4- Using of materials with various conductivities (more conductive) in the numerical electrostatic spray coating procedure.

5- The Faraday cage effect and the edge effect need more investigation. The Faraday Cage Effect can occur when painting more complicated surfaces with recessed areas

6- Accuracy of deposition as a function of various target shape, with curvature or sharp surface, can be examined by using the introduced model.

7- More empirical experiments need to be carried out. Advanced measurement devices and techniques should be used to get good quality measures that can be trusted to build the computer simulations and validate the results.

8- For the plasma flow simulation, the influence of the gas composition can be added to the developed model.

9- For disinfectants of the contaminated area due to the ejected saliva droplets with the virus during the sneezing, the ERBS with a high-voltage control ring can be used as a sanitizer's sprayer.

Electrostatic spray is of great advantage to industry, not only for its contribution to cost-savings, but also to its effect on the environment by minimizing solvent usage. Understanding electrostatic spray will facilitate the achievement of these benefits and contribute to the overall betterment of the coatings community.

Bibliography

Abbas, M.A. and Latham, J., 1967. The instability of evaporating charged drops. Journal of Fluid Mechanics, 30(4), pp.663-670.

Abdollahzadeh, M., Páscoa, J. and Oliveira, P., 2012. Numerical modeling of boundary layer control using dielectric barrier discharge. In MEFTE IV Conferencia Nacional em Mecanica de Fluidos.

Abdollahzadeh, M., Pascoa, J.C. and Oliveira, P.J., 2016. Implementation of the classical plasma–fluid model for simulation of dielectric barrier discharge (DBD) actuators in OpenFOAM. Computers & Fluids, 128, pp.77-90.

Abdollahzadeh, M., Pascoa, J.C. and Oliveira, P.J., 2018. Comparison of DBD plasma actuators flow control authority in different modes of actuation. Aerospace Science and Technology, 78, pp.183-196.

Adamiak, K., 1997. Numerical modelling of tribo-charge powder coating systems. Journal of Electrostatics, 40, pp.395-400.

Adamiak, K., 2001. Numerical investigation of powder trajectories and deposition in tribocharge powder coating. IEEE Transactions on Industry Applications, 37(6), pp.1603-1609.

Adamiak, K. and Floryan, J.M., 2011. Dynamics of water droplet distortion and breakup in a uniform electric field. IEEE Transactions on Industry Applications, 47(6), pp.2374-2383.

Agostinho, L.L.F., Bos, B., Kamau, A., Brouwer, S.P., Fuchs, E.C. and Marijnissen, J.C.M., 2018. Simple-jet mode electrosprays with water. Description, characterization and application in a single effect evaporation chamber. Journal of Aerosol Science, 125, pp.237-250.

Ahmed, M. and Youssef, M.S., 2014. Influence of spinning cup and disk atomizer configurations on droplet size and velocity characteristics. Chemical Engineering Science, 107, pp.149-157.

Ahmed, M. and Youssef, M.S., 2012. Characteristics of mean droplet size produced by spinning disk atomizers. Journal of Fluids Engineering, 134(7), p.071103.

Akafuah, N.K., Poozesh, S., Salaimeh, A., Patrick, G., Lawler, K. and Saito, K., 2016. Evolution of the automotive body coating process—A review. Coatings, 6(2), p.24.

Akafuah, N.K., Salazar, A.J. and Saito, K., 2009, January. Infrared visualization of automotive paint spray transfer process. In Fluids Engineering Division Summer Meeting (Vol. 43727, pp. 759-765).

Akansu, Y.E., Karakaya, F. and Şanlısoy, A., 2013. Active control of flow around NACA 0015 airfoil by using DBD plasma actuator. In EPJ web of conferences (Vol. 45, p. 01008). EDP Sciences.

Almstrand, A.C., Bake, B., Ljungström, E., Larsson, P., Bredberg, A., Mirgorodskaya, E. and Olin, A.C., 2010. Effect of airway opening on production of exhaled particles. Journal of applied physiology, 108(3), pp.584-588.

Allen, J., 2004. An electrostatic atomiser, WO 2004/071670 A1.

Amitay, M. and Glezer, A., 2002. Controlled transients of flow reattachment over stalled airfoils. International Journal of Heat and Fluid Flow, 23(5), pp.690-699.

Andersson, B., Golovitchev, V., Jakobsson, S., Mark, A., Edelvik, F., Davidson, L. and Carlson, J.S., 2013. A modified TAB model for simulation of atomization in rotary bell spray painting. Journal of Mechanical Engineering and Automation, 3(2), pp.54-61.

Anestos, T.C., Sickles, J.E. and Tepper, R.M., 1977. Charge to mass distributions in electrostatic sprays. IEEE Transactions on Industry Applications, (2), pp.168-177.

Artana, G., Bassani, L.C. and Scaricabarozzi, R., 1993. Specific charge of induction electrified sprays. Journal of electrostatics, 29(2), pp.127-145.

Arumugham-Achari, A.K., Grifoll, J. and Rosell-Llompart, J., 2015. A comprehensive framework for the numerical simulation of evaporating electrosprays. Aerosol Science and Technology, 49(6), pp.436-448.

Asadi, S., Bouvier, N., Wexler, A.S. and Ristenpart, W.D., 2020. The coronavirus pandemic and aerosols: Does COVID-19 transmit via expiratory particles?.

Atten, A. and Oliveri, S., 1992. Charging of drops formed by circular jet breakup. Journal of electrostatics, 29(1), pp.73-91.

Bai, Y., Yao, L., Wei, T., Tian, F., Jin, D.Y., Chen, L. and Wang, M., 2020. Presumed asymptomatic carrier transmission of COVID-19. Jama, 323(14), pp.1406-1407.

Bailey, A.G., 1974. Electrostatic atomization of liquids. Science Progress (1933-), pp.555-581.

Bailey, A.G., 1988. Electrostatic Spraying of Liquids, New York: John Wiley and Sons Inc.

Bailey, A.G., Balachandran, W. and Williams, T.J., 1983. The rosin—rammler size distribution for liquid droplet ensembles. Journal of aerosol science, 14(1), pp.39-46.

Bailey, A.G., Hashish, A.H. and Williams, T.J., 1998. Drug delivery by inhalation of charged particles. Journal of Electrostatics, 44(1-2), pp.3-10.

Balachandran, W., Miao, P. and Xiao, P., 2001. Electrospray of fine droplets of ceramic suspensions for thin-film preparation. Journal of Electrostatics, 50(4), pp.249-263.

Beale, J.C. and Reitz, R.D., 1999. Modeling spray atomization with the Kelvin-Helmholtz/Rayleigh-Taylor hybrid model. Atomization and sprays, 9(6).

Beans, C., Fluid dynamics work hints at whether spoken word can spread COVID-19, Proc. Natl. Aacd. Sci. U. S. A. (2020), http://blog.pnas.org/2020/ 04/fluid-dynamics-work-hints-at-whether-spoken-word-can-spread-covid-19/.

Bell, G.C. and GC, B., 1981. Mechanics of electrostatic atomization, transport, and deposition of coatings.

Benard, N., Jolibois, J. and Moreau, E., 2009. Lift and drag performances of an axisymmetric airfoil controlled by plasma actuator. Journal of Electrostatics, 67(2-3), pp.133-139.

Bensow, R.E., Fureby, C., 2007. On the justification and extension of mixed methods. LES J. Turbul. 8, N54.

Bhardwaj, R. and Agrawal, A., 2020. Likelihood of survival of coronavirus in a respiratory droplet deposited on a solid surface. Physics of Fluids, 32(6), p.061704.

Blocken, B., Malizia, F., van Druenen, T. and Marchal, T., 2020. Towards aerodynamically equivalent COVID-19 1.5 m social distancing for walking and running. Preprint. Available at:

http://www. urbanphysics. net/Social% 20Distancing% 20v20_White_Paper. pdf. Accessed April, 20.

Böttner, C.U. and Sommerfeld, M., 2002. Numerical calculation of electrostatic powder painting using the Euler/Lagrange approach. Powder Technology, 125(2-3), pp.206-216.

Bologa, A.M. and Makalsky, L.M., 1989. Electrostatic pneumatic sprayer of water solutions. Journal of Electrostatics, 23, pp.227-233.

Bouchmal, A., 2011. Modeling of Dielectric-Barrier Discharge Actuator: Implementation, validation and generalization of an electrostatic model.

Bourouiba, L., 2020. Turbulent gas clouds and respiratory pathogen emissions: potential implications for reducing transmission of COVID-19. Jama.

Bourouiba, L., Dehandschoewercker, E. and Bush, J.W., 2014. Violent expiratory events: on coughing and sneezing. Journal of Fluid Mechanics, 745, pp.537-563.

Brentjes, A., Pozarlik, A.K. and Brem, G., 2020. Numerical simulation of evaporating charged sprays in spray chilling. Journal of Electrostatics, 107, p.103471.

Buckland, F.E. and Tyrrell, D.A.J., 1964. Experiments on the spread of colds: 1. Laboratory studies on the dispersal of nasal secretion. Epidemiology & infection, 62(3), pp.365-377.

Castle, G.P., 2011. A century of development in applied electrostatics; nothing static here. IEEE Transactions on Dielectrics and Electrical Insulation, 18(5), pp.1361-1365.

Centers for Disease Control (CDC), 2020. CDC Guidelines on Social Distancing. Available at: https: //www.cdc.gov/coronavirus/2019-ncov/prevent-getting-sick/social-distancing.html.

Chao, C.Y.H., Wan, M.P. and Sze To, G.N., 2008. Transport and removal of expiratory droplets in hospital ward environment. Aerosol Science and Technology, 42(5), pp.377-394.

Chao, C.Y.H., Wan, M.P., Morawska, L., Johnson, G.R., Ristovski, Z.D., Hargreaves, M., Mengersen, K., Corbett, S., Li, Y., Xie, X. and Katoshevski, D., 2009. Characterization of expiration air jets and droplet size distributions immediately at the mouth opening. Journal of Aerosol Science, 40(2), pp.122-133.

Chen, D., Asada, K., Sekimoto, S., Fujii, K. and Nishida, H., 2021. A high-fidelity body-force modeling approach for plasma-based flow control simulations. Physics of Fluids, 33(3), p.037115.

Chen, W., Qiao, W., Duan, W. and Wei, Z., 2021. Experimental study of airfoil instability noise with wavy leading edges. Applied Acoustics, 172, p.107671.

Chernyshev, S.L., Gamirullin, M.D., Khomich, V.Y., Kuryachii, A.P., Litvinov, V.M., Manuilovich, S.V., Moshkunov, S.I., Rebrov, I.E., Rusyanov, D.A. and Yamshchikov, V.A., 2016. Electrogasdynamic laminar flow control on a swept wing. Aerospace science and technology, 59, pp.155-161.

Cho, Y.C. and Shyy, W., 2011. Adaptive flow control of low-Reynolds number aerodynamics using dielectric barrier discharge actuator. Progress in Aerospace Sciences, 47(7), pp.495-521.

Chigier, N., and Beer, J., 1964, “The Flow Region Near the Nozzle in Double Concentric Jets,” ASME J. Fluids Eng., 86 (4), pp. 797–804.

Clément, Z., Fredrik, E., Andreas, M., and Oliver, H., 2014. Efficient Numerical Simulation of Spray Painting Processes in Automotive Manufacturing. SAE Technical Paper 2014-36-0418.

Clift, R., Grace, J. R. and Weber, M. E., 1978. Bubbles, Drops and Particles, New York: Academic Press.

Colbert, S.A. and Cairncross, R.A., 2005. A computer simulation for predicting electrostatic spray coating patterns. Powder technology, 151(1-3), pp.77-86.

Colbert, S.A., 2007. Numerical simulations of droplet trajectories from an electrostatic rotary-bell atomizer. Drexel University.

Cooper, S.C., Es Product Development LLC, 2021. Electrostatic fluid sprayer with active fluid cloud dispersal feature and method of electrostatic spraying. U.S. Patent 10,894,262.

Corbeels, P.L., Senser, DW and Lefebvre, A.H., 1992. Atomization characteristics of a highspeed rotary-bell paint applicator. Atomization and Sprays, 2(2).

Cross, J.A., 1987. Electrostatic: Principles, Problems, and Applications, Adam-Hilger: Bristol, UK.

Darwish Ahmad, A., Singh, B.B., Doerre, M., Abubaker, A.M., Arabghahestani, M., Salaimeh, A.A. and Akafuah, N.K., 2019. Spatial Positioning and Operating Parameters of a Rotary Bell Sprayer: 3D Mapping of Droplet Size Distributions. Fluids, 4(3), p.165.

Darwish Ahmad, A., Abubaker, A., Salaimeh, A. and Akafuah, N., 2018. Schlieren Visualization of Shaping Air during Operation of an Electrostatic Rotary Bell Sprayer: Impact of Shaping Air on Droplet Atomization and Transport. Coatings, 8(8), p.279.

Dastourani, H., Jahannama, M. R., & Eslami-Majd, A., 2018, “A physical insight into electrospray process in cone-jet mode: Role of operating parameters,” International Journal of Heat and Fluid Flow, 70, 315–335.

Davies, J.T., 1961. E. K. Rideal, Interfacial Phenomena, New York: Academic Pres, Chap. 3.

Davies, J.T. and Makepeace, R.W., 1978. Measurement of the surface ages of water jets. AIChE Journal, 24(3), pp.524-530.

Davies, C.N. and Cheah, P.K.P., 1984. Spinning generators of homogeneous aerosols. Journal of aerosol science, 15(6), pp.719-739.

Dbouk, T. and Drikakis, D., 2020a. On coughing and airborne droplet transmission to humans. Physics of Fluids, 32(5), p.053310.

Dbouk, T. and Drikakis, D., 2020b. On respiratory droplets and face masks. Physics of Fluids, 32(5), p. 063303.

Dickinson, D.R. and Marshall Jr, W.R., 1968. The rates of evaporation of sprays. AIChE Journal, 14(4), pp.541-552.

Domnick, J., Scheibe, A. and Ye, Q., 2005. The Simulation of the Electrostatic Spray Painting Process with High-Speed Rotary Bell Atomizers. Part I: Direct Charging. Particle & Particle Systems Characterization, 22(2), pp.141-150.

Domnick, J., Scheibe, A. and Ye, Q., 2006. The Simulation of Electrostatic Spray Painting Process with High-Speed Rotary Bell Atomizers. Part II: External Charging. Particle & Particle Systems Characterization, 23(5), pp.408-416.

Domnick, J., Scheibe, A. and Ye, Q., 2005. The Simulation of the Electrostatic Spray Painting Process with High-Speed Rotary Bell Atomizers. Part I: Direct Charging. Particle & Particle Systems Characterization, 22(2), pp.141-150.

Dominick, J., Thieme, M., 2006. Atomization characteristics of high-speed rotary bell atomizers. Atomization and Sprays. 16, pp. 857–874.

Doyle, A., Moffett, D.R. and Vonnegut, B., 1964. Behavior of evaporating electrically charged droplets. Journal of Colloid Science, 19(2), pp.136-143.

Duguid, J.P., 1946. The size and the duration of air-carriage of respiratory droplets and droplet-nuclei. Epidemiology & infection, 44(6), pp.471-479.

Durao, D., and Whitelaw, J., 1978, "Velocity Characteristics of the Flow in the Near Wake of a Disk," J. Fluid Mech., 85 (2), pp. 369–385.

Duvigneau, R. and Visonneau, M., 2006. Simulation and optimization of stall control for an airfoil with a synthetic jet. Aerospace Science and Technology, 10(4), pp.279-287.

Eberle, M.K., Boulouchos, K., Schneider, B., Stebler, H., Stöckli, M., Tanner, F.X. and Weisser, G., 1996. Mathematical modeling and advanced diagnostics in IC engine research. FISITA Technical Paper, Prague.

Elegant, N. X., 2020. Coronavirus outbreak changes US's mind on everyone wearing face masks. Fortune. Available at: https://fortune.com/2020/04/03/coronavirus-face-mask-cdc/.

Ellwood, K.R. and Braslaw, J., 1998. A finite-element model for an electrostatic bell sprayer. Journal of Electrostatics, 45(1), pp.1-23.

Ellwood, K.R., Tardiff, J.L. and Alaie, S.M., 2014. A simplified analysis method for correlating rotary atomizer performance on droplet size and coating appearance. Journal of Coatings Technology and Research, 11(3), pp.303-309.

Elmoursi, A.A., 1989. Laplacian fields of bell-type electrostatic painting systems. IEEE Transactions on industry applications, 25(2), pp.234-240.

Elmoursi, A.A., 1992. Electrical characterization of bell-type electrostatic painting systems. IEEE Transactions on industry applications, 28(5), pp.1174-1181.

Erfani, R., Erfani, T., Utyuzhnikov, S.V. and Kontis, K., 2013. Optimisation of multiple encapsulated electrode plasma actuator. Aerospace Science and Technology, 26(1), pp.120-127.

Fan, H.T., Kuo, H. and Simmer, J., 2011, January. Measuring paint droplet size, velocity, and charge-to-mass ratio distribution for electrostatic rotary bell spray simulation. In ASME International Mechanical Engineering Congress and Exposition (Vol. 54921, pp. 703-709).

Filippov, A.V., 1991. Electrostatic deposition of inertially moving charged aerosol particles onto the earthed disk. Journal of electrostatics, 26(1), pp.81-98.

Fish, F.E. and Battle, J.M., 1995. Hydrodynamic design of the humpback whale flipper. Journal of morphology, 225(1), pp.51-60.

Fraser, R.P., Dombrowski, N. and Routley, J.H., 1963. The atomization of a liquid sheet by an impinging air stream. Chemical Engineering Science, 18(6), pp.339-353.

Frost, A.R., 1981. Rotary atomization in the ligament formation mode. Journal of Agricultural Engineering Research, 26(1), pp.63-78.

Fujimoto, H., Tsukasa, HORI. and SENDA, J., 2009. Effect of breakup model on diesel spray structure simulated by large eddy simulation (No. 2009-24-0024). SAE Technical Paper.

Gañán-Calvo, A.M., López-Herrera, J.M., Herrada, M.A., Ramos, A. and Montanero, J.M., 2018. Review on the physics of electrospray: from electrokinetics to the operating conditions of single and coaxial Taylor cone-jets, and AC electrospray. Journal of Aerosol Science, 125, pp.32-56.

Gao, N. and Niu, J., 2006. Transient CFD simulation of the respiration process and inter-person exposure assessment. Building and environment, 41(9), pp.1214-1222.

Gerone, P.J., Couch, R.B., Keefer, G.V., Douglas, R.G., Derrenbacher, E.B. and Knight, V., 1966. Assessment of experimental and natural viral aerosols. Bacteriological reviews, 30(3), p.576.

Ghosal, S., 1996. An analysis of numerical errors in large-eddy simulations of turbulence. J. Comput. Phys. 125, 187–206.

Guettler, N., Knee, P., Ye, Q. and Tiedje, O., 2020. Initial droplet conditions in numerical spray painting by electrostatic rotary bell sprayers. Journal of Coatings Technology and Research, 17(5), pp.1091-1104.

Guoqiang, L., Weiguo, Z., Yubiao, J. and Pengyu, Y., 2019. Experimental investigation of dynamic stall flow control for wind turbine airfoils using a plasma actuator. Energy, 185, pp.90-101.

Gupta, J.K., Lin, C.H. and Chen, Q., 2009. Flow dynamics and characterization of a cough. Indoor air, 19(6), pp.517-525.

Gödeke, L., Oswald, W., Willenbacher, N. and Ehrhard, P., 2020. Dimensional analysis of droplet size and ligament length during high-speed rotary bell atomization. Journal of Coatings Technology and Research, pp.1-7.

Hartman, R.P.A., Borra, J.P., Brunner, D.J., Marijnissen, J.C.M. and Scarlett, B., 1999. The evolution of electrohydrodynamic sprays produced in the cone-jet mode, a physical model. Journal of Electrostatics, 47(3), pp.143-170.

Han, Z.Y., Weng, W.G. and Huang, Q.Y., 2013. Characterizations of particle size distribution of the droplets exhaled by sneeze. Journal of The Royal Society Interface, 10(88), p.20130560.

Harouni, A.G., 2014. Flow control of a boundary layer ingesting serpentine diffuser via blowing and suction. Aerospace Science and Technology, 39, pp.472-480.

Haslbeck, K., Schwarz, K., Hohlfeld, J.M., Seume, J.R. and Koch, W., 2010. Submicron droplet formation in the human lung. Journal of Aerosol Science, 41(5), pp.429-438.

Higashiyama, Y., Tanaka, S.I., Sugimoto, T. and Asano, K., 1999. Size distribution of the charged droplets in an axisymmetric shower. Journal of electrostatics, 47(3), pp.183-195.

Hines, R.L., 1966. Electrostatic atomization and spray painting. Journal of Applied Physics, 37(7), pp.2730-2736.

Hinze, JO, Milborn, H, 1950. Atomization of Liquids by Means of a Rotating Cup. J. Appl. Mech., 17 (2) 145–153.

Holmgren, H., Ljungström, E., Almstrand, A.C., Bake, B. and Olin, A.C., 2010. Size distribution of exhaled particles in the range from 0.01 to 2.0 μm. Journal of Aerosol Science, 41(5), pp.439-446.

Honma, K. and Yamasaki, I., Toyota Motor Corp, 1999. Rotary atomizing electrostatic coating apparatus and method. U.S. Patent 5,980,994.

Hrynuk, J.T. and Bohl, D.G., 2020. The effects of leading-edge tubercles on dynamic stall. Journal of Fluid Mechanics, 893.

Huang, H., Lai, M.C. and Meredith, W., 2000, July. Simulation of spray transport from rotary cup atomizer using KIVA-3V. In ICLASS 2000.

Hughes, J.F., 1984. Electrostatic Powder Coating. SOUTHAMPTON UNIV (UNITED KINGDOM) DEPT OF ELECTRICAL ENGINEERING.

Hurevich, V., Gusarov, A. and Smurov, I., 2002. Simulation of coating profile under plasma spraying conditions. In Proceeding: International Thermal Spray Conference.

Ilieva, G., Páscoa, J., Dumas, A. and Trancossi, M., 2012. A critical review of propulsion concepts for modern airships. Open Engineering, 2(2), pp.189-200.

Im, K.S., Lai, M.C., Yu, S.T.J. and Matheson Jr, R.R., 2004. Simulation of spray transfer processes in electrostatic rotary bell sprayer. J. Fluids Eng., 126(3), pp.449-456.

Im, K.S., Lai, M.C., Liu, Y., Sankagiri, N., Loch, T. and Nivi, H., 2001. Visualization and measurement of automotive electrostatic rotary-bell paint spray transfer processes. J. Fluids Eng., 123(2), pp.237-245.

Inkpen, S., 1986. Electrical and mechanical mechanisms for color variation in the spraying of metallic paints (Doctoral dissertation, Massachusetts Institute of Technology).

Issa, R.I., 1986. Solution of the implicitly discretised fluid flow equations by operator-splitting. Journal of computational physics, 62(1), pp.40-65.

Ivosevic, M., Cairncross, R.A. and Knight, R., 2006. 3D predictions of thermally sprayed polymer splats: Modeling particle acceleration, heating and deformation on impact with a flat substrate. International Journal of Heat and Mass Transfer, 49(19-20), pp.3285-3297.

Jasak, H., 2009. OpenFOAM: open source CFD in research and industry. International Journal of Naval Architecture and Ocean Engineering, 1(2), pp.89-94.

Johari, H., Henoch, C., Custodio, D., Levshin, L., 2007. Effects of leading-edge protuberances on airfoil performance, AIAA J. 45, 2634–2642.

Jukes, T.N., Choi, K.S., Johnson, G.A. and Scott, S.J., 2006. Characterization of surface plasma-induced wall flows through velocity and temperature measurements. AIAA journal, 44(4), pp.764-771.

Kazama, S., 2003. Steady-state paint flow under high centrifugal force:: atomization in spray painting. JSAE review, 24(4), pp.489-494.

Kim, S., Hwang, J., Lee, C., 2010, “Experiments and modeling on droplet motion and atomization of diesel and biodiesel fuels in a cross-flowed air stream,” International Journal of Heat Fluid Flow, 31, pp. 667–679.

Kimura, T., Udagawa, K. and Yamasaki, H., 2013. Experimental study of DBD plasma actuator with combination of AC and nanosecond pulse voltage. Electrical Engineering in Japan, 185(2), pp.21-29.

Ko, N. W. M., and Chan, W. T., 1978, “Similarity in Initial Region of Annular Jets: Three Configurations,” J. Fluid Mech., 84 (4), pp. 641–656.
Kolahan, A., Roohi, E. and Pendar, M.R., 2019. Wavelet analysis and frequency spectrum of cloud cavitation around a sphere. Ocean Engineering, 182, pp.235-247.
Kotsonis, M. and Ghaemi, S., 2012. Performance improvement of plasma actuators using asymmetric high voltage waveforms. Journal of Physics D: Applied Physics, 45(4), p.045204.
Kuhnhenn, M, Luh, MF, Joensen, TV, Reck, M, Roisman, IV, Tropea, C, 2018. Modelling of the Breakup Process of Viscous Fluids by a High-Speed Rotary Atomizer. Exp. Fluids, 59 117.
Liu, J., Yu, Q. and Guo, Q., 2012. Experimental investigation of liquid disintegration by rotary cups. Chemical Engineering Science, 73, pp.44-50.
Liu, A.B. and Reitz, R.D., 1993. Mechanisms of air-assisted liquid atomization. Atomization and sprays, 3(1).
Liu, Y., Lai, M.C., Im, K.S., Sankagiri, N., Loch, T. and Nivi, H., 1998. An experimental investigation of spray transfer processes in an electrostatic rotating bell applicator. SAE transactions, pp.1235-1243.
Laín, S., and Grillo, C. A., 2007. Comparison of turbulent particle dispersion models in turbulent shear flows. Brazilian Journal of Chemical Engineering, 24, pp. 351 - 363.
Mark, A., Andersson, B., Tafuri, S., Engstrom, K., Sorod, H., Edelvik, F. and Carlson, J.S., 2013. Simulation of electrostatic rotary bell spray painting in automotive paint shops. Atomization and sprays, 23(1).
Martinez, L.A., 2013. Automotive Rotary-Bell Spray Painting (Master of Science thesis). Department of Physics, University of Gothenburg, Sweden.
Miklosovic, D.S., Murray, M.M., Howle, L.E. and Fish, F.E., 2004. Leading-edge tubercles delay stall on humpback whale (Megaptera novaeangliae) flippers. Physics of fluids, 16(5), pp.L39-L42.
Miklosovic, D.S., Murray, M.M. and Howle, L.E., 2007. Experimental evaluation of sinusoidal leading edges. Journal of aircraft, 44(4), pp.1404-1408.
Moreau, E., 2007. Airflow control by non-thermal plasma actuators. Journal of physics D: applied physics, 40(3), p.605.
Morgado, J., Abdollahzadeh, M., Silvestre, M.A.R. and Páscoa, J.C., 2015. High altitude propeller design and analysis. Aerospace Science and Technology, 45, pp.398-407.
Nolte, H.J., Fischer, A., Marquardt, P., Berkowitsch, J. and Schneider, J., Duerr Systems AG, 2019. Electrode assembly for an electrostatic atomizer. U.S. Patent 10,464,084.
Nordin, P.N., 2001. Complex chemistry modeling of diesel spray combustion (Vol. 18). Sweden: Chalmers University of Technology.

Im, K.S., Lai, M.C., Liu, Y., Sankagiri, N., Loch, T. and Nivi, H., 2001. Visualization and measurement of automotive electrostatic rotary-bell paint spray transfer processes. J. Fluids Eng., 123(2), pp.237-245.

Im, K.S., Lai, M.C., Yu, STJ and Matheson Jr, RR, 2004. Simulation of spray transfer processes in electrostatic rotary bell sprayer. J. Fluids Eng., 126(3), pp.449-456.

Johnson, G.R. and Morawska, L., 2009. The mechanism of breath aerosol formation. Journal of Aerosol Medicine and Pulmonary Drug Delivery, 22(3), pp.229-237.

Jukes, T.N., Choi, K.S., Johnson, G.A. and Scott, S.J., 2006. Characterization of surface plasma-induced wall flows through velocity and temperature measurements. AIAA journal, 44(4), pp.764-771.

Kolahan, A., Roohi, E. and Pendar, M.R., 2019. Wavelet analysis and frequency spectrum of cloud cavitation around a sphere. Ocean Engineering, 182, pp.235-247.

Leder, K. and Newman, D., 2005. Respiratory infections during air travel. Internal medicine journal, 35(1), pp.50-55.

Lefebvre, A.H., 1989. Atomization and Spray, New York: Hemisphere Publishing Co., 1989.

Leonas, K.K., Jones, C.R. and Hall, D., 2003. The relationship of fabric properties and bacterial filtration efficiency for selected surgical face masks. J Text Apparel Technol Manag, 78, pp.1-8.

Li, Y.Y., Wang, J.X. and Chen, X., 2020. Can a toilet promote virus transmission? From a fluid dynamics perspective. Physics of Fluids, 32(6), p.065107.

Loeb, L.B., 1965. Electrical coronas, their basic physical mechanisms. Univ of California Press.

Mazumder, M.K., Banerjee, S., Ware, R.E., Mu, C., Kaya, N. and Huang, C.C., 1994. Characterization of tribocharging properties of powder paint. IEEE transactions on industry applications, 30(2), pp.365-369.

Meesters, G.M.H., Zevenhoven, C.A.P., Brons, J.F.J. and Verheijen, P.J.T., 1990. Fast computer simulation of open-air electrostatic spray painting. Journal of electrostatics, 25(3), pp.265-275.

Michelson, D, 1990. Electrostatic Atomization, Adam-Hilger: Bristol, UK.

Mittal, R., Ni, R. and Seo, J.H., 2020. The flow physics of COVID-19. Journal of Fluid Mechanics, 894.

Moyle, B.D. and Hughes, J.F., 1985. Powder coating-corona versus tribo charging. Journal of Electrostatics, 16(2-3), pp.277-286.

Nordin, P.N., 2001. Complex chemistry modeling of diesel spray combustion (Vol. 18). Sweden: Chalmers University of Technology.

Ogasawara, S, Daikoku, M, Shirota, M, Inamura, T, Saito, Y, Yasumura, K, Shoji, M, Aoki, H, Miura, T, 2010. Liquid Atomization Using a Rotary Bell Cup Atomizer. J. Fluid Sci. Technol., 5 (3) 464–474.

OpenFOAM, https://www.openfoam.com.

O'Rourke, P.J. and Amsden, A.A., 2000. A spray/wall interaction submodel for the KIVA-3 wall film model. SAE transactions, pp.281-298.

Osman, H., Adamiak, K., Castle, G.P., Fan, H.T. and Simmer, J., 2015a, November. Comparison between the numerical and experimental deposition patterns for an electrostatic rotary bell

sprayer. In ASME International Mechanical Engineering Congress and Exposition (Vol. 57366, p. V02BT02A003). American Society of Mechanical Engineers.

Osman, H., Ghazian, O., Adamiak, K., Castle, G.P., Fan, H.T. and Simmer, J., 2015b. Charging level of a ligament-droplet system atomized in a uniform electric field. IEEE Transactions on Industry Applications, 52(2), pp.1814-1822.

Osman, H., Castle, G.S.P., Adamiak, K., Fan, H.T. and Simmer, J., 2015c, October. Estimation of droplet charge forming out of an electrified ligament in the presence of a uniform electric field. In Journal of Physics. Conference Series (Online) (Vol. 646, No. 1).

Oswald, W, Go¨ deke, L, Ehrhard, P, and Willenbacher, N, 2018. Effect of Elongational Flow Behavior on Ligament Disintegration and Drop Formation by Means of High-speed Rotary Bell Atomizer. 14th Triennial International Conference on Liquid Atomization and Spray Systems, Chicago, IL, USA, July 22–26.

Oswald, W., Gödeke, L., Ehrhard, P. and Willenbacher, N., 2019. Influence of the elongational flow resistance and pigmentation of coating fluids on high-speed rotary bell atomization. Atomization and Sprays, 29(10).

Patel, M.P., Ng, T.T., Vasudevan, S., Corke, T.C., Post, M.L., McLaughlin, T.E. and Suchomel, C.F., 2008. Scaling effects of an aerodynamic plasma actuator. Journal of aircraft, 45(1), pp.223-236.

Panneton, B., 2002. Geometry and performance of a rotary cup atomizer. Am. Soc. Agric. Eng. 18, pp. 435–441.

Páscoa, J.C., Rodrigues, F.F., Das, S.S., Abdollahzadeh, M., Dumas, A., Trancossi, M. and Subhash, M., 2014, November. Exit flow vector control on a coanda nozzle using dielectric barrier discharge actuator. In ASME International Mechanical Engineering Congress and Exposition (Vol. 46421, p. V001T01A006). American Society of Mechanical Engineers.

Patankar, S.V. and Spalding, D.B., 1983. A calculation procedure for heat, mass and momentum transfer in three-dimensional parabolic flows. In Numerical Prediction of Flow, Heat Transfer, Turbulence and Combustion (pp. 54-73).

Pendar, M.R., Esmaeilifar, E. and Roohi, E., 2020. LES study of unsteady cavitation characteristics of a 3-D hydrofoil with wavy leading edge. International Journal of Multiphase Flow, 132, p.103415.

Pendar, M.R. and Roohi, E., 2016. Investigation of cavitation around 3D hemispherical head-form body and conical cavitators using different turbulence and cavitation models. Ocean Engineering, 112, pp.287-306.

Pendar, M.R. and Roohi, E., 2015. Detailed investigation of cavitation and supercavitation around different geometries using various turbulence and mass transfer models. In Journal of Physics: Conference Series (Vol. 656, No. 1, p. 012070). IOP Publishing.

Pendar, M.R., Roohi, E., 2018. Cavitation characteristics around a sphere: an LES investigation. Int. J. Multiphase Flow. 98, pp. 1–23.

Pendar, M.R. and Roohi, E., 2015, May. Investigation of cavitation around disk and conical cavitators using different sets of turbulence and cavitation models. In 4th International Conference on Advances in Mechanical Engineering-ICAME 2015.

Peng, H., Wang, N., Wang, D. and Ling, X., 2016. Experimental study on the critical characteristics of liquid atomization by a spinning disk. Industrial & Engineering Chemistry Research, 55(21), pp.6175-6185.

Perel, J., J.F. Mahoney, B.E. Kalensher, R. Mehrabian. Electrohydrodynamic Techniques in Metals Processing. Advances in Metal Processing. Proceedings of the Twenty-Fifth Sagamore Army Materials Research Conference, p. 79-89, 1981.

Pilch, M. and Erdman, C.A., 1987. Use of breakup time data and velocity history data to predict the maximum size of stable fragments for acceleration-induced breakup of a liquid drop. International journal of multiphase flow, 13(6), pp.741-757.

Post, M.L. and Corke, T.C., 2004. Separation control on high angle of attack airfoil using plasma actuators. AIAA journal, 42(11), pp.2177-2184.

Post, M.L. and Corke, T.C., 2004. Separation control on high angle of attack airfoil using plasma actuators. AIAA journal, 42(11), pp.2177-2184.

Rami, M.H. and Pascoa, J., 2019a. Numerical analysis of a cycloidal rotor under diverse operating conditions and altitudes (No. 2019-01-1872). SAE Technical Paper.

Ranz, W.E. and Marshall, W.R., 1952. Evaporation from drops. Chem. eng. prog, 48(3), pp.141-146.

Rami, M.H. and Pascoa, J., 2019b. ANN assisted flow modeling and analysis for a cyclorotor in ground effect. Aerospace Science and Technology, 95, p.105495.

Rarraud, R., 1992. Comparative electric field calculations and measurements on high voltage insulators. Electra, 141, pp.68-81.

Rayleigh, L., 1882. XX. On the equilibrium of liquid conducting masses charged with electricity. The London, Edinburgh, and Dublin Philosophical Magazine and Journal of Science, 14(87), pp.184-186.

Rayleigh, L, 1878. On the instability of jets, Proc. London Math. Soc., vol.10, pp.4-13, 1878.

Reitz, R.D. and Diwakar, R., 1986. Effect of drop breakup on fuel sprays. SAE transactions, pp.218-227.

Reitz, R.D. and Diwakar, R., 1987. Structure of high-pressure fuel sprays. SAE transactions, pp.492-509.

Reitz, R., 1987. Modeling atomization processes in high-pressure vaporizing sprays. Atomisation and Spray technology, 3(4), pp.309-337.

Reznik, S.N., Yarin, A.L., Theron, A. and Zussman, E., 2004. Transient and steady shapes of droplets attached to a surface in a strong electric field. Journal of Fluid Mechanics, 516, p.349.

Richard, M., van den Brand, J.M., Bestebroer, T.M., Lexmond, P., de Meulder, D., Fouchier, R.A., Lowen, A.C. and Herfst, S., 2020. Influenza A viruses are transmitted via the air from the nasal respiratory epithelium of ferrets. Nature communications, 11(1), pp.1-11.

Rodrigues, F., Mushyam, A., Pascoa, J. and Trancossi, M., 2019. A new plasma actuator configuration for improved efficiency: the stair-shaped dielectric barrier discharge actuator. Journal of Physics D: Applied Physics, 52(38), p.385201.

Rodrigues, F., Páscoa, J.C., Dias, F. and Abdollahzadeh, M., 2015, November. Plasma actuators for boundary layer control of next generation nozzles. In ASME International Mechanical Engineering Congress and Exposition (Vol. 57342, p. V001T01A005). American Society of Mechanical Engineers.

Rodrigues, F.F. and Pascoa, J.C., 2020. Implementation of Stair-Shaped Dielectric Layers in Micro-and Macroplasma Actuators for Increased Efficiency and Lifetime. Journal of Fluids Engineering, 142(10).

Roohi, E., Pendar, M.R. and Rahimi, A., 2016. Simulation of three-dimensional cavitation behind a disk using various turbulence and mass transfer models. Applied Mathematical Modelling, 40(1), pp.542-564.

Roohi, E., Pendar, M.R. and Rahimi, A., 2016. Simulation of three-dimensional cavitation behind a disk using various turbulence and mass transfer models. Applied Mathematical Modelling, 40(1), pp.542-564.

Rosell-Llompart, J., Grifoll, J. and Loscertales, I.G., 2018. Electrosprays in the cone-jet mode: from Taylor cone formation to spray development. Journal of Aerosol Science, 125, pp.2-31.

Saha, A., Lee, J.D., Basu, S. and Kumar, R., 2012. Breakup and coalescence characteristics of a hollow cone swirling spray. Physics of fluids, 24(12), p.124103.

Sato, M., Okada, K., Asada, K., Aono, H., Nonomura, T. and Fujii, K., 2020. Unified mechanisms for separation control around airfoil using plasma actuator with burst actuation over Reynolds number range of 103–106. Physics of Fluids, 32(2), p.025102.

SAMES Technology, 2019. ⟨http://www.sames-kremlin.com⟩.

Schiller, L. and Neumann, A., 1933. Uber die Grundlegenden Berechnurgen bei der Schwerkraftaufbereitung. Ver. Deutsch. Ing. 77, pp. 318-320.

Schneider, J.M., Lindblad, N.R., Hendricks Jr, C.D. and Crowley, J.M., 1967. Stability of an electrified liquid jet. Journal of applied Physics, 38(6), pp.2599-2605.

Schneider, B., 1995, May. Experimental investigation of diesel sprays. CRFD and Laser Diagnostic Workshop. In 21st CIMAC Congress.

Seitz, D. M., 2009. Shaping air and bell cup combination, WO 2009/012025 A2.

Shawpittman, M. D. B., 2001. Electrostatic sprayer, US 2001/0032897 A1.

Shen, B., Ye, Q., Guettler, N., Tiedje, O. and Domnick, J., 2019. Primary breakup of a non-Newtonian liquid using a high-speed rotary bell atomizer for spray-painting processes. Journal of Coatings Technology and Research, pp.1-16.

Shen, B., Ye, Q., Tiedje, O. and Domnick, J., 2017, July. Primary breakup of liquids using a high-speed rotary bell atomizer for spray painting processes. In Ilass Europe. 28th european conference on Liquid Atomization and Spray Systems (pp. 355-361). Editorial Universitat Politècnica de València.

Shkadov, V.Y. and Shutov, A.A., 2001. Disintegration of a charged viscous jet in a high electric field. Fluid Dynamics Research, 28(1), p.23.

Shrimpton, J.S. and Laoonual, Y., 2006. Dynamics of electrically charged transient evaporating sprays. International journal for numerical methods in engineering, 67(8), pp.1063-1081.
Stalling, D. and Hege, H.-C., 1997. LIC on Surfaces. Texture Synthesis with Line Integral Convolution, pp. 51-64.
Sidorenko, A., Zanin, B., Postnikov, B., Budovsky, A., Starikovskii, A., Roupassov, D., Zavialov, I., Malmuth, N., Smereczniak, P. and Silkey, J., 2007, January. Pulsed discharge actuators for rectangular wing separation control. In 45th AIAA aerospace sciences meeting and exhibit (p. 941).
Stefanitsis, D., Strotos, G., Nikolopoulos, N. & Kakaras, E., 2019, "Improved droplet breakup models for spray applications," International Journal of Heat and Fluid Flow, 76, 274–286.
Sterling, A.M. and Sleicher, C.A., 1975. The instability of capillary jets. Journal of Fluid Mechanics, 68(3), pp.477-495.
Stevenin, C., Béreaux, Y., Charmeau, J.-Y., Balcaen, J., 2015. Shaping air flow characteristics of a high-speed rotary-bell sprayer for automotive painting processes. J. Fluids Eng., 137 (11), 111304.
Subbotin, A.V. and Semenov, A.N., 2018. Micro-cones on a liquid interface in high electric field: Ionization effects. Physics of Fluids, 30(2), p.022108.
Suzen, Y., Huang, G., Jacob, J. and Ashpis, D., 2005, June. Numerical simulations of plasma based flow control applications. In 35th AIAA Fluid Dynamics Conference and Exhibit (p. 4633).
Sumiyoshi, T., 2003. Electrostatic spray device, WO 03/072263 A1.
Taglia, C. D., 2003, "Numerical Investigation of the Non-Reacting Unsteady Flow Behind a Disk Stabilized Burner With Large Blockage," Ph.D. Thesis, Technische Wissenschaften ETH, Zurich.
Tanasawa, Y., Miyasaka, Y., Umehara, M., 1978. Effect of shape of rotating disks and cups on liquid atomization. In: Proceedings of the 1st International Congress on Liquid Atomization and Spray Systems, pp. 165–172.
Tanasescu, F.T., Cramariuc, R., Toma, I. and Ionescu, I., 1989. Charged particle trajectories in electrostatic fields. Journal of Electrostatics, 23, pp.453-462.
Tanner, F.X., 1997. Liquid jet atomization and droplet breakup modeling of non-evaporating diesel fuel sprays. SAE transactions, pp.127-140.
Taylor, G.I., 1950. The instability of liquid surfaces when accelerated in a direction perpendicular to their planes. I. Proceedings of the Royal Society of London. Series A. Mathematical and Physical Sciences, 201(1065), pp.192-196.
Terebessy, T., Sumitomo Chemical Co Ltd, 2019. Electrostatic atomizer, and method for electrostatically atomizing by use of the same. U.S. Patent 10,179,338.
Toljic, N., Castle, G.S.P. and Adamiak, K., 2010. Charge to radius dependency for conductive particles charged by induction. Journal of Electrostatics, 68(1), pp.57-63.
Toljic, N., Adamiak, K., Castle, G.S.P., Kuo, H.-H., Fan, H.-T., 2011. Three-dimensional numerical studies on the effect of the particle charge to mass ratio distribution in the electrostatic coating process. J. Electrostat. 69, pp. 189–194.

Toljic, N., Adamiak, K., Castle, G.P., Kuo, H.H.H. and Fan, H.T.C., 2012. 3D numerical model of the electrostatic coating process with moving objects using a moving mesh. Journal of Electrostatics, 70(6), pp.499-504.

Toljic, N., Adamiak, K., Castle, G.S.P., Kuo, H.H.H. and Fan, H.T.C., 2013. A full 3D numerical model of the industrial electrostatic coating process for moving targets. Journal of Electrostatics, 71(3), pp.299-304.

Tolman, R.C., 1949. The effect of droplet size on surface tension. The journal of chemical physics, 17(3), pp.333-337.

Thomas, A., Saleh, K., Guigon, P. and Czechowski, C., 2008, December. Tribocharging behaviour of automotive powder coatings. In Journal of Physics: Conference Series (Vol. 142, No. 1, p. 012031). IOP Publishing.

Tsang, C. W., Trujillo, M. F., & Rutland, C. J. 2014. Large-eddy simulation of shear flows and high-speed vaporizing liquid fuel sprays. Computers & Fluids, 105, pp. 262-279.

Tsubakino, D., Tanaka, Y. and Fujii, K., 2007. Effective layout of plasma actuators for a flow separation control on a wing. In 45th AIAA Aerospace Sciences Meeting and Exhibit (p. 474).

Van den Bogaert, R. and Joos, P., 1979. Dynamic surface tensions of sodium myristate solutions. Journal of Physical Chemistry, 83(17), pp.2244-2248.

Van Doremalen, N., Bushmaker, T., Morris, D.H., Holbrook, M.G., Gamble, A., Williamson, B.N., Tamin, A., Harcourt, J.L., Thornburg, N.J., Gerber, S.I. and Lloyd-Smith, J.O., 2020. Aerosol and surface stability of SARS-CoV-2 as compared with SARS-CoV-1. New England Journal of Medicine, 382(16), pp.1564-1567.

van der Steur, G., EFC Systems Inc, 2006. Apparatus and method for electrostatic spraying of conductive coating materials. U.S. Patent 7,056,387.

Viti, V., Kulkarni, J., 2008. CFD analysis of the electrostatic spray painting process with a rotating bell cup. In: ILASS Americas, 21st Annual Conference on Liquid Atomization and Spray Systems, Orlando, Florida, USA.

Viti, V., Kulkarni, J., 2008. CFD analysis of the electrostatic spray painting process with a rotating bell cup. In: ILASS Americas, 21st Annual Conference on Liquid Atomization and Spray Systems, Orlando, Florida, USA.

Wan, M.P., Chao, C.Y.H., Ng, Y.D., Sze To, G.N. and Yu, W.C., 2007. Dispersion of expiratory droplets in a general hospital ward with ceiling mixing type mechanical ventilation system. Aerosol Science and Technology, 41(3), pp.244-258.

Wan, M. P. & Chao, C. Y. H., 2007. Transport characteristics of expiratory droplets and droplet nuclei in indoor environments with different ventilation airflow patterns. Journal of biomechanics engineering, 129, 341–353.

Wang, S., 2004. Method and apparatus for electrostatic spray, WO 2004/041443 A2.

Weber, C, 1931. Disintegration of liquid jets, Z. Angew, Math. Mech., vol. 11, No. 2, pp.136-159.

Wells, W.F., 1934. ON Air-Borne Infection: Study II. Droplets and Droplet Nuclei. American journal of Epidemiology, 20(3), pp.611-618.

Wilson, J., Grib, S., Darwish Ahmad, A., Renfro, M., Adams, S. and Salaimeh, A., 2018. Study of near-cup droplet breakup of an automotive electrostatic rotary bell (esrb) atomizer using high-speed shadowgraph imaging. Coatings, 8(5), p.174.

World Health Organization, 2002. Active ageing: A policy framework (No. WHO/NMH/NPH/02.8). Geneva: World Health Organization.

World Health Organization (WHO), 2020. Advice for public – maintain at least 1 metre (3 feet) distance between yourself and anyone who is coughing or sneezing. Available at: https: //www.who.int/emergencies/diseases/novel-coronavirus-2019/advice-for-public.

Wu, B., Gao, C., Liu, F., Xue, M. and Zheng, B., 2019. Simulation of NACA0015 flow separation control by burst-mode plasma actuation. Physics of Plasmas, 26(6), p.063507.

Xie, X., Li, Y., Sun, H. and Liu, L., 2009. Exhaled droplets due to talking and coughing. Journal of the Royal Society Interface, 6(suppl_6), pp.S703-S714.

Yagiz, B., Kandil, O. and Pehlivanoglu, Y.V., 2012. Drag minimization using active and passive flow control techniques. Aerospace Science and Technology, 17(1), pp.21-31.

Yagiz, B., Kandil, O. and Pehlivanoglu, Y.V., 2012. Drag minimization using active and passive flow control techniques. Aerospace Science and Technology, 17(1), pp.21-31.

Yan, J., Grantham, M., Pantelic, J., de Mesquita, P.J.B., Albert, B., Liu, F., Ehrman, S., Milton, D.K. and EMIT Consortium, 2018. Infectious virus in exhaled breath of symptomatic seasonal influenza cases from a college community. Proceedings of the National Academy of Sciences, 115(5), pp.1081-1086.

Yasumura, K., Saito, Y., Shoji, M., Matsushita, Y., Aoki, H., Miura, T., Ogasawara, S., Daikoku, M., Shirota, M., Inamura, T., 2011a. Development of quantitative evaluation method for droplet behavior with high speed rotary bell-cup atomizer. Kagaku Kogaku Ronbunshu, 37, pp. 296–304.

Yasumura, K., Saito, Y., Shoji, M., Matsushita, Y., Aoki, H., Miura, T., Ogasawara, S., Daikoku, M., Shirota, M., Inamura, T., 2011b. A numerical investigation of the factor decreasing transfer efficiency in a high-speed rotary bell-cup atomizer. Kagaku Kogaku Ronbunshu, 37, pp. 251–260.

Ye, Q., Steigleder, T., Scheibe, A. and Domnick, J., 2002. Numerical simulation of the electrostatic powder coating process with a corona spray gun. Journal of Electrostatics, 54(2), pp.189-205.

Ye, Q. and Domnick, J., 2003. On the simulation of space charge in electrostatic powder coating with a corona spray gun. Powder technology, 135, pp.250-260.

Ye, Q., Domnick, J. and Scheibe, A., 2003, June. Numerical simulation of spray painting in the automotive industry. In Proceedings of the 1st European Automotive CFD Conference Bingen, Germany.

Ye, Q., Domnick, J., Scheibe, A. and Pulli, K., 2005. Numerical simulation of electrostatic spray-painting processes in the automotive industry. In High Performance Computing in Science and Engineering'04 (pp. 261-275). Springer, Berlin, Heidelberg.

Ye, Q, Shen, B, Tiedje, O, Bauernhansl, T, Domnick, 2015. J, Numerical and Experimental Study of Spray Coating Using Air-Assisted High Pressure Atomizers. At. Sprays, 25 (8) 643–656.

Yu, H., Goldsworthy, L., Ghiji, M., Brandner, PA., Garaniya, V. 2017. A parallel volume of fluid-Lagrangian Parcel Tracking coupling procedure for diesel spray modelling. Comput Fluids, 150, pp. 46–65.

Yu, H. and Zheng, J., 2020. Numerical investigation of control of dynamic stall over a NACA0015 airfoil using dielectric barrier discharge plasma actuators. Physics of Fluids, 32(3), p.035103.

Zhang, X., Cui, Y.D. and Li, H.X., 2021. Acoustic streaming flow generated by surface dielectric barrier discharge in quiescent air. Physics of Fluids, 33(5), p.057117.

Zeleny, J., 1917. Instability of electrified liquid surfaces. Physical review, 10(1), p.1.

Zhao, S., Castle, G.P. and Adamiak, K., 2005. Comparison of conduction and induction charging in liquid spraying. Journal of Electrostatics, 63(6-10), pp.871-876.

Zhao, B., Zhang, Z. and Li, X., 2005. Numerical study of the transport of droplets or particles generated by respiratory system indoors. Building and environment, 40(8), pp.1032-1039.

Zheng, J.G., Cui, Y.D., Zhao, Z.J., Li, J. and Khoo, B.C., 2016. Investigation of airfoil leading edge separation control with nanosecond plasma actuator. Physical Review Fluids, 1(7), p.073501.

Zhu, S., Kato, S. and Yang, J.H., 2006. Study on transport characteristics of saliva droplets produced by coughing in a calm indoor environment. Building and environment, 41(12), pp.1691-1702.

Zuzio, D., Estivalezes, J.-L. & Dipierro, B. 2017. An improved multiscale Eulerian– Lagrangian method for simulation of atomization process. Comput. Fluids, 176 (4), pp. 285-301.

Appendix A

Publications and Achievements During Current Project

A.1 Articles in international journals

1. Pendar, M.R. and Páscoa, J.C., 2019. Numerical modeling of electrostatic spray painting transfer processes in rotary bell cup for automotive painting. International Journal of Heat and Fluid Flow, 80, p.108499.

2. Pendar, M.R. and Páscoa, J.C., 2020. Atomization and spray characteristics around an ERBS using various operational models and conditions: numerical investigation. International Journal of Heat and Mass Transfer, 161, p.120243.

3. Pendar, M.R. and Páscoa, J.C., 2020. Numerical modeling of the distribution of virus carrying saliva droplets during sneeze and cough. Physics of Fluids, 32(8), p.083305.

4. Pendar, M.R. and Pascoa, J., 2019. Numerical Investigation of Electrostatic Spray Painting Transfer Processes for Vehicle Coating. SAE International Journal of Advances and Current Practices in Mobility, 2(2019-01-1856), pp.747-754.

5. Pendar, M.R. and Páscoa, J.C., 2021. Numerical analysis of charged droplets size distribution in the electrostatic coating process: Effect of different operational conditions. Physics of Fluids, 33(3), p.033317.

6. Pendar, M.R. and Páscoa, J.C., 2021. Numerical Investigation of Plasma Actuator Effects on Flow Control over a Three-dimensional Airfoil with a Sinusoidal Leading Edge. Journal of Wind Engineering & Industrial Aerodynamics (Under Review), n◦ pages (42).

A.2 Articles in international conferences

1. Pendar, M.R. and Páscoa, J.C., Study of droplet characteristics and spray deposition during coating produced by an electrostatic rotary bell sprayer on OpenFoam. Canadian Society for Mechanical Engineering (CSME) International Congress, 2020.

2. Pendar, M.R. and Pascoa, J., 2021. Numerical Simulation of the Electrostatic Coating Process: the Effect of Applied Voltage, Droplet Charge and Size on the Coating Efficiency (No. 2021-01-0022). SAE Technical Paper.

3. Pendar, M.R. and Pascoa, J., 2021. Bioinspired Study of the Plasma Actuator Effect on the Flow Characteristics of an Airfoil with Wavy Leading Edges (No. 2021-01-0016). SAE Technical Paper.

A.3 Patent

1. Pendar, M.R., Rodrigues, F. and Pascoa, J., 2021. Electrostatic Sprayer Based on High-voltage Retractable Blades or High-voltage Adjustable Control Ring, Application Ref.: PAT 117317 L.